UNIVERSITY OF SOUTHAMPTON

FACULTY OF ENGINEERING, SCIENCE AND MATHEMATICS

INSTITUTE OF SOUND AND VIBRATION RESEARCH

ACOUSTIC SENSING OF RENAL STONE FRAGMENTATION IN EXTRACORPOREAL SHOCKWAVE LITHOTRIPSY

by

Fiammetta Fedele

Thesis submitted for the partial fulfilment of the requirements for the degree of Doctor of Philosophy

University of Southampton

June 2008

Abstract

UNIVERSITY OF SOUTHAMPTON

FACULTY OF ENGINEERING, SCIENCE AND MATHEMATICS

INSTITUTE OF SOUND AND VIBRATION RESEARCH

Doctor of Philosophy

ACOUSTIC SENSING OF RENAL STONE FRAGMENTATION IN EXTRACORPOREAL SHOCKWAVE LITHOTRIPSY

by Fiammetta Fedele

This thesis describes the research carried out by the author on the exploitation of acoustic emissions detected during extracorporeal shockwave lithotripsy (a non-invasive procedure for the treatment of urinary stones) to develop a new diagnostic system. The work formed part of a research project on lithotripsy undertaken by the University of Southampton in collaboration with Guy's and St Thomas' NHS Foundation Trust (London) and a UK based company, Precision Acoustics Ltd (Dorchester). It takes to a clinical conclusion the proposition made by Leighton and Coleman in 1992 that it might be possible to build a sensor which would automatically exploit these passive acoustic emissions to monitor the efficacy of a lithotripsy treatment. The work, predominantly experimental, involved both *in vitro* and *in vivo* investigations. In particular, a first prototype diagnostic system (i.e. sensor plus analysis software) was developed and tested *in vitro* during trials which included the use of a novel cavitation sensor (on loan from the National Physical Laboratory, Teddington) and stone phantoms designed by the author. This initial system was, then, refined and tested during clinical trials that involved 130 patients. A preliminary trial on 51 patients aimed at refining the system and gathering knowledge on the features of emissions recorded *in vivo* to produce an on-line monitoring system. This trial was followed by other two trials that compared the output of the on-line acoustic system against the 'gold standard' X-Ray assessment of treatments outcomes. The former of these two trials involved 30 patients, and empirically defined the values of the key parameters (identified during the *in vitro* tests) that would be used as the basis of the diagnosis. In particular, a classification rule of treatments as being *successful* or *unsuccessful* was identified, and shown to agree significantly (kappa=0.95) with the 'gold standard' follow-up assessment. The latter trial tested the final system on 49 patients and confirmed an accurate treatment classification (kappa=0.94) in terms of the *successful*/*unsuccessful* criterion.

Table of contents

List of figures

List of tables

List of accompanying material

- CD with SEAC software and SEAC demo for *successful* treatment

Acknowledgements

It has been six exciting years and so many people have accompanied me in this journey that I am afraid to forget to thank someone! Please forgive me in advance if I do so.

First, I would like to thank Professor Timothy Leighton, my PhD supervisor, and Dr Andrew Coleman, my manager at Guy's and St Thomas' NHS Trust, for all the support received. Tim, Andy thanks for giving me the great opportunity of working with you. You both have taught me many lessons ranging from principles of science to a new way of approaching every day life. I would also like to thank Mrs Siân Leighton for her great and kind moral support. The whole experience, of course, would not have been possible without the funding received by The Engineering and Physical Science Research Council (grant numbers GR/N19243/01 and EP/D503310/1); therefore the council has all my gratitude.

At both institutions where I have been working, the Institute of Sound and Vibration (ISVR) and Guy's and St Thomas' NHS Foundation Trust (GSTT) I have received great support.

In particular, at ISVR I would like to thank Professor Paul White, Dr David Simpson, Dr Christopher James and Dr Christian Hesse for their advice on signal processing. I would like to thank Dr Cary Turangan and Dr Riza Jamaluddin for their advice on computational fluid dynamics in lithotripsy. I would like to thank Professor Victor Humphrey and Mr Daniel Finfer for equipment loan and for their precious advice on data acquisition and interfacing. I would also like to thank Mrs Sue Brindle for her advice on administrative matters. Finally my eternal gratitude goes to Mrs Maureen Mew for proof reading the English of this thesis. Thanks Maureen, I could not have done it without you!

At GSTT allow me to thank first Dr Keith Ison, Head of the Medical Physics Department, and Mr. Jonathan Glass and Mr Richard Tiptaft, Heads of the Urology Department, for granting me consent to perform my experiments in their departments, for their support and advice. I would then like to thank Mr Simon Ryves, Ms Debbie Phillips and Mr Timothy

Jessop at the Stone Unit GSTT, who shared with me the experience of the clinical trials, for their support and their advice on the clinical aspects of the lithotripsy procedure. My special thank you is reserved for the research nurse, Miss Catherine McCarthy, for helping me in the last stage of the project with the acquisition of data from patients. Thanks Cat, it was a nice and refreshing experience working with you! I need then to thank all the staff at Medical Physics who have given me technical support of any form. I would like to thank Mr Barry Waldron, previous Head of the Biomedical Engineering Section who unfortunately is not anymore among us, for his advice and support in solving matters arising during RS232 communication between testing equipment. Barry, I hope this thank you will reach you! I would like to thank Mr John Pilmer, Mr Phil Halsted, Mr Mick Kelly, Mr Phil Sands, Mr Steve Turner and Mr Mark Stanton at the Mechanical Workshop for manufacturing tools and repairing equipment. I would also like to thank Mr Rashid Brora, Mr Fuat Zorba, Mr Terry Gorman, Mr Tony Beckett and Mr Mo Elazoui at the Electronic Equipment Management Service for repairing and safety testing of electronic equipment. I would also like to thank Mr Ian Miller and Mr Lou Boddie, at Radiotheraphy Equipment Servicing, for repairs and testing on the experimental shockwave source. I would like to thank Dr Peter Rudd in Radiotherapy and Mr Tony Page in Radiotheraphy Equipment Servicing, for lending me their picture scanners. Finally, a special thank you goes to thank Prof. MinJoo Choi, Visiting Professor at GSTT, for his support and his advice on shockwaves

The first part of this work would not have been possible without support from the National Physical Laboratory. In particular, I would like to thank Dr Bajram Zequiri, Ms Catherine Bickley and Dr M Hodnett for lending me the novel cavitation sensor and for their advice in the use of experimental shock sources and acoustic measurements.

A constant guide in the development of the several prototypes has then been Dr Andrew Hurrell at Precision Acoustics Ltd. Thanks Andrew! I would also like to thank all the rest of the staff at PAL for their support and for making the different prototypes, in particular Ms Terri Gill and Mr David Bell.

I would also like to thank Dr Antonio De Stefano, at Portsmouth NHS Trust, for his help in designing the SEAC interface and Mr Colin McKinnon (Centre for Innovations and Research, University of Southampton) and Mr Terry Parlett (Intellectual Property Officer, Guy's & St Thomas' NHS Trust) for organising commercial contracts.

Finally yet importantly, in my list of acknowledgments are all those who have given me their constant moral support. In particular, my husband Antonello, who has almost lived a second PhD experience with me, and both my parents. I would also like to thank for their support my relatives in law: Franco, Rosetta, Alberto and Linda and my friends Nunzia, Giusy, Anita, Guglielmo, Gianluca, Maria, Mario, Anna, Silvia, Paolo, Elena, and Leonardo. Finally my everlasting gratitude is for my colleagues at work, Dr Paul Freeman, Dr Prashant Verma (now at Northern General Hospital, Sheffield) and Mr Stephen Steel for their daily support and their advice.

TO YOU ALL *GRAZIE*[1]!

[1] 'Grazie' means 'thank you' in Italian, which is the mother language of the author.

List of symbols

A	Empirical constant of the liquid used in the Tait equation (7)
Avg	Operation of statistical average
$\mathbf{a_j'}_{j=1..m}$	Row vector $[a_{j1}, a_{j2},..a_{jn}]$
a	Correction constant in the van der Waals equation of state for a real gas (18)
$a_{ij\ i=1..n\ j=1..m}$	Generic parameter used in the principal components decomposition (48)
$a_{ri\ i=0..5}$	Parameters of the AR parametric spectrum (61)
B	Empirical constant of the liquid used in the Tait equation (7)
b	Correction constant in the van der Waals equation of state for a real gas (18)
$\mathbf{C}$	Covariance matrix
C	Value assumed by the speed of sound in a liquid (c) at the surface of a bubble.
C_i	Initial concentration of the gas in a liquid
C_s	Saturation concentration of the gas in a liquid
c	Velocity of sound in a liquid
c_L	Longitudinal velocity of sound in a medium
c_0	Speed of sound in the liquid at infinitesimal amplitudes
cov	Covariance function
c_T	Transverse velocity of sound in a medium
D	Diameter of soda lime glass ball
D_c	Diameter of the coil in the electromagnetic source
D_{eq}	Equivalent pore diameter defined in Equation (26)
D_g	Diffusion constant of a gas in a liquid
D_M	Maximum distance between two packed spheres
D_{PV}	Diameter of the PVdF element part of the passive acoustic prototype. Equal to half of the maximum allowed difference between two paths of an acoustic emission propagating from the kidney to the sensor (Figure 7.3)

D_p	Distance between two packed spheres
D_{pp}	Diameter of a ping-pong ball
D_1	Generic diameter of a soda lime glass ball
D_2	Generic diameter of a soda lime glass ball equal to $2D_1$
D_3	Generic diameter of a soda lime glass ball equal to $4D_1$
d	Position along the x-axis of the sensor developed in collaboration with Precision Acoustic during *in vitro* experiments
d_i	Duration of the i^{th} burst in the secondary acoustic emission, with $i = 1, 2$
d_V	Indentation of a Vicker's Intender
d_1	Duration of the first burst in the secondary acoustic emission
d_2	Duration of the second burst in the secondary acoustic emission
F	Stone fragmentation ratio
FP_1	Number of first bursts of emissions in a sample set whose length was overestimated by the detection algorithm
$FP_1\%$	Percentage of first bursts of emissions in a sample set whose length was overestimated by the detection algorithm
FP_2	Number of second bursts of emissions in a sample set that was wrongly detected
$FP_2\%$	Percentage of second bursts of emissions in a sample set that was wrongly detected.
F_S	Sampling frequency
F_{Sd}	Sampling frequency after decimation
f	Frequency
f_c	Cut-off frequency of a filter at 3 dB
f_{HI}	Frequency that separates the LF and HF bands (400 kHz)
f_{max}	Maximum frequency present in a signal
f_R	Frequency of the maximum amplitude in the respiratory lobe in the power spectrum of m_1
f_0	Resonating frequency of a bubble pulsator

f_{0i}	Central frequency of the i^{th} burst in the secondary acoustic emission
f_{0S}	Central frequency of the shock wave
f_{01}	Central frequency of the first burst in the secondary acoustic emission
f_{02}	Central frequency of the second burst in the secondary acoustic emission
G	Invariant of the bubble motion defined in Equation (11)
H	Enthalpy of a liquid
h	Function used in the Gilmore model of bubble dynamics and defined by Equation (22)
I	Power distribution function of the acoustic emission
I_i	Power distribution function of the burst i, with $i = 1, 2$
I_c	Electric current
ku_i	Kurtosis of the i^{th} burst in the secondary acoustic emission, with $i = 1, 2$
ku_1	Kurtosis of the first burst in the secondary acoustic emission
ku_2	Kurtosis of the second burst in the secondary acoustic emission
L	Length of each of the N segments in which a signal q is divided to estimate its PSD
L_1	Possible path followed by an acoustic emission propagating from the kidney to the acoustic sensor on the surface of a patient's torso (Figure 7.3)
L_2	Possible path followed by an acoustic emission propagating from the kidney to the acoustic sensor on the surface of a patient's torso (Figure 7.3)
M	Number of moles of the gas within a bubble
M_i	Initial number of moles of the gas within a bubble
m	Number of principal components used in (48)
m_1	Maximum amplitude of the first burst in the secondary acoustic emission
m_2	Maximum amplitude of the second burst in the secondary acoustic emission
N	Number of segments in which a signal q is divided to estimate its PSD
N_{FFT}	Number of points used for FFT calculations
N_s	Number of measurements made under the same conditions
n_c	Number of coil turns in the solenoid of the EM source

n_T	Empirical constant used in the Tait equation (7)
P	Ambient pressure of the fluid surrounding a bubble
P_g	Pressure of the gas inside a bubble
P_{gi}	Initial pressure of the gas inside a bubble
P_{ld}	Indenter load
$P(R)$	Pressure of the liquid at the bubble wall
$P_r(t)$	Pressure irradiated at the distance r from the surface of a bubble at the time t
P_v	Pressure of the vapour inside a bubble
P^+	Peak-positive pressure of a lithotripter pulse
P^-	Peak-negative pressure of a lithotripter pulse
P_∞	Pressure of the liquid far from a bubble
p	Instantaneous pressure of a liquid
$p_a(t)$	Acoustic emission
p_{EM}	Pressure produced by an EM source
$\bar{p}_i$	Average amplitude of the i^{th} burst in the secondary emission
p_{id}	Ideal lithotripter pulse
p_o	Instantaneous pressure of a liquid outside a bubble
$\|Q_{\Delta i}(f)\|$	Modulus of the Amplitudes Spectrum of the i^{th} segment (of duration Δ) of the signal q
$\boldsymbol{q}$	Column vector $[q_1, q_2,..q_n]'$
q	Stochastic signal
$q(t)$	Stochastic signal q as a function of the time t
$q_T(t)$	Stochastic signal $q(t)$ of duration T
$q_{Wi}(n)$	i^{th} windowed segment (of duration Δ) of the signal q
$q_1, q_2, .. q_n$	Generic variables describing a phenomenon
$q_{\Delta i}$	segment i^{th} (of duration Δ) of the signal q
R	Instantaneous bubble radius
$\mathcal{R}$	Universal gas constant for an ideal gas (8.314 $JK^{-1}mol^{-1}$)

R_i	Initial bubble radius
R_0	Bubble equilibrium radius
R_{0i}	Time varying equilibrium radius of a bubble
r	Radial distance from the wall of a bubble
r_c^2	Square of the cross-correlation coefficient
r_{qq}	Autocorrelation function of the signal
$\boldsymbol{S}$	Correlation matrix
S	Sensitivity of the detection or classification algorithm
S_1	Sensitivity of the detection algorithm in identifying the 1st burst
S_2	Sensitivity of the detection algorithm in identifying the 2nd burst
$\tilde{S}$	PSD estimate of a signal q
SCL_1	Score Confidence level for TS_1
SCL_2	Score Confidence level for TS_2
S_p	Specificity of the classification algorithm
S_{qq}	PSD of a signal q
$\hat{S}_{qq_i}$	PSD of the i^{th} segment in the signal q, with $i = 1..N$
sk_1	Skewness of the first burst in the secondary emissions
sk_2	Skewness of the second burst in the secondary emissions
s_T	Statistical significance derived from t-test analysis (Section 6.3)
T	Generic time interval
T_g	Temperature of the gas inside a bubble
T_{gi}	Initial temperature of the gas inside a bubble
TN_1	Number of first bursts of emissions in a sample set that were correctly identified as absent
$TN_1\%$	Percentage of first bursts of emissions in a sample set that were correctly identified as absent
TN_2	Number of second bursts of emissions in a sample set that were identified as absent

TN_2%	Percentage of second bursts of emissions in a sample set that were identified as absent
TP_1	Number of first bursts of emissions in a sample set that were correctly Localised
TP_1%	Percentage of first bursts of emissions in a sample set that were correctly localised
TP_2	Number of second bursts of emissions in a sample set that were correctly localised
TP_2%	Percentage of second bursts of emissions in a sample set that were correctly Localised
TS_0	Treatment efficiency score given by the SEAC system exploiting rule (65)
TS_1	Treatment Score one based on the first opinion of a radiographer
TS_2	Treatment Score two based on the treatment follow-up assessment
t	Time
t_c	Collapse time calculated using the method proposed in this work (Section 5.2.5)
t_{co}	Collapse time estimation introduced by Coleman and Leighton (Section 3.2)
t_i	Central time of the i^{th} burst in the secondary acoustic emission, with i = 1, 2
$t_{i\min}$	Starting time of the i^{th} burst in the secondary acoustic emission, with i = 1, 2
$t_{i\max}$	Ending time of the i^{th} burst in the secondary acoustic emission, with i = 1, 2
$t(r)$	Time istant at which a pressure perturbation is at a distance r from the wall of the bubble
$t(R)$	Time istant at which a pressure perturbation is at a distance R from the wall of the bubble
t_T	Parameter used in t-test (Section 6.3)
t_1	Central time of the first burst in the secondary acoustic emission
t_2	Central time of the second burst in the secondary acoustic emission
U	Velocity of the wall of a bubble in the liquid ($dp/d\rho$)
V_g	Volume of the gas inside a bubble

V_{gi}	Initial volume of the gas inside a bubble
VH	Vickers' (stone) Hardness
W	Weight of a ping-pong stone phantom
W_0	Weight of a soda lime ball the same size as a ping-pong ball
W_{100}	Weight of an empty ping-pong ball
α_1	Time constant used in the equation of the ideal lithotripter pulse (23)
α_2	Time constant used in the equation of the ideal lithotripter pulse (23)
βu	Function of r defined in Equation (13)
βU	Function of r defined in Equation (14)
γ	Ratio of specific heat at pressure and volume constant for a gas
Δ	Duration of the segments in which a signal q is divided to estimate its PSD
Δf	Frequency resolution
ϕ	Generic feature extracted from an acoustic emission
$\bar{\phi}_i$	Statistical average of the generic feature ϕ over the set i
$\bar{\phi}_j$	Statistical average of the generic feature ϕ over the set j
η	Gas polytrophic constant
η_p	Packing ratio of a sphere
λ	Wavelength
λ_{0S}	Main wavelength of a shockwave (cxf_{0S})
λ_{g1}	Lagrange multiplier
λ_{g2}	Lagrange multiplier
λ_{3M}	Acoustic wavelength at 3 MHz
μ_0	Induction constant (4πx10^{-7} Hm^{-1})
μ	Coefficient of shear viscosity of a liquid
ν_d	Number of degrees of freedom used in the evaluation of t-test results for paired data (Section 6.3.1)

ν_i	Number of degrees of freedom used in the evaluation of t-test results for independent data (Section 6.3.1)
θ	Angle between two paths at maximum distance, which can be followed with equal probability by emissions travelling from the kidney to the surface of the patient's torso (see Section 7.3.1)
ρ	Time varying density of a liquid
ρ_{gl}	Density of the soda-lime balls
ρ_0	Equilibrium density of the liquid
ρ_s	Density of a kidney stone
σ	Surface Tension of the liquid surrounding the bubble
σ_i	Standard deviation of the i^{th} burst in the secondary emission, with i = 1, 2
τ	Function used in the Gilmore model of bubble dynamics and defined by Equation (21)
$\boldsymbol{\zeta}$	Vector $[\zeta_1, \zeta_2, .. \zeta_m]'$
$\zeta_1, \zeta_2, .. \zeta_m$	Principal components describing a phenomenon
ψ	Dimensionless constant used in Equation (23) so that the ideal lithotripter pulse peak-positive pressure mathematically equals to P^+

List of abbreviations

A/D	Analogue to Digital conversion
AR	Auto Regressive
CFD	Computational Fluid Dynamics
COM	Calcium Oxalate Monohydrate (stone)
EH	Electrohydraulic
EM	Electromagnetic
EPSRC	Engineering and Physical Science Research Council
ESWL	Extra Corporeal Shock-Wave Lithotripsy
FFT	Fast Fourier Transform
FN	False Negatives in the detection (Section 5.2.1) or classification (Chapter 8 and Chapter 9) algorithm
FP	False Positives in the detection (Section 5.2.1) or classification (Chapter 8 and Chapter 9) algorithm
GSTT	Guy's and St Thomas' NHS Foundation Trust
HF	High Frequencies (band)
ISVR	Institute of Sound and Vibration Research
LF	Low Frequencies (band)
NHS	National Health System
NPL	National Physical Laboratory
PAL	Precision Acoustics Ltd
PC	Personal Computer
PCA	Principal Components Analysis
PMMA	Polymethyl methacrylate
PSD	Power Spectral Density
PVdF	Polyvinylidene Fluoride
PZ	Piezoelectric
SCL	Score confidence level

SEAC	Secondary Emissions Analysis in Clinic
TN	True Negatives in the detection (Section 5.2.1) or classification (Chapter 8 and Chapter 9) algorithm
TP	True Positives in the detection (Section 5.2.1) or classification (Chapter 8 and Chapter 9) algorithm
TS	Treatment Score

Chapter 1 Introduction

1.1 Introduction

This thesis describes the research carried out by the author on the exploitation of acoustic emissions detected during extracorporeal shockwave lithotripsy to develop a new diagnostic system. It takes to a clinical conclusion the proposition made by Leighton and Coleman in 1992 that it might be possible to build a sensor which would automatically exploit the passive acoustic emission to monitor the efficacy of a lithotripsy treatment [1-3]. The work, predominantly experimental, involved both *in vitro* and *in vivo* investigations. It formed part of a collaborative research project on lithotripsy undertaken by the University of Southampton in collaboration with Guy's and St Thomas' NHS Foundation Trust (London) and a UK based company, Precision Acoustics Ltd (PAL), Dorchester. The first *in vitro* part of the project involved also the National Physical Laboratory (NPL), which loaned one of its novel cavitation sensors [4-7] to the group. Ethical approval for the *in vivo* work was obtained (EC/3462 and 06/Q0702/12) and the project was sponsored by the EPSRC (GR/N19243/01 and EP/D503310/1; Principal Investigator, Prof. T.G. Leighton). Key results of other researchers in the team are outlined in the thesis. The original authors are clearly cited in the text.

1.2 Background

1.2.1 Extracorporeal shock wave lithotripsy

Extracorporeal shock wave lithotripsy (ESWL) is currently used in the non-invasive treatment of 90% of all kidney stones. Kidney stones represent a concretion of salts that, for metabolic reasons, have crystallized out of solution. Untreated, they can lead to severe pain, loss of renal function and even death.

In ESWL (Figure 1.1) thousands of externally generated shock waves are focused onto the stone so that it fragments into particles that are small enough to pass down the urinary tract or can be dissolved by drugs [8]. The stone may be localised using X-ray and/or Ultrasound imaging.

Figure 1.1: Extracorporeal shockwave lithotripsy. The patient lays down on the treatment table that is coupled to the shock source (a) by means of the water cushion (b). The stone targeting is done using (c) the x-ray and (d) ultrasound system. The photo was downloaded from the website of Storz Medical **http://www.storzmedical.ch/** and is published with Storz's permission.

Despite the wide-spread use of ESWL, the treatment may induce some collateral damage (haemorrhages, thrombi, arrhythmias, hypertension, reduction of renal functionality, infections [1, 9-13]). Most significantly the re-treatment rate is still around 50% [14-16] suggesting that stones either reform or are not fully fragmented.

1.2.2 Limitations

Patients undergo up to ten sessions of ESWL treatment before complete fragmentation is achieved [8, 16]. Re-treatment involves increased collateral damage to soft tissue [13]. It also means higher treatment costs for a hospital, as more resources (e.g., staff and theatre time) are required per patient, and longer waiting lists for the patients.

Treatments will be improved if the limitations of the present lithotripters are overcome. The main limitation of the current technology is the stone imaging system. Both X-ray and diagnostic ultrasonic systems are affected by alignment errors [17] such that shock wave focusing may be misdirected. The performance of the ultrasound system, for example, depends on the size of the stone and its location. A high degree of skill is needed to interpret such images [18]. X-ray images, whilst sometimes easier to interpret, cannot be used in all cases and could deliver an undesirable radiation exposure to the patient [19], which prevents its use for continuous monitoring.

In many cases, fragments remain grouped together following shock exposure. Neither X-ray nor ultrasound allow the operator to distinguish this situation from an intact stone. The urologist assesses whether the stone is breaking by observing changes in the density and size of the stone features in the X-ray image.

A very significant limitation of the current technology is the absence of any on-line objective and quantitative measure of the degree of fragmentation. This thesis examines, specifically, quantitative measures of stone fragmentation that can be used to monitor the treatments.

1.2.3 Quantitative approaches to 'treatment end-point' determination

It has been demonstrated that the shock-stone interaction produces audible sounds and expert lithotripter operators claim that they can recognise a 'hit' sound from a 'miss' sound [3, 20]. Olsson *et al.* [20] presented some preliminary results from sound recorded during the treatment of two patients, that showed that they could discriminate the two categories of sounds on the basis of their different frequency characteristics. In particular, a sound that the operator of the lithotripter had classified as a 'hit' was characterised by a predominant spectral component below 20 kHz (i.e. in the range of audible sounds). On the contrary, a 'miss' sound had most of its energy distributed at frequencies above 20 kHz (i.e. above human hearing). Olsson's study indicated that an automatic audio classifier system might have the potential to assist the operator in determining the end point of treatment. Such a system might also classify different kinds of stones from different sound spectra they emit [20]. Chang *et al.* [18, 21] developed a real-time tracking system for renal stones. This involved processing of the ultrasound image. The system increased the efficiency of a treatment by 45% when tested *in vitro* [18]. Bohris *et al.* [22] proved, *in vitro,* that ultrasound Doppler spectra assisted the identification of the targeted stones in cases where the conventional X-ray and ultrasound imaging gave dubious information. The system also provided information about the stone size and hence the grade of fragmentation. The origin of the change in the ultrasound Doppler signal was attributed to changes in the quantity of stone fragments and gas contained in the body fluids. Preliminary *in vivo* experiments performed by the same group [22] were in agreement with the *in vitro* results.

1.2.4 Mechanisms of stone fragmentation

Several studies indicate that both direct stress damage of the impacting shock and the indirect erosion caused by cavitation (which is the violent collapse of microscopic bubbles present in the body fluids or soft tissues surrounding the stone [3, 23, 24]) are necessary to obtain eliminable fragments [3, 9, 24-33]. The urinary stones are brittle materials, and therefore more fragile to tension than compression [9, 28-31, 33-35]. The initial fracture of a stone is caused by either spallation (which consists in tensile failure caused by reflection and phase inversion of the shock due to impedance mismatch between the stone and the surrounding medium), or failure due to compression induced tensile cracks [28-31]. The cavitational erosion, on the other side, has a fundamental role in reducing the initial fragments in fine passable ones [31]. Coleman, Crum and co-workers [1, 9, 24] proved the presence of cavitation during ESWL and were able to monitor it *in vivo* by the recording of the associated secondary acoustic emissions. This was achieved by placing a passive acoustic sensor on the patient's abdomen. It was also shown that cavitation was generated within regions of increased echogenicity in the ultrasound image [36]. Exploiting the same fact, Hausler *et al.* [37] developed a re-positioning system that used an ultrasound camera (made of an active ultrasound beam and a receiving matrix of piezoelectric transducers) to visualise the cavitation cloud produced at the focus of an experimental lithotripter.

1.2.5 Objectives of the Research

The primary objective of the research was to design an acoustic device to confirm the targeting and quantify the degree of fragmentation of the stone during ESWL.

The initial objectives of this study, therefore, were to examine the acoustic emission and its dependence on the quality of the targeting and on the degree of fragmentation of the stone. On the basis of these preliminary results the clinical diagnostic prototype was to be developed. A practical objective was to ensure that any design was optimised to provide a high signal to noise ratio and to be safe and effective in use.

An important component of the study, to achieve these objectives, was to process the acoustic signal in a manner that provided unequivocal results of targeting or stone fragmentation. In addition, the acquisition system was designed to be able to detect the acoustic scattering of the lithotripter shocks from the stone (Figure 3.2), which contains information about the size of the stone. Particular attention was paid to the design of the sensing elements. They are, in fact, the parts applied to the patient and need to be electrically safe and comfortable.

Finally the processing of the recorded acoustic signals was developed in order to recognise the two different components (cavitation and scattering) and to present the clinicians with a simple and clear output.

1.2.6 Thesis Plan

This Chapter introduces the project and its objectives.

-Chapter 2 provides an overview of clinical lithotripsy. The technique and the different available lithotripters designs are introduced. The different kinds of urinary stones are reported because their characteristics influence the output of the ESWL treatment. The mechanisms of fragmentation of the stone are presented.

-Chapter 3 describes the acoustic emission and the numerical code exploited in this study to simulate shock-bubble interactions. This is based on the Gilmore model[2] of bubble dynamics for describing a single bubble-shock interaction, and was previously implemented

[2] It will be shown in Chapter 3 that the code, though useful, suffers of some limitations. In particular, the model is limited by the assumption that the bubble environment is an infinite liquid. As part of the same EPSRC grant which funded this work (GR/N19243/01; Principal Investigator, Prof. T.G. Leighton), A more complex Free Lagrange code was developed [38-40] by Ball, Leighton and PhD students Turangan and Jamaluddin to simulate shock bubble interactions in proximity of a solid boundary (such as a kidney stone). The two elements of the project (this code development and experimentation) formed two halves of a coherent programme of work.

by Choi [41,42]. In this study, minor modifications were done on Choi's code to improve simulations based on measured shockwaves.

Chapters 4-9 concentrate on the original contribution of this thesis to the EPSRC project.

-Chapter 4 describes the three experimental components used to perform the preliminary *in vitro* experiments, first, a bench-top electromagnetic lithotripter designed at St Thomas', specifically for the EPSRC project; second, an experimental cavitation sensor, developed by Zequiri and collaborators [4-7] at the National Physical Laboratory (NPL), Teddington, which was used to detect the emission *in vitro*; third, the renal stone phantoms designed and exploited by the author.

-Chapter 5 describes the analysis processes applied to the experimental data and the related software application developed by the author using MATLAB™. All the described analyses represent an original contribution provided by this work. The description of the produced MATLAB™ software is reported in Appendix A.

-Chapter 6 gives the results of the analyses of the *in vitro* data. These results provide preliminary knowledge about the characteristics of the secondary emissions adjacent to stone samples that was used to design the clinical sensor and to develop the signal processing technique. Some comparison is made with theoretical predictions.

-Chapter 7 reports on the design of the proposed diagnostic system. First, the main hardware components are described: clinical sensors and signal preconditioning blocks. The design of these components (done in collaboration with Precision Acoustics Ltd (PAL), Dorchester) represents an original contribution to knowledge of this thesis. Second, a preliminary clinical trial on 51 patients that was used to refine and test the prototype is described. This trial, besides showing the potential of the prototype ultrasound system *in vivo*, constitute an original contribution, since little had previously been known about secondary acoustic emission obtained *in vivo*.

-Chapter 8 describes a second clinical study where the real time acoustic output of the system (during 30 treatments) is compared against the gold standard treatment follow-up assessment performed by the urologist several days after the procedure. The aim of this trial was to characterise acoustic emissions recorded during treatments where at least 50% of the stone has fragmented (indicated in this work as *successful* treatments). As a result of this characterisation, a set of rules upon which the effectiveness of each shock is estimated was established. These rules were incorporated in the monitoring system, which can estimate on-line the effectiveness of each shock and produce a feedback on the outcome of treatment, once a statistically significant number of shocks have been administered.

-Chapter 9 shows the results of a final clinical study. The real time binary treatment classification (*successful/unsuccessful*) of the system is compared against the gold standard treatment follow-up of 49 treatments. Some conclusions are drawn, then the chapter discusses future development of the prototype diagnostic system developed.

The project raised the interest of the media and lithotripter companies, and an addendum with copies of articles from newspapers and news websites is included at the end of the thesis (Appendix C). The developed system was nominated for the London NHS Innovator Awards 2007 (see website http://www.nhsinnovationslondon.com/events/31/).

Chapter 2 Extracorporeal shock wave lithotripsy

2.1 Introduction

The aim of this Chapter is to give a non expert reader basic information about the difficulties underlying clinical lithotripsy and the approach taken here to address these practical problems.

2.2 Lithotripsy

Extracorporeal shock wave lithotripsy (ESWL) is a common procedure for the non-invasive treatment of urinary stones and is also being introduced in the management of pancreatic and salivary calculi and some orthopaedic diseases [8, 43-45]. It has also been proposed for bactericidal, cancer and cardiac treatment [43, 46-51], although some of these applications remain experimental.

Through the use of ultrasound shocks, the practice of ESWL aims to break a stone (or stones) into fragments small enough (less than 1 mm in diameter) to be passed naturally by the body during urination or to be dissolved with drugs [8]. Usually several treatment sessions are necessary. Each session is performed as day surgery and lasts about half an hour, in which a total of 2000-3000 shocks are directed at the stone.

Figure 2.1 shows a schematic representation of the process. During the treatment the patient lies on a table that is coupled to a shock source via a water cushion. The source generates shocks with peak-positive pressure up to 100 MPa, for a duration of a few microseconds (Figure 2.2) and a pulse repetition rate of 60-120 shocks per minute [52, 53]. The shocks are focused on the stone, which is localised using X-ray and/or ultrasound imaging.

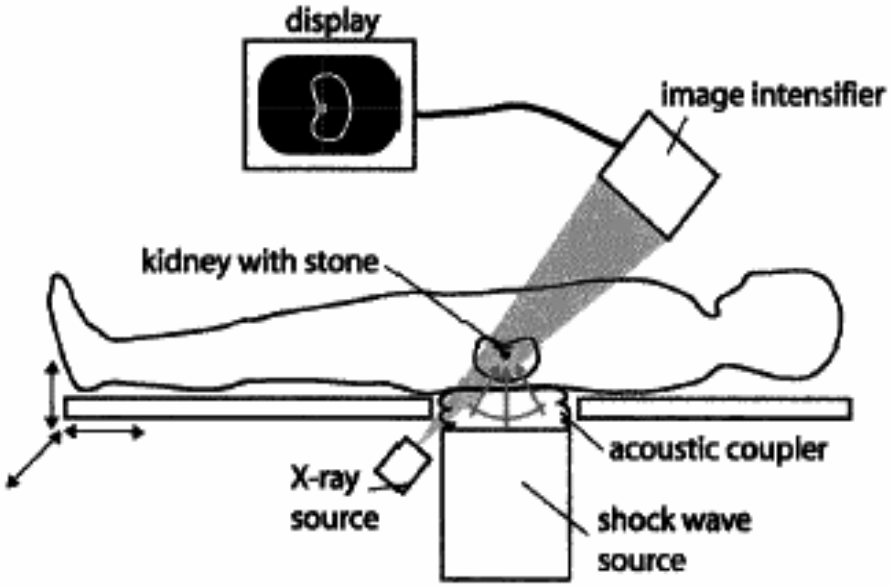

Figure 2.1: Schematic description of ESWL from Cunningham *et al*. 2001 [54]. Reprinted with permission of the Acoustic Bulletin.

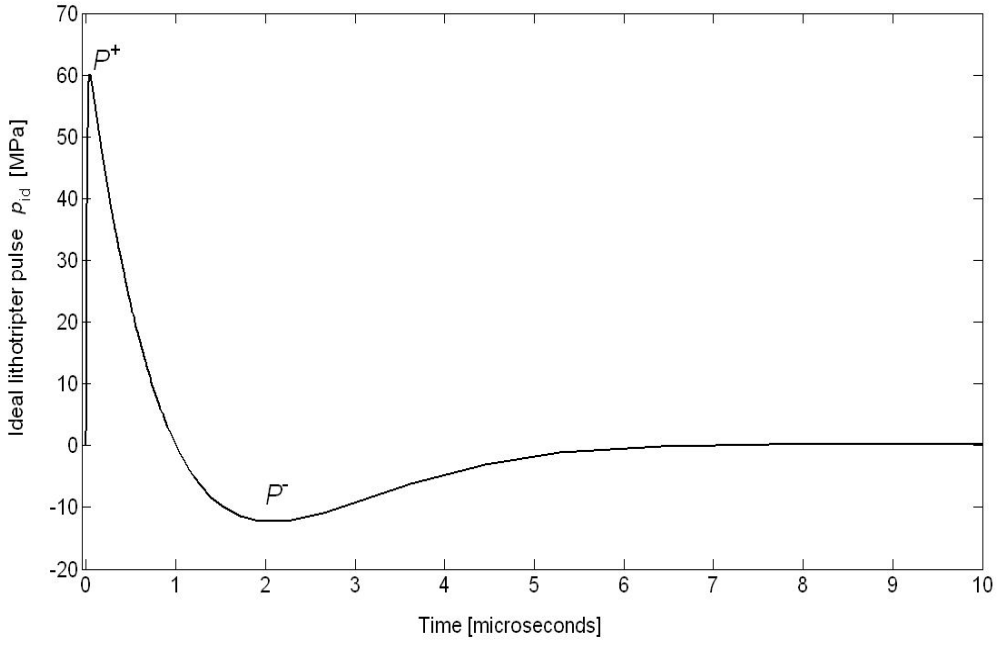

Figure 2.2: An idealisation of a lithotripter shock wave pressure pulse (after Church [55]).

Several types of shock generators have been produced over the years, using a range of mechanisms to convert electrical energy into acoustic pressures. These are categorised as: electrohydraulic (EH), piezoelectric (PZ) or electromagnetic (EM) [8, 52, 53, 55, 56]. The following subsections give details about these three configurations.

2.2.1 The electrohydraulic lithotripters

In the electrohydraulic (EH) lithotripters (Figure 2.3) the shock wave is generated through the discharge of a high voltage capacitor across the gap between two electrodes situated underwater. The electrode gap is located in one focus (Figure 2.3, F_1) of a metal reflector which is the shape of an incomplete ellipsoid, so that the emitted spherical wave converges at the position which would be occupied by the second focus (Figure 2.3, F_2) were the ellipsoid to be completed. The electrodes necessitate regular replacement because the high spark temperatures cause their vaporisation and erosion [57].

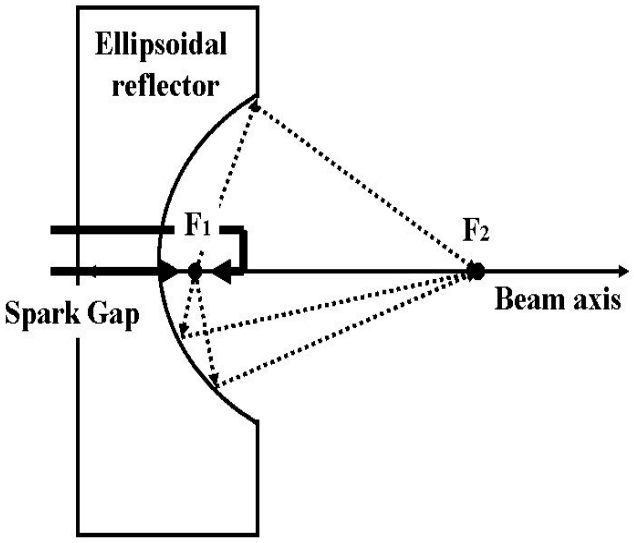

Figure 2.3: Elecrohydraulic lithotripter.

2.2.2 The piezoelectric lithotripters

Piezoelectric (PZ) lithotripters use an array of small ceramic crystals (about 50 mm diameter) mounted on a hemi-spherical dish filled with water so that they are all at the same distance from the focus of the lithotripter (Figure 2.4)**.** When these elements are driven simultaneously by the discharge of a high voltage capacitor, they generate waves that converge at the focus.

The wave energy released per generator area is low with this method because of the larger area of the generator area. Depending on the type of lithotripter, several hundreds or several thousands of piezoelectric crystals are needed to cause stone fragmentation [56]. The life of the crystals is limited by mechanical damage and electrical breakdown [56].

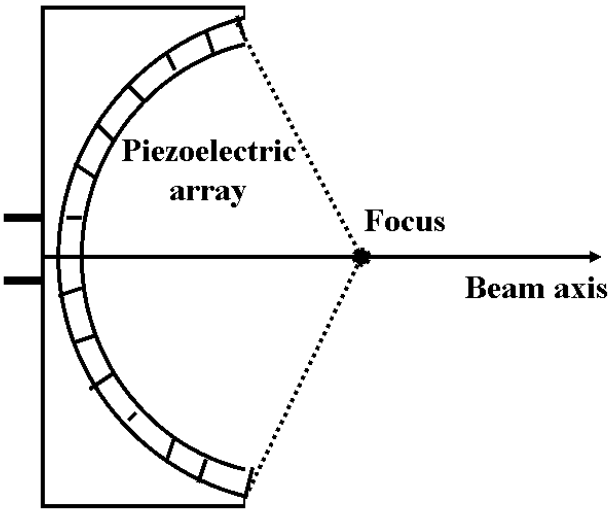

Figure 2.4: Piezoelectric lithotripter.

2.2.3 The electromagnetic lithotripters

Electromagnetic (EM) lithotripters exploit EM coupling. A high voltage capacitor is discharged through a coil that is close to a thin metal membrane placed in water (Figure 2.5). The coil and the membrane act as the primary and secondary coils of a transformer and a current is induced in the membrane. As a result the membrane (which can oscillate freely) is repelled by the coil and its movements generate a plane wave in water. The high amplitude plane wave that propagates through the shock tube is distorted by non-linear effects [33, 56-58]. That is to say, its compressive phase is amplified and its tensile part is attenuated (Figure 2.6). The waveform becomes "shocked" at a specific distance termed 'discontinuity length' [59].

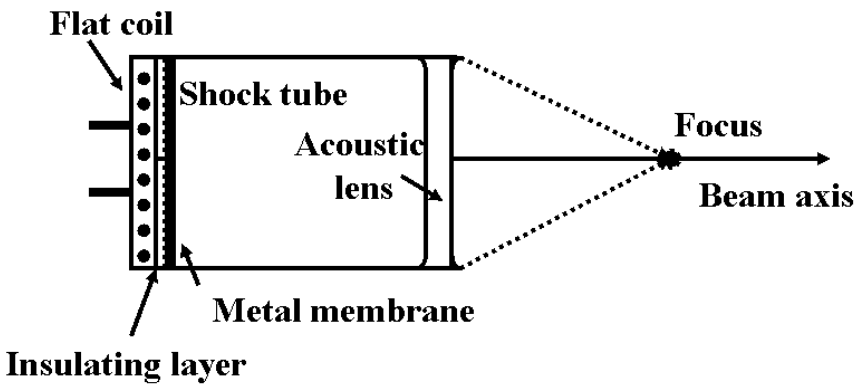

Figure 2.5: Electromagnetic lithotripter.

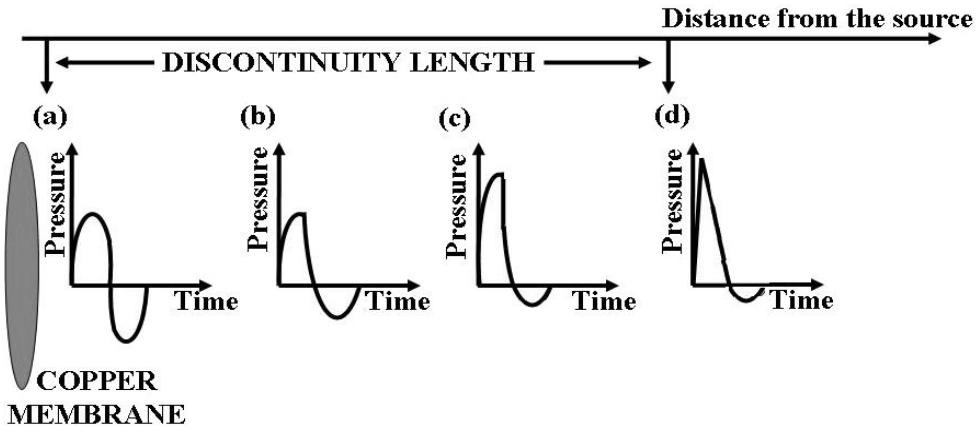

Figure 2.6: This plot shows a schematic representation of the non linear propagation of the ultrasound from the EM source membrane. The time histories of the pressure waveforms at different distances from the source are represented. At the source a sinusoidal wave (a) is produced, as the wave propagates, the waveform is distorted (b-c); until a distance termed 'discontinuity length' the waveform (d) becomes shocked.

The membrane is affected by the repeated mechanical impact limiting its lifetime [56]. However its replacement is less expensive than the spark gap in the EH lithotripters or the piezoelectric crystals in the PZ lithotripters.

2.3 Characteristics of the urinary stones

The effectiveness of ESWL treatment is strongly conditioned by the characteristics of the targeted stone. Several features of a stone that determine its fragility are: chemical composition, shape and volume, crystalline structure, size and distribution of flaws, microhardness, fracture strength and elasticity [9, 28].

In particular, urinary stones behave as brittle materials, and their fracture strength is highly influenced by the properties of their surface and those of the surrounding fluid [9, 28-31, 33-35]. Some researchers investigated the possibility of using X-ray scattering in order to determine the composition of calculi *in vivo* before the ESWL treatment [60]. Such analysis is not practicable under *in vivo* ESWL conditions.

The characteristics of the stones change according to their site in the urinary system. The various stones are described in the following subsections.

2.3.1 Kidney stones

The majority of kidney stones are calcium oxalate calculi (either in pure or admixed forms), which results in them being the hardest of all renal stones [61]. Struvite stones, made of magnesium phosphate and calcium apatite, are also common in the kidneys (and in many other parts of the body). The structure of both kinds of stones consists of an outer layer crust and an inner core (Figure 2.7).

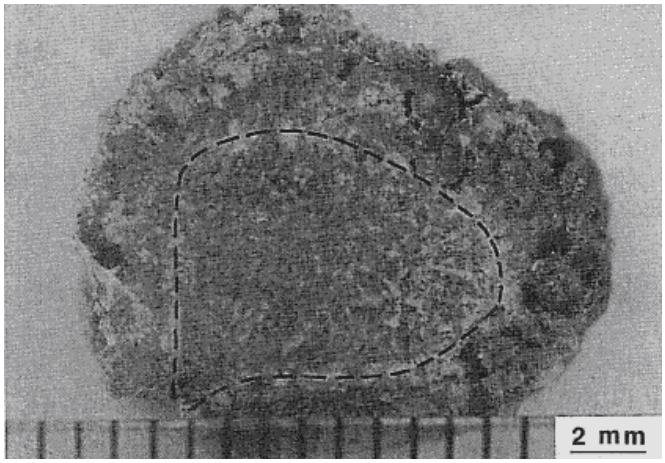

Figure 2.7: Optical micrograph of a calcium oxalate stone from Ebrahimi *et al*. [62]. Copyright © (1989, J. Biomed. Mat. Res.). Reprinted with permission of John Wiley & Sons, Inc. The dashed line indicates the boundary between the crust and the core.

The hardness[3] of dry calcium oxalate stones is between 68 and 85 kg mm^{-2} and it is reduced up to 50% after immersion in urine [61-63, 65, 66]. The hardness of Calcium Oxalate Monohydrate stones (COM) is reduced in urine regardless of the urine pH, while that of mixed calcium oxalate stones is further reduced if the urine pH is acid [65]. The struvite stones hardness is less or comparable to that of the oxalate stones [62].

[3] The hardness of a stone is measured compressing the stone with a known load using indenters. The area of the resulting surface indentation is measured using a microscope and the results are reported as load (kg) divided by indentation area (mm^2) [63]. Hence for a given load a small indentation indicates a harder stone. The conversion of microhardness measurements in applied pressures depends on the particular indenter and dwell time used [64].

Higher values of kidney stones hardness correspond to higher fracture strengths. Those for the human kidney have been reported to range from 0.45-2.9 MPa [61, 63, 65].

Ebrahimi *et al*. [62] studied the fracture behaviour of struvite and oxalate stones. They observed that both types of stones, when compressed, initially undergo a pseudo-elastic deformation but, as the load is increased, microcracks appear in the specimens. When the load reaches a value, denoted *maximum load* [62], pieces of the crust may be observed to separate from the core (Figure 2.8) of oxalate stones. In struvite samples, instead, the 'maximum load′ corresponds to the development of large cracks parallel to the compressive axis. Therefore the compressive strength of the struvite samples depends on the orientation of the lamellae relative to the loading axis.

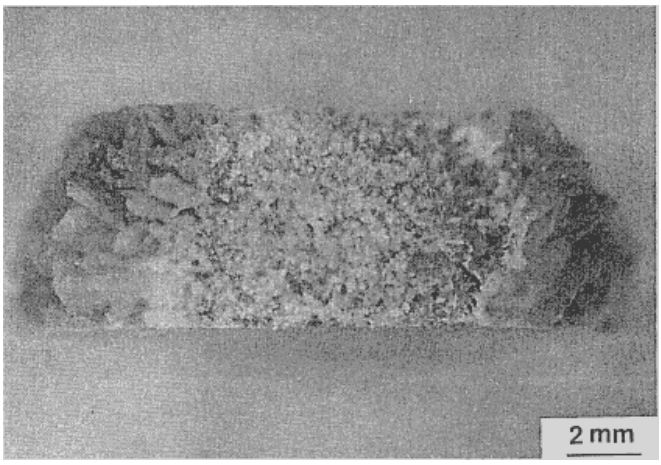

Figure 2.8: Optical micrograph of a calcium oxalate stone showing its side view after it was loaded beyond the *maximum load*. From Ebrahimi *et al*. [62]. Copyright © (1989, J. Biomed. Mat. Res.). Reprinted with permission of John Wiley & Sons, Inc.

Microscopic and optical analyses of oxalate stones [67] reveal the presence of an organic matrix with a bigger proportion in the surface (5.7%) than in the core (2.7%). This matrix is made of mucoproteins, mucopolysaccharides, inorganic material and bound water [67]. Richness in organic matrix in kidney stones can be associated with infections [67], but its role in the stone fracture behaviour is not clear.

Some studies concentrated on the measurements of the acoustic parameters of the renal stones, such as the velocity of sound [65, 66]. Sound speed values between 1500 m s^{-1} (for the softest stone) and 3000 m s^{-1} (for the hardest stones) were found [65, 66].

Interestingly, it has also, been discovered [68] that renal stones are piezoelectric in nature and that stress generates a voltage potential across them.

2.3.2 Biliary stones (Gallstone)

Gallstones can be classified in two groups: cholesterol gallstone (usually yellow) and pigment gallstones (usually black) [63]. Most gallstones have a hardness of about one order of magnitude lower than kidney stones [63]. However *in vitro* experiments [63] show that gallstones are more difficult to fragment during ESWL than are kidney stones. This confirms that the hardness is only one of the factors determining the fragility of the stone.

2.4 Stone phantoms

The development of urinary stone phantoms to carry out *in vitro* studies of the shock-stone interactions during ESWL is very important, because the success of the procedure has drastically reduced the availability of real stones for investigative purposes [62].

Artificial stone models made of the same materials as natural stone may be produced [64, 69, 70], but they are quite complicated to fabricate reproducibly and not commercially available. The phantom material most used in lithotripsy studies is 'plaster of Paris' which is cheap and can be easily moulded in different geometries and sizes [64, 69, 70]. Its acoustic properties

are quite similar to the struvite stones (Table 1) [64]. A commercial material recently used in ESWL is 'Begostone', a plaster produced for dental application [64], whose properties are very similar to those of the hardest COM stones (Table 1).

Materials	c_L **[m s^{-1}]**	c_T **[m s^{-1}]**	ρ_s**[kg m^{-3}]**	*VH* **[MPa]**
Plaster of Paris	2714±0.52	1369±0.15	1274±0.70	238±73
Begostone	4400±65	2271±18	2174±29	549±25
Struvite	2798±82	1634±25	1587±68	257±80
COM	4476±41	2247±14	1823±69	1046±88

Table 2.1: Properties of natural kidney stones and stone phantoms [64, 69]. The longitudinal acoustic velocity (c_L), the transverse acoustic velocity (c_T), the stone density (ρ_s) and the Vickers hardness[4] (*VH*) of the stone.

2.5 Mechanisms of stone fragmentation during ESWL

The physical mechanisms responsible for the stone fragmentation during ESWL are still subject to investigation. Nowadays most researchers agree that minute eliminable fragments are obtained through the joint action of stress solicitations produced by the shocks (mainly in the form of spallation), and of erosion activity generated by bubbles collapsing against the stone (cavitation) [1, 3, 9, 24-29, 31-34]. Eisenmenger *et al.* [35, 71] have suggested the presence of a third mechanism, named *squeezing*. This consists of circumferential quasi-static compressions that squeeze the stone and cause it to break into two parts along a fracture plane. The fracture plane may be parallel or perpendicular to the direction of propagation of the wave. The fragmentation of these first two big fragments continues as a binary process. This process of fragmentation plays an important role only when the focus of the lithotripter is wider than the dimensions of the stone. This is not a feature common to most lithotripters [35, 71]. As a result, Einsenmenger and his collaborators [35, 71] have

[4] The Vickers hardness (see footnote 3) is measured using a device named Vickers indenter. It can be calculated in terms of the indenter load in Kg (P_{ld}) and the average length of the indentation impression in mm (d_V). The mathematical expression is $VH = 18169\text{x}10^9 P_{ld} d_V^{-2}$ [64].

produced a new wide focus and low energy prototype which is now undergoing clinical trials.

This study has concentrated on current commercially available lithotripters, where stress and cavitation are the predominant mechanisms. The following Subsection 2.5.1 will present a review of the principal investigations regarding the role of stress and cavitation.

2.5.1 ESWL stone fragmentation by stress and cavitation

When the first commercial lithotripters were introduced in the clinical practice in 1981 the process was explained in terms of pressure gradients and 'tear and shear' forces due to internal reflections of the shock absorbed by the stone. These internal reflections arose from the acoustic impedance mismatch between the stone and the surrounding fluid [72, 73].

In 1987, Coleman *et al*. [73] identified the presence of cavitation activity driven by the shock in the area surrounding the focus of a Dornier EH lithotripter. They observed that bubbles which collapsed against a target, such as a thin aluminium foil, emitted jets strong enough to puncture it (Figure 2.9).

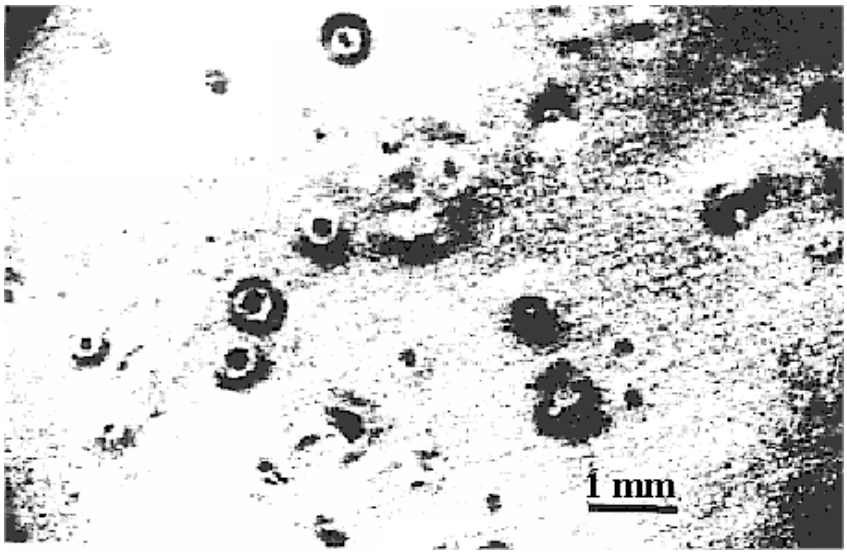

Figure 2.9: View of a 0.02 mm aluminium foil exposed to shock waves in Coleman *et al*. Reprinted from [73]. Copyright (1987), with permission from Elsevier. Millimetric holes due to cavitation are evident in the picture.

The role of cavitation microjets in the disintegration of renal calculi was specifically investigated by Crum [24]. He explained that the rarefaction part of the shock wave causes the expansion of gas pockets (cavitation nuclei) already present in the liquid. This expansion is followed by a collapse, when the local pressure experienced by the bubbles comes back to positive values after the passage of the shock. The collapse occurs as the bubbles convert the potential energy, gained during the expansion phase, to kinetic energy. During the collapse, temperatures of the order of 10000 K and pressures around 1000 MPa can be reached inside the cavities. When this collapse happens near a rigid boundary the bubbles collapse asymmetrically emitting high-speed jets (Figure 2.10) that can impress on the boundary pressures of the order of hundreds of MPa [24].

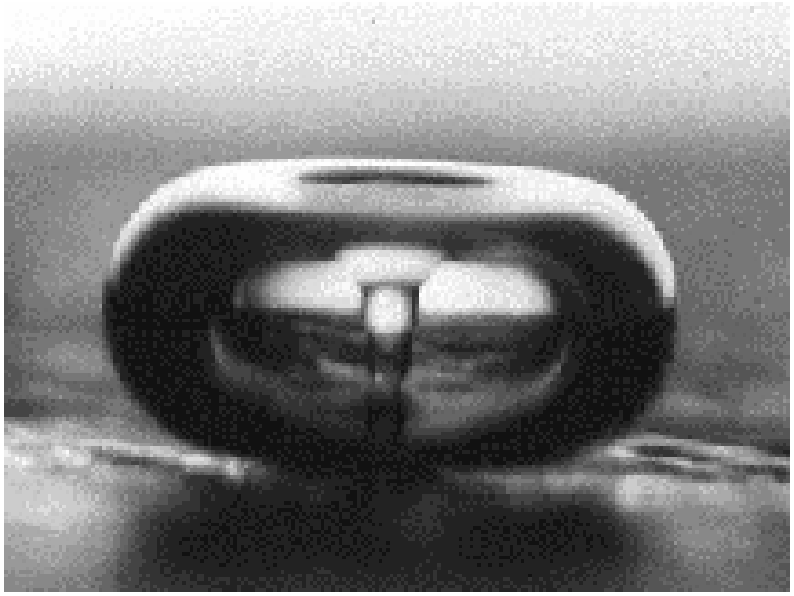

Figure 2.10: Photograph of a liquid jet produced by a collapsing bubble from Crum. Reprinted from [24]. Copyright (1988), with permission from Elsevier.

In the early 1990s observations of side effects in animals showed a transient and diffuse increase in the echogenicity of ultrasound B-scan images in regions correlated with tissue damages [36]. Coleman *et al.* [36] also showed the evidence of cavitation *in vivo* that appeared as transient echoes in the ultrasound images given by the lithotripsy system. They suggested a quantitative measurement of the echogenicity given by the mean pixel value of a digital ultrasound image over a region of interest. Using this parameter, Coleman *et al.* were able to identify, in several patients, a range of threshold lithotripter peak negative pressures (P^-) above which cavitation appeared. The threshold for cavitation was measured to lie between 1.5 MPa and 3.5 MPa.

Subsequently Lifshitz *et al*. [74] proposed a similar index for cavitation based on the analysis of the pixel distribution of gray-scale digitized light microscopic images on 8 bits (256 levels). They placed aluminium foils immersed in gassed or degassed media at the focus of a lithotripter and observed the differences in the gray-scale distributions of their images. A control histogram, corresponding to the image of a non damaged foil, was used to make the comparisons. The histogram of the cavitating medium showed a wider spread than that of the degassed medium, when compared to the control histogram (Figure 2.11). The difference was greater at the two extremes of the gray-scale. Two threshold levels were set to mark these regions (respectively Bright and Dark region in Figure 2.11) so that they contained no more then 0.5% of the control histogram. The cavitation index was defined as the proportion of pixels in the histogram of the gray image having values inside these two regions.

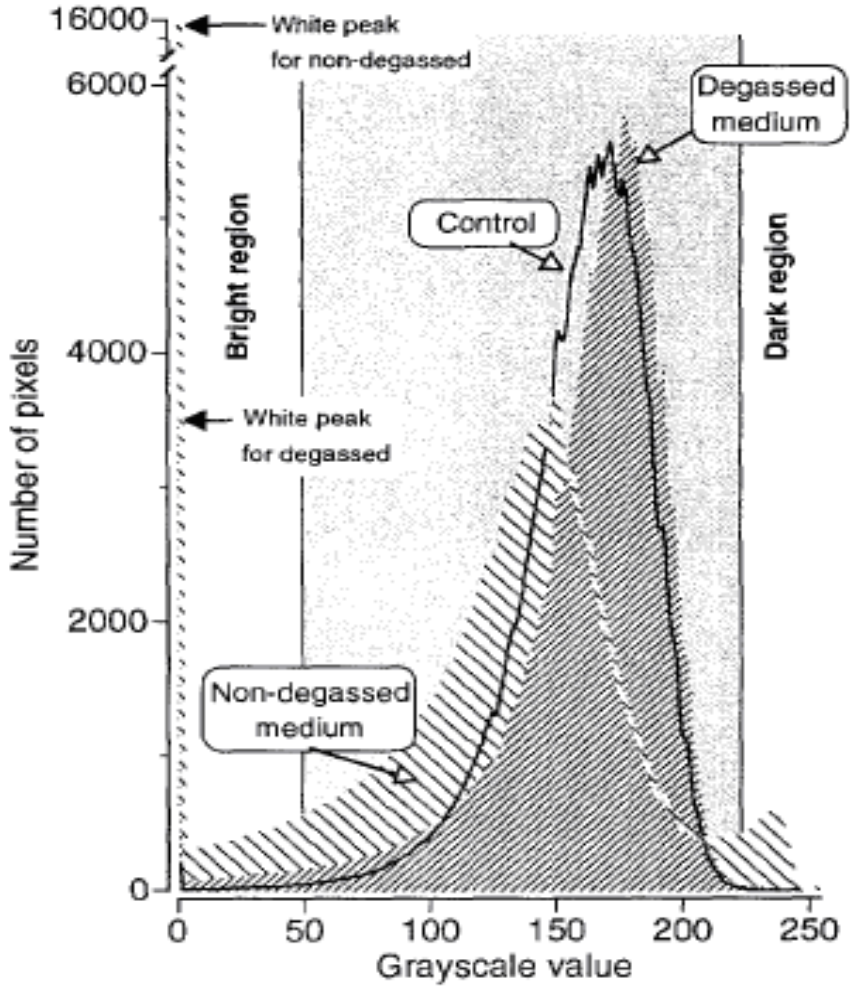

Figure 2.11: Histograms of data derived from 8 bits (256 levels) gray-scale digital light microscopic images of (solid line) non-shocked foils, (narrow hatching) shocked foils in degassed water and (wide hatching) non-degassed water. The numbers of pixels at the two extremes of the gray-scale, indicated in the picture as bright and dark regions, were used as a *damage index*. From Lifshitz *et al*. Reprinted from [74]. Copyright (1997), with permission from Elsevier.

Sass *et al*. [25] observed *in vitro* the mechanisms of stone destruction, exploiting high-speed photography. They concluded that both direct stress damage and indirect cavitation erosion are present. The impacting shock wave produces the first fissures in the stone and excites bubble activity around the stone (Figure 2.12 frames (a) to (b)). The actual disintegration of the stone happens only after the liquid has penetrated inside the cracks. This is a

consequence of collapsing bubbles (Figure 2.12 frames (i) to (k)), which are known to be drawn into cracks [3].

The original bubble cloud appears to be arranged symmetrically around the shock axis with a maximum concentration at the impact point of the shock (Figure 2.12(c)). Bubbles are visible inside small cracks in the stone (Figure 2.12(c), indicated by white arrow). Most bubbles surrounding the stone disappear after 0.3-0.4 ms (Figure 2.12(f)). The life span of each bubble depends on the final size of the bubble and the expansion experienced. After about 0.8 ms from the impact between the shock and the stone a bubble cloud is observed again. This appears inside a burst of dispersed material that is ejected from the stone from the original point of impact of the shock (Figure 2.12 frames (i) to (l)). The jet is due to secondary shocks that are re-emitted by the bubble cloud surrounding the stone.

Secondary cavitational emissions can be identified in Figure 2.13 frames (g) to (h) [75]. Figure 2.13 shows a sequence of photographs capturing the shock-bubble interaction in the focal region of an EH Dornier lithotripter. The individual bubbles (Figure 2.13 frames (c) to (e)) aggregate into larger bubbles during their expansion (Figure 2.13 frames (f) to (h)) before the second collapse.

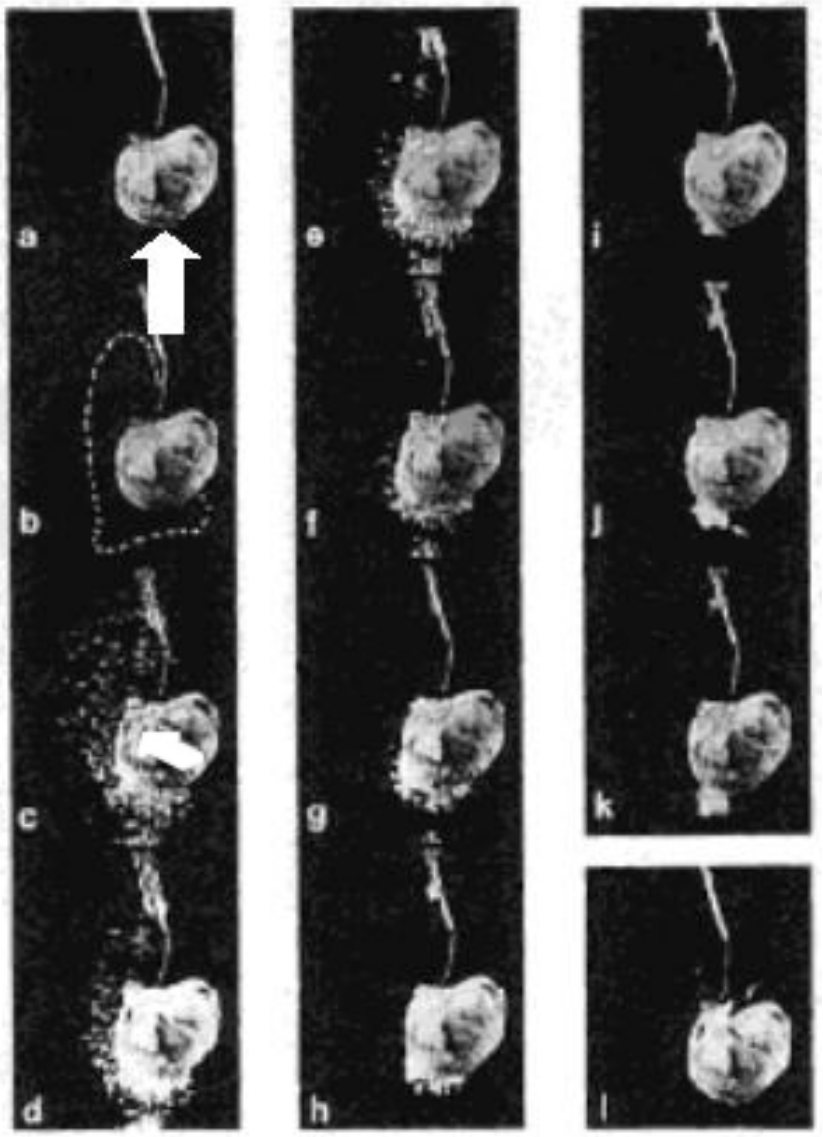

Figure 2.12: Sequence of high speed photographic pictures of human gallstone being hit by a shock wave from Sass *et al*. Reprinted from [25]. Copyright (1991), with permission from Elsevier. The stone is placed on target using a thin string (visible in all the frames) glued on its surface. The interval between each frame is of 0.1 ms. (a) This frame was taken 0.1ms prior to the moment when the shock impacts the stone. The white arrow shows the direction of propagation of the shock wave. The shock reaches the stones between (a) and (b). Frames (b) to (h) show cavitational activity. Note that the bubbles are on both the stone surface and the surrounding water. These bubbles are located in a region symmetrical around the shock axis. The dotted area in (b) marks the region in which small bubbles were visible in the original 16 mm negative. The white arrow in frame (c) points towards the location of the bubbles within stone cracks. Frames (i) to (k) show rapid material outburst as a result of cavitation jetting. Frame (l) show disintegration of the stone by erosion within the crack.

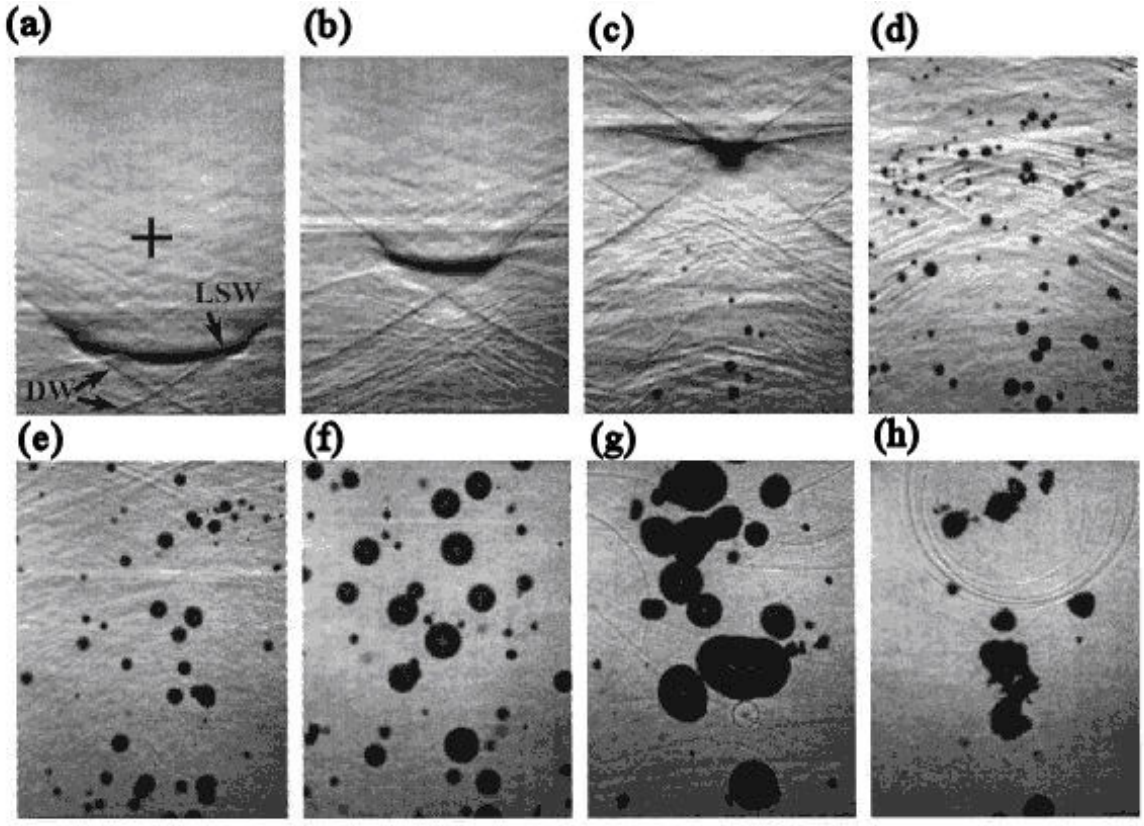

Figure 2.13: High-speed sequence of shadowgraphs illustrating shock-bubble interactions in the focal region of a Dornier XL-1 EH lithotripter, from Zhong *et al.* Reprinted with permission from [75]. Copyright 1999, Acoustical Society of America. Each frame is taken at a specific time after the spark discharge. In frame (a) this time is 138 μs, the lithotripter shock wave (LSW) propagates from the bottom towards the focus (+) and a diffracted wave (DW) is also indicated. In frame (b) this time is 142 μs and the shock wave reaches the focus. At times between (c) 147 μs and (d) 157 μs, the cavitation seed bubbles excited by the shock wave are in expansion. At times between (e) 164 μs and (f) 245 μs, the expanding bubbles aggregate and coalesce to form larger bubbles. When the time is between (g) 740 μs and (h) 900 μs, the bubbles and aggregates collapse emitting secondary shocks.

Several other authors [26, 29, 31, 76] have observed the contribution of the two phenomena as mechanisms of stone disintegration during ESWL.

Holmer *et al*. [76] stated that the presence of liquid around the stone was necessary to obtain fine fragments. This was because the acoustic streaming, caused by the shock wave in the liquid surrounding the stone, contributed to the disintegration.

Cleveland *et al*. [29] used micro-computed tomography to observe *in vitro* the damages on calcium oxalate monohydrate (COM) kidney stones caused by ESWL. The images in Figure 2.14 show the presence of both shock action and cavitation erosion. In particular, the damage due to the shock appears in the form of spallation [29]. This is a tensile action, generated by the inversion of the compressive part of the shock inside the stone. The inversion, as explained at the beginning of this section, is caused by the impedance mismatch between the distal surface of the stone and the surrounding fluid.

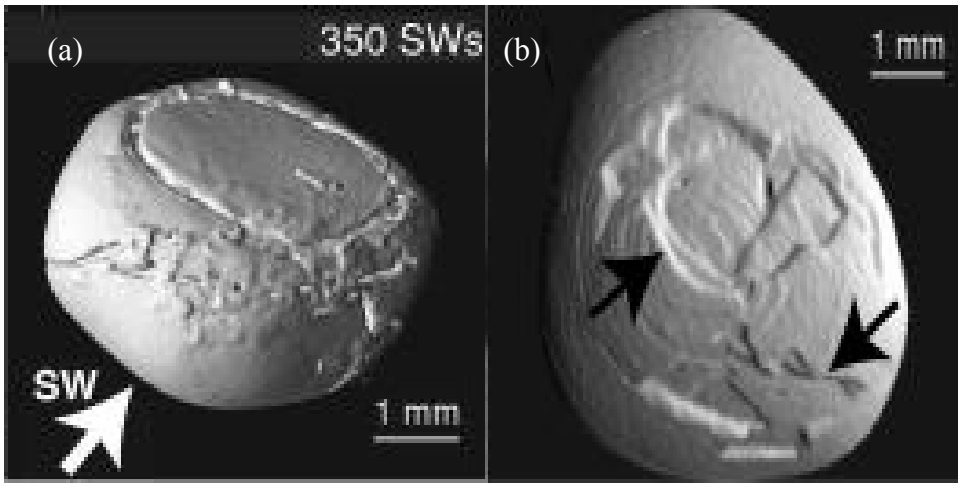

Figure 2.14: Frame (a) shows a three-dimensional surface rendering of a kidney stone after 350 shocks. Spallation damage is evident on the distal surface. Frame (b) shows the proximal surface of a COM stone showing damage consistent with cavitation mechanisms. The arrow in frame (a) indicates the direction of propagation of the shock. From Cleveland *et al*. Reprinted with permission from [29]. Copyright 2001, Acoustical Society of America.

Recent observations by Zhu *et al*. [31], using a system that mimics the fragmentation of the stone in renal pelvis, confirm that the fracture induced by the stress wave is important for the initial disintegration of the stone. However cavitation is necessary to produce fine eliminable fragments. In contrast, Owen *et al.* [77], during experiments that exploited stone phantoms that were either intact glass spheres or glass spheres produced by gluing two glass hemispheres together (i.e. modelling two stages in the fragmentation), only observed the action of shearing stress. However, the cavitation action had been intentionally suppressed *a priori* by using degassed water.

2.6 Summary

In this Chapter ESWL and the key aspects that influence the outcome of the treatment have been described. The lithotripters are devices that exploit ultrasound shock waves to fragment urinary stones [8]. The main factors that influence the success of the procedure are the characteristics of the targeted stone (composition, shape, volume, hardness, acoustic parameters etc.) and its site in the urinary system [28].

Shock wave-stone phantoms interactions have been studied to investigate the mechanisms of fragmentation. The use of stone phantoms is necessary because the success of the procedure has reduced the availability of real stones [62]. It will be shown in Chapter 4 that part of the original contribution of this work was to design the appropriate stone samples to simulate different grades of stone fragmentation.

In commercially available lithotripters, the dual action of direct stress damage and indirect cavitation erosion (generated by bubble collapses) is necessary to obtain eliminable fragments [25, 31]. Acoustic emissions are generated during the process. In particular, secondary shocks are produced during shock-bubble interactions [78, 79]. Chapter 3 shows that these acoustic emissions can be generated *in vivo* and detected remotely, and that their characteristics depend on the strength of the interaction.

Chapter 3 Secondary acoustic emissions in Extracorporeal Shockwave Lithotripsy

3.1 Introduction

The previous Chapter discussed the mechanisms of ESWL stone fragmentation, in particular the stress and cavitation mechanisms. Both mechanisms redistribute the primary shock wave energy in the region of the beam focus. Part of this energy is, in turn, re-radiated in acoustic form, providing an acoustic signal that is characteristic of each mechanism. This energy is termed here as 'secondary acoustic emission' to distinguish it from the 'primary' ESWL shock wave.

This Chapter describes the previous experimental approaches used to detect the *secondary emission*. A mathematical model used to explain these emissions is also described and a further model developed by researchers in the EPSRC project team is only shortly introduced [38-40, 80-83]. Secondary emissions arise from mechanisms that fragment the stone and they can be expected to convey information on the stone itself and its grade of fragmentation. This is the focal idea behind the work presented in this thesis.

3.2 Secondary Acoustic emissions in ESWL

In Chapter 2 the process of fragmentation of a urinary stone by ultrasound shock wave was analysed. It was explained that the properties of the stone affect the grade of fragmentation (Section 2.3) and that the process is controlled by two mechanisms: 'stress' and 'cavitation' (Section 2.5). It was also shown that acoustic emissions were generated during the procedure (Section 2.5.1). In fact, experts in lithotripsy claim that they can hear the sound generated by the shock-stone interaction and classify it as a 'hit' or 'miss' sound [20]. In this Section attention is focused on these acoustic emissions.

Three main sources of acoustic emissions are expected:

a. The incident stress wave
b. The shock wave reflections and reverberations in the stone
c. The secondary cavitation shocks

These are shown in Figure 3.1, which is a Shlieren optical image of a cylindrical brass stone phantom (Section 2.4) exposed to ESWL shock waves in a bench-top lithotripter [84]. Shlieren imaging exploits the fact that variations in the density of a transparent medium due to pressure gradients cause changes in the light refractive index. As a result, the illumination in a Shlieren image is proportional to the pressure gradients present in the medium [26, 85]. The shock wave, represented by the bright semispherical edges (Figure 3.1(a)) propagates from right to left. To distinguish the shock scatter Figure 3.1(b) and the cavitation rebounds Figure 3.1(c) from the ESWL shock wave, we term them as 'secondary acoustic emissions'.

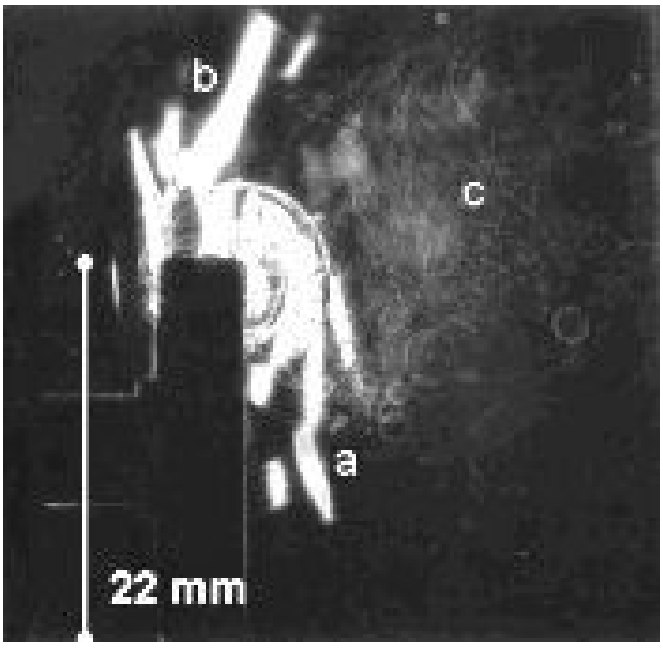

Figure 3.1: Shlieren photograph of a stone phantom exposed to ESWL shock wave from Carnell *et al.* [26, 85]. Reprinted from [26]. Copyright (1995), with permission from Elsevier. Three sources of acoustic emissions are identified: (a) stress, (b) reflections and (c) cavitation.

The main idea of this work was that the secondary acoustic emissions generated during ESWL sessions carry information about the fragmentation process and the targeting. Chapter 7 will illustrate that a first practical task in utilising this information was to develop a suitable clinical sensor to detect the emissions. Figure 3.2 shows an idealisation of the acquisition process, in which all three different types of emission are collected by a broadband sensor. A second objective was to signal process these emissions to extract the desired diagnostic information.

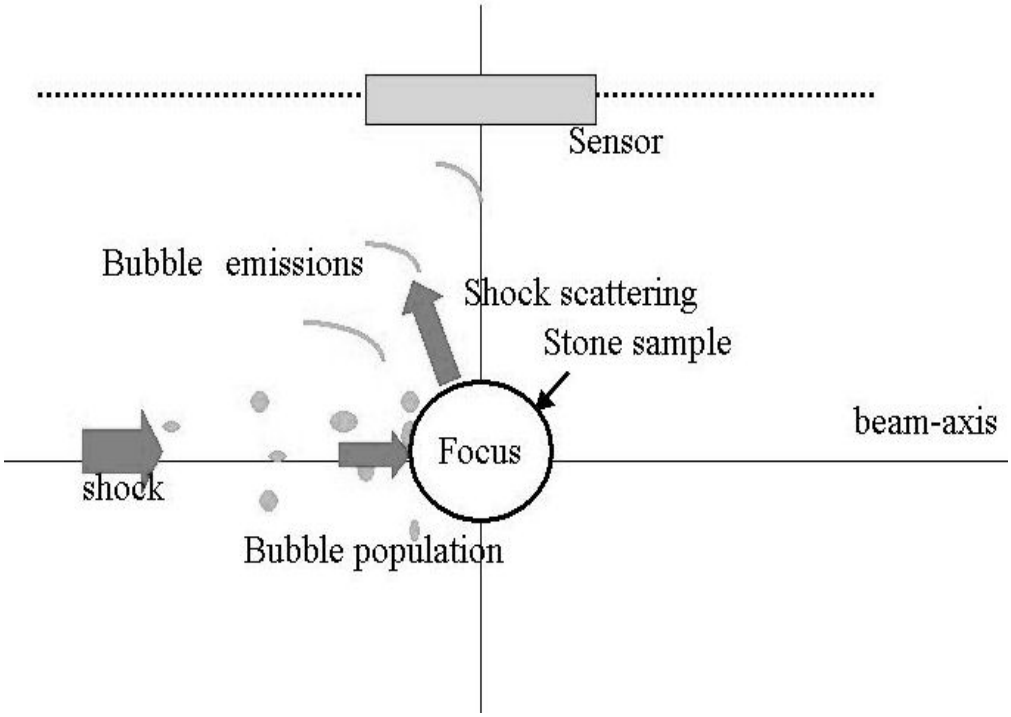

Figure 3.2: Idealisation of acoustic emissions detection during ESWL by means of a broadband acoustic detector

The following Section reports the findings of previous studies of acoustic emissions in lithotripsy. This preliminary knowledge was important for the design of the experiments for the present work.

3.2.1 Secondary acoustic emissions observed *in vitro* and *in vivo*

In 1992 Coleman, Leighton *et al.* [2] were the first to examine cavitation acoustic emission at the focus of a lithotripter exploiting an experimental focused broadband piezoelectric sensor of their invention, which could be directed anywhere in the lithotripter field. Their system or variations of it have been subsequently exploited by other authors [79, 86-88]. In particular Cleveland *et al.* [86-88] were able to localise the origin of the acoustic emission within 5 mm using a dual passive cavitation detector, made of two orthogonal confocal receivers.

The signals that can be detected, using one of these passive sensors, show a reproducible structure with two bursts (Figure 3.4(a)) [2, 79, 88], which are associated respectively with the observed first and second collapses of the bubbles in the cloud surrounding the stone (Section 2.5.1). Coleman, Leighton and co-workers [2] were the first to draw attention to the interval between the peaks of the two bursts (indicated as t_{co} in this work, see Section 5.2.5 for explanations). This interval can be used as an estimate of a global collapse time to describe the collapse of the whole bubble cloud. Use of t_{co} has since been of value in a range of studies internationally [79, 87-89].

The *in vitro* investigations correlated the detected emissions with the bubble collapses using auxiliary techniques such as high-speed photography [2, 79, 90] or light emission measurements [1, 2, 91].

The high speed photography (up to 30000 frames per second [79]) allows the investigator to capture the dynamics of the cavitation bubbles induced during lithotripsy, while the use of a photomultimeter records any light emissions[5] associated with these bubbles. For example, Figure 3.3 shows the sequence of the dynamics of a bubble cluster (Figure 3.3(a)) and the relative cavitation emissions (Figure 3.3(b)). Figure 3.4(b) gives an example of the light emission associated with an acoustic emission. The light signal shows a two peaks structure, likewise the acoustic one.

Comparison of the cavitation field with the acoustic field of a lithotripter [1, 88] also showed that there is a good agreement between the -6dB regions of the peak negative pressure and the origin of the first burst in the emission.

The positions on the focal axis of the maximum peak positive pressure and of the maximum peak negative pressure in a lithotripter field do not coincide [1]. This is an effect of the non linear propagation involved with acoustic signals of such amplitudes (up to 100 MPa) [1, 3]. The exact position of the two foci depends on the energy settings. In a Dornier EH lithotripter operating at 21 kV, for example, the peak positive pressures reach their maximum at about 20 mm beyond the geometric focus, while the peak negative pressure maximum is at about 26 mm before the focus.

[5] Bubble collapses can generate light emission [23, 92-95], which is termed sonoluminescence. There are a range of proposed mechanisms for this phenomenon, including the recombination of free radicals generated by the high temperatures (10000 K [3, 23, 24]) reached within the gas during the bubble collapse.

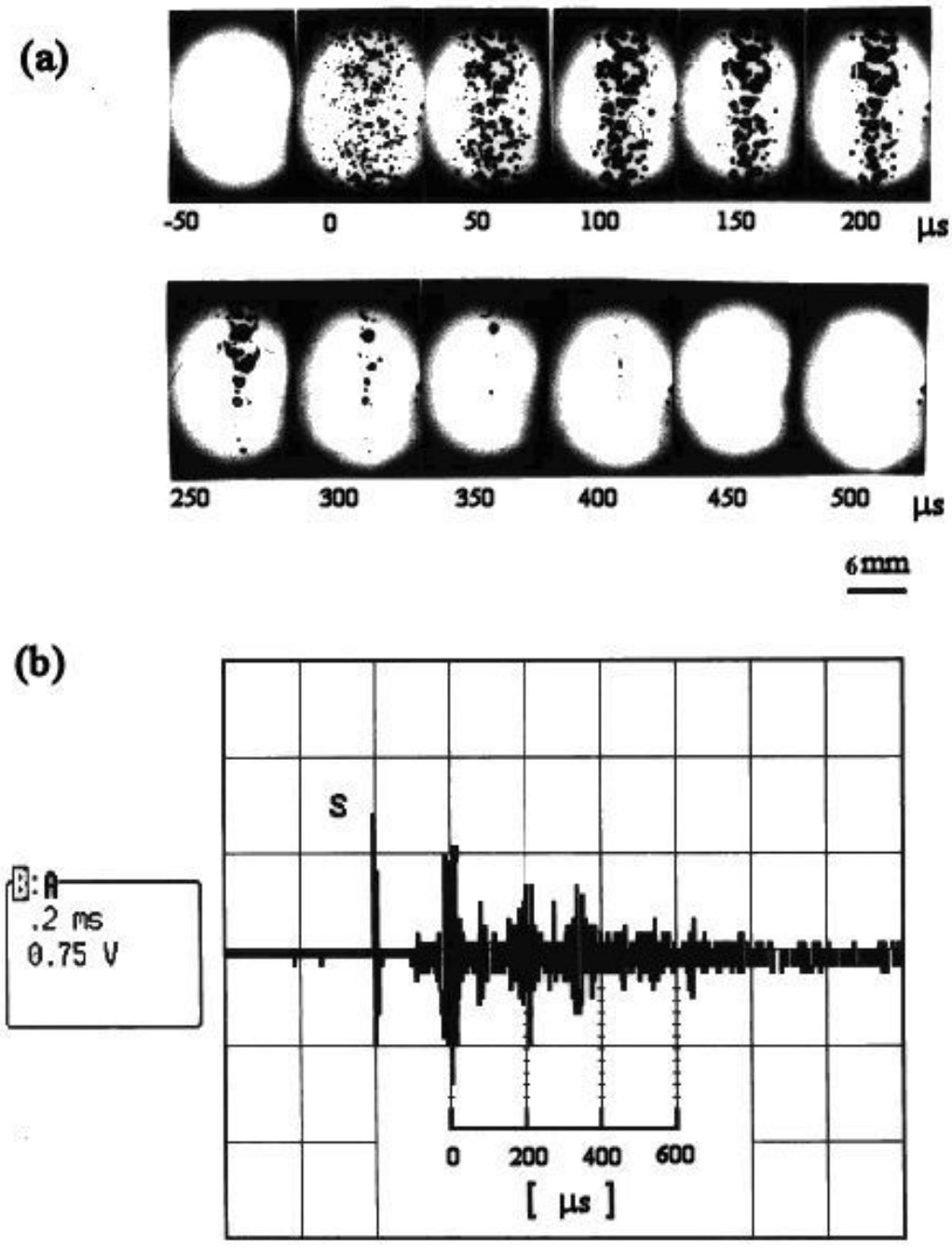

Figure 3.3: (a) High speed sequence of a cavitation bubble cluster and (b) associated acoustic emissions, recorded by Zhong *et al.* Reprinted with permission from [79]. Copyright 1997, Acoustical Society of America.

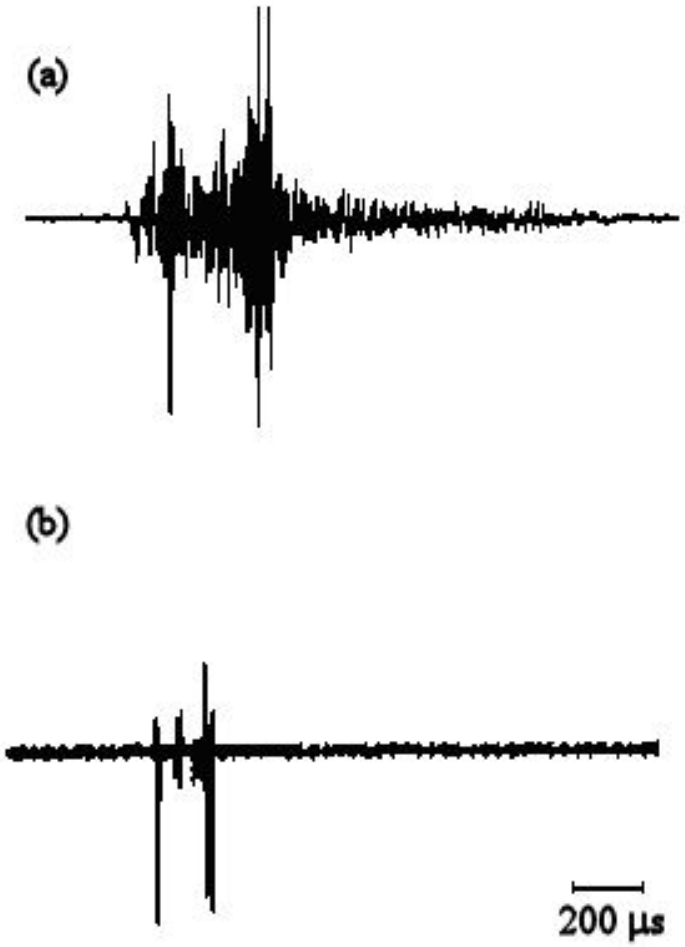

Figure 3.4: (a) Secondary acoustic emissions and (b) relative light emission recorded by Coleman *et al.* [2] at the focus of an experimental EH lithotripter. Reprinted from [2]. Copyright (1987), with permission from Elsevier.

A contour plot of the amplitudes of the first and second bursts in the cavitation emission (Figure 3.5) shows that the first burst is emitted from a small region along the beam axis before the lithotripter focus (Figure 3.5(a)), which is in good agreement with the -6dB region of the peak negative pressure. In this region also the longest collapse times are measured (Figure 3.5(c)). Whilst, as a result of the bubble movement between the two collapses, the second burst emanates from a region that extends further beyond the focus (Figure 3.5(b)).

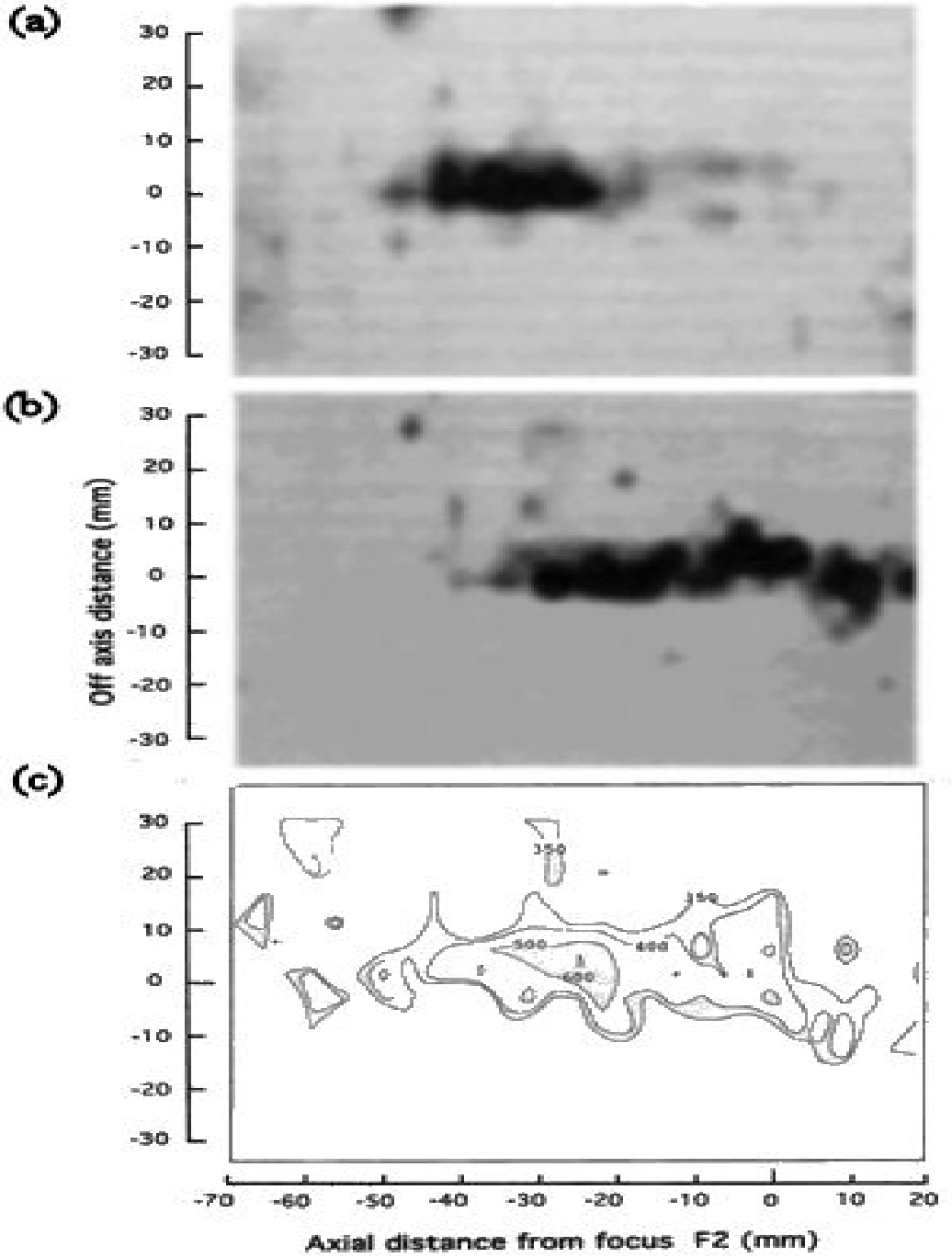

Figure 3.5: Grey scale image of the amplitudes of (a) the first and (b) the second bursts of the cavitation acoustic emissions in water. Frame (c) shows a contour plot of the collapse time (t_{co}) in microseconds. Note that higher amplitudes are represented by darker tones of grey. The picture appeared in Coleman *et al.* [1]. Reprinted with permission of IOP Publishing Ltd.

The values measured for t_{co} depend on the power settings of the ESWL source [1, 2]. This result was confirmed internationally [54, 79, 88, 89, 91]. The parameter also depends on the gas content of the water [1, 41] and increases with the peak-negative pressure (P^-) of the lithotripter pulse. Typical average values measured *in vitro* for Dornier EH sources with settings from 12 to 24 kV are in the range 158-420 μs [2, 79, 88].

Values of t_{co} measured *in vivo* are normally considerably lower and show a weaker increase with the source settings [95, 96]. Coleman *et al.* [96] measured, in 3 patients treated with an Storz Modulith EM lithotripter, an average inter-patient t_{co} increasing slowly from 73 μs to 130 μs, when the source setting varied from '1' to '6'.

Exposing juvenile pigs to a Dornier EH lithotripter and changing the source voltage from 16 kV to 24 kV, Zhong *et al.* [79] measured a negligible change in t_{co} from 71±2 μs to 72±3 μs. Measurements on swine also show that, *in vivo*, more than 87% of the acoustic emission energy is produced only by the first burst [79].

Lower values measured for t_{co} *in vivo* and their weaker dependence on the source settings are explained in terms of constraining effect of the renal parenchyma[6] on the bubble expansions that can reach a maximum size (circa 100 μm) about ten times smaller than expected in water (around 1-2 mm) [79]. This is consistent with explanations based on inertial effects [23, 93, 95, 97-100]. However, Bailey *et al*. [89] have reported recent animal experiments (that as Zhong *et al.* exploited a Dornier EH lithotripter), where the values of t_{co} (150-450 μs) are similar to those measured *in vitro* [2, 79, 88]. This was for emissions originating in both the collecting system and the parenchyma of the kidney, and source voltages varying from 15 to 24 kV. The localisation of the emitting zone (within 5 mm) was done exploiting the joint use of ultrasound B-scan and the dual PCD system mentioned above. Bailey *et al.* [89] repeated the experiments after injecting the pigs with X-Ray contrast agents (i.e. after

[6] The functional structural unit of the renal parenchyma is the nephron, which consists of a glomerulus and a urinary tubule, filled with blood and urine. It is in these tubules that cavitation nuclei can exist and their maximum dimension is in the range 10-100 μm [79, 95].

increasing the bubble population), and found an average increase of 50% in the collapse time. On the basis of these experiments and observations *in vitro* [90], Bailey *et al.* concluded that the dominant factor of influence on the collapse times observed was the density of bubble population rather than the tissue constraint.

Acoustic emission can be usefully represented in the time-frequency domain using a two dimensional representation, termed 'spectrogram', in which the amplitudes of the signal frequency spectra are coded in a gray scale. Cunningham *et al*. [54] used spectrograms to analyse acoustic emission *in vivo*. Figure 3.6 shows the emissions (Figure 3.6-left column) and the related spectrograms (Figure 3.6-right column) obtained from a patient under increasing source settings. In the spectrograms, the main cavitation components are shown as broadband events, with main frequency content between 0.5-1.5 MHz. Cunningham *et al.* [54] showed that the interval between the two groups of broadband events increased with the source settings and could be used as an estimate of the global collapse time. Cunningham *et al.* limited themselves to visual inspections of the spectrograms. A new method to estimate the collapse time quantitatively from a spectrogram has been developed as part of this work and it will be presented in Section 5.4.

Time-frequency analyses of multiple traces are generally longer and computationally less efficient than those in one domain (i.e. time domain or frequency domain). Therefore an alternative method, suitable for on-line monitoring[7] and based entirely in the time domain, has also been developed in this work. The method, which will be presented in Section 5.2.2, is the one used by the real time analysis software (see Chapter 7 for details).

Mathematical models have been developed to explain the double burst structure of the acoustic emissions and, in particular, its cavitation component. Two have been used in this work and they will be presented in Section 3.3.

[7] The continuous introduction in the market of computers with better overall performances and, in particular, higher computational speeds may, of course, make the difference between the efficiency of the two methods insignificant in the future.

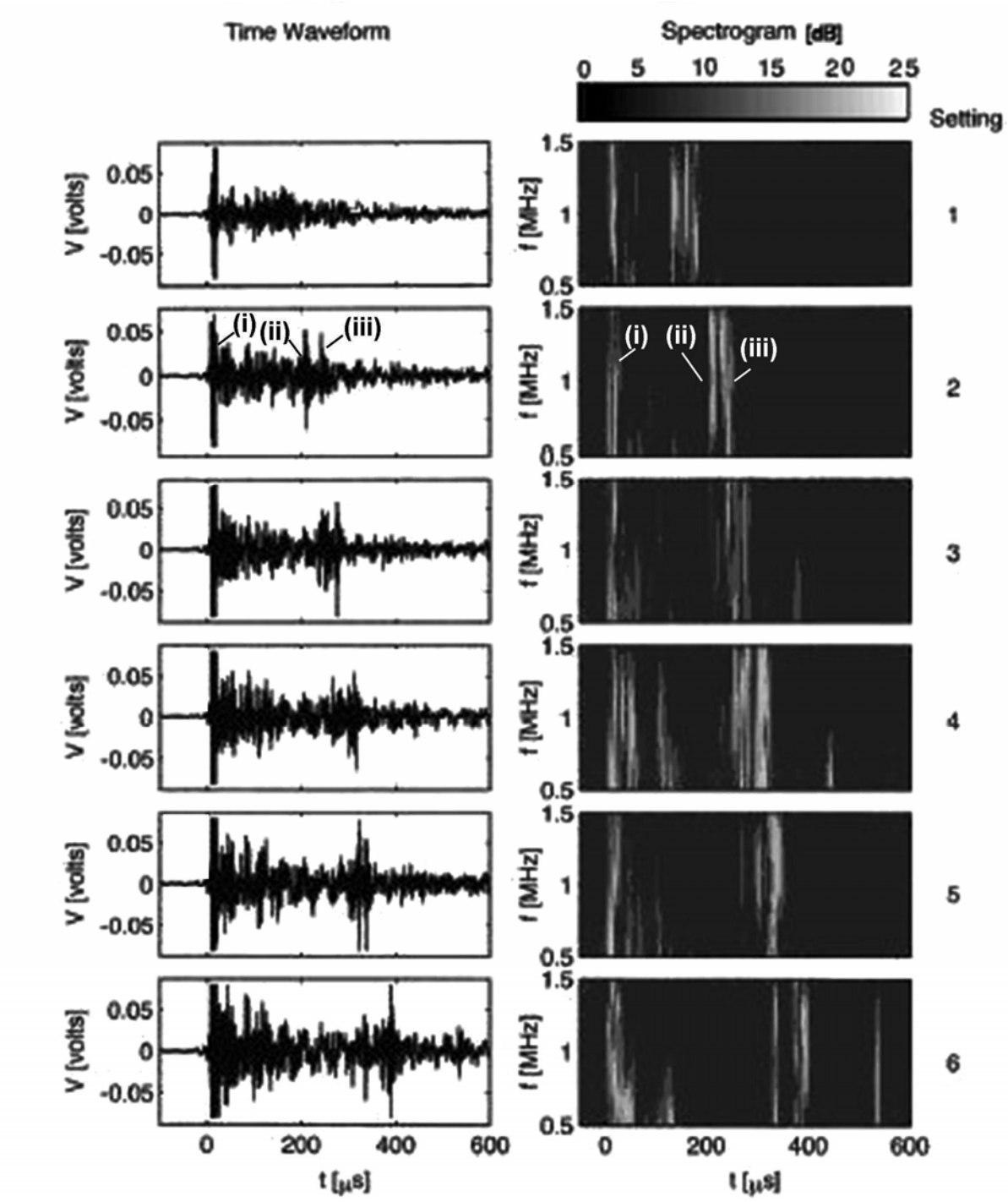

Figure 3.6: *In vivo* acoustic emissions (left column) and their spectrograms (right column) recorded during the same treatment under different energy settings of a Storz Modulith EM lithotripter. Image courtesy of Cunningham *et al.* [54]. The labels (i), (ii) and (iii) in the two frames relative to setting 6 indicate respectively the first, the second and the third bubble collapse (see Section 3.3.7).

3.3 The Gilmore model of bubble dynamics

Cavity collapses have been studied since 1859 to explain cavitation erosion of hydraulic machinery and ship propellers [82, 92] by means of mathematical formulations.

In the linear limit, an unforced free bubble may be likened to a free oscillator oscillating around its equilibrium radius with a resonant frequency that is inversely proportional to its equilibrium radius [3]. Whilst this linear limit may be appropriate for the final phase of oscillation, after an ESWL pulse excites a bubble, the earlier stages of the bubble response (order of hundreds of microseconds) require a nonlinear model. The feature which best distinguishes one nonlinear model from another is the treatment of damping. The Rayleigh-Plesset equation contains only viscous damping losses, and so neglects all other forms of loss (which are usually taken as being due to acoustic radiation damping and thermal dissipation) [3].

Several authors have artificially enhanced the shear viscosity term in the Rayleigh-Plesset equation to try to account for radiation and thermal losses, although such formulations include no more information in these loss factors than is available from linear models [101-103]. Fully nonlinear descriptions of the thermal losses are difficult to include [104-107] and beyond the scope of this thesis. However it is not difficult to incorporate a nonlinear description of radiation losses, as can be found in the family of equations termed Herring-Keller or Keller-Miksis, which reduce to the Rayleigh-Plesset equation when the sound speed in the liquid is taken to be infinite [104, 108, 109].

Influential work of Church [55] in the 1980's modelled the response of bubbles to ESWL using the Gilmore-Akulichev formulation of bubble dynamics. Church's choice was explained by the fact that the model is particularly well suited to conditions of high pressure and conveys a large quantity of results in a reasonable time [55]. Since then authors in the field have adopted this approach [2, 41, 55, 82, 92, 110, 111], in part to allow easy

comparison with Church's benchmark results, and in part because the Gilmore equation readily incorporates the mass flux phenomenon which can be important during ESWL.

In particular, Choi, Coleman *et al.* [38] successfully used an implementation of the model to describe the influence of the liquid properties on the bubble dynamics during ESWL [42]. Given the simplicity of use and the usefulness it has proved in other studies in the field, in the research described in this thesis the Gilmore model was widely used to formulate predictions, and then to validate the results of experiments. In particular, a modified MATLAB^{TM} version of the Gilmore code of Choi [42] was implemented in this study.

3.3.1 The assumptions of the Gilmore model

The fundamental assumptions of the model are [42, 55]:

(a) the bubble is initially at the equilibrium in an infinite liquid and it remains spherical throughout its motion;
(b) the radius of the bubble is much smaller than the wavelength of the applied field;
(c) the motion of the liquid surrounding the bubble is isentropic. That is to say, the fluid compressions and expansions happen at constant entropy [59, 112].

However, the real bubble undergoes, of course, a host of other behaviours that are not included in the model. These include [93, 94, 100]:

- departure from sphericity;
- bubble fragmentation and coalescence;
- interaction with other bodies (bubbles, stone, etc.) in the liquid;
- the presence of pressure fields and flows which are not spherically symmetric with respect to the bubble centre, and which may change over length scales which are not very much greater than the bubble radius.

On the other hand, the Gilmore model has proved to be an extremely useful tool. As regards assumption (a), there are phenomena which bring the overall behaviour of a cloud of bubble into closer agreement with this rather limiting assumption. An example of this is when fragmentation during a collapse can be reversed through coalescence of the fragments during the subsequent expansion phase [93, 94, 100].

Assumption (b) is in general well satisfied, since the main shock wavelength[8] is around 1 cm and the maximum bubble radius is about 1 mm [79].

The issue of assumption (c) is less simple. The assumption of constant entropy is frequently used in acoustics to model propagation under conditions of low dissipation, and can be well satisfied away from boundaries. The isentropic assumption is, in fact, equivalent to adiabatic conditions if the processes are reversible [59, 112]. It might be considered that this assumption is inadequate when high amplitude shock waves propagate through the liquid, particularly when bubbles are present. However the isentropic assumption has provided to be adequate for predicting nonlinear propagation of high amplitude waves [59, 113]. In particular, the Taylor series expansion of the isentropic equation of state has proved to be sufficiently useful for engineering purposes. This expansion has led to predictions of waveform distortion and the generation of harmonics during nonlinear propagation, and allowed the prediction of the B/A ratio for liquids, that are consistent with the measured waveform distortion observed during nonlinear propagation [59, 112]. For the specific application of the Gilmore model, this has proven to be sufficiently robust to provide useful engineering predictions, as for example quantitatively predicting how the interbust interval would increase with increasing shockwave amplitude [1, 2, 41].

Nevertheless the Gilmore-Akulichev model is not sufficient to fully understand the nature of the secondary acoustic emissions adjacent to stones (where clearly the assumptions of a free

[8] The main wavelength of a shock λ_{0S} can be calculated as $\lambda_{0S} = c\, f_{0S}^{-1}$, where f_{0S} is the main shock frequency (i.e. the inverse of the pulse duration), which is about 0.15 MHz, and c is the speed of sound in liquid and soft tissues, which is ~ 1500 m/s.

spherical bubble in a free field is violated). Because of this, collaborating researchers from the University of Southampton have been working on a Computational Fluid Dynamics (CFD) Free-Lagrange method [38-40, 80-83], which does not suffer from the limitations of the Gilmore code. The predictions of this code [83], which was developed at the same of this study, are in good agreement with the experimental results reported by this and other authors [25, 31]. However the code was not exploited in this thesis and a description of it is beyond the scope of this thesis [40, 83]. Interested readers are referred to reference [40,83].

3.3.2 *The Gilmore equation*

The Gilmore equation of motion of a bubble can be written as [42, 55]

$$\frac{\mathrm{d}U}{\mathrm{d}t} = \frac{1}{R\left(1-\frac{U}{C}\right)}\left[H\left(1+\frac{U}{C}\right)-\frac{3}{2}\left(1-\frac{U}{3C}\right)U^2\right]+\frac{1}{C}\frac{\mathrm{d}H}{\mathrm{d}t} \qquad (1)$$

where R is the bubble radius, U is the velocity of the bubble wall

$$U = \mathrm{d}R/\mathrm{d}t \quad , \qquad (2)$$

and where C is the speed of sound in the liquid at the bubble wall, which in isentropic conditions can be related to variations in pressure and density as

$$C = \left(\frac{\mathrm{d}p}{\mathrm{d}\rho}\right)_R^{1/2} \quad , \qquad (3)$$

where p is instantaneous pressure, ρ is instantaneous density of the liquid calculated on the bubble surface and R is, as explained above, the bubble radius.

The enthalpy, H, of the liquid at the surface of the bubble (radial distance R) is calculated as

$$H = \int_{P_\infty}^{P(R)} \frac{1}{\rho} \mathrm{d}\, p \tag{4}$$

where P_∞ is the pressure far from the bubble, that in an acoustic field is given by

$$P_\infty(t) = p(t) + P_0 \tag{5}$$

with P_0 the instantaneous ambient pressure of the surrounding fluid, *p(t)* the time history of the acoustic pressure and *P(R)* the pressure at the bubble wall on the liquid side

$$P(R) = P_\mathrm{v} + P_\mathrm{g} - \frac{2\sigma}{R} - 4\mu\frac{U}{R} \tag{6}$$

where P_v and P_g are the pressure of the vapour and the gas within the bubble, σ is the surface tension of the liquid and μ is the coefficient of shear viscosity of the liquid.

Assumption (c) of Section 3.3.1 of isentropic liquid behaviour concerns the relationship between the instantaneous liquid pressure (p) and density (ρ) by means of a modified Tait equation [111]

$$p = A\left(\frac{\rho}{\rho_0}\right)^{n_\mathrm{T}} - B \tag{7}$$

where A, B and n_T are empirical constants depending on the specific liquid and ρ_0 is the liquid equilibrium density.

By combining Equation (6) with Equations (3) and (4), C and H may be expressed as

$$C = \left(c_0^2 + (n_\mathrm{T} - 1)H\right)^{1/2} \tag{8}$$

$$H = \frac{n_\mathrm{T}}{(n_T - 1)} \frac{A^{1/n_\mathrm{T}}}{\rho_0} \left(\left(P(R) + B\right)^{\frac{n_\mathrm{T}-1}{n_\mathrm{T}}} - \left(P_\infty(t) + B\right)^{\frac{n_\mathrm{T}-1}{n_\mathrm{T}}} \right) \tag{9}$$

where c_0 is the speed of sound in the liquid at infinitesimal amplitudes.

3.3.3 *The pressure radiation*

The pressure distribution in the liquid surrounding the bubble may be calculated using an approximation made by Akulichev [42, 55]

$$p(r,t) = A\left[\frac{2}{n_\mathrm{T} + 1} + \frac{n_\mathrm{T} - 1}{n_\mathrm{T} + 1} \left(1 + \frac{n_\mathrm{T} + 1}{r c_0^2} G \right)^{1/2} \right]^{\frac{2n_\mathrm{T}}{n_\mathrm{T}-1}} \tag{10}$$

where r is the radial distance from the centre of the bubble and G is an invariant of the bubble motion that may be specified at the bubble surface as follows

$$G = R\left(H + \frac{U^2}{2} \right) \tag{11}$$

Using the same approximation [42], the time required for the pressure wave to travel the distance from r to R may be calculated as

$$t(r) - t(R) = \frac{2G}{c_0^3} \left[\frac{1 + 2\beta u}{\beta u (1 + \beta u)} - \frac{1 + 2\beta U}{\beta U (1 + \beta U)} - 2 \ln\left(\frac{(1 + \beta u)\beta U}{(1 + \beta U)\beta u} \right) \right] \tag{12}$$

with

$$\beta u = \frac{1}{2}\left[\left(1+\frac{n+1}{rc_0^2}G\right)^{\frac{1}{2}}-1\right] \tag{13}$$

$$\beta U = \frac{1}{2}\left[\left(1+\frac{n+1}{Rc_0^2}G\right)^{\frac{1}{2}}-1\right] \tag{14}$$

3.3.4 *The pressure and temperature of the gas*

The change of pressure and temperature of the gas in the bubble with the bubble radius may be calculated in a first approximation assuming a model of ideal gas [42, 55, 111]

$$P_g V_g = MRT_g \tag{15}$$

where P_g, V_g, T_g and M are respectively the pressure, the volume, the temperature and the number of moles of the gas within the bubble and R is the universal gas constant.

The temperature (T_g) and pressure (P_g) reached by the gas at a specific bubble radius (R), during the expansion, may be related to their initial equilibrium values (T_{gi} and P_{gi}) and the bubble initial radius (R_i) by polytrophic laws [42, 55, 111]

$$T_g(R) = T_{gi}\left(\frac{R_i}{R}\right)^{3(\eta-1)} \tag{16}$$

$$P_g(R) = P_{gi}\left(\frac{R_i}{R}\right)^{3\eta} \tag{17}$$

where η is the polytrophic exponent of the gas[9].

However, especially at high gas pressures (~10 GPa [55]) as in ESWL, the use of the van der Waals equation of state for a real gas [42] gives more accurate predictions than Equation (15). The van der Waals equation is

$$\left(P_g + \frac{aM^2}{V_g^2}\right)(V_g - bM) = MRT_g \tag{18}$$

with *a* and *b*, known as the van der Waals constants. These constants introduce corrections in Equation (15), which compensate for the presence in a real gas of intermolecular forces and finite volumes of the individual molecules, which are negligible in a ideal gas. Hence the pressure of a real gas may be related to its initial value by

$$P_g = \left(P_{gi} + \frac{aM_i^2}{V_{gi}^2}\right)\left(\frac{V_{gi} - bM_i}{V_g - bM}\right)\left(\frac{M}{M_i}\right)\left(\frac{T_g}{T_{gi}}\right) - \frac{aM^2}{V_g^2} \tag{19}$$

with V_{gi} the initial volume of the real gas and M_i its initial number of moles.

3.3.5 Gas diffusion

The number of moles of gas in the bubble does not remain constant at its initial value M_i, because the gas tends to diffuse into the surrounding liquid and vice versa. This latter effect (exsolution) is particularly important in high pressure fields such as in ESWL [41, 55] and needs to be incorporated in the Gilmore model to obtain realistic descriptions of the bubble dynamics. The instantaneous number of moles of gas (M) may be calculated from the zero-order solution to the diffusion equation given by Eller and Flynn [42, 55] as

[9] The polytrophic exponent η equals 1 if the process is isothermal. If the process is adiabatic, $\eta = \gamma$ (ratio of the specific heat of a gas at constant pressure to that at constant volume), and $1 < \eta < \gamma$ in all the other cases when reversible heat conduction is considered [42].

$$M = M_{\mathrm{i}} - 4\sqrt{\pi D_g}\int_0^{\tau}\frac{h(\tau')}{\sqrt{\tau-\tau'}}d\tau' \tag{20}$$

where M_i is the initial number of moles present in the bubble gas, D_g is the diffusion constant of the gas in the liquid and τ and h are functions defined as

$$\tau = \int_0^t R^4(t')dt' \tag{21}$$

$$h(\tau) = C_{\mathrm{s}}\frac{P_{\mathrm{g}}}{P_0} - C_{\mathrm{i}} \tag{22}$$

where C_{s} is the saturation concentration of the gas in the liquid and C_{i} is the initial concentration of gas in the liquid far from the bubble. The instantaneous gas pressure P_g is given by Equation (17) or (19) according to model used for the gas (ideal vs. real). In both cases the parameter R_{i} is replaced by a time varying equilibrium bubble radius $R_{0\mathrm{i}}$ [42, 55].

3.3.6 Numeric implementation of the Gilmore model

In this thesis a modified version of Choi's implementation of the Gilmore-Akulichev model of bubble dynamics [42] has been used to simulate bubble-shock interactions. The code exploits a Runge-Kutta-Merson method [42] to solve simultaneously the Equations (1),(6),(8)-(22) and the equation representing the shock waveform. The latter is formulated in the code using a model of the lithotripter pulse provided by Church [55]

$$p_{\mathrm{id}}(t) = \psi P^+\left(1-e^{-\alpha_1 t}\right)e^{-\alpha_2 t}\cos\left(2\pi f_{0S}t + \frac{\pi}{3}\right) \tag{23}$$

where P^+ is the peak positive pressure of the lithotripter pulse and ψ is a dimensionless scaling constant added to Equation (23) to make equal to P^+ the temporal peak of the

'shocked' oscillation (see Section 2.2.3). The dimension of the two parameters α_1 and α_2 is the inverse of time. They are linked respectively to the rise and decay time of the pulse (Figure 2.2). The central frequency of the pulse is indicated as f_{0S}. In Choi's code these parameters are $\psi=2$, $P^+=60$ MPa, $\alpha_1=9.2\text{x}10^7$ s^{-1}, $\alpha_2=8.33\text{x}10^5$ s^{-1}, $f_{0S}=83.3$ kHz [42].

In this study, the original code developed by Choi has been adapted in order to execute simulations using real shock waves recorded during experiments (Chapter 4). To be precise, the new code uses modified versions of the recorded waveforms. It applies a correction to the waveforms as suggested by Bailey [111] to compensate for the underestimation of the tensile part of the shock waves made by PVdF (Polyvinylidene Fluoride) membrane hydrophones (see Section 4.3). The correction is based on the assumption that it is the integral action of all the tensile part of the shock wave over time, rather than just its peak negative pressure (P^-) as supposed by Choi [41], which influences the cavitation bubble dynamics [3, 111]. It consists of lengthening the duration of the measured negative tail by about 300% [111]. The code assumes a single air bubble in water at 20°C. The empirical constants present in the equations are set to the values reported in Table 3.1 [42].

Parameter	Value
P_0	$1.0\text{x}10^5$ Pa
P_v	0
σ	0.0725 N m^{-1}
μ	0.001 kg m^{-1} s^{-1}
A	$3.2\text{x}10^8$ Pa
B	$B = P_0$-A
ρ_0	1000 kg m^{-3}
c_0	1500 m s^{-1}
n_T	7
a	0.3184 m^6 Pa mol^{-2}
b	$0.377\text{x}10^{-4}$ m^3 mol^{-1}
η	γ (adiabatic process)
γ	1.4
D_g	$2.42\text{x}10^{-9}$ m^2 s^{-1}
C_s	0.7899 mol m^{-3}
C_i/C_s	0.9

Table 3.1: Parameters used in the Gilmore code implemented by Choi [42].

3.3.7 Results of the Gilmore code

Figure 3.7 shows the time histories obtained by the author using the Gilmore code. The bubble radius $R(t)$ is shown in Figure 3.7(b) and the pressure radiated from the bubble $P_r(t)$ is shown in Figure 3.7(c) as measured at a distance r= 1.5 mm from the bubble centre. These simulations are for the interaction of a bubble of initial radius R_{0i}= 7 μm with the ideal lithotripter pulse [42, 55] which is shown in Figure 3.7(a).

When the lithotripter pulse (Figure 3.7(a)) passes over the location of the bubble (which defines t=0 μs moment), the bubble is forced to a sudden collapse (Figure 3.7(b)). This event, which occurs just after t= 0 μs, is called the 'first collapse', and it emits a pressure spike which can be seen in Figure 3.7(c) at t= 0.15 μs.

When the tensile part of the shock arrives (Figure 3.7(a) t~1 μs), the bubble undergoes an explosive growth to collapse again ('second collapse', Figure 3.7(b) t= 215 μs), under the pressure of the surrounding fluid, after a time named collapse time (t_c), emitting another pressure pulse (Figure 3.7(c) t= 215 μs). If the bubble survives the second collapse, indicated as (ii) in Figure 3.7(c), without fragmenting (which it must in the Gilmore code), it continues to rebound free (acting as a damped oscillator) around the new equilibrium radius (~ 10 μm). Note that when additional gas is added to the bubble by diffusion (Figure 3.7(b) dotted line) this final equilibrium radius is increased (~ 50 μm) and the bubble continues to ring for a longer time. The expansion-collapse phase, which is mainly controlled by the inertia of the liquid [3, 23], does not appear to be affected significantly by the gas diffusion.

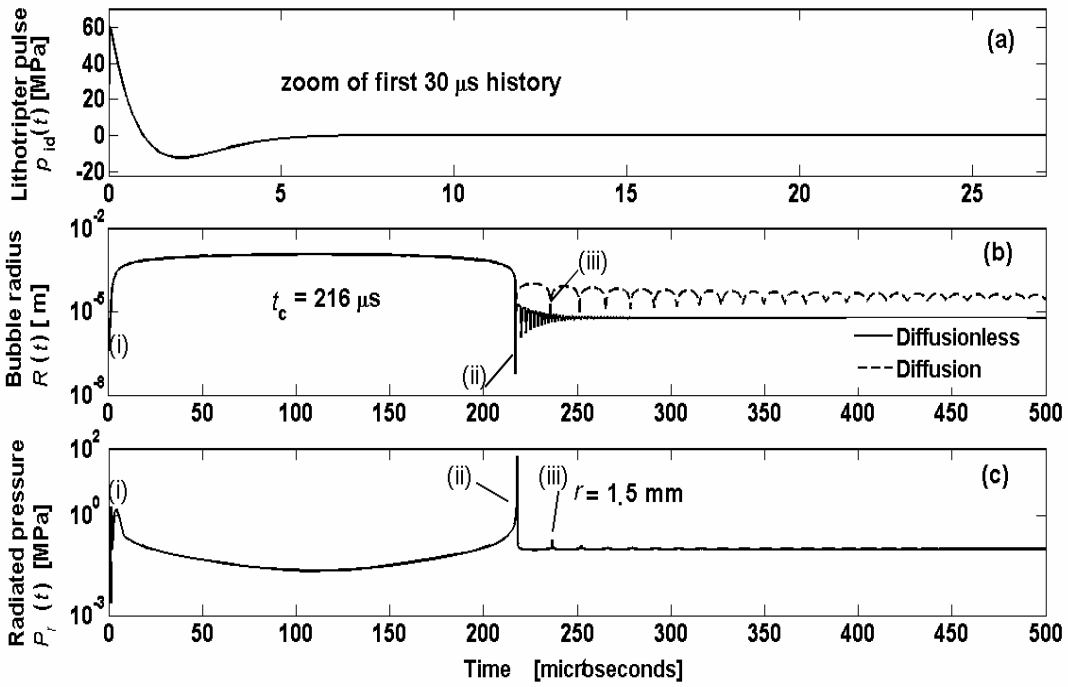

Figure 3.7: Lithotripter pulse-bubble interaction according with the prediction of the Gilmore model of bubble dynamic. The initial bubble radius was set to 7 μm. (a) Lithotripter pulse. The time axis used in this frame is different from that in the others. In particular, it shows only the first 30 μs so that the characteristics of the lithotripter pulse can be appreciated. (b) Bubble radius (log-scale). (c) Pressure emitted by the bubble (log-scale) at 1.5 mm from the bubble centre. The labels (i), (ii) and (iii) in frames (b) and (c) indicate, respectively, the first bubble collapse immediately after the impact with the shock, the second bubble collapse and the third bubble collapse.

Gilmore software simulations [41, 42] predict that the collapse time[10] t_{co} is almost independent on the initial bubble radius, and it increases with the amplitude of the peak-negative pressure of the shock (P^-). In particular, the interval t_{co} depends on the strength of the tensile part of the lithotripter pulse, which is defined as the integral over time of the negative part of the lithotripter pulse [3, 111].

Numerical simulations [42] also clarified the influence of the parameters of the surrounding liquid on the bubble dynamics. Choi and Coleman [41] found that, in the range of tensile pressures of a lithotripter field (P^->2 MPa), the most relevant influence is that of the gas content of the liquid. If, for example, tap water (90% air saturated) is degassed to a gas saturation level of 10%, then a reduction of more than 50% is found in the decay time of bubble oscillations [41]; while the oscillation frequency is almost doubled. Further investigations [41] indicated that the effects on bubble dynamics of the differences in the viscosity, surface tension and temperature of body fluids and the initial bubble size are negligible compared with those expected in water.

Cunningham *et al.* [54] used the Gilmore model of bubble dynamics to estimate the radius of cavitation nuclei *in vivo* [54]. A maximum bubble radius of about 40 μm was estimated [54]. Using this single bubble model, they estimated the nuclei radius exploiting equation (38) which links the radius of a free oscillating bubble to its resonating frequency [3]. The resonating frequency was calculated as the inverse of the time interval between the second and third collapse of the bubble (indicated, respectively, as (ii) and (iii) in Figure 3.6 and Figure 3.7). The instant of occurrence of these events was derived from time-frequency representations (spectrogram) of the cavitational emissions as that shown in Figure 3.6. In this representation each collapse is shown as a broadband event (see Section 2.5). In the example shown in Figure 3.7(b), going back to a time representation and considering the

[10] Here the collapse time is indicated as t_{co}, i.e. the time between the two peaks in the secondary emission (see Section 3.2.1). However, in the case of a single bubble, where the emission consists of two short pulses (Figure 3.7(c)) t_{co} and t_c are identical. See section for the mathematical derivation of t_c.

contribute of diffusion, the free bubble oscillation period considered is the interval between (ii) the second collapse at t= 215 μs and (iii) the third collapse at t~ 235 μs.

3.3.8 Comparison of the Gilmore predictions and measured secondary acoustic emissions

The Gilmore model of bubble dynamics, as seen in the previous section, predicts two pressure pulses, (i) and (ii) in Figure 3.7(c). The emissions recorded during ESWL, in this and previous studies (see Section 3.2) are represented by two bursts. A series of motivations explain the difference between the two signals (predicted and recorded).

First, in ESWL the shockwave interacts with a bubble cloud dispersed around the lithotripter beam axis (Section 3.2) and not a single bubble as in the Gilmore model. The bubbles in the cloud experience a different waveform (i.e. a different peak negative pressure) according with their distance from the geometrical focus (see Subsection 4.3.3). This results in a range of different collapse times experimented by the single bubbles. In addition, the emissions are not simultaneous, as the bubbles are not reached by the shock at the same time, and their emissions travel different distances (therefore experience different attenuations, phase changes, and propagation times) before reaching the sensor.

The impulse response of the particular receiver used, has also to be considered. If the receiver were much smaller than the wavelength, the recorded waveform would be the convolution of this impulse response with the pressure field that would be present at the location of the receiver as if this were absent. The pressure field at this location differs from the pressure field close to the bubble source because of propagation effects, which will include nonlinear propagation and absorption. Because of this, even for a single bubble, the narrower the band of the receiver, the more the recorded form deviates from the pressure field at its location. It might, for example, consists of a packet of oscillations centred at the resonant frequency of the receiver [88]. In this work, both data acquisition system used were

broadband[11], therefore this effect is less than produced by narrowband systems used in some other studies [1, 2, 88, 114, 115]. However a quantitative analysis the effect of the impulse response of the data acquisition systems on the emissions recorded was beyond the scope of this work and was not pursued.

Another complicating factor is the scattering of the field by the bubble [88]. Not only can this perturb the incident lithotripter pulse, but also means that the far field waveform detected by the receiver will not just be the idealised signal produced by superimposing, with appropriate propagations delays, the far field acoustic radiations from single bubbles predicted by the Gilmore equation.

If a stone is introduced in the field, scattering from the stone is also superimposed to the first cavitation emission [77, 115, 116]. Because of the relative dimensions of kidney stones treated with ESWL (2 mm-1 cm) and the main shock wavelength (λ_{0S}= 1cm), resonant scattering can occur [117]. If we assume that the diameter of kidney stones treated with ESWL ranges from 2-10 mm, and the speed of sound in a kidney stone is about 3000 ms^{-1} (see Table 2.1), then resonant scattering emissions in the frequency range of 150-750 kHz might be expected. The presence of scattering is one of the reasons that can explain why (in contrast to predictions of the Gilmore model) the amplitude of the first burst was higher than that of the second burst for most of the emissions recorded in this work[12].

In addition, the presence in the acoustic field of a stone (which might to first approximation be modelled as a rigid boundary, although there is transmission of the wave into the stone) also affects the bubble dynamics (and therefore the bubble emissions). There are two principle effects. First, as part of the shockwave impacting on the stone is reflected, the bubbles in front of the stone experience a second shock. This (see Subsection 6.2.4) results in longer collapse times than those predicted for free forced bubbles. Second, some of these

[11] See Chapter 4 for details of the data acquisition system used *in vitro* and Chapter 7 for details of the data acquisition system used *in vivo*.
[12] See Chapter 6 for information about the features of the emissions recorded *in vitro*, and Chapter 7 and Chapter 8 for features of emissions recorded *in vivo*.

bubbles energies will be dissipated during the impact on the stone rather than being reradiated as acoustic emissions [24, 40]. This might result in pressures emitted at the second collapse, indicates as (ii) in Figure 3.7(c), lower than those predicted by Gilmore model.

The scenario is even more complex *in vivo*. For example, the medium surrounding the stone is not homogeneous, and the shockwave can be scattered by discontinuities and other possible obstacles (such as other secondary stones). The interpretation of the nature of the emissions is, of course, not as clear as *in vitro*. Despite this, Chapter 7 and Chapter 8 will show that the model developed *in vitro* for stone targeting and fragmentation (Chapter 6) was useful to predict diagnostic information.

3.4 Summary

Acoustic emissions are generated during ESWL. They present three main different components (direct stress, reflection and reverberations in the stone, and cavitation) directly linked to the fragmentation mechanisms. These emissions carry information about the fragmentation process. The proposition of this thesis is that this feedback can be extrapolated by signal processing the emissions. Chapter 6 and Chapter 7 will demonstrate that this thesis is verified.

Cavitation emissions collected by previous authors present a characteristic two bursts structure [2, 79, 88]. Mathematical models have been developed to explain the characteristics of these emissions. This study has been using an adapted version of a code that implements the Gilmore-Akulichev model of bubble dynamics [38, 39, 42, 55]. The main differences between predicted and detected emissions are listed.

The following Chapters will describe how the objectives of this thesis were fulfilled. Chapter 4 will describe the design of the *in vitro* experiments.

Chapter 4 *In vitro* experimental set-up

4.1 Introduction

The previous two Chapters discussed the mechanisms of stone fragmentation (Chapter 2) and the acoustic emissions generated during the process (Chapter 3). The first objective of this study was to examine these acoustic emissions and their dependence on the quality of the targeting, and on the degree of fragmentation of the stone. A series of *in vitro* experiments were designed to accomplish this. This Chapter describes the equipment used in these experiments. Components of the shock source and the stone phantoms, have been designed by the author and are part of the original contributions of this thesis. The results of these preliminary experiments were used to design the prototype of the diagnostic system to be tested *in vivo.*

4.2 The laboratory set-up

The objective of the *in vitro* experiments was to characterise passive acoustic emissions adjacent to stone samples generated during ESWL [118-122] to facilitate the design of a prototype diagnostic system. Stone samples were placed at the focus of a bench-top EM lithotripter (see also Section 2.2.3), specially designed for the project by the Medical Physics Department of Guy's and St. Thomas' Hospitals NHS Foundation Trust (London). A novel cylindrical broadband cavitation sensor [4-7], made by the National Physical Laboratory (NPL), was used to detect the secondary acoustic emissions. As explained in Chapter 3, these are broadband signals that present a significant cavitation component. A schematic representation of the equipment used is shown in Figure 4.1.

The discharge potential of the EM source was set and maintained at 16 kV, which gave lithotripter shocks of 19±4 MPa peak-positive pressure and 3±0.6 MPa peak-negative pressure at the geometric focus (Table 4.1). A 16 kV setting is below those normally used in clinical practice (see Section 2.2). Therefore the pressures produced are also lower than those measured *in vitro* for clinical lithotripters [52, 53]. The average peak positive pressure

(P^+) measured *in vitro* by Coleman *et al.* [52, 53] during their survey on clinical lithotripters was 40 MPa. The average peak negative pressure (P^-) was 7 MPa. However, it has to be considered that the shock waves propagating through the patient's body are attenuated before they reach the stone. Cleveland *et al.* [114] measured *in vivo* (in pigs), attenuation up to 50% for the peak-positive and peak-negative pressures of the shocks produced by a Dornier HM3 EH lithotripter. Applying such a 50% reduction to the average values measured by Coleman *et al.* a P^+ of 20 MPa and a P^- of 3.5 MPa are obtained. These values agree with the averages of those produced by the experimental lithotripter at 16kV to within 15%.

The raw acoustic signals collected with the NPL sensor were filtered using an analogue high pass filter with a cut-off frequency of 0.2 MHz. This was done to suppress the background noise due to the EM source itself (main frequency of 0.15 MHz). Then, the filtered signals were acquired using a LeCroy 9354L digital scope (sampling frequency of 100 Msamples/s) and transferred to a Personal Computer (PC). A specific LabVIEW interface was developed and used for the data acquisition. Finally, the digital data were processed off-line using MATLAB™.

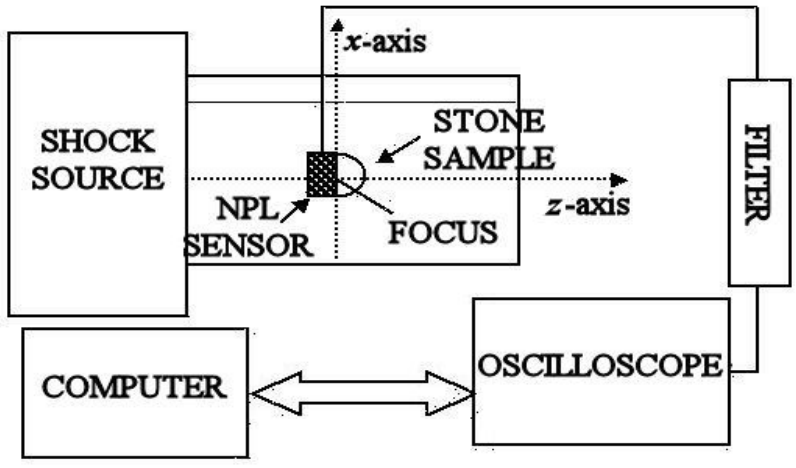

Figure 4.1: Schematic representation of the experimental set-up.

The following sections will describe the individual pieces of equipment, starting from the EM lithotripter.

4.3 The bench-top Electromagnetic lithotripter

Figure 4.2 shows a picture of the bench-top EM lithotripter. Three main features may be distinguished: (a) the EM shock wave source, (b) a shock tube and (c) a water tank. The source, which works on the principle illustrated in Section 2.2.3, will be described in the next Subsection. The tank is made of transparent Plexiglas, so that it is possible to see through it, and it is 90 cm long, 46 cm wide, and 31 cm high. The shock wave tube is a Polymethyl methacrylate (PMMA) tube with a diameter of 180 mm and a length of 37 cm. The tube, as explained in Section 2.2.3, is used to propagate the ultrasound wave as a plane wave until it is focused by the acoustic lens. The length of the shock tube was designed to be greater than the discontinuity length (Section 2.2.3). This ensured that the waveform that reached the lens was a shock wave.

Direct measurements of the pressure waveforms generated by the source at different distances from the copper membrane were used to estimate the discontinuity length. The length was estimated to be between 35 cm and 37 cm and, consequently, the length of the shock tube was designed to be 37 cm.

The shocked waveform, at the output of the shock tube, is focused by means of an acoustic PMMA lens, with a focal length of 10 cm.

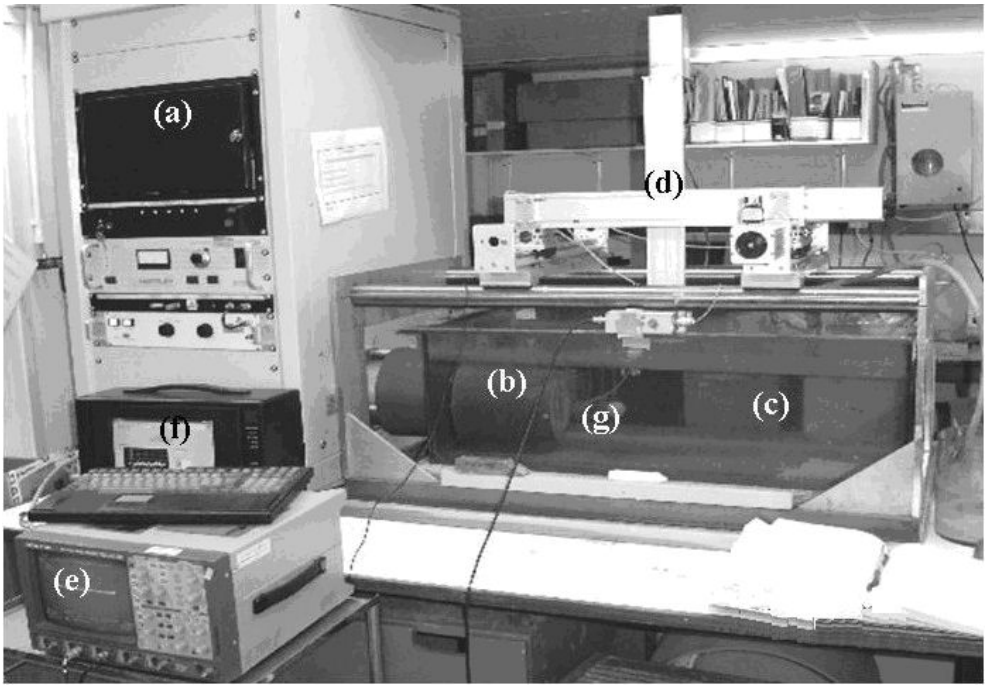

Figure 4.2: Experimental set-up designed for this project, Non-Ionising Section Laboratory, Guy's and St Thomas' NHS Trust, London. The main components of the bench-top lithotripter are labelled: (a) the EM source, (b) the shock tube and (c) the water tank. The label (d) indicates the three dimensional positioning system, (e) the LeCroy oscilloscope, (f) the PC and (g) shows the stone sample and sensor.

4.3.1 The Electromagnetic source

An electromagnetic (EM) source, as explained in Section 2.2, exploits the physical phenomenon that a condenser discharging through a solenoid produces an intense EM field. A simplified diagram of the discharge circuit of the experimental source used in this study is shown in Figure 4.3. A high voltage capacitor (Figure 4.3-C) of 1.4 μF capacitance (Maxwell Inc., San Diego, USA) is discharged through a flat coil (Figure 4.3-SC) of 126 mm diameter, made of high temperature enamelled copper wire of 1.18 mm diameter (inductance ~1000 μH, Scientific Wire Co., London). The coil is separated from a pure copper foil (MF) of 0.125 mm thickness (Goodfellows, Cambridge) by an insulating (Figure 4.3-TF) 0.05 mm polyamide Kapton film (Goodfellows). The coil and the copper foils have the same diameters and act as the primary and secondary coil of a transformer. The

discharge of the capacitor is triggered by a high voltage pulse (15-22 kV) supplied to a GXG250L (EEV Ltd., Lincoln) three electrode spark gap (Figure 4.3-TSP). The capacitor is linked to a bleed resistor of 10 MΩ (Figure 4.3-R) so that when the power is off, the capacitor will discharge through it. The electrical insulation of the triggering circuit is obtained by means of a high voltage capacitor of 80nF (MPE Ltd., Liverpool). All these components are stored in a metallic box (Figure 4.3(a)).

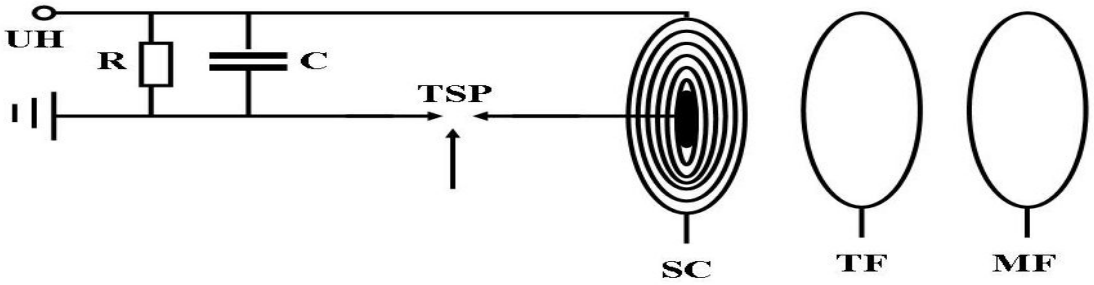

Figure 4.3: Scheme of the EM source: source discharge potential (UH); high voltage capacitor (C); high voltage discharging resistor (R); triggered spark-gap (TSP); flat solenoid (SC); polyamide film (TF); copper membrane (MF).

The mechanical pressure obtained (p_{EM}) is proportional to the square of the capacitor discharge current, I_c [123]:

$$p_{EM} = \frac{2\mu_0 n_c^2 I_c^2}{D_c^2} \qquad (24)$$

where μ_0 is the induction constant ($4\pi \times 10^{-7}$ H/m), n_c is the number of coil turns in the solenoid, D_c the coil diameter.

Shock waves with peak positive pressure up to 40 MPa can be obtained with the described source. The characteristics of the acoustic output of the experimental source will be described in the following Subsections.

4.3.2 The source acoustic output and working conditions

The experimental source has a lifetime that may vary between 1000-5000 shocks, depending on whether it operates at low settings (16-17 kV) or high settings (18-22 kV). Mending a damaged source is an expensive (cost of a coil around £1000) and time consuming process (up to 4-6 weeks). In order to maximise the source lifetime, it was decided to operate it for most experiments at the lowest setting of 16 kV and to limit measurements to single shot, when possible. At these operating settings, peak positive pressures (P^+) of 19±4 MPa and peak negative pressures (P^-) of 3±0.6 MPa, were recorded from a series of 3 different experiments spread during the 2 years of operation. In those years the source fired a total of about 2500 shocks. The waveforms were recorded at the geometric focus of the lithotripter using a Marconi bilaminar membrane hydrophone (Y-34-3598 IP116), with a sensitivity of 53 mV/MPa.

Previous studies [52] show that, when hydrophone measurements of shock waves are performed, a total systematic uncertainty of circa 30% (at 95% confidence level) has to be added to the random uncertainty in the estimate of P^+. The addition of this uncertainty gives an estimate of P^+ equal to 19±9 MPa. Unfortunately, the measurement of the tensile part of a lithotripter shock is affected by cavitation at the hydrophone [52, 111]. Cavitation mainly affects the estimation of the length of this phase [52, 111], but it is still reasonable to limit the random uncertainty in the measurements of P^- to 30%. This assumption gives an estimate of P^- equal to 3±1 MPa.

Figure 4.4 shows typical waveforms recorded under discharging voltages increasing from 16 kV (a) to 21 kV (f). Table 4.1 reports the peak positive pressures (P^+) and peak negative pressures (P^-) measured for the waveforms in Figure 4.4. These values were derived from single shot measurements, therefore they are to be considered as indicative only. Nevertheless it is noticeable the characteristic linear increase of the peak-positive pressure with the voltages of an EM source [52].

Voltage [kV]	P^+ **[MPa]**	P^- **[MPa]**
16	23.4	3.8
17	27.3	2.8
18	30.5	2.9
19	32.8	3.9
20	33.3	2.6
21	34.7	4.4

Table 4.1: Principal parameters of the waveforms measured at the focus of the experimental lithotripter (Medical Physics Department of St. Thomas' Hospital, London) for different discharge potential of the EM source; peak positive pressure (P^+) and peak negative pressure (P^-). These parameters were extracted from single shot measurements at the geometric focus of the lithotripter. The measurements were made exploiting a Marconi bilaminar membrane hydrophone (Y-34-3598 IP116).

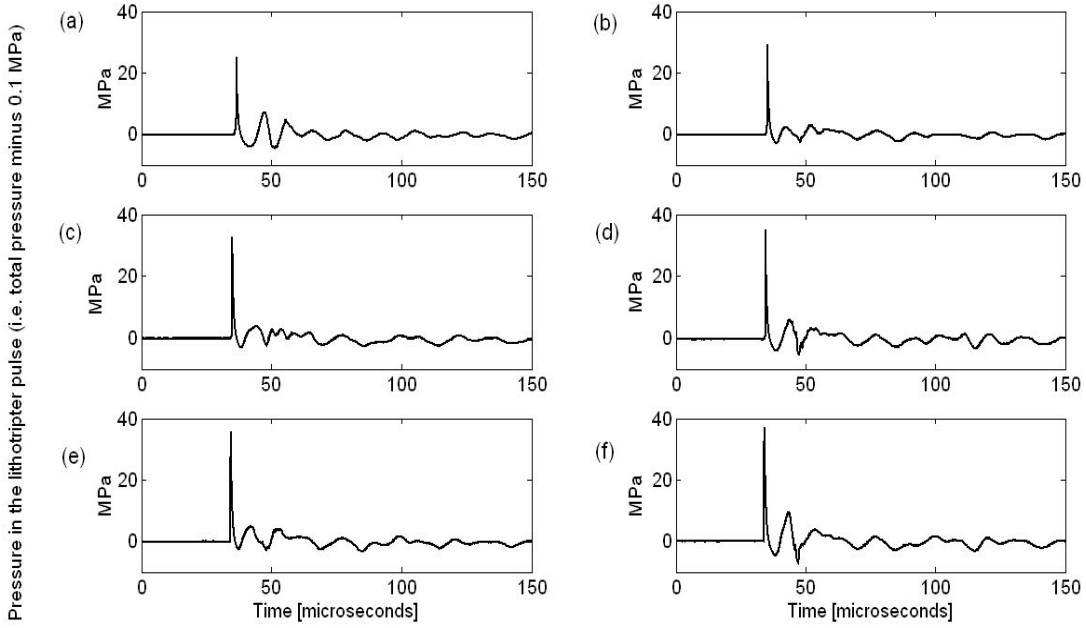

Figure 4.4: Waveforms recorded at the geometric focus of the experimental lithotripter, held in Medical Physics Department of St. Thomas Hospital (London), for different discharge voltage of the EM source: (a) 16 kV, (b) 17 kV, (c) 18 kV, (d)19 kV, (e) 20 kV, (f) 21 kV**.** A Marconi bilaminar membrane hydrophone (Y-34-3598 IP116) was used for the measurements.

4.3.3 The Acoustic field

The focus of the bench-top lithotripter has a cigar shape[13], centred on the beam axis. Its length is 70 mm and its diameter is 20 mm. Figure 4.5 displays the map of the acoustic field along the beam axis (z) and the two transverse axes (x and y). It can be noticed that the highest peak-negative pressures (Figure 4.5(c) right panel) are reached before the focus, That is the region where the strongest shock-bubbles interactions will, as explained in Section 3.3.

[13] The focal volume is defined as the volume contained within the surface described by the –6 dB peak-compressional acoustic pressure measured around the focus (BS EN 61846:1999). Its shape is in practice approximated from measurements taken in three z, x and y axes. The focus of the clinical lithotripter has a cigar shape too; its dimensions are 28 mm × 6 mm × 6 mm .

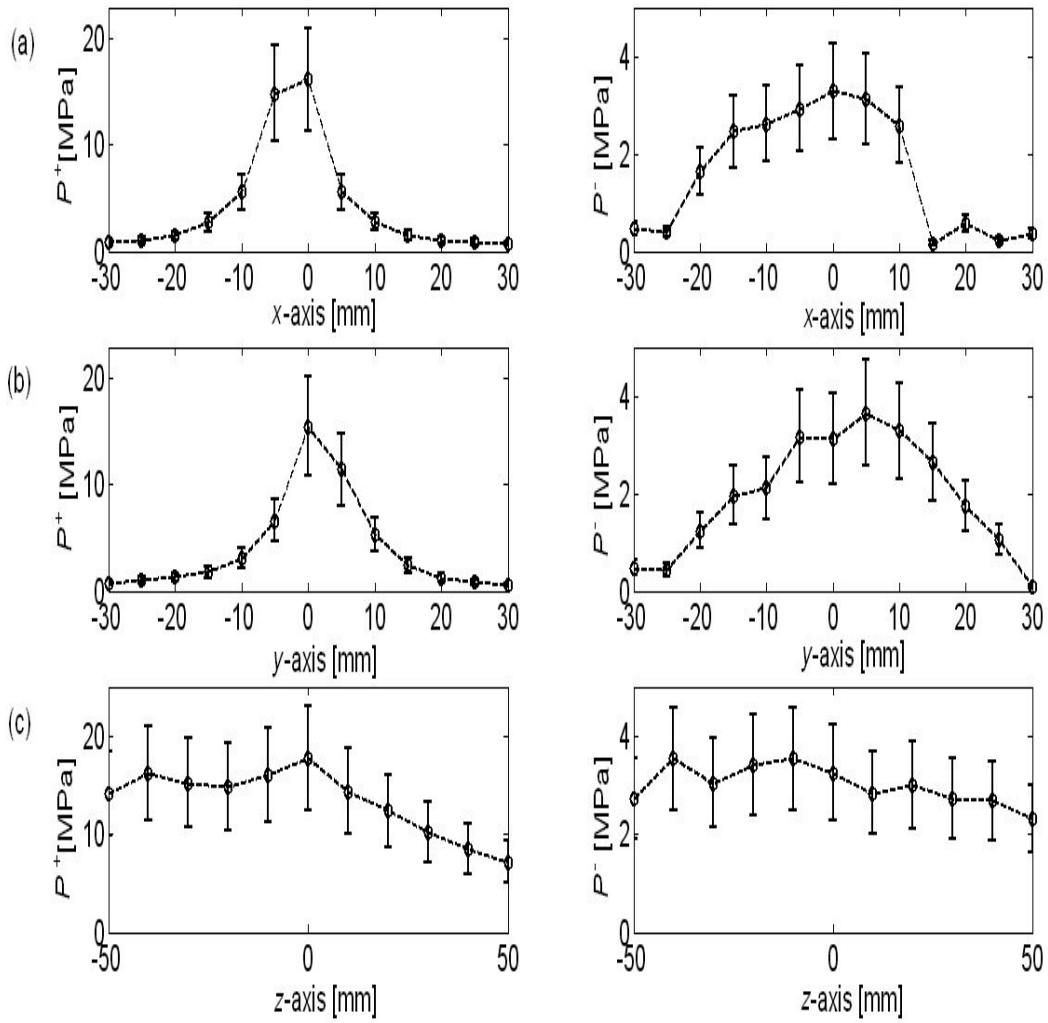

Figure 4.5: Map of the peak-positive and peak negative pressures along the two orthogonal axes, specifically (a) the *x*-axis and (b) the *y*-axis, and (c) the beam axis, that is the *z*-axis. The values were measured under a discharge voltage of 16 kV for the experimental EM source. The error bars in the plots take account of the 30% systematic uncertainty present in the measurements [52]. The dotted lines represent a linear interpolation.

4.4 The novel National Physical Laboratory cavitation sensor

An early prototype of a novel ultrasound cavitation sensor (Figure 4.6), developed by the National Physical Laboratory (NPL, Teddington) [4-7], was used to monitor cavitation in the bench-top EM lithotripter. The sensor was exploited, first to analyse cavitation phenomena in the focal region of the lithotripter and, then, to characterize cavitation emissions adjacent to stone phantoms [118].

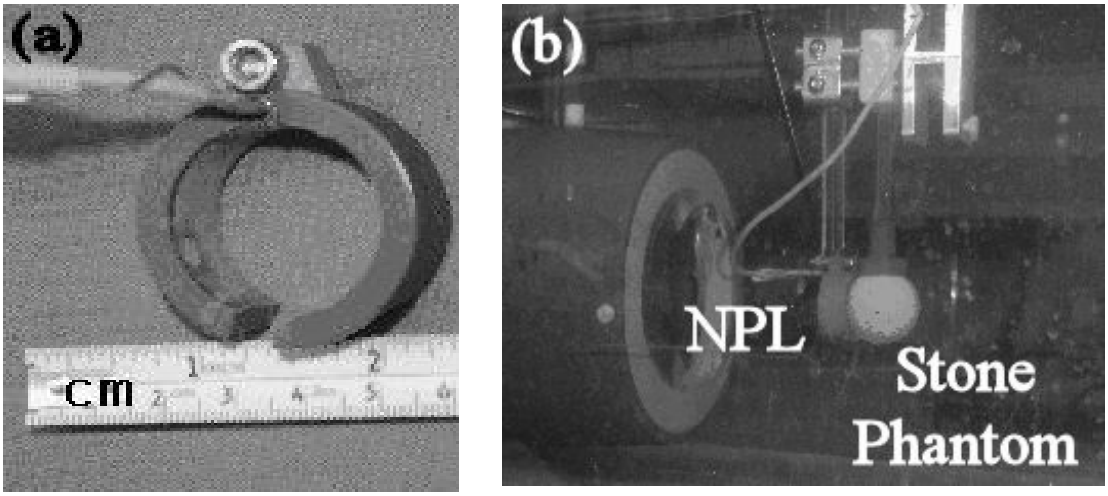

Figure 4.6: (a) Novel NPL cavitation sensor and (b) the same sensor used adjacent to a stone phantom in the bench-top lithotripter tank.

The sensor, designed to monitor cavitation in industrial equipment (such as ultrasonic cleaning chambers), is able to monitor broadband cavitation emissions (see Section 3.2.1) occurring within its hollow body (Figure 4.7). The frequency bandwidth of the sensor covers up to 10 MHz (see below). Cavitational events occurring outside the cylinder are shielded by a layer of acoustic absorber coating on its external surface [5-7].

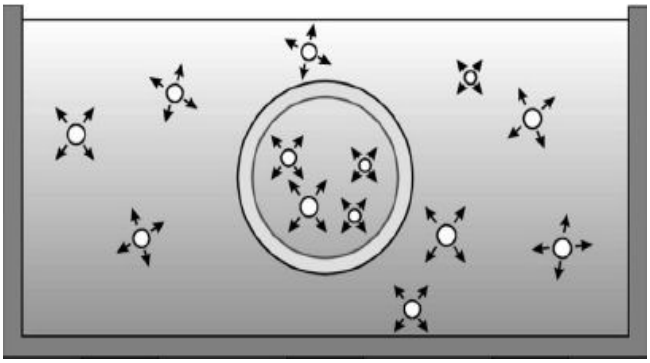

Figure 4.7: Representation of the concept behind the NPL cavitation cylindrical sensor. The sensor was designed to be sensitive only to events occurring within its hollow body (picture courtesy of Zeqiri *et al.* [7]).

Figure 4.8 shows a diagram of the specific NPL prototype used. The inside diameter of the sensor is 30 mm and its overall height is 17 mm. The loop situated on the side of the sensor is fabricated from synthetic epoxy and is used for rigid mounting to a rod. The outer surface is encapsulated within a 4 mm thick polyurethane cavitation shield developed from a rubber material normally used in naval applications. The use of rubber-base coating provides the sensor with an additional protection against cavitation erosion. The 4 mm shield presents an attenuation that increases with frequencies and it is about 1.7 dB at 40 kHz and at least 7.5 dB at 1MHz. Its acoustic impedance is designed to match that of water in order to induce a minimal perturbation on the acoustic field to which it is exposed. The electrical contacts are embedded inside the cavitation shield in order to be protected by cavitation. The inner cylindrical surface is formed from a 110 μm piezoelectric film (Measurement Specialist Industries, Valley Forge, PA) with a thickness resonance of 10 MHz and a capacitance in the range 1.9-2.1 nF. The prototype used was not calibrated because the NPL does not yet have a calibration procedure [4]. Therefore a measure of the magnitude of the acoustic emissions detected with it, during the experiments described in this thesis, is not available at this time.

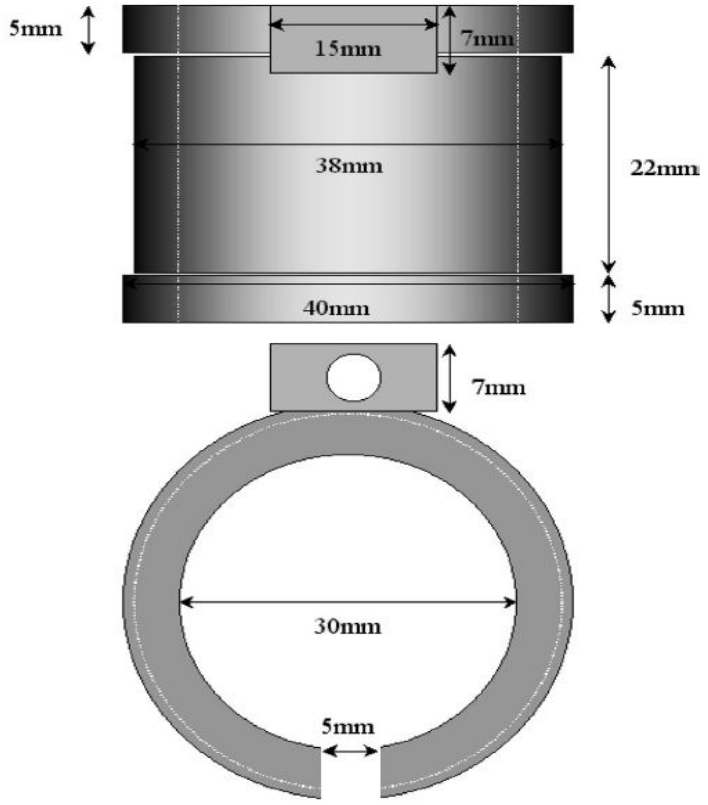

Figure 4.8: Diagram of the prototype cavitation sensor designed by NPL (courtesy of Zeqiri *et al.* [7]).

4.5 The stone Phantoms

A variety of stone phantoms was used in the course of this study to analyse the influence of the quality of the targeting and of the grade of fragmentation of a stone on the characteristics of the acoustic emissions [118, 120 121]. The most useful data were derived from stone samples made of plaster of Paris, the material predominantly used in lithotripsy experiments (Section 2.4), and phantoms made of glass micro-spheres. The latter phantoms mimicked stones at specific stages of fragmentation. The design of the two types of phantoms was part of the original contribution of this work. They will be described in the following subsections.

4.5.1 Plaster of Paris samples

Cylindrical samples were prepared using a ratio 2:1 of plaster of Paris (Section 2.4) and water. Cylinders of 1 cm diameter and 8 cm length were produced by means of a special purpose-built mould (Figure 4.9(a)) in order to limit trapped air. The material for the samples was chosen for the similarity of its acoustic properties to those of real stones and for the simplicity of the moulding process. The cylindrical shape was used for symmetrical reasons, as it matched the NPL sensor shape.

The samples were used to analyse the influence of targeting on the characteristics of the acoustic emissions and to make preliminary investigations on fragmentation phenomena.

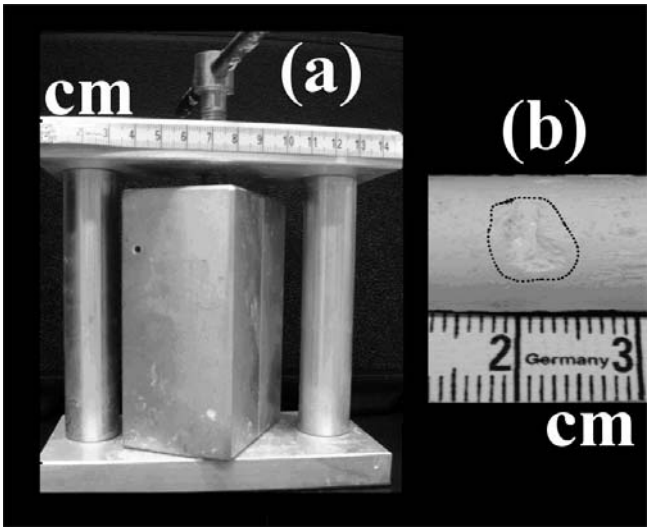

Figure 4.9: (a) Special mould used to produce cylindrical plaster stone samples and (b) detail of a sample partially eroded by cavitation. The damaged area is encircled by a dotted line.

4.5.2 Design concept for use of the glass micro-spheres phantoms

The aim of this project was to develop a new acoustic diagnostic system for lithotripsy that could complement the existing imaging systems by providing information about the degree of fragmentation of the stones. Normally, unless a stone is very small or a lot of gas is present in the body shielding it, the diagnostic imaging systems of a lithotripter give clear feedback when the fragmentation is violent (i.e. when the initial stone is completely shattered or only a small fragment is left after the treatment). The ambiguous cases are those in which the stone has had some fragmentation, but the fragments stay close together. In these cases images of stones appear less dense, but appear to have about the same size of the intact stone. In order to investigate these ambiguous cases, simple stone phantoms that model an ideal stone of a given volume, but at different grades of fragmentation and different densities, have been designed.

It should be clarified at the outset that these phantoms could only reproduce fragmentation up to 60%. Therefore predictions made using these phantoms can only be extrapolated to the case of higher grades of fragmentation if great care is used. The next subsection will describe how the phantoms were built.

4.5.3 Manufacture of the glass micro-spheres phantoms

Glass micro-spheres of equal density (ρ_{gl}=2500 kgm^{-3}) but different diameters (D) were used to build the different phantoms. This is to say, that each phantom was made by packing soda lime glass-spheres of a given diameter D (Figure 4.10) into a thin spherical container (ping-pong ball[14]) of diameter D_{pp}=38 mm. In each ping-pong phantom the tolerance admitted in the distribution of diameters around the average was smaller than 20%. The range of diameters used in the different ping-pong balls was 0.6-10 mm.

[14] Tests ensured that the wall of the ping-pong ball did not affect the characteristics of the lithotripter field. That is to say an attenuation less than 25% and a correlation coefficient greater of 0.8 was found between the waveforms measured, in water, at the focus of the lithotripter inside the holder, and the waveforms measured at the focus of the lithotripter in absence of the holder under the same source settings. In both cases the waveforms were measured using an Imotec 80-0.5-4.0 needle hydrophone, with a diameter of 0.5 mm.

The contents of each ping-ping ball were packed randomly. An ultrasonic shaker (Model S30H, Camlab Ltd., Cambridge, UK) was used to minimise the gaps between the micro-spheres used to fill in the ping-pong ball. After the filling, the ping-pong balls were sealed. Millimetric holes were drilled in the surface of each ping-pong balls to let water penetrate within the phantom and fill-in the gaps between the glass.

Soda lime glass was used because its hardness (6-7 on the Mohs scale) was considered high enough to expose repeatedly the phantoms to shock waves without damage. In addition, soda-lime micro-spheres were commercially available in a wide range of diameters.

It has to be noted that the size of these phantoms (D_{pp}=38 mm) is bigger than that of a real stone treated by ESWL (which normally has a diameter not larger than 10-15 mm). It is also bigger than the ESWL shock wavelength (~1 cm). Having such a large phantom helps to isolate the acoustics dynamics purely due to the grade of fragmentation of the stone from phenomena linked to its global size. However, such a difference from real stones has to be taken into account when evaluating the results of the *in vitro* experimentations.

Figure 4.10: (a) Soda lime glass micro-spheres and (b) stone phantom.

4.5.4 Packing density of the glass micro-spheres phantoms

The density of each phantom (built as explained in the previous section) could be directly related to the diameter of the filling microspheres (D) if the microspheres packing density (η_p) was known. This unfortunately was not the case.

The problem of sphere packing has been investigated by mathematicians since Kepler's time in the 17th century [124]. The theory states that if the used container dimensions were considerably bigger (at least one order of magnitude) than those of the packing spheres, a constant random packing ratio η_p~0.6 [125] could be expected. For situations when this is not the case, as in these phantoms where each container is a ping-pong ball, a theory has not been formulated yet. Therefore the packing density of most of these phantoms (D > 3 mm) could not be predicted *a priori*.

Direct weight measurements were used to determine the fraction of volume occupied by the micro-glass spheres in each phantom. Figure 4.11 shows that the phantoms appeared to be decreasing in weight and (being of equal volume) in density with the diameter of the filling glass spheres (D). In particular the weight resulted in being well approximated by a linear function of the glass balls diameter. The square of the correlation coefficient for the linear fitting shown in Figure 4.11was r_c^2=0.9.

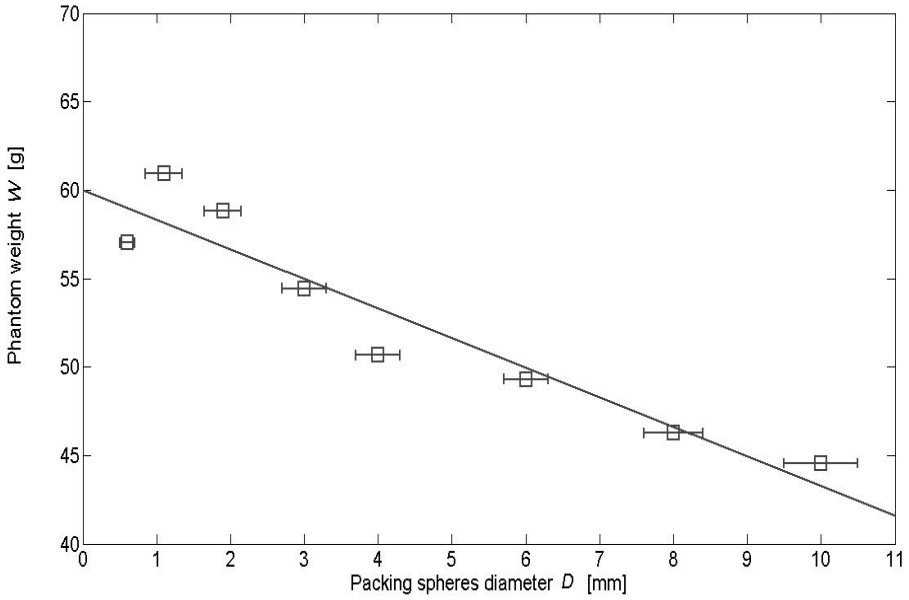

Figure 4.11: Correlation between the weight of each ping-pong stone phantoms (*W*) and the diameter (*D*) of the glass micro-spheres used to fill it. The error bars represent the range of micro-spheres diameters present in each phantom. The line between the samples represents the best linear fitting. The square of the correlation coefficient between the straight line and the interpolated data was 0.9. Each weight was measured by a precision scale with an uncertainty of 0.01%.

4.5.5 Interstitial gaps of the glass the micro-spheres phantoms

It is self-evident that a collection of spheres will not fill a given space and that, using the same packing, the size of the gaps between the spheres increases with their diameters. Figure 4.12 shows three examples with the sphere diameter *D* increasing binary, using regular hexagonal packing of spheres in a box. The hexagonal packing is such that the centres of three adjacent spheres form the vertices of an equilateral triangle (Figure 4.12(d)). This packing is used as an example as it was proved to have the maximum packing density possible (η_p~0.6) [124].

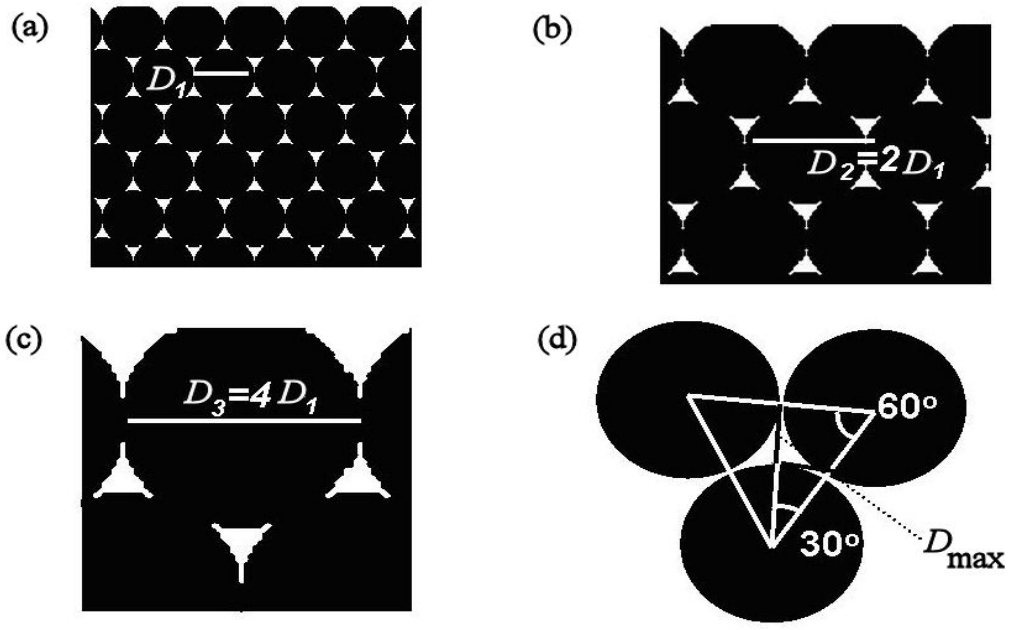

Figure 4.12: Example of sphere packing using a regular three dimensional hexagonal arrangement for (a) spheres of a given diameter D_1, (b) spheres with diameter D_2=2D_1 and (c) spheres with diameter D_3=4D_1. The detail of the arrangement of three adjacent spheres in these packing at the vertices of an equilateral triangle is showed in panel (d).

Applying the rules of trigonometry to the triangles in Figure 4.12(d) it can be shown mathematically that, for the considered packing, the maximum distance between two packed spheres (D_{max}) would be directly proportional to their diameter (D):

$$D_{\max} = D\sin(60^o) - \frac{D}{2} = \frac{(\sqrt{3}-1)D}{2} \tag{25}$$

Recently, more complex numerical simulations [126] have also estimated an equivalent pore diameter (D_{eq}) for random sphere packing:

$$D_{eq} = \sqrt{\frac{(2\sqrt{3}-\pi)}{2\pi}}D \tag{26}$$

This latest result confirms that also for random packing, as that used in our phantoms, the size of the pores between the packing spheres is proportional to their diameter.

4.5.6 Fragmentation ratio of the glass micro-spheres phantoms

The previous Subsections have described how stone phantoms of equal volumes but different densities were built using glass microspheres of different diameters D. The phantoms showed smaller weights (Figure 4.11), and consequently smaller average densities, and larger pores (Equation (26)), when the packing spheres diameters (D) were larger.

Each phantom (Figure 4.13(b),(c)) can be considered to be a specific fragmentation state of an ideal glass phantom. This ideal phantom would be made of a ping-pong ball filled by a single glass sphere the same size as the ping-pong ball (Figure 4.13(a)).

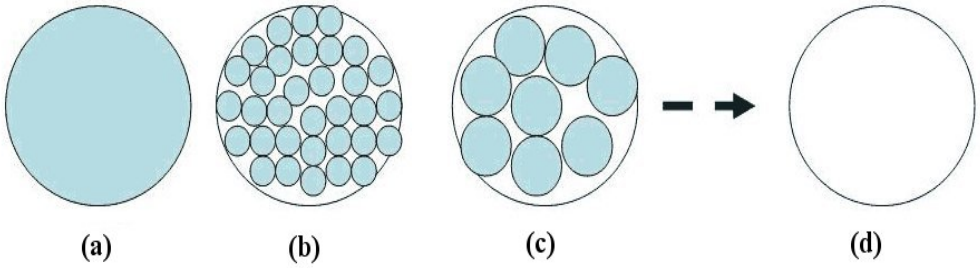

Figure 4.13: Stone phantoms that from left to right represent a stone at increasing grade of fragmentation from (a) intact glass ball with fragmentation 0% to (d) empty ping-pong ball with fragmentation 100%.

The fragmentation ratio of each sample (F) can be quantified as the percentage of weight loss from the weight of the ideal stone (W_0).

The weight of the ideal phantom can be calculated, knowing the density of the glass spheres (ρ_{gl}), as:

$$W_0 = \frac{4}{3}\pi\rho_{gl}\left(\frac{D_{pp}}{2}\right)^3 + W_{100} = 83.91g \tag{27}$$

where ρ_{gl} = 2.5 kgdm^{-3}, D_{pp}=38 mm is the diameter of the ping-pong ball, and W_{100}= 10.96 g is the weight of the empty ping-pong ball.

Therefore, assigning to an empty ping-pong ball a fragmentation F=100%, the fragmentation of a phantom of weight W can be expressed as:

$$F = 100\frac{W_0 - W}{W_0 - W_{100}} \tag{28}$$

where W_0=10.96 g is the weight of the empty ping pong ball and W_{100}=83.91 g is the weight of the ping-pong size glass ball. A hypothesis of linearity was applied to generate a law of variation of the fragmentation ratio from 100% to 0%. This was assumed reasonable considering the linear dependence of the average densities of the phantoms on their weights.

Figure 4.14 shows the fragmentation ratio (F) of each ping-pong phantom, and its weight (W) as functions of the diameter (D) of the filling glass microspheres. The same parameters are reported in Table 4.2, which shows that the described phantoms represent fragmentation grades between 31% and 54% (31%<F<54%). Therefore these phantoms, as anticipated in Section 4.5.2, strictly describe only the dynamics of processes with fragmentation grades F<60%.

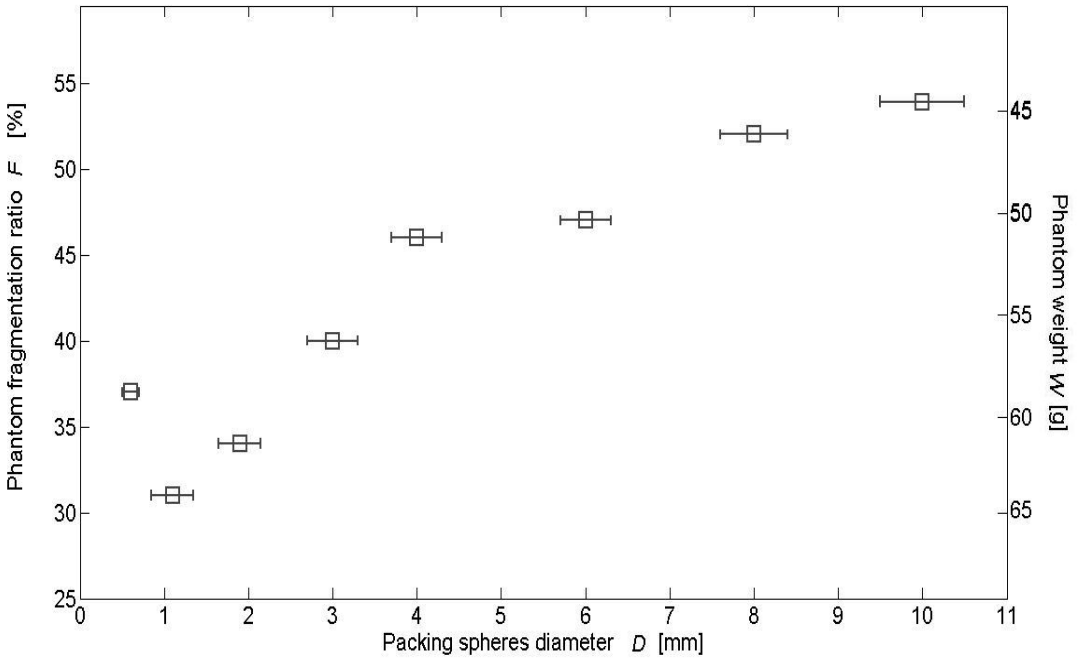

Figure 4.14: Dependence of the fragmentation ratio (*F*) of each glass-microspheres phantom and its weight (*W*) on the diameter of the filling microspheres (*D*). The error bars represent the range of micro-spheres diameters present in each phantom. The linear dependence between *W* and *D* was derived empirically. The linear dependence of (*F*) on both parameters was imposed by Equation (28).

D [mm]	*W* [g]	*F* [%]
10 ± 0.40	44.54	54
8 ± 0.40	46.25	52
6 ± 0.30	49.30	47
4 ± 0.30	50.67	46
3 ± 0.30	54.44	40
1.9 ± 0.25	58.81	34
1.1 ± 0.25	60.93	31
0.6 ± 0.10	57.01	37

Table 4.2: (*D*) diameter (average ± half a range) of the microspheres filling the sample of weight (*W*) and fragmentation ratio (*F*). The values are reported for all the produced samples.

4.6 Summary

This Chapter describes the instrumentation used to investigate, *in vitro*, the influence of the quality targeting and grade of fragmentation of a stone on the characteristics of the secondary acoustic emissions. This *a priori* knowledge was essential to design the different components of a clinical prototype diagnostic system (Chapter 7).

The equipment described includes the different components of a specially designed bench-top EM lithotripter that was operated at 16 kV, giving shocks of P^+= 19±4 MPa and P^- = 3±0.6 MPa, and a novel cavitation sensor, developed by NPL, that was used to record the acoustic emissions.

Stone samples of the same hardness of kidney stones (plaster of Paris samples), and stone phantoms harder than kidney stones that mimicked a stone at a specific stage of fragmentation (glass microsphere samples), were designed and were placed at the focus of the lithotripter, adjacent to the NPL sensor. This was done in order to evaluate the influence of these phantoms on the characteristics of the emissions. The following Chapter 5 will illustrate the signal processing procedures developed to analyse the acoustic signal, which are among the key original contributions of this work, and Chapter 6 will present the information extracted.

Chapter 5 Signal processing

5.1 Introduction

Chapter 2 and Chapter 3 described the spontaneous generation of secondary acoustic emissions during ESWL and showed that the acoustic emissions contain information which is relevant to processes (direct stress, reflection, reverberation and cavitation), that are directly linked to the fragmentation mechanisms. This Chapter will illustrate the mathematical methods used in this work to extract these embedded data from the recorded acoustic signals. The first step was to characterise the emissions in the time, frequency and time-frequency domains. The second was to extract the features of the emissions that were predominantly affected by the targeting and fragmentation processes.

5.2 Time analysis

The first features observed in a typical secondary acoustic emission (Figure 5.2(a)) are the two bursts emerging from the background noise. Previous studies (Chapter 3) examined the two bursts and identified an important feature in the interval between them. The author has analysed the two bursts, introducing new characteristic parameters (that will be described in Section 5.2.2) and developing a MATLAB^{TM} software for automatic feature extraction. The software, which has been called SEAC (Secondary Emissions Analysis in Clinic), is the core of the diagnostic processing developed in this work. A complete description of the SEAC algorithm is given in Appendix A. The next subsection will describe the approach used to detect the location of the two bursts in the emission. Localisation is the first problem usually encountered in analysing transient signals such as the bursts.

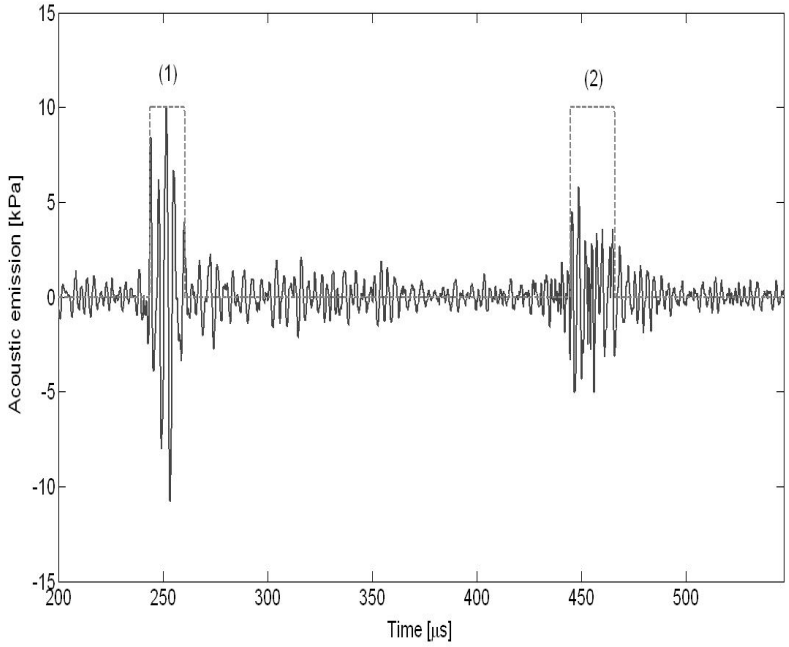

Figure 5.1: (a) An example of a double-peak acoustic emission detected during the ESWL treatment of a patient during the clinical trial described in Chapter 8. Two characteristic bursts (1) and (2) can be extracted above the noise level. These bursts are marked by the dotted line. The signal was acquired using the clinical passive ultrasound system developed, as part of this work, in collaboration with the supervisors of this project and Precision Acoustics Ltd. The system will be described in Section 7.3.The technique used to detect the bursts will be explained in the following subsections.

5.2.1 The Detection algorithm

Looking at a typical secondary emission (Figure 5.1), one observer can easily identify the two bursts (regions (1) and (2)). This is because the human brain automatically focuses its attention on those components of the signal above a common level of no interest, termed as 'noise'. Behind this selection there is a processing that needs to be reproduced when developing automatic software to analyse these emissions. The most straightforward solution is to train the software to choose those parts of the signal above an established threshold. Threshold detection algorithms may use fixed or adaptive thresholds. A fixed threshold is a given value, constant for all signals. In contrast, an adaptive threshold is a value specific for each signal and depends on some chosen proprieties of the signal.

Secondary acoustic emissions amplitudes depend on the lithotripter energy setting, on the positioning of the sensor, and on the absorption happening in the medium. This means that, as such conditions change from patient to patient (as it will be shown in Chapter 7), an adaptive threshold had to be used to detect the two bursts in the secondary acoustic emissions. In addition, to increase the signal to noise ratio before doing the localisation, the detection was done on the distribution of the acoustic power levels in the signal rather than that of the amplitudes. Given an acoustic emission $p_a(t)$ of duration T, its power distribution function ($I(t)$) was calculated as:

$$I(t) = \frac{p_{\mathrm{a}}(t)^2}{\int_0^T p_{\mathrm{a}}(t)^2 \, dt} \tag{29}$$

The distribution function $I(t)$ was defined such as its integral over time T is unit. Figure 5.2(b) shows the power distribution function $I(t)$ of the signal in Figure 5.2(a). The comparison of the two signals in Figure 5.2 shows that the bursts in the power distribution signal (Figure 5.2 (b)) are emphasised above the noise level.

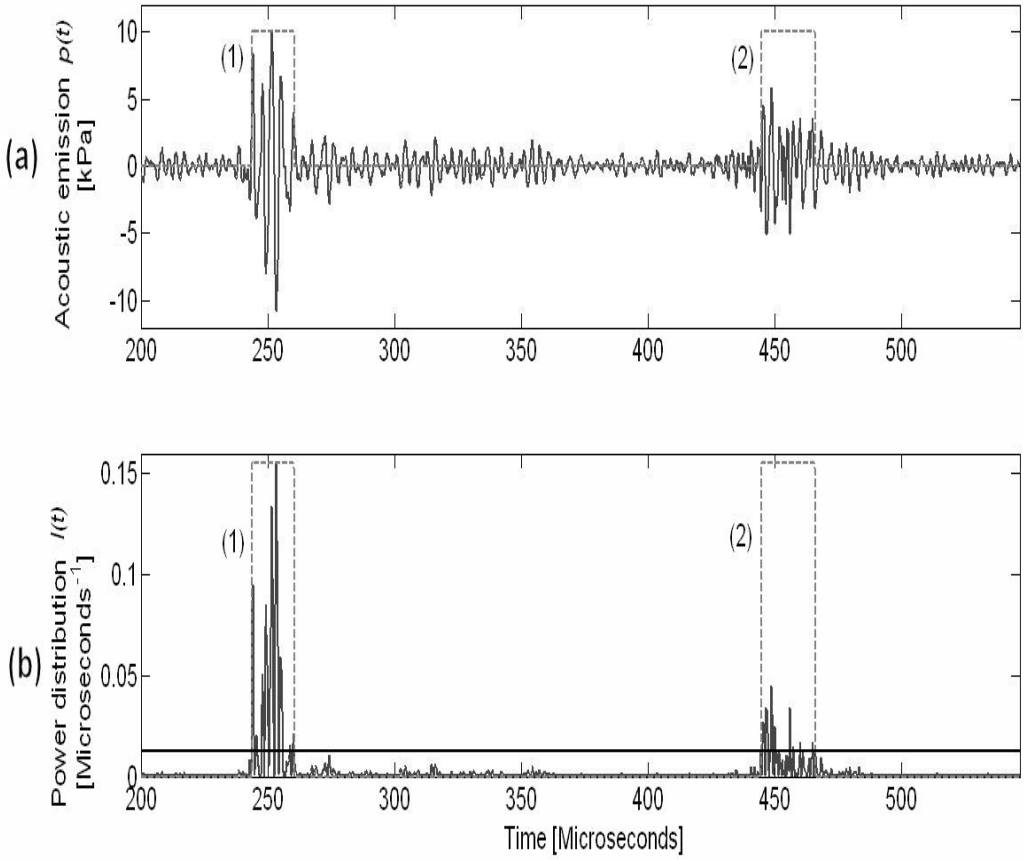

Figure 5.2: (a) Typical acoustic emission shown in Figure 5.1. The dotted lines mark the first (1) and second (2) burst. The signal was acquired from a patient using the clinical passive ultrasound system developed, as part of this work, in collaboration with the supervisors of this project and Precision Acoustics Ltd. The system will be described in Section 7.3. (b) Power distribution function of the signal in (a) and corresponding threshold level used by the detection algorithm described in Subsection 5.2.1.

5.2.2 Selection of the Threshold level

The SEAC algorithm was developed to identify the two bursts as those two portions of signal whose power levels were higher than 96% of all the power levels present in the distribution function $I(t)$. The details regarding the choice of this specific percentage will be explained in Subsection 5.2.4. Briefly, it was observed that in a typical emission, Figure 5.2(a)), the two bursts contain the highest power levels (Figure 5.2(b)), but the only last a small portion of time (less than 50%). This fact was used as a discriminant between the bursts and the noise level to develop a first version of the algorithm that used the median value (or in other words the 50^{th} percentile) of the power distribution $I(t)$ as threshold for the detection. The algorithm was tested using this threshold (Subsection 5.2.3) on a set of signals recorded in the bench-top EM lithotripter (Section 4.3) in tap-water using the NPL cavitation sensor (Section 4.4). This first test failed as the threshold was too low and two different regions above the noise level could not be identified.

Subsequently the test was repeated using gradually increasing percentiles until a sensitivity (S) of 100% was obtained for both bursts using a threshold equal to a 90^{th} percentile. The sensitivity is a parameter used in evaluating the performances of either detection or classification algorithms [127]. According to the application (i.e. detection or classification), the parameter is used to indicate either the correct detection or classification of a event. In this context, as will be explained in the next subsection, it indicates the percentage of correct localisations.

It is evident from Figure 5.2(b) that each burst also contains points with powers below the threshold level. This is to say, each burst is made up of few adjacent regions above the threshold. A maximum separation time was imposed between those regions to be considered as part of the same burst. This time was equal to 50 μs for *in vitro* data and 20 μs for *in vivo* data. The latter time is shorter than the former because the intervals between the two bursts

observed *in vivo* (50-300 μs, see Chapters 7 and 8) were generally lower than those observed *in vitro* (200-400 μs, see next Chapter).

Once a prototype clinical ultrasound sensor was developed in collaboration with Precision Acoustics Ltd, and before any *in vivo* investigation, the detection algorithm was tested on signals recorded in the clinical lithotripter *in vitro* (adjacent to stone phantoms, see Subsection 5.2.4). In this new configuration, the threshold equal to the 90th percentile failed in the detection of the second burst in 50% of the cases, as the noise levels were higher than those present in the traces recorded in the bench-top lithotripter with the NPL sensor.

Therefore further tests were necessary to re-establish the optimum threshold. This value turned out to be equal to the 96th percentile for correct detection in 97% of the cases. The following subsections will illustrate the details of the two sets of experimentations.

5.2.3 Optimisation of the threshold in the *in vitro* experimental set-up

In the *in vitro* experimental set-up (Chapter 4), the algorithm was tested on a set of 30 traces recorded in tap-water at the focus of the bench-top EM tank using the NPL cavitation sensor (Section 4.4) under the EM source discharge voltage settings of 16 kV. As explained in Section 4.3, these voltage settings produced acoustic pressures comparable (within 15%) with acoustic pressures used clinically, once the applied shockwave has been attenuated by absorption by the body.

All 30 traces used showed the reproducible two burst structure and the aim of the test was to find the adaptive threshold that would allow the algorithm to detect these two bursts in each trace. The adaptive threshold was set to be a specific percentile of the power distribution $I(t)$ calculated by the algorithm using Equation (29). This value was varied from 50 to 95 and the performance of the algorithm were evaluated in each case against the visual detection of three independent observers. Few parameters usually used in the evaluation of detection or classification algorithms [127], were used to measure these performances; they will be described as follows. The number of True Positives (TP), that is the number of correct

localisations on the whole set of 30, was calculated for the first (TP_1) and second burst (TP_2). The number of False Negatives (FN), that is the number of bursts completely missed on the whole set of 30, was calculated for the first (FN_1) and second burst (FN_2). The number of False Positives (FP), as intended for the aim of this test, was the number of bursts that were localised at the wrong time or whose duration was overestimated. This number was calculated for the first (FP_1) and second burst (FP_2). It has to be clarified that usually the term 'False Positive' is reserved for the wrong detection of an event that has not really happened on the specific occasion. This meaning would not apply to the data set chosen, whose signals, as explained, always showed two bursts over the noise level, when visually inspected. The number of True Negatives, that is the percentage of bursts genuinely not present in the signal, was zero in all tests, for the same reason. The results of this testing are reported in Table 5.1, where the parameters are expressed as percentages based on 30 trials rather than absolute numbers. It has to be clarified that the algorithm is structured so that it always detects a first burst (see Appendix A for details on the software). However for low thresholds (less than 70th percentile, see Table 5.1) its duration is extended to the whole burst. As explained above, this was considered a FP. Table 5.1shows that 90 was the best performing threshold, giving a percentage of true positives for both the first and second bursts (TP_1% and TP_2% respectively) equal to 100%. Figure 5.3 shows what portion of signal was identified as 'Bursts' (dotted line) under thresholds varying from the 70th (Figure 5.3(a)) to the 95th (Figure 5.3(e)) percentile, for one of the traces in the test subset recorded in tap water. Specifically the different boxes illustrate the result of following values: (a) 70th percentile, (b) 80th percentile, (c) 85th percentile, (d) 90th percentile and (e) 95th percentile.

Percentile	TP_1%	TP_2%	FN_1%	FP_1%	FN_2%	FP_2%
50	0	0	0	100	100	0
60	0	0	0	100	100	0
70	0	0	0	100	100	0
80	80	80	0	20	17	3
85	100	80	0	0	0	20
90	100	100	0	0	0	0
95	100	93	0	0	7	0

Table 5.1: The results of the testing on the detection algorithm in the laboratory set-up. The symbol of $TP_1\%$ equals the percentage of True Positives (TP) obtained in attempts to detect the 1st bursts. The symbol of $TP_2\%$, equals the percentage of TP obtained in attempts to detect the 2nd burst. The symbol of $FN_1\%$ equals the percentage of False Negatives (FN) obtained in attempts to detect the 1st burst. The symbol of $FP_1\%$ indicates the percentage of False Positives (FP) obtained in attempts to detect the 1st burst. All the analysed emissions contained a first and second burst. The term FP is intended, here, as an overestimate of the first burst duration when the 2nd burst was missed. The symbol of $FN_2\%$ equals the percentage of FN obtained in attempts to detect the 2nd burst. The symbol of $FP_2\%$ equals the percentage of FP in attempts to detect the 2nd burst. In the case of the second bursts, a FP indicated either an overestimate of their duration or a misallocation.

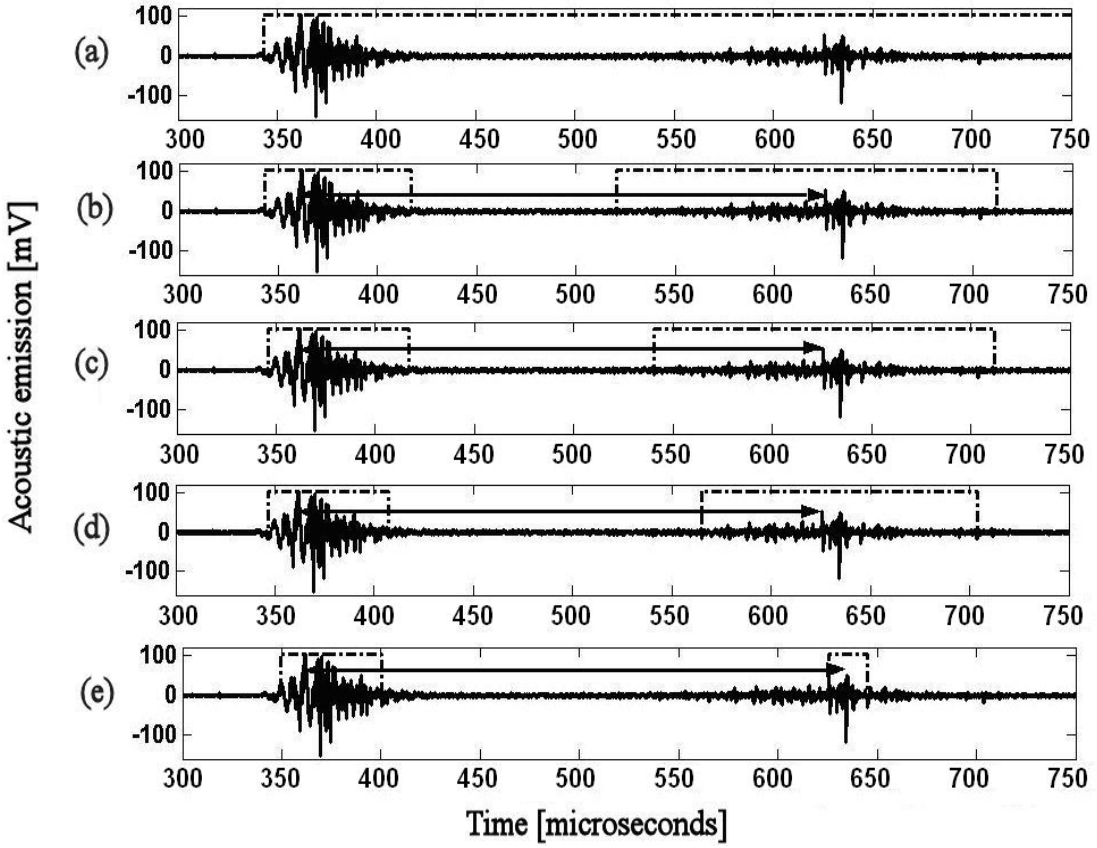

Figure 5.3: Bursts detected (dotted line) in a typical trace recorded in tap water (using the set-up described in Chapter 4) under thresholds varying from (1) the 70th to (5) the 95th percentile. Each box illustrates the portions of signal identified as 'bursts' by the algorithm at a specific threshold. The thresholds in the various panels of Figure 5.3 are (a) 70th percentile, (b) 80th percentile, (c) 85th percentile, (d) 90th percentile and (e) 95th percentile. Three independent observers considered as best detection the one obtained under the threshold of 90th percentile.

5.2.4 Optimisation of the threshold in the clinical set-up

The clinical set-up is described in detail in Chapter 7. Figure 5.4(a) shows the treatment couch of the lithotripter (an EM Storz Modulith SLX-MX), where a patient lies during the procedure. For the aim of this test, a body phantom made of a PMMA water tank, filled with tap water, was placed on the treatment couch (Figure 5.4(a)). The tank had an acoustically transparent window at the bottom (shown in Figure 5.4(b)) to allow the transmission of the shockwave. Four glass lime stone phantoms (described in Subsections from 4.5.2 to 4.5.6) were placed, in turn, in the tank at the focus of the lithotripter. These phantoms simulated stones at 4 different grades of fragmentation: F= 31 %, F= 46 %, F= 54 % and F= 100 % (see Subsection 4.5.6 for a definition of F). A set of 30 traces was collected for each phantom (i.e. for each fragmentation grade), using the clinical data acquisition and conditioning module developed in this work, in collaboration with supervisors and PAL. The system, which includes a passive ultrasound sensor, a preamplifier and high pass filter at 300 kHz is described in Chapter 7. The prototype sensor (Figure 5.4(b)) was positioned close (1 cm) to the stone phantoms (Figure 5.4(c)).

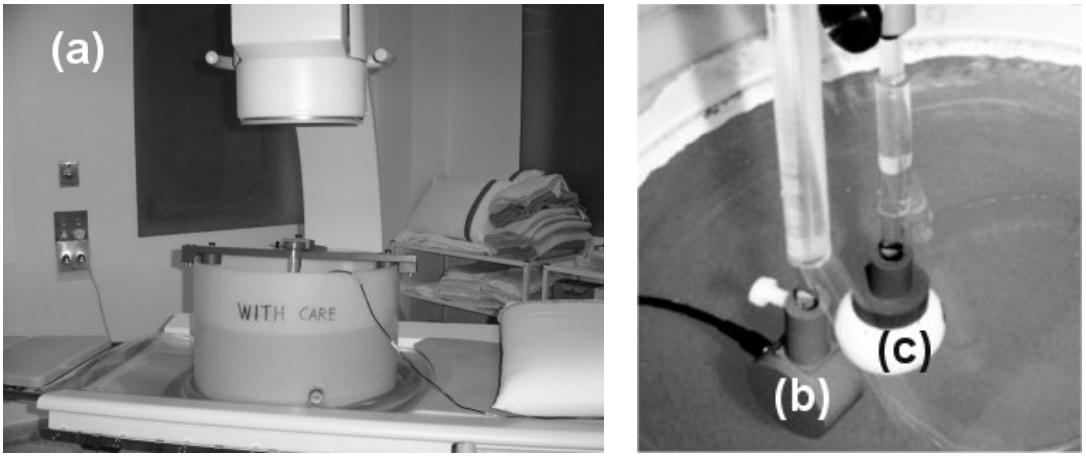

Figure 5.4: Frame (a) shows the body phantom placed on the treatment couch. The contents of the body phantom are shown in the second panel. They include (b) the prototype sensor developed in collaboration with supervisors and PAL (see Chapter 7 for a description of the prototype) and (c) the stone phantom. The body phantom is made of a PMMA tank with an acoustic transparent window at the bottom that allows the transmission of the shock wave.

The performances of the detection algorithm were evaluated for each fragmentation grade F, using the threshold of 90th percentile. This threshold, as described in the previous subsection, was the optimum threshold for burst detection in traces recorded in tap-water in the bench-top EM lithotripter. The performances of the algorithm were measured exploiting the key parameters defined in the previous section (TP_1, TP_2, FP_1, FP_2, FN_1, FN_2) against the detection made by three independent observers, when visually inspecting the traces. In addition, the information contained in these parameters was summarised in two global parameters (S_1 and S_2), which expressed the sensitivity of the algorithm in detecting the first (S_1) and the second burst (S_2). The two additional parameters S_1 and S_2 were calculated as follow:

$$S_1 = \frac{TP_1}{TP_1 + FN_1} \times 100 \tag{30}$$

$$S_2 = \frac{TP_2}{TP_2 + FN_2} \times 100 \tag{31}$$

The sensitivity is another standard parameter used in the evaluation of detection or classification algorithms [127]. As expressed in Equations (30) and (31), this indicates for each burst the percentage of TP among total number of bursts to be detected. In the case of the first burst the number of TN (TN_1) was equal to zero, therefore S_1 was equal to the percentage of TP on the whole set (TP_1%).

The threshold of the 90th percentile gave the algorithm a S_1 of 100% for all four sets. However the inter-sets average S_2 was only about 40% (Figure 5.5) using that threshold.

Subsequently the percentile threshold was varied from the 90th to 97th, and for each sample were estimated again TP_1, TP_2, FP_1, FP_2, FN_1, FN_2, S_1 and S_2. As the threshold was increased from 90 to 95, S_2 increased linearly for all stone phantoms (Figure 5.5) except that of water (F=100%). The sensitivity S_2 of this phantom stayed equal to zero up to a threshold

of 95 to reach its maximum at 96. A different behaviour for the water phantom, and in particular the necessity of a higher threshold level, was to be expected, as in water the cavitational component of the secondary emissions is stronger. This affects the shape of the second burst which, as explained in Section 3.2, represents mainly cavitational activity. It will be shown in Section 6.3 that second bursts in emissions collected adjacent to the water phantom have a higher amplitude (Subsections 6.3.3 and 6.3.8) and are more peaked (Subsection 6.3.7) than those collected in proximity of the other phantoms. The particular behaviour shown for this phantom under the different thresholds, however, was not predictable and depended on the specific power distributions of the traces collected. Figure 5.7 shows, for one of the traces collected adjacent to the water sample, the changes in the localisation of the two bursts (dotted line), when the threshold level was increased from the 90^{th} percentile (a) to the 97^{th} percentile (f). At threshold levels of 90^{th} and 91^{th} percentiles (Figure 5.7(1),(2)) the first burst duration was overestimated, to include the second burst. At 93^{th} and 95^{th} percentiles the first burst duration was estimated correctly, but that of the second burst was highly overestimated (> 100% of the real duration). Using the terminology explained, we can say that the threshold of 95 percentile, when applied to this trace, gave 1 TP_1, 0 FP_1, 0 FN_1, 0 TP_2, 0 TN_2 and 1 FP_2. At 96 the localisation of the second burst was correct, but at 97 most of it was missed by the algorithm. The threshold level of 96^{th} percentile gave the best average S_2 over all the four phantoms. Figure 5.5 shows that at this level the S_2 of all samples converged towards 97%. If the threshold was increased further the average sensitivity started to decrease again.

Unfortunately the increase of the threshold from the 90^{th} to 95^{th} percentile also increased the number of FP in the detection of the second burst (FP_2). Figure 5.6 illustrates the effect on FP_2 of the different thresholds used from the 90^{th} to 97^{th} percentile. The smallest average FP_2 was about 10% at a threshold of the 90^{th} percentile. As the threshold was increased, FP_2 increased to reach its maximum of 40% under the threshold of the 95^{th} percentile. At the 96^{th} percentile, FP_2 started decreasing and was about 20%. In conclusion the threshold level of the 96^{th} percentile was the best compromise between having a high S_2 (>90%) and a low FP_2 (20%) for the different grades of fragmentation.

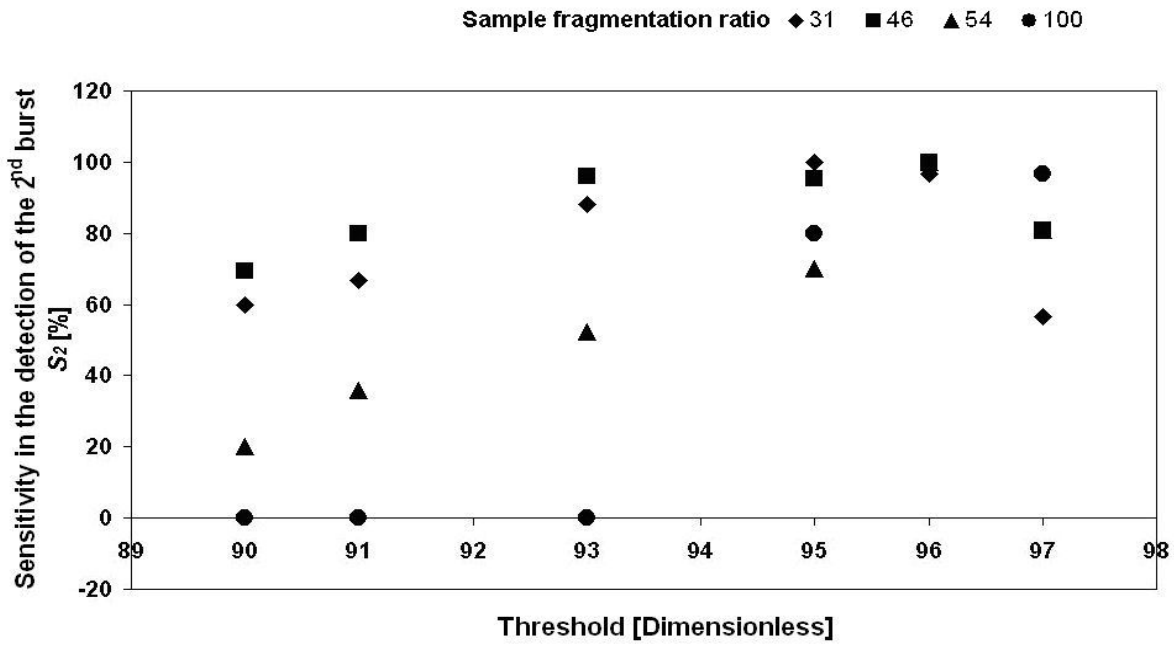

Figure 5.5: Sensitivity in the detection of the second burst in the emissions for threshold varying from the 90th to the 97th percentile and samples at different stages of fragmentation.

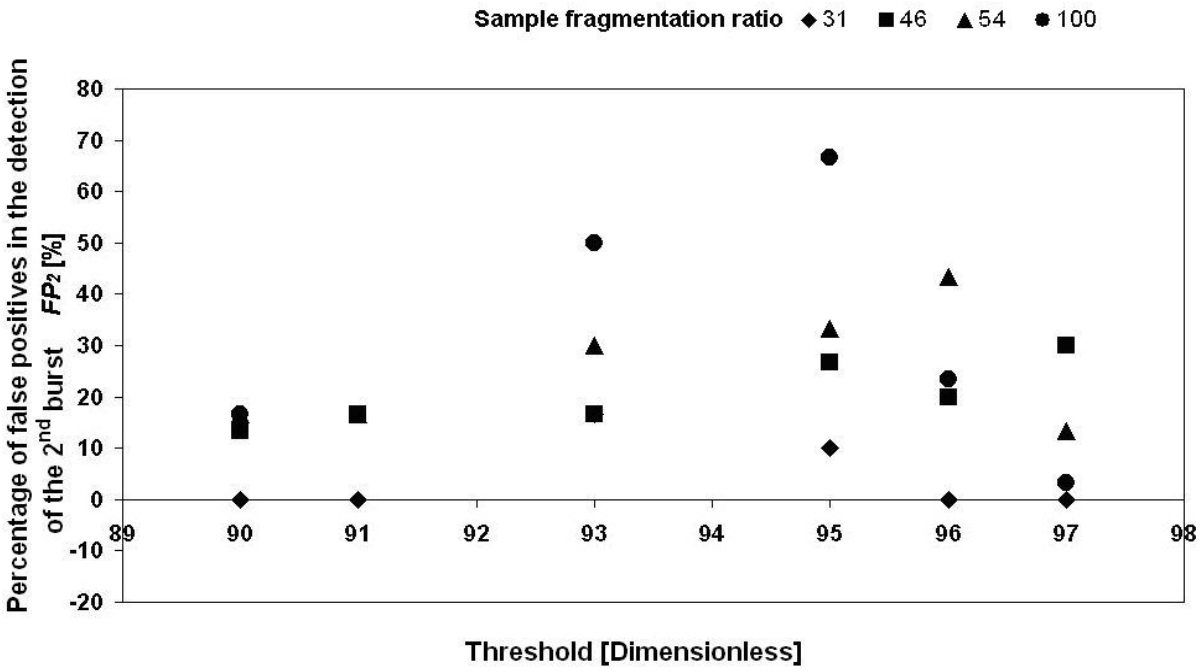

Figure 5.6: False positives percentage in the detection of the second burst in the emissions for threshold varying from the 90th to the 97th percentile and samples at different stages of fragmentation.

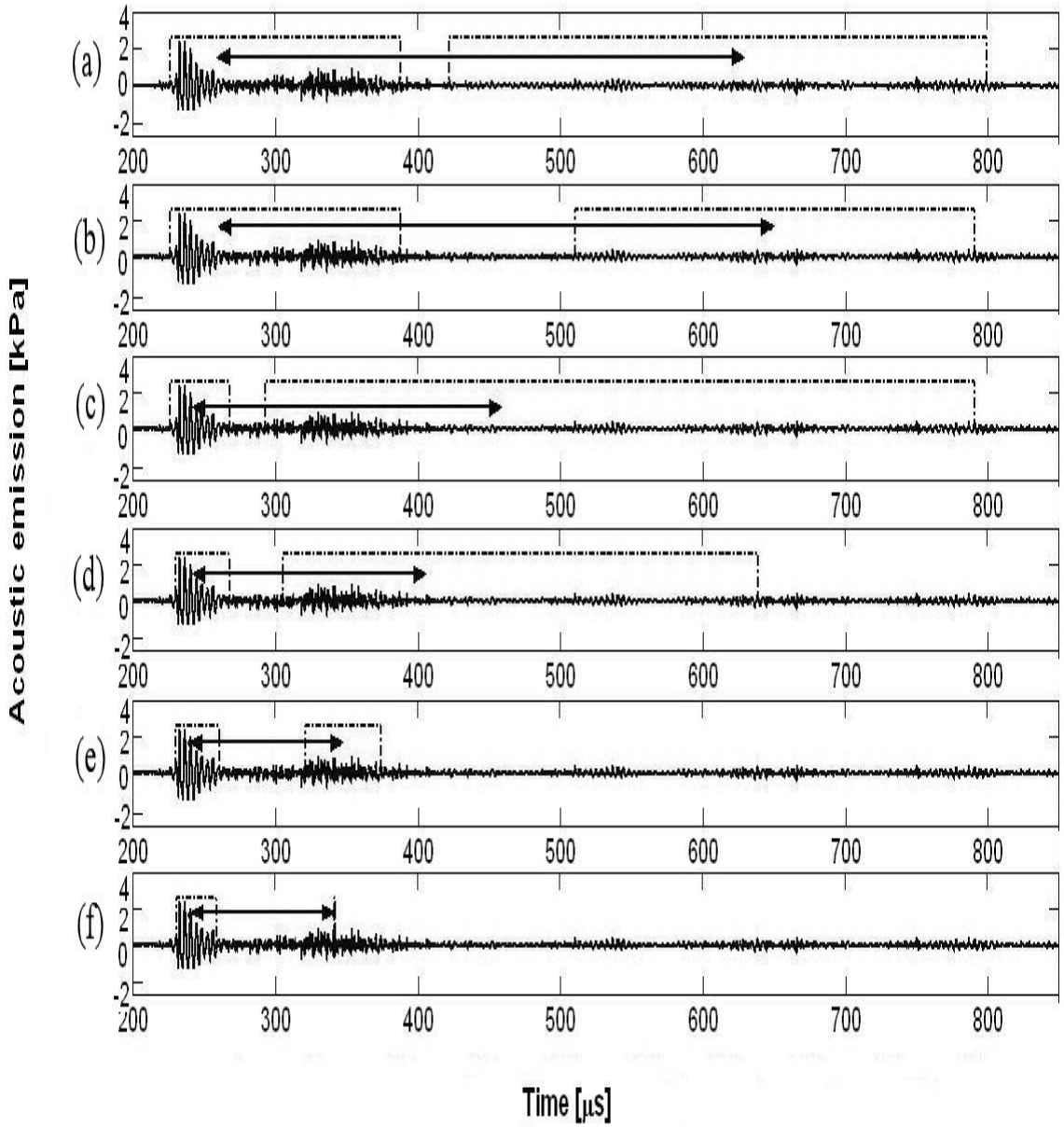

Figure 5.7: Bursts detected (dotted line) in a trace collected in tap water in the clinical set-up under thresholds varying from (a) 90th to (f) 97th percentile. Each box illustrates the portions of signal identified as 'bursts' by the algorithm at a specific threshold. The thresholds in the various panels of Figure 5.7 are (a) 90th percentile, (b) 91th percentile, (c) 93th percentile, (d) 95th percentile, (e) 96th percentile, (f) 97th percentile. Three independent observers chose as optimum the threshold of 96th percentile.

5.2.5 Feature extraction

Once the two bursts in the secondary acoustic emissions were detected, as explained in the previous sections from 5.2.1 to 5.2.4, they were characterised in terms of few features (Figure 5.8):

- m_1 and m_2, the maximum amplitudes of the first and second burst, which are indicators of the strongest acoustic interaction occurring during the relative burst. In the typical two-peak example in Figure 5.8(a) m_1= 10 kPa and m_2=5 kPa. In the multi-peak example in Figure 5.8(b), which shows a spread and asymmetrical second burst, the values are m_1= 2.5 kPa and m_2= 1.5 kPa. Both kinds of traces were recorded *in vivo* and show a higher m_1 with a ratio of about 2:1 between m_1 and m_2. The pressure levels in the two traces are different as they were recorded from two different patients[15].
- t_1 and t_2, the central times of the first and second burst, are unique times for each burst that represent the central time of its power distribution. The power distributions of the two bursts (I_1 and I_2) are calculated using Equation (29) and integrating over the time allocated to each burst. The two central times (t_1 and t_2) are derived as a statistical averages weighted by the bursts power distributions [128]:

$$t_i = \int_{t_{i\min}}^{t_{i\max}} t I_i(t) dt \qquad (32)$$

where t_{imin} and t_{imax} are the start and end time of the burst i.

In a typical two-peak emission, such as that illustrated in Figure 5.8(a), the central times (t_1=251 μs and t_2=453 μs) are close to the time of occurrence of m_1 and m_2. In

[15] The traces featured in the examples of signal processing presented form now on in this Chapter (unless differently stated) refer to patient data, as they were retained more interesting for the reader than *in vitro* data. These data were recorded with the developed prototype system that will be described in Chapter 7, which includes a passive ultrasound sensor, a preamplifier and a high pass filter at 300 kHz. However next Chapter will show also the features of the typical traces recorded *in vitro*.

such traces one could equivalently just consider the time of occurrence of m_1 and m_2. It is in traces with asymmetrical bursts, such that shown in Figure 5.8 (b), that the use of these parameters becomes fundamental as they represent two average times that consider the global structure of the burst and are not influenced by the random position of the highest peak. In the example shown in Figure 5.8 b), only t_1= 241 μs is close to the time of occurrence of m_1, whilst t_2= 347 μs occurs earlier than m_2 and it is less dependent on the particular time of occurrence of m_2.

- the duration of each burst d_1 and d_2, estimated as the length of that fraction of burst, around its centre, which contains at least 99.9% of its energy content [128]:

$$d_i = 6 \times \sigma_i \tag{33}$$

with i=1,2, σ_i the standard deviation of I_i calculated as follows.

$$\sigma_i = \sqrt{\int_{t_{i\min}}^{t_{i\max}} (t - t_i)^2 I_i(t) dt} \tag{34}$$

where t_{imin} and t_{imax} are the start and end time of the burst.

Applying these calculations to the bursts shown in the emissions in Figure 5.8, d_1 = 21 μs and d_2 = 20 μs are estimated for the typical emission (a). Trace (b) shows a similar duration of the first burst (d_1 = 35 μs), but a more spread second burst (d_2=151 μs).

- sk_1 and sk_2, the skewness of each burst (not shown in the picture), which are parameters that indicate whether the bursts are symmetric around their centre. If the distribution of powers in a burst is symmetric then its skewness is zero, otherwise it is positive if the values are skewed right (right tail of the distribution is longer than the left one), and negative if they are skewed left. The defining equations are:

$$sk_i = \frac{\int_{t_{i\min}}^{t_{i\max}} \left(t - t_i\right)^3 I_i(t)dt}{\sigma_i^{\,3}} \qquad (35)$$

where $I_i(t)$, t_i and σ_i are respectively the power distribution, the central time and the standard deviation of the i^{th} burst (i=1, 2) described as above.

In the typical emission considered in Figure 5.8(a), the first burst is slightly skewed left (sk_1 = -0.30), and the second burst is slightly skewed right (sk_2 = 0.67). On the contrary the emission in Figure 5.8(b) shows a first burst slightly skewed right (sk_1 = 0.37), whilst the second burst is slightly skewed left (sk_2 = -0.23). The aim of these parameters is to help in detecting and quantifying the differentiation of a trace from a typical two-peak structure.

- ku_1 and ku_2, the kurtosis of each burst (not shown in the picture), which are parameters that indicate if the bursts are flatter or more peaked than a bell-shape distribution, named Gaussian distribution [128]. That is to say, the excess kurtosis are considered, which assume negative values for 'flat' distributions and positive values for 'peaked' distributions and are defined as [128]:

$$ku_i = \frac{\int_{t_{i\min}}^{t_{i\max}} \left(t - t_i\right)^4 I(t)dt}{\sigma_i^{\,4}} - 3 \qquad (36)$$

where $I_i(t)$, t_i and σ_i are respectively the power distribution, the central time and the standard deviation of the i^{th} burst (i=1, 2) described as above.

The first burst in Figure 5.8(a), for example, has almost a Gaussian distribution (ku_1 = 0.07), while the second burst is less peaked (ku_2 = -0.75). By contrast both bursts of the atypical emission shown in Figure 5.8(b) presents a flatter distribution than a

Gaussian a (ku_1= -0.57 and ku_2= -1.06), with the second burst flatter than the first. The aim of these parameters is, similarly to the skewnesses, to help in detecting whether a trace differs from a typical two-peak structure.

- t_c, the collapse time that, as explained in Section 3.2, represents a global collapse time for the bubbles in the cluster adjacent to the stone sample, around the lithotripter focus. This time is estimated in this work as:

$$t_c = t_2 - t_1 \qquad (37)$$

where t_i with i=1,2 are the central times defined by Equation (32).

The estimate of t_c, proposed in this work, differs from the one previously used [1, 2, 79, 88, 123] that calculates t_c as the time between those instants when the peak value of each of the two bursts was obtained. We shall refer to this historical parameter as t_{co}. The two estimates are close if, for both bursts, the maximum value occurs at a time close to the centre of the burst. This happens, as explained above, when both the distributions of amplitudes within the bursts are symmetric in time (see definition of kurtosis above). In the typical two-peak emission shown in Figure 5.8, for example t_c (251 μs) and t_{co} (195 μs) agree within 3% (Figure 5.9(a)). When the emission structure diverges from a symmetrical two peak structure, as in Figure 5.9(b), the estimate proposed in this work (Figure 5.9, t_c) represents an average collapse time.

In contrast the old estimate (Figure 5.9, t_{co}) represents only the strongest detected bubble-shock interaction. In Figure 5.9(b) the value of t_{co} is calculated to be 143 μs. However the value of t_c (calculated with the new method) is 106 μs (about 50% less than t_{co}), which appears to be a more correct estimate of the ensemble average collapse time for all the events that constitute the second burst. The old estimate, for example, would overestimate the time (of about 70 μs) between the first burst and the first noticeable event in the second burst (which occurs at 300 μs) of about 100%.

The new method, as shown, is more flexible and robust in those cases when the emission structure differs from a symmetrical two peak structure.

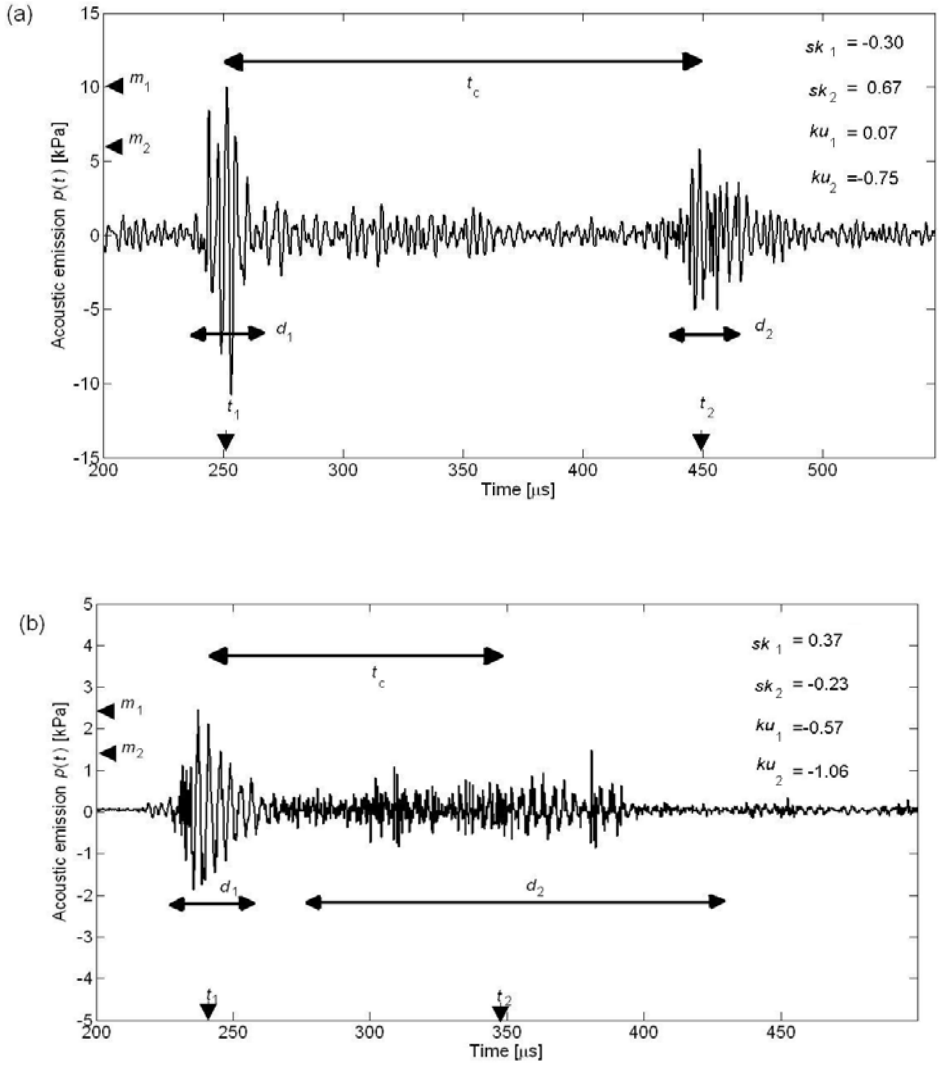

Figure 5.8: Features extracted in the time domain for (a) the typical two burst trace illustrated also in Figure 5.2 and (b) for a multi-peak trace. The symbol m_1 indicates the maximum amplitude of the first burst. The symbol d_1 indicates the duration of the first burst. The symbol t_1 indicates the central time of the first burst. The symbol t_c indicates the collapse time. The symbol m_2 indicates the maximum amplitude of the second burst. The symbol d_2 indicates the duration of the second burst. The symbol t_2 indicates the central time of the second burst. In the picture are also reported, for each trace, the values assumed by the two skewnesses (skw_1, skw_2) and the two kurtosis (ku_1, ku_2). These two sets of parameters as described in this subsection are respectively measurements of symmetry and "flatness".

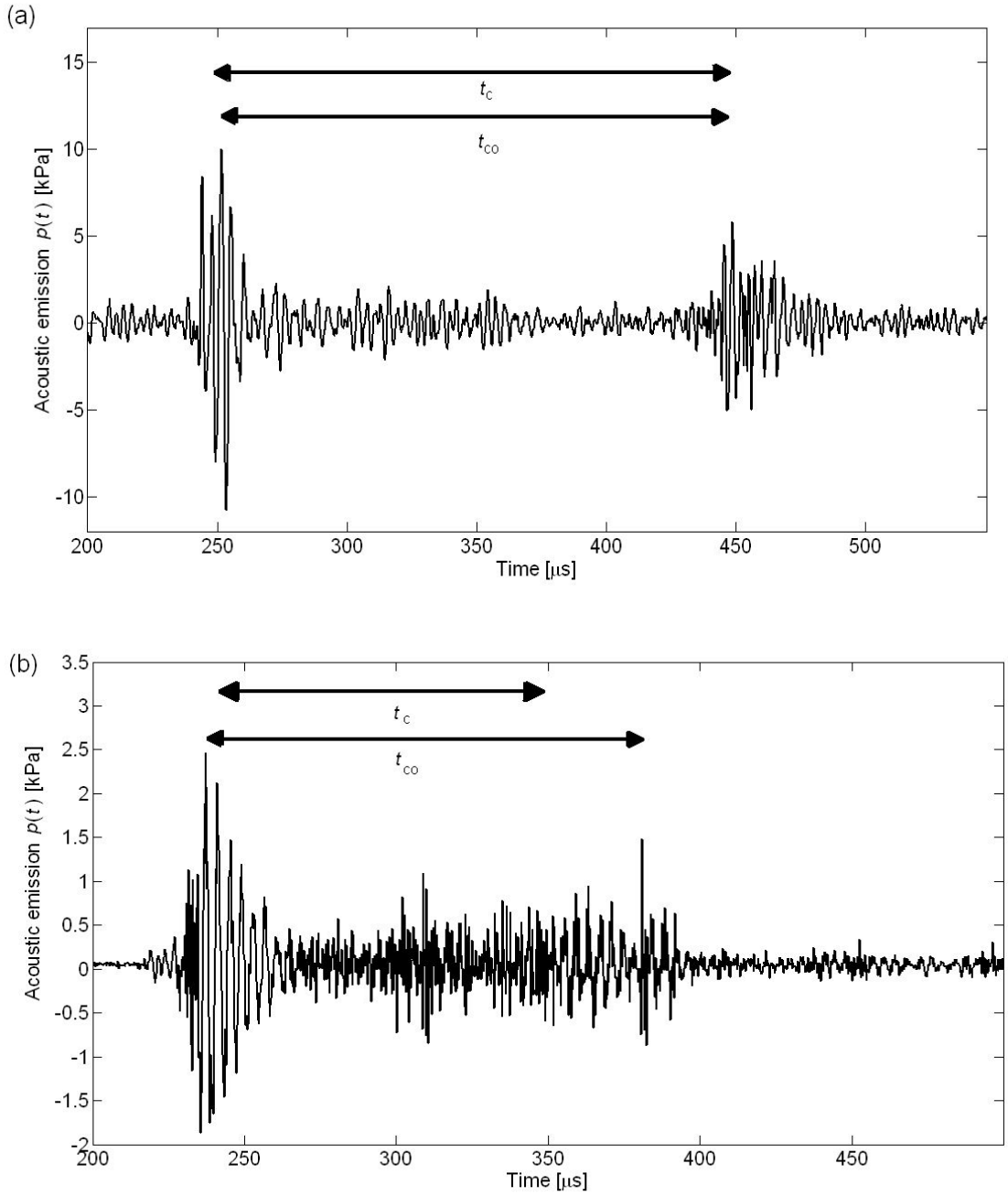

Figure 5.9: Comparison of the estimate of the collapse time proposed in this work (t_c) with that used in previous works (t_{co}). In a typical two peak emission (a) the two estimates are close (agreement within 3%). In an emission that does not show a two peak structure (b), the two estimate show less agreement. In the example shown, the agreement is poor and t_{co} is about 50% greater than t_c. It can be observed that in such cases, the new estimate t_c is more robust. This is because the parameter is less influenced by the particular time of occurrence and number of peaks. It always indicates an ensemble average collapse time for the whole bubble cloud.

5.3 Frequency analysis

The frequency analysis of a signal consists of decomposing the signal into its different frequency components. A secondary acoustic emission (as explained in Chapter 3) is a broadband signal generated by different contributions: incident stress wave, shock wave reflections, reverberations in the stone and secondary cavitation shocks. The frequency analysis helps in separating these three components. This is because the first two components are in the same frequency regime as was the original shock wave (0.15 MHz for the machines used), whilst the third component depends on the size of the stone [3, 77, 117] and the cavitational component depends on the bubble population or, better, on the bubble size distribution [3]. That is to say, free-oscillating bubbles, such as those present at the focus of the lithotripter at times greater than about 100 μs after the shock pulse, act as oscillators at a frequency linked to their radius by the equation [3]:

$$f_0 = \frac{1}{2\pi R_0}\sqrt{\frac{3\gamma p_o}{\rho_0} + \frac{2\sigma}{p_0 R_0 \rho_0}(3\gamma - 1)} \qquad (38)$$

where ρ_0, p_o and σ are respectively the equilibrium density, hydrostatic pressure and surface tension of the liquid surrounding the bubble, γ is the ratio of specific heat of a gas at constant pressure to that at constant volume and R_0 is the radius of the bubble at equilibrium.

The range of frequencies examined in this work was from 300 kHz (see Section 4.2 for explanations on this lower limit) up to 2.5 MHz. The range upper limit was chosen because there will not be significant energy detectable at higher frequencies by the receiver which is placed on the patient's torso. The absorption of acoustic energy in tissue increases linearly with the frequencies, and at 2.5 MHz the attenuation in the amplitudes is about 0.75 dB/cm [114, 117, 129]. In an average man the kidneys, from which the emissions are originating, will be at a depth of about 17 cm of depth [130]. This means that already emissions at 2.5 MHz will be attenuated by about 13 dB (78%).

The frequency analysis was performed separately on the two bursts in the emissions. Each burst was assumed to be a stochastic stationary process [128, 131]. Stochastic stationary processes are such that it is possible to consider their Power Spectral Density (PSD), which expresses the power distribution of a signal over the considered frequency range [128, 131]. Subsection 5.3.1 describes the method used for the PSD estimation of each burst.

5.3.1 Power Spectral Density Estimation

The PSD, S_{qq}, of a stationary stocastic signal $q(t)$ can be defined as follows [131]:

$$S_{qq}(f) = \int_{-\infty}^{+\infty} r_{qq}(\tau) e^{-j2\pi f\tau} d\tau \qquad (39)$$

where

$$r_{qq}(\tau) = Avg[q(t)q(t+\tau)] \qquad (40)$$

and *Avg* represents the operation of statistical average [131]. In order to have the 'true' PSD of a process, all of its infinite realisations should be available. This is not practically possible and a spectrum can only be estimated.

The methods of spectral estimation can be divided into two main categories: *non-parametric methods* (which estimate the spectrum directly from its samples) and *parametric methods* (which consider the samples of the signal as the output of a linear system driven by white noise) [131].

In this study Welch's non parametric method is adopted [131]. Given a series of samples $q_T(t)$ with sampling interval Δt and duration T, the method consists of dividing $q_T(t)$ into N segments q_i (with $i = 1..N$) of length L samples and duration in time:

$$\Delta = L \times \Delta t \tag{41}$$

Then the segments are windowed and the periodogram of each windowed segment is computed and divided by the length of the segment [131]:

$$\hat{S}_{qq_i} = \frac{\left|Q_{\Delta_i}(f)\right|^2}{\Delta} \tag{42}$$

where $Q_{\Delta i}(f)$ is the discrete-time Fourier transform of the i^{th} windowed sement $q_{Wi}(n)$:

$$Q_{\Delta_i}(f) = \sum_{n=0}^{L-1} q_{W_i}(n) e^{-j2\pi f n \Delta t} \tag{43}$$

Finally, the average of the single segments PSDs is calculated as:

$$\tilde{S}_{qq} = \frac{1}{N} \sum_{i=1}^{N} \hat{S}_{qq_i} \tag{44}$$

In Welch's PSD estimation (as applied in this work), the signals were divided into overlapping segments of 6 μs length (about half of a shock duration). An overlap of 50% was used between adjacent segments. The digital PSD of each segment was calculated using Fast Fourier Transform (FFT) algorithms on $N_{FFT}= 2^{11}= 2048$ points. This was done exploiting the *pwelch* function available in the MATLAB™ library.

A sampling frequency of F_S=5 MHz was used for the clinical data. This is because this was the smallest available sampling frequency of the digital scope that adequately captured the frequency band of interest (0-2 MHz). The data collected in the laboratory (originally sampled at 100 MHz by the oscilloscope, see 4.2) were decimated at that same frequency to reduce the size of the data sets before performing any FFT computation[16].

[16] It is the memory of the PC used that limits the number of samples that can be used in such algorithms. In the future the use of PCs with larger memory could make this decimation unnecessary.

5.3.2 Frequency parameter estimation

A series of parameters was extracted from the PSD of each burst i (i=1,2) in order to characterise its spectrum. These parameters consist of the central frequency f_{0i}, the ratio of the low frequency contribution to the burst total power (LF_i) and the ratio of the high frequency contribution to the total burst power (HF_i). The three parameters will be defined in the next subsections. This kind of analysis, as will be explained below, was only pursued for *in vitro* data.

5.3.2.1 The central frequency

Given the estimate $S_{qq}(f)$ of the PSD of a signal $q(t)$, the central frequency of the spectral distribution (f_0) is calculated as [131]:

$$f_0 = \frac{\int_0^{f_{\max}} f S_{qq}(f)\,df}{\int_0^{f_{\max}} S_{qq}(f)\,df} \qquad (45)$$

where the variable f indicates a generic frequency and $f_{\max}$ is the maximum frequency at which the PSD of the signal $q(t)$ shows a significant component above the noise. This equation was applied to the Power Spectral Densities of the two bursts to calculate their central frequencies, denoted f_{01} for the first burst and f_{02} for the second burst. The Power Spectral Density of the each burst was estimated as described in Section 5.3.1,

where the signal $q(t)$ was that portion of the emission allocated to the specific burst (by the detection algorithm described in Section 5.2.1). The choice of f_{max} was conditioned, by the characteristics of the analysed bursts. That is to say, care must be taken to ensure that this frequency is high enough to include any significant spectral component of the signal and to exclude noise. Preliminary experiments *in vitro* [118, 120-121, 132] showed that the PSDs of both bursts showed a not negligible component up to 2 MHz (see Figure 5.10(b)). Precisely from 2 MHz onwards each PSD assumes values that are less than 1% of the maximum value. Therefore, for these signals, f_{max} was set equal to 2 MHz. Observation of the spectra *in vivo* (see Figure 5.11), show however that such limit would not be suitable for those signals, where a lower limit (for example 0.6 MHz) should be employed. However, as explained later in this subsection, such analysis was not pursued on *in vivo* data.

The same preliminary experiments [118, 120-121, 132] also revealed that the power of the first burst was mainly concentrated at frequencies lower than 0.4 MHz, and the power of the second burst was mainly concentrated above this frequency[17]. In particular, the PSD of the first burst showed a peak below 0.2 MHz, which is the cut-off frequency of the filter used (see Section 95). This highlights the fact that the considerable amount of energy present in the raw signal below 0.2 MHz, which led to the use of high pass filtering[17] was localised in the first burst. This phenomenon limits, of course, the validity of any calculated value of f_{01}, which can be used only as indication of whether the predominant contribution to the power of the first burst at frequencies below 0.2 MHz was maintained.

As an example, if the two features are calculated for the signal in Figure 5.10 a f_{01} = 0.37 MHz. and f_{02} = 0.64 MHz, respectively are obtained. Given the limitations of calculated

[17] It can be argued that the spectra of both *in vitro* and *in vivo* data show a significant component below the cut-off frequencies of the filters used (200 kHz and 300 kHz, respectively). This is because the unfiltered data (see Figure 7.8 for an example of raw data) contain a dominant component (1 order of magnitude higher) at those frequencies. The filtering reduces this contribution (up to 90%, see Subsection 7.3.3, for the PAL filter characteristics) and enhances the cavitation contribution, but does not eliminate it completely. Filterers with higher cut-off frequencies could be used in the conditioning if only cavitation was of interest. However this was not the aim of the work described in this thesis, which was interested in cavitation, but also in preserving information related to scattering and reflections of the lithotripter pulse.

values of f_{01}, comparisons between the two features were only used to observe if the two different frequency distributions among the two bursts changed under different experimental conditions. Such comparisons are still meaningful as the filtering, which causes an overestimate of f_{01}, is actually reducing any separation between the calculated values for both features. Chapter 6 will illustrate how stone phantoms at different grades of fragmentation showed the same behaviour as emissions collected in tap-water. Conversely, no statistically significant difference was found in each of these two features among different phantoms (see Subsection 6.3.9), this led to the mentioned abandonment of the frequency analysis when moving to *in vivo* experiments.

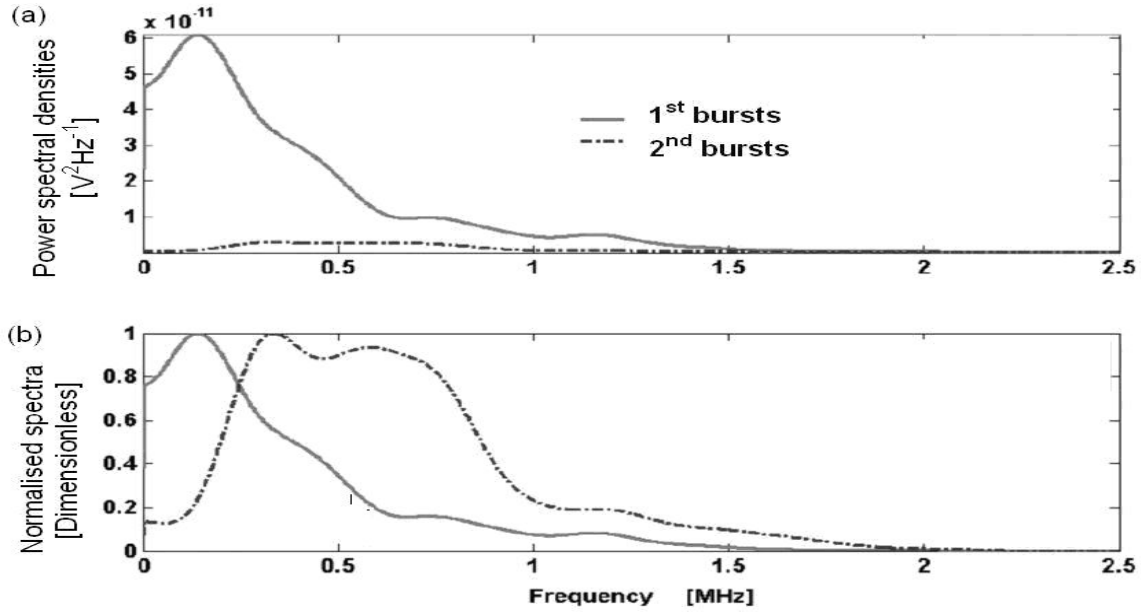

Figure 5.10: (a) Power Spectral Densities (PSDs) of the two bursts detected in a emission recorded at the geometrical focus of the bench-top lithotripter in tap-water. The PSDs were estimated using Welch's method (see Section 5.3.1). The trace was recorded using the NPL novel cavitation sensor and a high pass filter at 200 kHz (see Section 4.2 for details).Frame (b) shows the same spectra after being normalised so that their maximum amplitude is unit. The lithotripter was operated under voltage discharge settings of 16 kV. The vertical line in frame (b) denotes the separation frequency f_{HI}= 0.4 MHz. The estimated values for the central frequencies of the coherent average of the first and second burst, were respectively f_{01}= 0.37 MHz and f_{02}= 0.64 MHz. As explained in the text, f_{01} can only be used for qualitative evaluations or relative comparisons as it is affected by the cut-off frequency of the used filter.

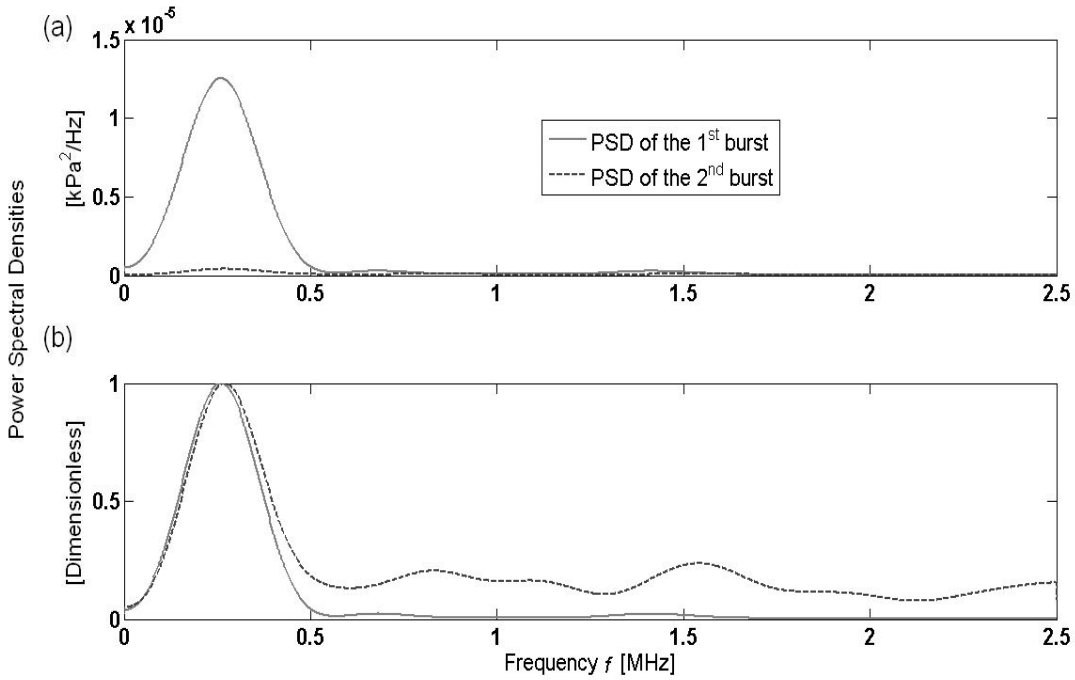

Figure 5.11: (a) Power Spectral Densities estimated using Welch's method (see Section 5.3.1) for each burst in the typical emission signal shown in Figure 5.2(b) and (b) the same PSDs normalised so that their maximum is equal to 1.

5.3.2.2 The low frequencies and high frequencies ratios

As explained in the previous section, preliminary observations *in vitro* of the PSD of the bursts in the emissions showed that the power contained in the first burst was concentrated in a lower frequency band than was the power in the second burst [118, 120-122, 132] (see Section 6.2). Furthermore, it was noted that these bands were separated by a boundary frequency f_{HI} of circa 0.4 MHz [118-121, 132]. In order to quantify the power contributions in those two bands, for portions of signal of interests, a Low Frequencies ratio (*LF*) and a High Frequencies ratio (*HF*) were defined as:

$$LF = \frac{\int_{0}^{f_{HI}} S_{qq}(f)df}{\int_{0}^{f_{max}} S_{qq}(f)df} \quad (46)$$

$$HF = \frac{\int_{f_{HI}}^{f_{max}} S_{qq}(f)df}{\int_{0}^{f_{max}} S_{qq}(f)df} \quad (47)$$

where *q(t)* indicates the portion of signal of interest and f_{max} was chosen equal to 2.0 MHz for the reasons explained in the previous section.. Four parameters (i.e. two for each burst) are obtained applying Equations (46) and (47) to each burst an emission: LF_1, HF_1, LF_2, HF_2. reports as an example LF_1 and HF_2 estimated for the two bursts in emission . The power of the first burst is mainly concentrated at the low frequencies, the emission in Figure 5.10 shows, for example, an LF_1 equal to 65%. The power of the second burst is more spread along the whole frequency range. This results in a HF_2 of 72%. In Section 6.2 it will be shown that this is a feature common to most emissions that derives from the different nature

of the two bursts (Section 3.2). Section 6.3.10 will also briefly describe how, recently, another research group [77, 115, 116] used a similar frequency analysis to investigate the sole contribute of scattering from the stone.

5.3.3 Coherent averaging

A secondary acoustic emission signal, as explained in Chapter 3, is the sum of deterministic and random components. Therefore, given a set of traces recorded under the same conditions, each trace presents a mixture of features common to the whole set and transient features characteristic of the specific emission. This study was particularly interested in comparing the key burst frequency components described in Subsection 5.3.2 for different data sets. Averaging the data in each set highlighted those deterministic components common to all the traces in each set. An operation of coherent averaging was used. This operation consists of different steps. Initially the tracts of signal of interest, the two bursts in the specific case (Figure 5.12 (a)), are extracted from each trace. Then these tracts are all realigned with respect to a reference time, which depends on some feature common to all traces. In this case the central time of a burst (Figure 5.12 (b)-(c)) was used as reference. Finally, the average of the realigned first bursts (Figure 5.12(d)) and the average of the realigned second bursts (Figure 5.12(e)) are calculated.

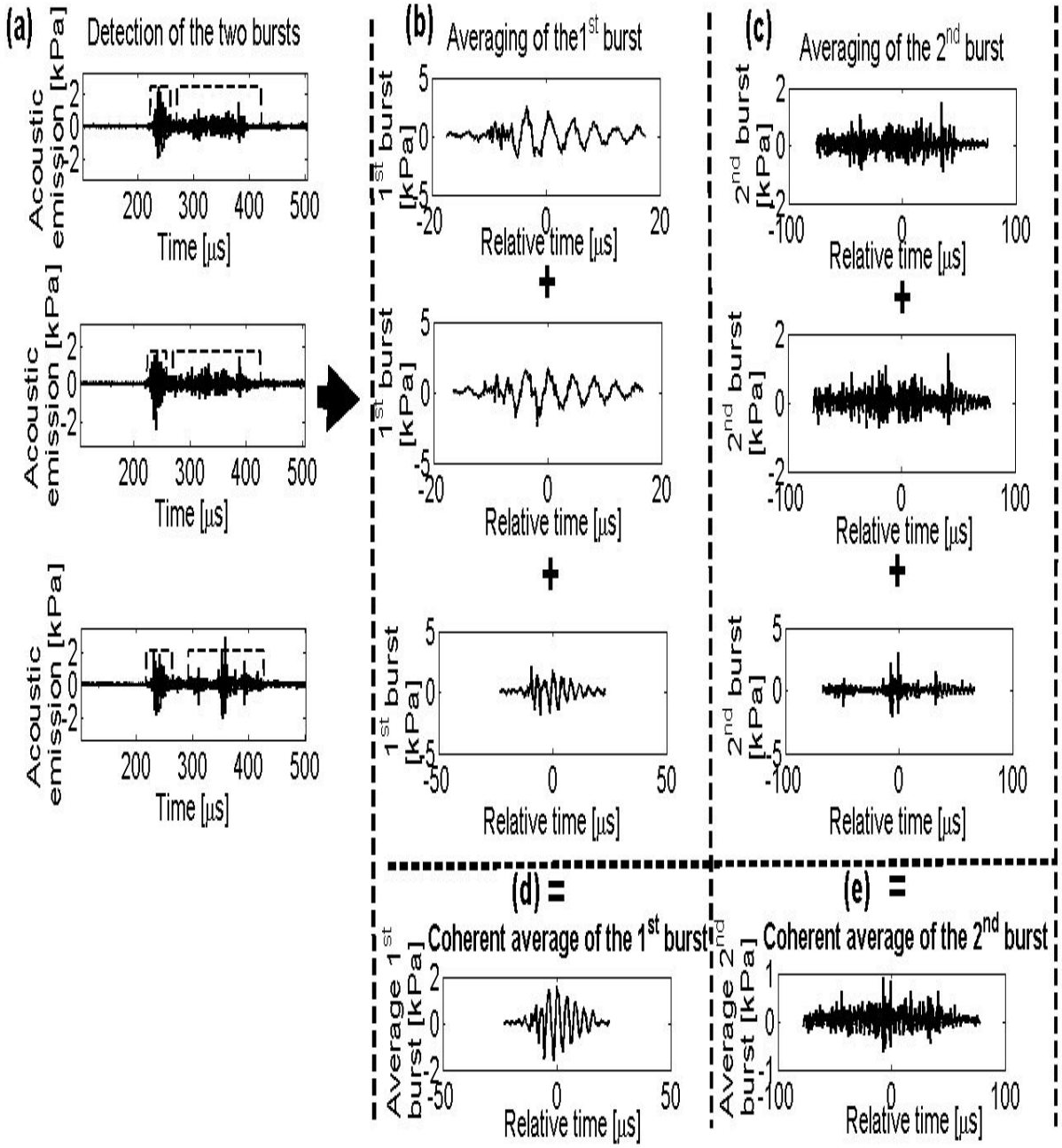

Figure 5.12: Example of coherent averaging of the two bursts. The averaging is performed over a set of three emissions recorded under the same conditions. The first emission in the set is the same as that shown in Figure 5.8(b). Frame (a) illustrate the three emissions and the two detected bursts (dotted lines). Frame (b) show the detail of the detected first bursts. Frame (c) show the detail of the detected second bursts. A relative time scale is considered for each burst. This scale assumes as zero the central time of the burst. (d) The coherent average of the first bursts is calculated as the average of the realigned bursts in frame (b). (e) The coherent average of the second bursts is calculated as the average of the realigned bursts in frame (c).

5.4 Time-Frequency Analysis

Time-Frequency analysis is very useful in examining the frequency changes in signals, such as the secondary acoustic emissions, in which the frequency parameters evolve with time (see Sections 3.2 and 5.3.2).

The technique, similarly to the PSD estimation (see Section 5.3.1) consists in segmenting the signal $q(t)$ in N slices by windowing, and in calculating the periodogram for each slice using Equation (42). The result of the operation, is called a spectrogram [131]. It can be represented in three dimensional plots (Figure 5.13) in the three axes time, frequency and amplitude. It can also be represented into two dimensional plots where the amplitudes for each pair of values in time and frequency are coded in a gray-scale colour map (Figure 5.14(a)). The latter is used more frequently because it can be easily aligned with the time-history (Figure 5.14(b)).

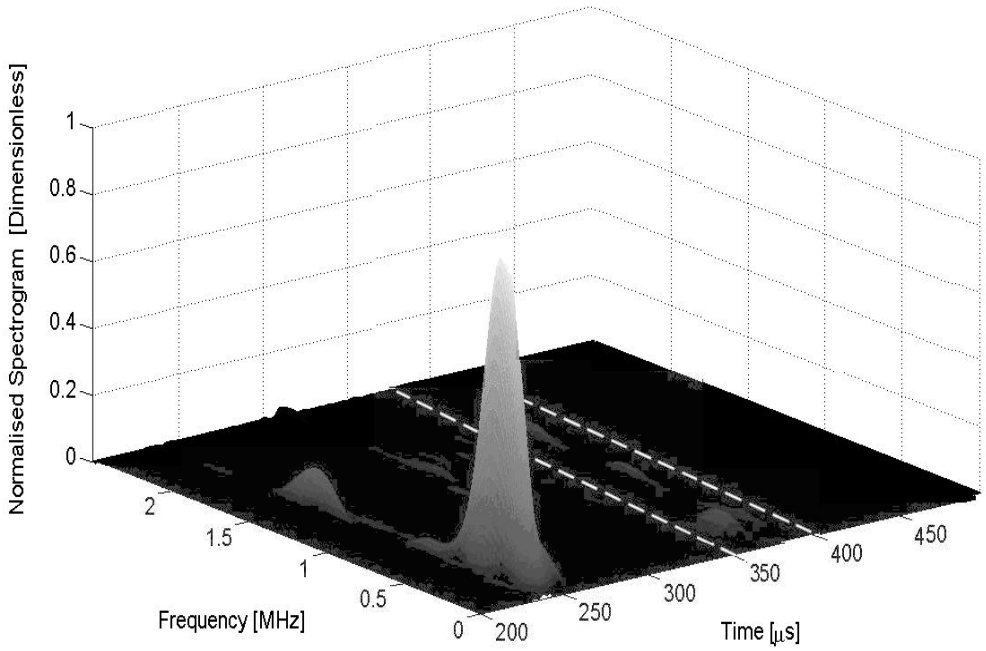

Figure 5.13: Three-dimensional representation of the normalised spectrogram of the signal in Figure 5.2(b). This spectrogram has been normalised to have maximum amplitude equal to unit. The dotted lines enclose the portion of the spectrogram corresponding to the second burst that is just visible to the naked eye.

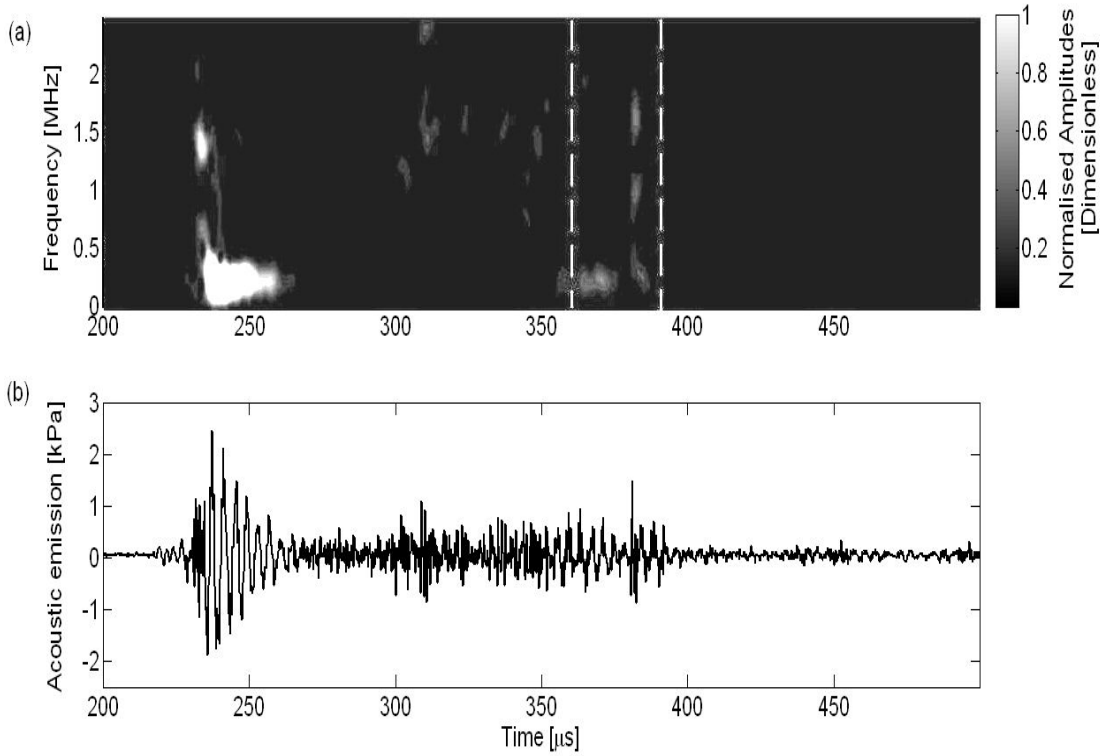

Figure 5.14: (a) Two-dimensional representation of the normalised spectrogram of (b) the secondary acoustic emission shown in Figure 5.2(b). The spectrogram amplitudes are colour coded in a grey-scale map, where the darkest colours represent the lowest amplitudes. The amplitudes have been normalised so that their maximum is unity. The two bursts are shown as two broadband events, the first burst as a clear white spot centred around 241 μs and the second burst as a set of pale grey spots between 360 μs and 390 μs marked by the white dotted lines

The spectrogram in Figure 5.14 shows clearly how the two burst are the two events in the emission with the broadest frequency content. The first burst is represented by a white spot that is centred in time around 241 μs and it is brightest at frequencies below 0.4 MHz. The second burst is shown as a set of pale grey spots along the whole frequency band, which are localised at times between 360 μs and 390 μs. The frequency content of the rest of the emission is negligible in comparison to that of the two bursts.

5.4.1 Estimation of the collapse time from the time-frequency representation

Cunningham *et al*. [54] were the first (and only prior to this work) to use time-frequency analysis to examine secondary acoustic emission and derive an indication of the collapse time (see Section 3.2). Cunningham *et al*. limited themselves to a visual estimation of the collapse time. However an appropriate processing of the spectrogram can be used to estimate this parameter numerically.

Several approaches may be followed. The approach adopted in this work was to extract from the spectrogram (Figure 5.15(a)) the time history of the power content of the signal in the high frequency band ($f > f_{HI}$). The time history derived from the spectrogram in Figure 5.15(b) is reported in Figure 5.15(a). This was considered to be the history of the cavitational component in the signal. Hence the collapse time was estimated as the time between the two instants when the two peaks occur in this signal (Figure 5.16(b)). This estimation of the collapse time is about the same as the one referred to as t_{co} (see Section 5.2.5) proposed by Coleman *et al.* [1, 2, 79]. In the example in Figure 5.15(b) a time equal to 144 μs is obtained. This agrees with t_{co} = 143 μs estimated in the time domain (see Section 5.2.5) within 0.7%.

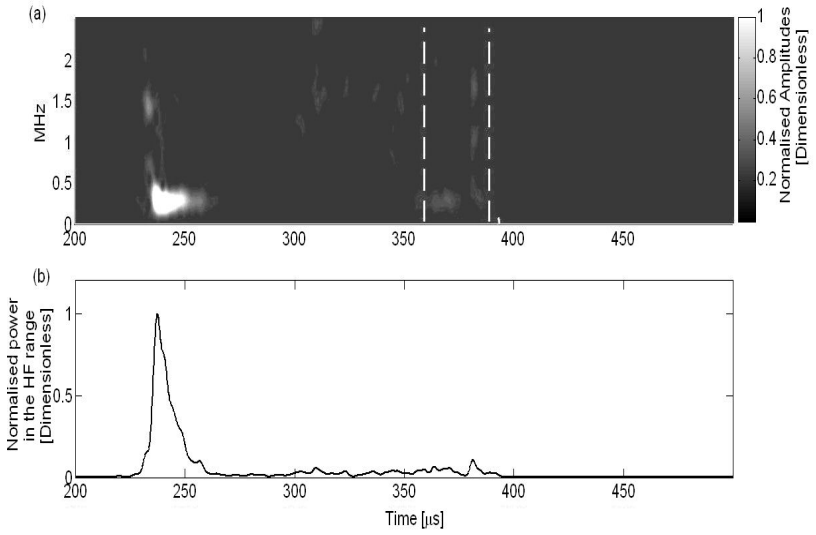

Figure 5.15: (a) Two-dimensional representation of the normalised spectrogram of the emission in Figure 5.14 (b). This spectrogram has been normalised to have a maximum amplitude equal to unity. The two bursts are shown as two broadband events. The first burst is represented by a clear white spot centred in time at around 241 μs. The second burst is represented as a set of pale grey spots occurring at times between 360 μs and 390 μs (marked by the white dotted lines). (b) Time history of the power content at the high frequency ($f>f_{HI}$) of the typical secondary acoustic emission shown in Figure 5.14 (b).

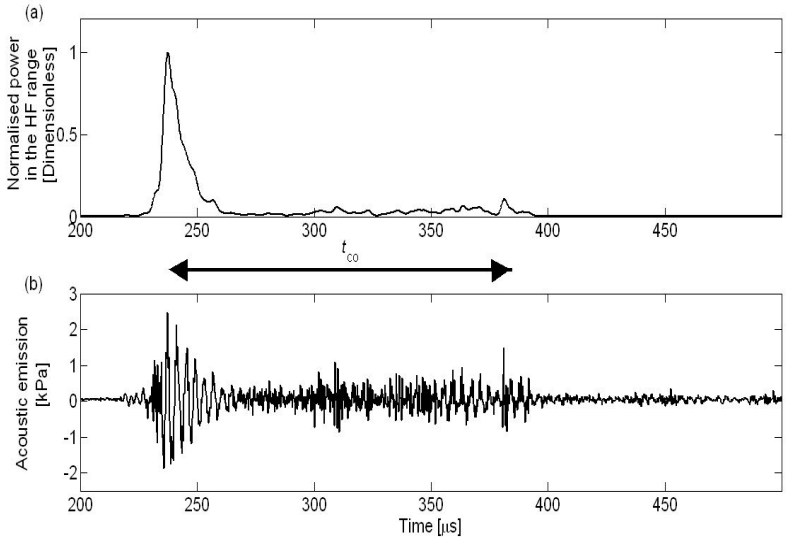

Figure 5.16: (a) Time history of the power content at the high frequency ($f>f_{HI}$) of (b) the typical secondary acoustic emission shown in Figure 5.2(b). The collapse time is estimated as the time between the occurrence of the two peaks of the signal in (a). These peaks occur in proximity to the maximum amplitudes of the two bursts. In this example it is obtained at a time of 144 μs.

Similarly to what was done in the time domain (see Section 5.2), the technique introduced by Cunningham *et al*. could be improved. This is to say that the collapse time could be calculated as the separation time between the two central times of the high frequency distributions corresponding to each burst. However the computation of PSD of multiple traces is too time-consuming[7] for on-line analysis and therefore was not pursued in this work. The other method developed in this work, based on the analysis of the emission in the time domain (described in Section 5.2.2) was used in developing the prototype ultrasound monitoring system.

5.5 Multiparametric analysis

Multiparametric analysis is used to analyse simultaneously, rather than separately, a series of parameters extracted from an observed phenomenon. In this work, the technique was applied to the features extracted from the secondary acoustic emissions (see Sections from 5.2 to 5.3 in this Chapter) to identify the most important. Principal Component Analysis (PCA), which is a powerful technique that is used in multiparametric analysis of biomedical data [133, 134] was used in this work. Section 5.5.1 will now explain the procedure.

5.5.1 Principal components analysis

Principal Component Analysis (PCA) is one of the most widely used multiparametric techniques. It allows simultaneously the separation of the initially correlated parameters, and the identification of those that contribute most significantly to the description of the process of interest.

Given a set of variables $q_1,q_2,..q_n$ PCA derives a new set of variables ζ_1, $\zeta_{2,..}$ ζ_m which are uncorrelated linear combinations of the former set:

$$\begin{aligned}
\xi_1 &= a_{11}q_1 + a_{12}q_2 + \ldots + a_{1n}q_n = \mathbf{a_1}'\mathbf{q} \\
\xi_2 &= a_{21}q_1 + a_{22}q_2 + \ldots + a_{2n}q_n = \mathbf{a_2}'\mathbf{q} \\
&\cdot \\
&\cdot \\
&\cdot \\
\xi_m &= a_{p1}q_1 + a_{p2}q_2 + \ldots + a_{pn}q_n = \mathbf{a_p}'\mathbf{q}
\end{aligned} \qquad (48)$$

where $m \leq n$ and

$$\mathbf{a_j}'\mathbf{a_j} = 1 \text{ and } \mathbf{a_j}'\mathbf{a_i} = 0 \text{ for } i<j \text{ and } j=1..p \qquad (49)$$

The new variables are obtained in order of importance. That is to say, the first PCA (ξ_1) is, more than any other component, responsible for variability in the original data. This is the component whose statistical variation is the greatest among all the linear combinations expressed in the system of Equations (48). The second component (ξ_2) is the one that describes most of the remaining variability and it is uncorrelated with ξ_1 ($\mathbf{a_2}'\mathbf{a_1}=0$). Similarly a generic component ξ_j is the component with the biggest statistical variation subject to the conditions (49).

In order to compute the coefficients of ξ_1 ($\mathbf{a_1}$), its variance can be calculated as:

$$\text{var}(\xi_1) = \text{var}(\mathbf{a}_1'\mathbf{q}) = \sum_{i=1}^{n}\sum_{j}^{n} a_{i1}a_{j1}\,\text{cov}(q_i, q_j) = \mathbf{a}_1'\mathbf{S}\mathbf{a}_1 \qquad (50)$$

where **S** is the covariance matrix of **q** under the constraint $\mathbf{a_1}'\mathbf{a_1}=1$.

The variance so calculated can then be maximised using the method of the Lagrange multipliers [135]. This method exploits the constraint $\mathbf{a_1'a_1}=1$ and introduces a new function $g(\mathbf{q},\lambda_1)$ defined as:

$$g(\mathbf{q},\lambda_1)=\mathbf{a}_1'\mathbf{S}\mathbf{a}_1+\lambda_1(1-\mathbf{a}_1'\mathbf{a}_1) \qquad (51)$$

where the additional variable $\lambda_1$is named a Lagrange multiplier.

This new function $g(\mathbf{q},\lambda_1)$ is maximised instead of Equation (50), as because of the constraint imposed ($\mathbf{a_1'a_1}=1$) the two equations are equivalent. The optimisation is performed by taking the derivative of Equation (51) with respect to $\mathbf{a_1}$ and setting it equal to zero:

$$\frac{\partial g(\mathbf{q},\lambda_1)}{\partial \mathbf{a_1}}=2(\mathbf{S}-\lambda_1\mathbf{I})\mathbf{a}_1=0 \qquad (52)$$

The solution of Equation (52), under the constraint $\mathbf{a_1'a_1}=1$, leads to the conclusion that $\mathbf{a_1}$ must be the largest eigenvector of $\mathbf{S}$ corresponding to the largest eigenvalue λ_1 [135, 136]. Furthermore the same constraint implies that the calculation of the variance of ξ_1 results in being mathematically equal to the eigenvalue λ_1 [135, 136]. Similarly it can be shown that the variance of the i^{th} principal component is λ_i (i=2,…m), where λ_i is the i^{th} largest eigenvalue of $\mathbf{S}$, and $\mathbf{a_j}$ is the associated eigenvector.

The total variance of the m principal components is, for condition (49), equal to the sum of the variances of the original components. This, as explained, is given by the sum of the m eigenvalues of $\mathbf{S}$:

$$\sum_{i=1}^{m}\lambda_i=\text{trace}(\mathbf{S}) \qquad (53)$$

Therefore the portion of variation of the i^{th} principal component is:

$$P_i = \frac{\lambda_i}{\text{trace}(\mathbf{S})} \qquad (54)$$

In cases, such as this study, where the variables $q_1,q_2,\ldots q_n$ are of different dimensions (amplitude, time, frequency), the variables with the intrinsically greater variances would dominate the early principal components. The analysis would therefore depend on the choice of units of measurement. This is avoided by standardising each variable to have unit variance before applying the analysis. This is equivalent to extracting the components from the correlation matrix **C** (that is the matrix of the correlation coefficients among the *n* variables $q_1,q_2,\ldots q_n$ [135]) rather than the covariance matrix **S** [135].

5.6 Summary

This Chapter presented the mathematical processes used in this work to characterise the secondary acoustic emissions, and to extract from them the desired information concerning the targeting and fragmentation of a urinary stone. Such mathematical tools have been applied to this kind of signals for the first time by the author [118-122], and the described processing, together with the design of the specifications of the clinical monitoring system (see Chapter 7), is among the most important original contributions of this work.

First, the structure of the emission is described by a series of parameters extracted from their time history (Section 5.2). In particular, the maximum amplitudes of the two burst distributions (m_1, m_2), the central time of each burst (t_1 , t_2) and the interval between the two bursts $t_c=t_2-t_1$ are defined. This last parameter is referred to as "the collapse time", because it is an estimate of the average cavitation collapse time (see Section 3.2).

Analysis in the frequency domain (Section 5.3) is used to reveal characteristic frequency components of the two bursts. In particular, the central frequencies (f_{01}, f_{02}), the percentages of power in the low frequency band (f<0.4MHz) LF_1 and LF_2, and high frequency band (f>0.4 MHz) HF_1 and HF_2 are estimated. In order to compare data recorded under different conditions, in particular (as will be shown in Chapter 6) under different grades of stone phantom fragmentation, a coherent average of the first and second bursts was introduced.

An analysis in the time-frequency domain (Section 5.4), also used by previous authors [54], was pursued as a way of introducing a new method for estimating the collapse time. It gives results corresponding to the estimate t_{co} of this time introduced by Coleman *et al.* [1, 2, 79].

Finally (Session 5.5), Principal Component Analysis (PCA) was used to characterise variations in the emissions under different conditions. This allows the identification of those parameters that describe the change from one condition to another. The technique was used, as will be shown in Chapter 6, to describe a simulated fragmentation process.

The following Chapter will present the preliminary results of the *in vitro* experiments. These results are the basic information used to design the prototype clinical system.

Chapter 6 Results of the *in vitro* experimentation

6.1 Introduction

This Chapter illustrates the results of the initial phase of this work, an *in vitro* experimentation aimed at characterising secondary acoustic emissions in ESWL.

The different components of the experimental set-up were detailed in Chapter 4. The ESWL shocks were generated using a bench-top lithotripter, purposely built for this EPSRC project (Section 4.3). The secondary emissions were recorded using a novel passive and unfocused ultrasound sensor developed by NPL (Section 4.4). It was the first time that this sensor, developed for industrial applications, was exploited in the field of medical ultrasound. The NPL sensor, not suitable for clinical use, was chosen to investigate the feasibility of employing an unfocused sensor to collect secondary acoustic emissions. This was done because a non focused sensor was considered to be the option to follow in the development of the clinical diagnostic system, which was the final objective of this EPSRC project (Section 1.2.5).

An initial knowledge of secondary acoustic emissions (presented in Chapter 3) had been gathered from the results of *in vitro* investigations of other authors. In the reviewed studies the emissions had been recorded *in vitro* using either passive or active focused ultrasound sensors. Non-acoustic methods, mainly optical, had been also exploited. The information, conveyed by those previous works, was that the emissions were broadband signals with a typical double-burst structure.

In this work, the characterisation of the emissions was taken further and new features, defined in Chapter 5, were extracted from these signals by exploiting some techniques widely used in the field of physiological measurements. It was the first time that the use of these techniques had been introduced in the analysis of these acoustic signals.

The initial aim of the *in vitro* experimentation was to characterise the emissions detected by the unfocused NPL sensor in tap-water and in the absence of any stone. Once this characterisation was completed, stone phantoms at different grades of fragmentation were placed at the focus of the lithotripter, prior to collecting any emission. The influence of either targeting or fragmentation of a stone on the different features of the acoustic emissions was examined. This allowed identifying the key emission parameters to incorporate in the signal processing module of the clinical prototype system, during its development.

6.2 Characterization of the acoustic emissions collected in tap-water

This Section is dedicated to the characterization of secondary emissions collected in tap-water in ESWL, at clinically relevant pressures (P^+= 19±4 MPa, P^- = 3±0.6 MPa). The shockwaves were generated using the benchtop EM lithotripter described in Section 4.3, at a discharge voltage of the source equal to 16 kV. The NPL sensor was placed at the focus of the lithotripter and 30 signals were recorded (Subsection 6.2.1). Having characterised the emissions at the focus, an examination of how their features changed when the sensor was moved around it was carried out (Subsection 6.2.2). Subsequently, the sensor was placed back at the focus and the source discharge voltage was increased gradually from 16 kV to 21 kV (Subsection 6.2.3). Previous studies had shown that the interval between the two bursts increased when this voltage was increased (see Subsection 3.2.1 for details). The new estimate t_c of this time introduced by the author [118-122] (see Subsection 5.2.5 for the definition of t_c) showed the same behaviour. In addition, experimental results and predictions made using the Gilmore software described in subsection 3.3.6 were compared.

Finally a solid plaster stone (made as described in Subsection 4.5.1) was introduced in the field and moved around the focus to explore the effect of stone targeting on the features of the emissions (Subsection 6.2.4).

6.2.1 Characteristics of emissions recorded at the focus of the lithotripter

A set of 30 emissions was recorded at the focus of the bench-top lithotripter, while the source was emitting shocks of peak positive pressures P^+= 19±4 MPa and peak negative pressures P^-= 3±0.6 MPa. Figure 6.1 shows (a) an example of the shockwaves generated and (b) the corresponding emission recorded at the focus of the lithotripter. As explained in subsection 4.3.2, these shockwaves were at clinically relevant pressures.

The emissions recorded in this experiment (Figure 6.1(b)) showed the typical double-burst structure reported by other authors (Subsection 3.2.1). Table 6.1 lists the value obtained for the different features extracted from these traces (see Subsections 5.2 and 5.3 for the definition of the emissions features). The emissions showed a peak in the first burst (m_1= 109±19 mV) about twice higher than that in the second burst (m_2= 57±21 mV). The first burst was also shorter than the second, and had a duration d_1= 66±5 μs against a duration d_2=168±41 μs for the second burst. The two bursts were separated by a collapse time t_c= 247±16 μs. The first burst was peaked with a kurtosis of 1.25±0.78. The second burst also was peaked for most of the records and showed a kurtosis of 1.79±1.83. The first burst was essentially symmetric or slightly skewed right (sk_1=0.77±0.24), while the second burst could be marginally skewed both ways (sk_2=0.48±0.94).

The values estimated for the collapse times (hundreds of microseconds) were comparable to those obtained by Coleman, Leighton and co-workers [1] for emissions recorded at the focus of an EH lithotripter (see Figure 3.5).

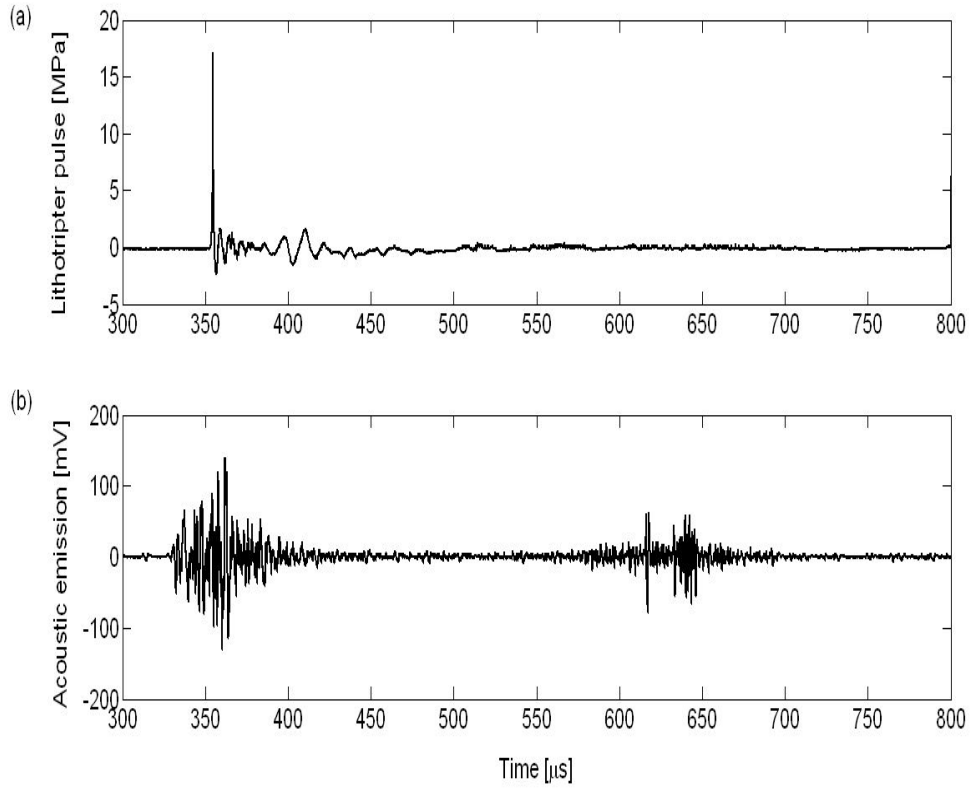

Figure 6.1: (a) Typical shock wave emitted by the bench-top EM source in tap-water under voltage settings of 16 kV. The waveform was recorded using a Marconi membrane hydrophone at the focus of the lithotripter. The time t=0 refers to the instant of discharge of the EM source. This discharge produces a high electrical noise, which is used for triggering the oscilloscope. Frame (b) shows the resulting secondary acoustic emission generated at the focus, recorded using the NPL broadband cavitation sensor.

The frequency content of the two bursts was also examined exploiting the technique of coherent averaging explained in Subsection 5.3.3. The first burst in the emission, which occurs shortly after the shock impacts on the bubble cloud, showed still a high frequency content at the same frequency of the shock waves (about 0.2 MHz, Figure 6.2). This result supports the hypothesis that the first burst contains most of the scattered shock power that leaks through the 200 kHz filter [119-121].

The second burst showed a main frequency component at about 0.5MHz [119-121] and a central frequency f_{02}=0.65±0.26 MHz. This burst mainly represents the activity of the bubbles oscillating in free evolution, after the interaction with the shocks has passed (see Section 3.3 for a description of bubble dynamics). Equation (38), which relates the radius of a free oscillating bubble to the frequency of oscillation, allows the use of this information to estimate the size of the bubbles (or bubble clusters) in the cloud around the focus of the bench-top lithotripter. In particular, that equation gives a radius of 7 μm for 0.5 MHz, the main frequency component of the second burst. Therefore it is possible to conclude that a considerable amount of bubbles in the cloud had a radius of 7 μm [119-121]. Subsequently, radii of the same order of magnitude (10 μm) were estimated by Bayley *et al.* [89] from experiments on pigs. Both estimates are smaller than the radius (40 μm) estimated *in vivo* by Cunningham *et al.* [54] for secondary cavitational nuclei. However, Gilmore simulations show that, under the effect of gas diffusion, a bubble of an initial radius 7 μm grows easily to a bubble of the magnitude found by Cunningham *et al.* (50 μm radius), when exposed to subsequent shock waves (see Subsection 3.3.7).

The predominance of low ($f<f_{HI}$) and high frequency ($f>f_{HI}$) components, in the first burst and second burst respectively, is also shown by the values assumed by the ratio of the low frequency components for the first burst LF_1 = 52±12 % and the ratio of the high frequency components for the second burst HF_2 = 74±6 %.

FEATURE	AVERAGE VALUE	STANDARD DEVIATION
m_1	109 mV	19 mV
d_1	66 μs	5 μs
ku_1	1.25	0.78
sk_1	0.77	0.24
m_2	57 mV	21 mV
d_2	168 μs	41 μs
ku_2	1.79	1.83
sk_2	0.48	0.94
t_c	247 μs	16 μs
m_2/m_1	0.53	0.03
f_{01}	0.32 MHz	0.25 MHz
f_{02}	0.65 MHz	0.26 MHz
LF_1	52 %	12 %
HF_2	74 %	6 %

Table 6.1: Parameters extracted from secondary acoustic emissions recorded in water at the focus of the benchtop lithotripter. The lithotripter was operated under voltage discharge settings of 16 kV. The symbol m_1 indicates the maximum amplitude of the first burst. The symbol d_1 indicates the duration of the first burst. The symbol ku_1 indicates the kurtosis of the first burst. The symbol skw_1 indicates the skewness of the first burst. The symbol m_2 indicates the maximum amplitude of the second burst. The symbol d_2 indicates the duration of the second burst. The symbol ku_2 indicates the kurtosis of the second burst. The symbol skw_2 indicates the skewness of the second burst. The symbol t_c indicates the interval between the two bursts, named collapse time. The symbol m_2/m_1 indicates the ratio between the maximum amplitudes of the two bursts. The symbol f_{01} indicates the central frequency of the first burst. The symbol f_{02} indicates the central frequency of the second burst. The symbol LF_1 indicates the low frequency ratio of the first burst. The symbol HF_2 indicates the high frequency ratio of the second burst. The definition of the listed features can be found in subsections 5.2 and 5.3. The values in the table represent averages and standard deviations calculated on 30 measurements.

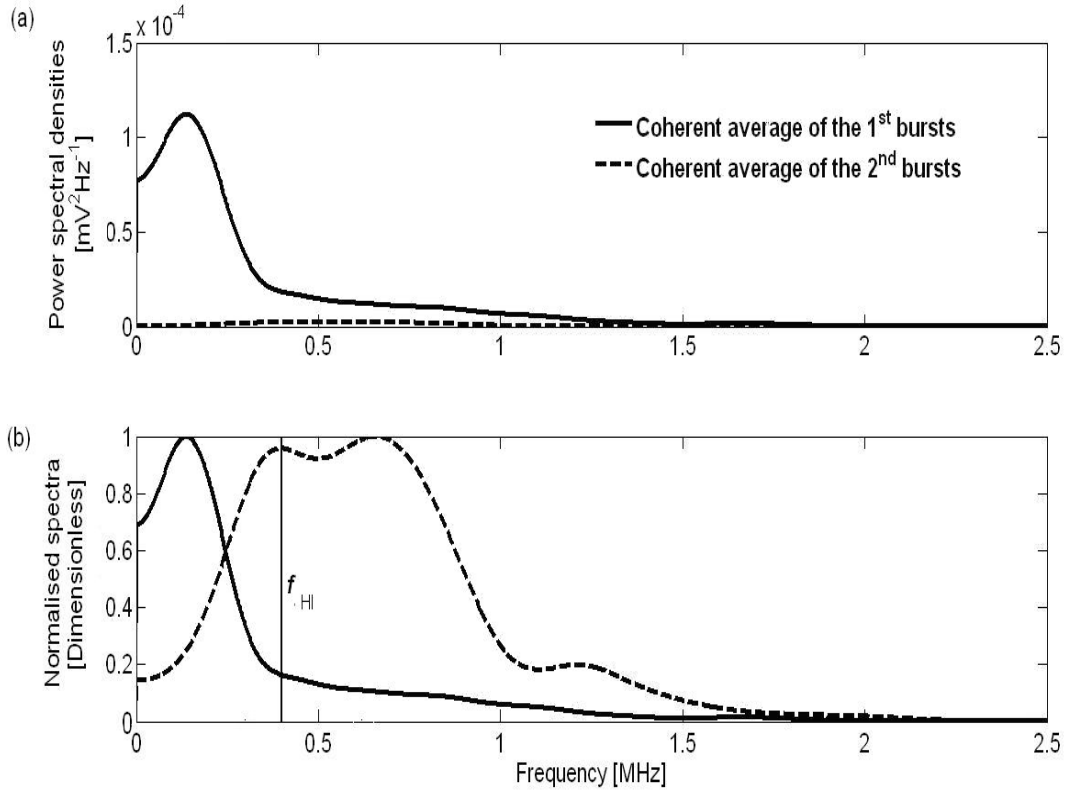

Figure 6.2: (a) Power Spectral Densities (PSDs) of the coherent averages of the two bursts detected in 30 emissions recorded at the focus of the bench-top lithotripter. Frame (b) shows the same spectra after being normalised so that their maximum amplitude is unit. The lithotripter was operated under voltage discharge settings of 16 kV. The vertical line in frame (b) denotes the separation frequency f_{HI}= 0.4 MHz. The estimated values for the central frequencies of the coherent average of the first and second burst, were respectively, f_{01}= 0.32 MHz and f_{02}= 0.65 MHz. As explained in section 5.3.2.1, f_{01} can only be used for qualitative evaluations or relative comparisons as it is affected by the cut-off frequency of the used filter.

.

6.2.2 Map of the emissions around the lithotripter focus

The previous section showed that emissions recorded in tap-water at the focus of the bench-top lithotripter using the NPL sensor had the typical structure of two bursts separated by a characteristic time t_c, described by previous authors (see subsection 3.2.1). A subsequent

experiment [119] consisted in mapping the variability of the main emissions parameters (m_1, m_2, t_c) around the focus (Figure 6.3).

A rectangular region (centred on the focus) with length 100 mm along the beam axis z and width 40mm along the transverse axis x was explored. The acoustic field on the y-axis is symmetrical to that on the x-axis (see Subsection 4.3.3) so a bidimensional map was sufficient to examine the variability in the emissions.

The aim of this experiment was to verify that the strongest emissions were generated in the focal area of the lithotripter. This is because any unfocused clinical sensor, positioned on the patient's skin, receives a signal that is a spatial average of all the emissions within its reception zone. This average emission has a diagnostic meaning only if its main contribution is generated in the proximity of the stone, i.e. the focal area. If the test had failed, the plan of using an unfocused sensor would have been abandoned.

Figure 6.3 shows the variability maps obtained for (a) m_1, (b) m_2 and (c) t_c. Each map was derived from the cubic (spline) interpolation of 99 points corresponding to estimates from emissions directly measured by the NPL sensor. These points were distributed on a rectangular grid with a distance of 10 mm along the z-axis and 20 mm along the x-axis. A smaller spacing along the x-axis was impossible because of the physical dimensions of the sensor (see section 4.4 for details on the sensor).

The maps show that the dominant emissions were coming from a region concentrated along the beam axis and ahead of the focal point. This was still contained in the elliptical focal region (see Subsection 4.3.3) and was the same area where the peak-negative pressures of the lithotripter shock (P^-) presented their highest values (Figure 4.5). It was there that the sonoluminescent cloud of cavitation bubbles was observed by Coleman and Leighton [1] (see also Figure 3.5 of this thesis). This prefocal region would be, of course, the ideal position of an unfocused sensor to capture the secondary acoustic emissions. Subsection 7.4

will show that the closest position to this area, which can be used *in vivo* is the side of the patient's torso.

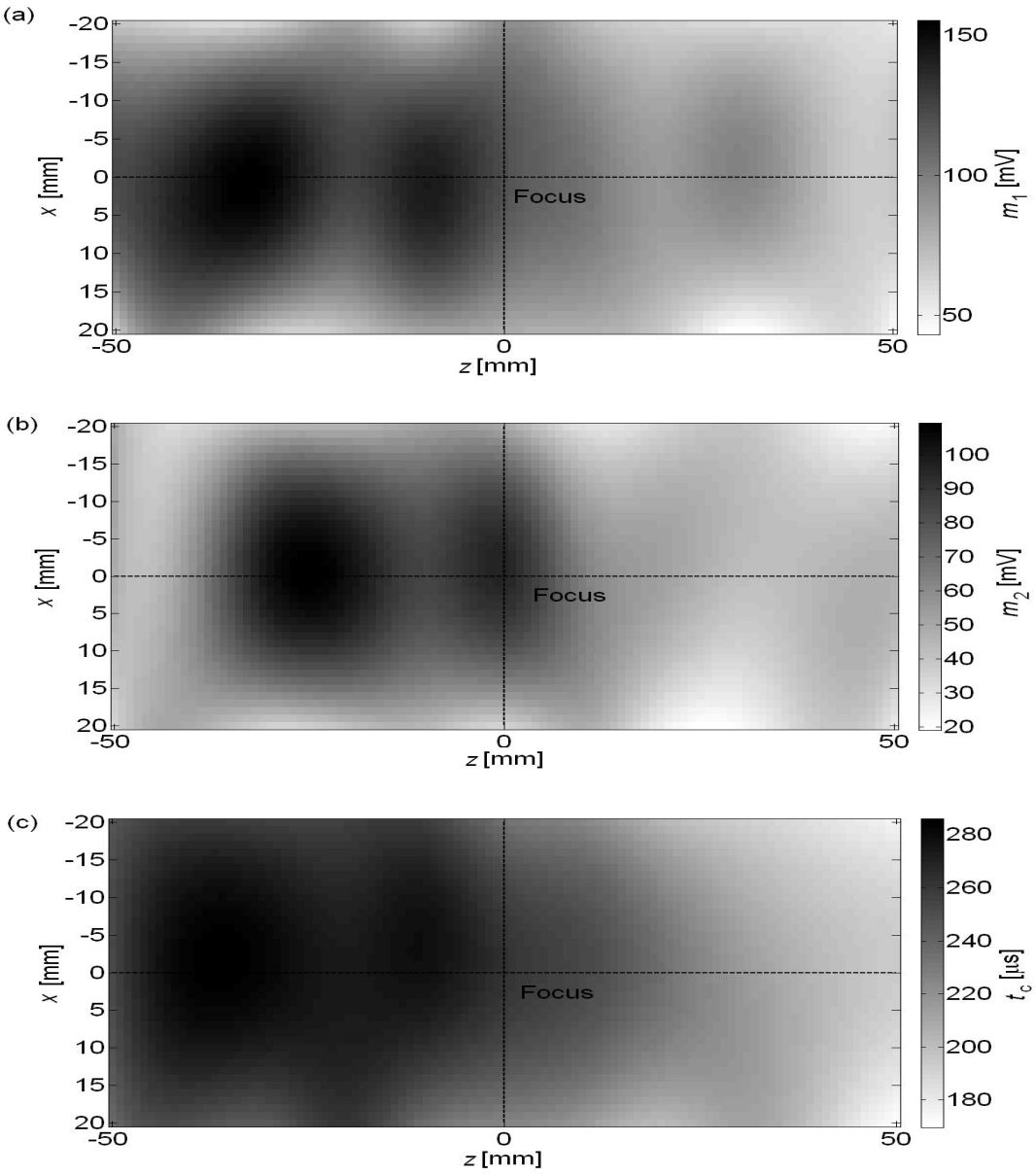

Figure 6.3: Frame (a) shows a map of the maximum amplitudes of the first burst m_1. Frame (b) shows a map of the maximum amplitudes of second burst m_2. Frame (c) shows a map of the collapse times t_c. The parameters were extracted from emissions measured using the NPL cavitation sensor in tap-water in the absence of stone samples. The z-axis is the beam axis. The x-axis is one of the two transverse axis. The shock wave propagates from far left to right.

6.2.3 Dependence of the estimated collapse time on the source settings

Coleman, Leighton and co-workers showed, in previous studies, that the interval between the two bursts in emissions (collapse time) increases linearly with the discharge voltage of an EM source [1, 2, 54]. This, following a cavitation interpretation of the signal, is explained by the fact bubble collapse times depends on the peak-negative pressure of the shockwaves (P^-) [1, 2 54], or better on the energy of the negative tail of the shock [3, 111], which increases about linearly with the voltage settings of the source.

Those authors, as explained in section 5.2.5, estimated this time as the interval between the two instants of occurrence of the peaks in the two bursts. This parameter is referred to in this work as t_{co} to distinguish it from the new estimate t_c, derived from an analysis of the power distribution in the two bursts (Subsection 5.2.5). The experiment was reproduced to test if emissions detected in tap-water with the novel NPL sensor showed the same feature.

The NPL sensor was placed at the focus of the bench-top lithotripter and the voltage of the source was increased gradually from 16 kV to 21 kV. Five traces were collected and an average collapse time t_c was calculated for each setting (Figure 6.4(a)). The average times derived were of magnitudes comparable to those measured by Coleman, Leighton and co-workers [1, 2, 54] and followed the expected positive trend (Figure 6.4(c)). This trend is the same as that predicted using the modified Gilmore software described in section 3.3.6 and assuming a single bubble of initial radius of 7 μm (Figure 6.4(d)). However the simulations predicted values of t_c about 150 μs lower than those measured (Figure 6.4(b)). This is certainly caused by the several simplifications used in the Gilmore simulations. First of all the estimate of the initial radius of the bubble used (7 μm) is based on the frequency content of the second burst. That is to say, is an indication of the radius of the unforced bubble after the shock-bubble interaction, rather than before. This was done, as a contribution to the shockwave to the first burst (direct or reflected, according to the configuration) could not be excluded. Therefore the PSD could not be considered representative exclusively of bubble activity. The results of the Gilmore simulations (see Figure 3.7) show a good agreement

(within 10%) between the initial bubble radius and the average radius of the unforced bubble after the second collapse. However the code makes strong simplifications (such as assuming a single spherical bubble) that certainly also contribute to the discrepancy between the measured and predicted values.

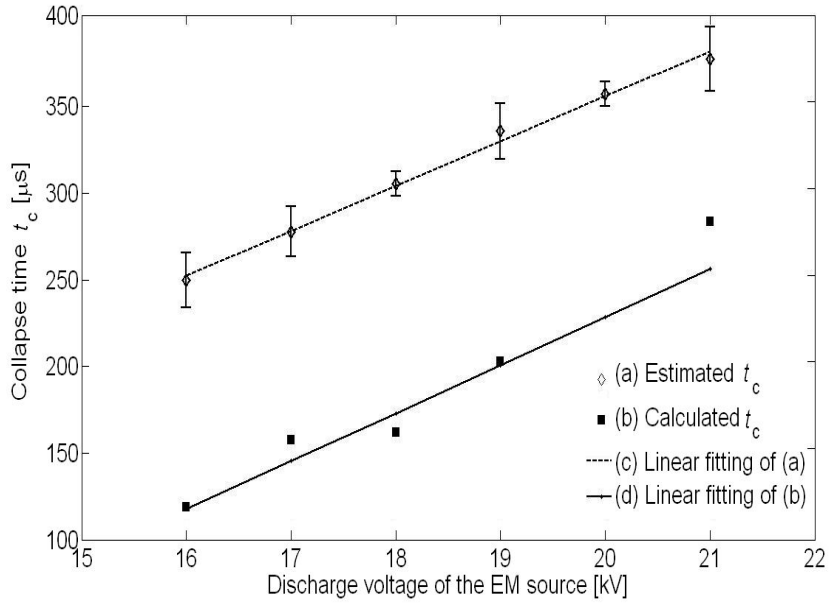

Figure 6.4: (a) Collapse times t_c estimated from emissions recorded at the focus of the bench-top EM lithotripter. (b) Collapse times predicted by the Gilmore model of bubble-dynamics when a bubble of 7 μm initial radius is excited by shock waves as those produced by the bench-top lithotripter. The values in (a) represent averages on five measurements and the error bars indicate ± one standard deviation from the average. The linear interpolations of the two sets of times, (c) measured and (d) predicted are also shown.

6.2.4 Influence of the stone targeting on the main emission features

In order to examine the influence of targeting on the main emissions features (m_1, m_2, t_c), a cylindrical plaster stone phantom (Figure 6.5) was inserted in the acoustic field. It was then moved around the focus of the bench-top lithotripter, while the NPL cavitation sensor was kept fixed there. The geometry of the sample was chosen as it matched that of the sensor and allowed the stone to move easily within the sensor. The phantom was made of plaster of Paris and water, using the special mould described in section 4.5.1. This experiment tried to

reproduce the scenario that would take place *in vivo* in case of mistargeting of a stone, whereby the stone moves away from the focus. The NPL sensor was left at the focus, under the hypothesis (supported by previous results in tap water, see Subsection 6.2.2) that the main contribution to an emission received by a remote sensor *in vivo* comes always from the focus.

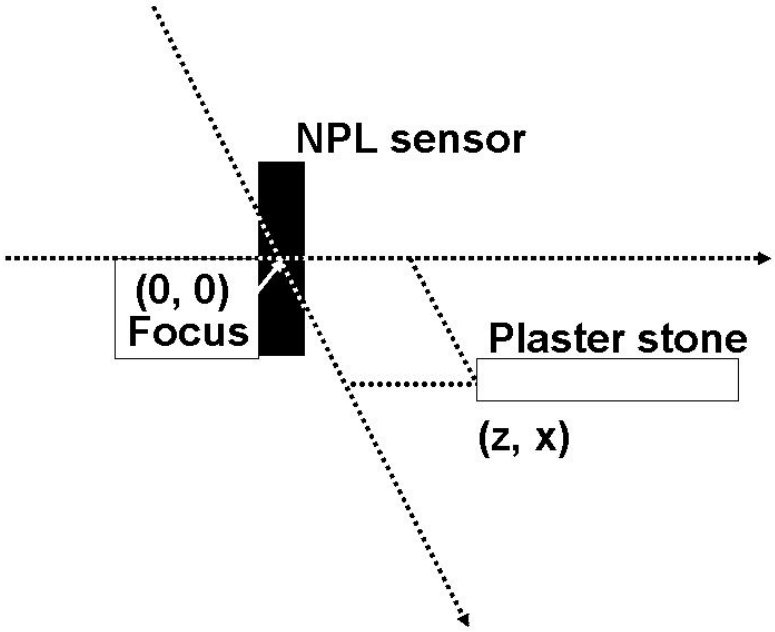

Figure 6.5: Schematic representation of the targeting experiment. The NPL cavitation sensor was kept at the focus of the lithotripter and the cylindrical plaster stone phantom was moved off-axis. The z-axis indicates the beam axis and the coordinates of the sample (z, x) refer to the front face of the stone.

The analysis of the emissions features started from the amplitude of the first bursts m_1. This is because, from previous experiments (see Subsection 6.2.2), it was hypothesized that m_1 is the main feature linked to scattering. That is to say is the main feature that was expected to be influenced by stone targeting.

The behaviour of m_2 was linked only to a lesser degree to targeting, as this feature is mostly linked to cavitation (see Subsection 6.2.2). However because of this partial dependence on scattering the variability of the feature with targeting was also examined.

Finally also the collapse time t_c was investigated. This feature is purely attributed to cavitation and it was, therefore, interesting to determine if targeting would affect cavitational phenomena in any way.

First of all it was observed (Figure 6.6(a)) that the introduction of the stone in the focal region gave, as expected, an increase in m_1 (40±30%). In contrast, whilst one would expect m_2 (Figure 6.7) to show some variation, as it is partially linked to scattering, which changes with the introduction of the stone, it does not show any significant change when the stone is introduced. The collapse time t_c showed a considerable increase (20±20% Figure 6.8), in the prefocal region, when the stone was introduced in the field. The parameter also presented a high sensitivity (average drops greater than 20%) to the movement of the stone from the focus, i.e. stone moving behind the focus (Figure 6.8(a)) or off x-axis (Figure 6.8(b)).

The phenomenon was explained as stronger shock-cavitation interaction at the interface between the water and the stone. This was attributed to the partial reflection of the tensile portion of the shock wave caused by the impedance mismatch [3]. Longer collapse times in emissions collected in proximity of stone samples were observed also by other researcher groups [90, 137, 138]. In particular, some of these groups (using high speed photography) correlated the longer bubble collapses with lager [137] and more numerous bubbles [90] being generated at the surface of the stone.

As a result of this experiment, both the amplitude of the first burst m_1 and the collapse time t_c appear suitable parameters to provide feedback information on stone targeting. The latter, in particular, shows a higher sensitivity to movements of the stone off-axis. This is to say, the separation between values of t_c off axis and that at the geometrical focus (Figure 6.8) is greater (i.e. relative smaller error-bars) than the separation between the corresponding values in m_1(Figure 6.6); even if, the values in m_1 showed the higher average increase.

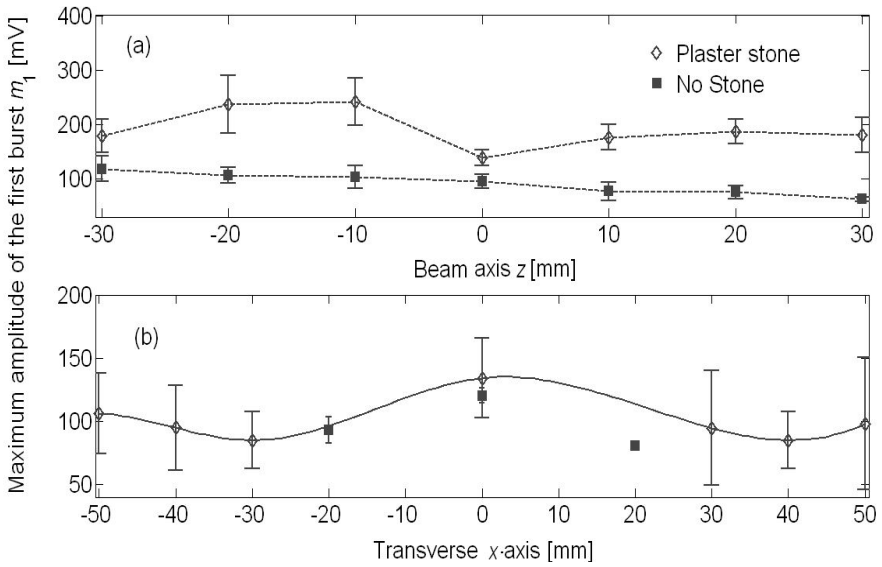

Figure 6.6: Plots of the variation in the maximum amplitude of the first burst m_1, when a plaster stone phantom (Figure 6.5) is moved along (a) the beam axis and (b) off–axis. The values (empty diamonds) are compared against reference values (solid squares) obtained moving the NPL sensor around the focus in absence of any stone sample. Each point is the average of five measurements and the error bars indicate ± one standard deviation from the average. The dotted lines in (a) indicate a linear interpolation. The solid line in (b) indicates a spline interpolation.

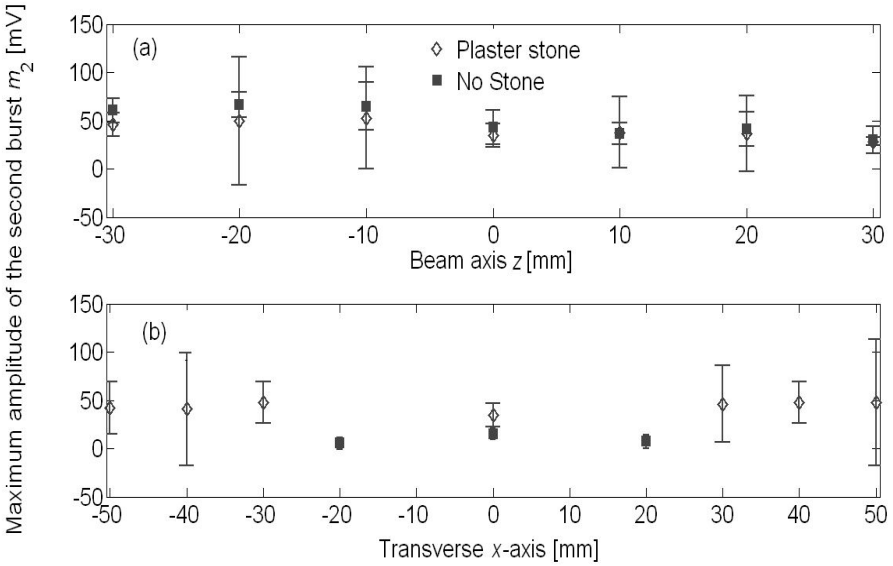

Figure 6.7: Plots of the variation in the maximum amplitude of second burst m_2, when a plaster stone phantom (Figure 6.5) is moved along (a) the beam axis and (b) off–axis. The values (empty diamonds) are compared against reference values (solid squares) obtained moving the NPL sensor around the focus in absence of any stone sample and no statistically significant difference is found between the two series. Each point is the average of five measurements and the error bars indicate ± one standard deviation from the average.

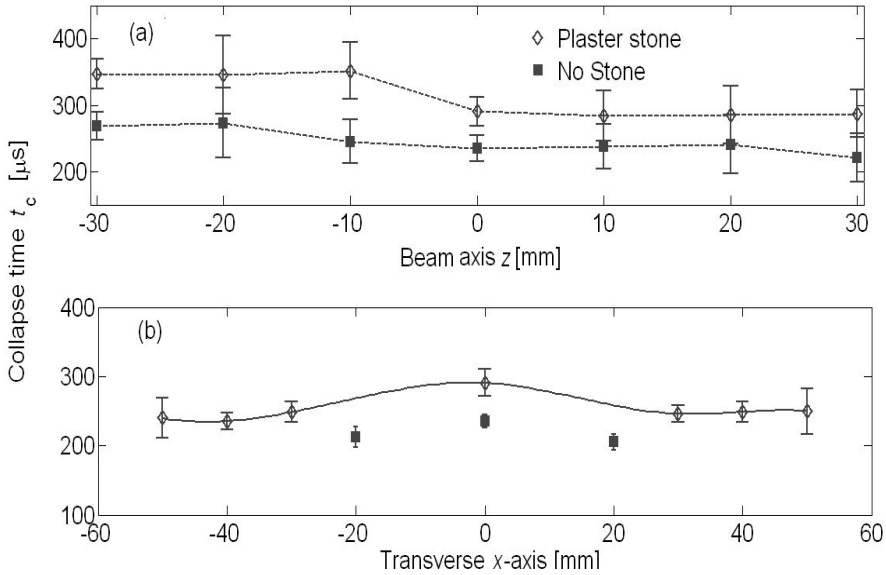

Figure 6.8: Plots of the variation in the maximum amplitude of the collapse time t_c, when a plaster stone phantom (Figure 6.5) is moved along (a) the beam axis and (b) off–axis. The values (empty diamonds) are compared against reference values (solid squares) obtained moving the NPL sensor around the focus in absence of any stone sample. Each point is the average of five measurements and the error bars indicate ± one standard deviation from the average. The dotted lines in (a) indicate a linear interpolation. The solid line in (b) indicates a spline interpolation.

6.3 Influence of the stone fragmentation on parameters extracted from emissions recorded adjacent to stone samples

The results of the previous subsection suggested that the collapse time t_c could possibly be used to gather information about the targeting of a stone also *in vivo*. Having identified a way to gather feedback about targeting, the second objective of the project was to discriminate between different grades of stone fragmentation. Therefore a series of experiments was performed to establish whether the stone fragmentation influenced any of the features extracted from the emissions adjacent to stone phantoms at different grades of fragmentation.

Initially, all the characteristics of emissions collected against an intact plaster stone sample (corresponding to 0% fragmentation) were compared to those obtained in previous

experiments (see Subsection 6.2.1), for tap water (representing an ideal 100% fragmentation). The results of this comparison are reported in Table 6.2.

Emissions collected adjacent to the plaster samples showed, as expected, a higher scattering component (m_1) and a more peaked first burst (ku_1 = 6.13±0.67 against 1.25±0.78 in tap water). They also showed longer collapse times (t_c) caused, as explained in section 6.3, by stronger bubble-shock interactions. On contrast, the plaster stone sample showed less significant cavitation emission above the noise level, i.e. lower m_2 to noise ratios. This resulted in flatter (ku_2 = -0.50±0.06 against 1.79±1.83 in tap water) and artificially longer second bursts (d_2= 428±55μs against 168±41μs in tap water).

A minor contribution of cavitation and a predominance of scattering in emissions collected adjacent to the plaster stone sample was shown by lower m_2/m_1 ratios (0.26±0.41 against 0.57±0.03 in tap-water). This was also manifested by the lower central frequency of the second burst (f_{02}=0.47±0.20 MHz against 0.65±0.26 MHz in tap water).

FEATURE	TAP WATER	PLASTER
m_1	109±19mV	139±14mV
d_1	66±5μs	65±16μs
ku_1	1.25±0.78	6.13±0.67
sk_1	0.77±0.24	2.21±0.11
m_2	57±21mV	34±12mV
d_2	168±41μs	428±55μs
ku_2	1.79±1.83	-0.50±0.06
sk_2	0.48±0.94	-0.42±0.31
t_c	247±16μs	291±10μs
m_2/m_1	0.53±0.03	0.26±0.41
f_{01}	0.32±0.25 MHz	0.40±0.17 MHz
f_{02}	0.654±0.26 MHz	0.47±0.20 MHz
LF_1	52±12%	45±32%
HF_2	74±6%	79±14%

Table 6.2: Parameters estimated for secondary acoustic emissions in water at the focus of the lithotripter in absence (left column) and presence (right column) of a plaster stone phantom. The symbol m_1 indicates the maximum amplitude of the first burst. The symbol d_1 indicates the duration of the first burst. The symbol ku_1 indicates the kurtosis of the first burst. The symbol sk_1 indicates the skewness of the first burst. The symbol m_2 indicates the maximum amplitude of the second burst. The symbol d_2 indicates the duration of the second burst. The symbol ku_2 indicates the kurtosis of the second burst. The symbol sk_2 indicates the skewness of the second burst. The symbol t_c indicates the collapse time. The symbol m_2/m_1 indicates the ratio between the maximum amplitudes of the two bursts. The symbol f_{01} indicates the central frequency of the first burst. The symbol f_{02} indicates the central frequency of the second burst. The symbol LF_1 indicates the low frequency ratio of the first burst. The symbol HF_2 indicates the high frequency ratio of the second burst. The values in the table represent averages and standard deviations calculated, respectively, on 30 measurements for tap-water and 5 values for plaster.

After this initial comparison, the effect of different grades of fragmentation on the emissions features was examined. This was done by positioning four of the soda-lime stone phantoms described in subsections 4.5.2 at the geometrical focus of the bench-top lithotripter, and adjacent to the NPL sensor (Figure 6.9). These phantoms reproduced stone samples of the same volume, but different fragmentation grades, which varied from values of F (as defined in section 4.5.6) of 31% to 54%. A phantom filled with tap-water, representing the ideal 100% fragmentation stage, was also used. The lithotripter was, once again (see Section 6.2), operated at 16 kV and a set of 10 traces was collected for each stone sample.

In order to isolate the effects of fragmentation, the stones phantoms and the sensor were positioned by means of a rigid mounting (Figure 6.9), that ensured a precision of alignment well within 5 mm. Precautions were also taken to reproduce the same experimental conditions. In particular, differences in the data due to degradations of the experimental source (see Section 4.3) were minimised by performing the experiments with all phantoms in the same day, and limiting the shockwaves per phantom to 10. The shocks were administered with a rate less than a shock per minute, and a pause of at least 10 minutes was taken between each set (i.e. each phantom) to minimise changes in the cavitation cloud caused by being exposed to multiple shockwaves (see Chapter 3 for details on bubble-shock interactions). In addition, to emphasize only possible trends due to fragmentation from any experimental artefact, the phantoms were exposed to the source in a random order of fragmentation ratio F.

A normal distribution was assumed for the features extracted from each set, and the separation among the means of the different populations was tested by means of an unpaired t-test [139]. The test is described in the following subsection 6.3.1. The results of the analysis are reported, for each parameter, in the subsections from 6.3.2 to 6.3.10. In brief, this showed that four parameters m_1, m_2, m_2/m_1, t_c could discriminate between different grades of fragmentation. Subsequently, these four features were analysed by means of multiparametric analysis. This was done to verify if any were more representative than

others of the simulated fragmentation process. Subsection 6.3.11 describes the results of this analysis.

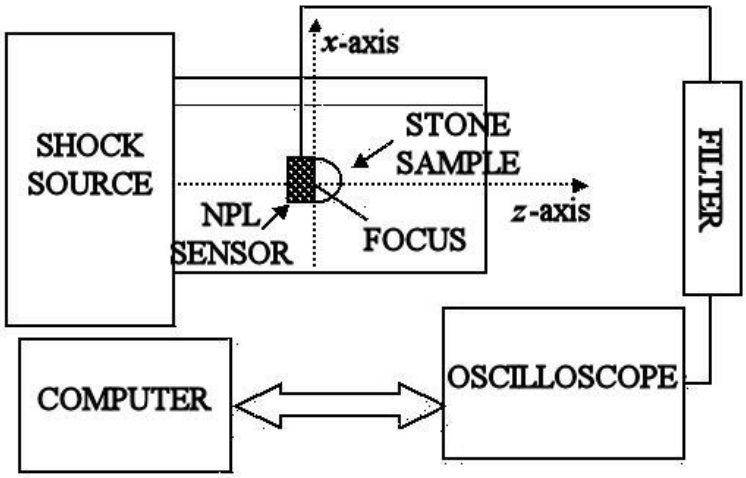

Figure 6.9: Schematic representation of the experimental set-up described in Chapter 4.

6.3.1 The *t*-test

The *t*-test is applied to assess if the separation between two populations is statistically significant. The test, particularly suitable for small sets of data [139], assumes that the two populations are normally distributed. It is based on the calculation of one parameter called the *t*-value. This calculation differs in the case of paired data (such as in case of repeated experiments) or independent data derived from two different experiments [139]. The different values compared in this experiment, for the reasons explained above (see Section 6.3) are neither strictly dependent nor independent. However to be more generic the expression of the *t*-value for unpaired data was used:

$$t_T = \frac{abs(\bar{\phi}_i - \bar{\phi}_j)}{\sqrt{\frac{\sigma_i^2 + \sigma_j^2}{N_s}}} \quad (55)$$

where ϕ is a generic feature extracted from the emissions (see list in Table 6.2), $\bar{\phi}_i$, $\bar{\phi}_j$ are the averages of ϕ over the two populations, and σ_i^2, σ_j^2 are the variances. The symbol N_s indicates the number of samples in the two populations, which in this case was equal to 10. The separation between the two averages $\bar{\phi}_i$ and $\bar{\phi}_j$ is considered statistically significant if t_T is greater than a critical value. This critical value depends on the degrees of freedom in the phenomena observed. In the case of dependent pairs, the degrees of freedom for two sets of measurements of the same dimensions are equal to:

$$\nu_d = N_s - 1 \quad (56)$$

In case of same dimensions and same standard deviations, but independent pairs, the degrees of freedom become:

$$\nu_i = 2N_s - 2 \quad (57)$$

A certain dependence between the sets compared, as explained, could not be ruled out. Therefore, for simplicity, it was decided to restrict the degrees of freedom to ν_d=9 for each comparison. This choice gave a critical value of t_T equal to 2.26 [139] for a statistical significance (**p**-value[18]) of 0.05.

Subsection 6.3.2 reports the results of this analysis for the maximum amplitude of the first burst m_1.

6.3.2 Influence of fragmentation on the maximum amplitude of the first burst

The maximum amplitude of the first burst m_1 (Figure 6.10) is, as shown in Section 6.2, a feature mainly linked to the shockwave scattering from the stone. In accordance with this, the feature showed significantly higher values (Table 6.3) for the stone samples at lower grades of fragmentation (F<40%). Values of m_1 for F≥47% did not present a significant difference[19]. These results suggested that m_1 would have be particularly suitable for distinguishing early stages of fragmentation (F<40%) from advanced fragmentation processes (F≥47%).

[18] The **p**-value is a risk factor that expresses the probability of making the same observations if the two populations were identical [139]. That is to say, a **p**-value of 0.05 means that there is a chance of only 5% of having the same results if the two populations are the same [139]. Typical levels of significance used are 0.05 and 0.01.

[19] It can be noted that the absolute value of this feature estimated for the water phantom is different from that obtained in the previous experiments in tap-water. This was attributed to differences in the experimental conditions, and in particular to the output of the EM source.

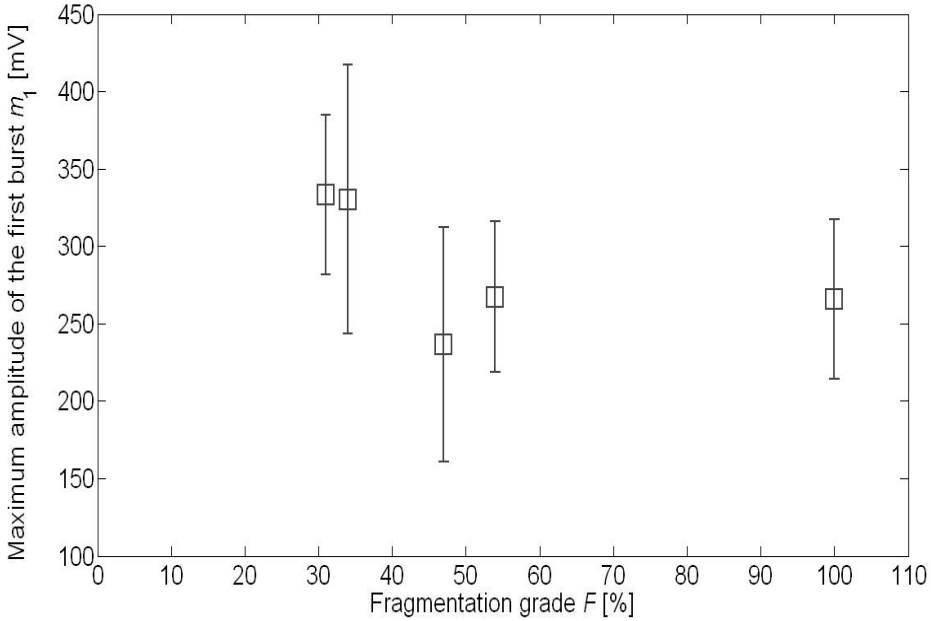

Figure 6.10: Maximum amplitude of the first burst (m_1) for soda-lime stone phantoms (see Subsection 4.5) at different grades of fragmentation. The average value over 10 measurements is shown for each set and the error bars represent ± one standard deviation from the average value of each set.

F [%]	**31**	**34**	**47**	**54**	**100**
31		0.10	**3.35**	**2.96**	**2.94**
34			**2.57**	2.00	2.02
47				1.08	1.01
54					0.06
100					

Table 6.3: Results of the *t*-test obtained for m_1 when comparing the different fragmentation stages represented in Figure 6.10, one couple a time. Each cell in the table indicates the *t*-value for the two stages indicated in its row and column headers. The *t*-values that satisfy the condition t_T>2.26 (which indicates that the difference between the averages of the two stages compared is statistically significant with **p**-value <0.05, see Subsection 6.3.1) are indicated in bold.

6.3.3 Influence of fragmentation on the maximum amplitude of the second burst

The maximum amplitude of the second burst m_2 (Figure 6.11), as shown in Section 6.2, is a feature associated primarily with cavitation. The parameter increased gradually with the grade of fragmentation[19], i.e. with increasing component of liquid present within the stone phantom and (for the specific phantoms used[20]) increasing size of the pores in the stone. A variety of linear fittings can describe this increase if the errorbars (i.e. the variances) of the different stages are taken into considerations. Figure 6.11 (dotted line) indicates only the best linear fitting between the averages. In particular, the feature could discriminate three different stages of fragmentation F<40%, 40%<F<54% and F>54% (Table 6.4). These results suggested that m_2 would be particularly suitable for following changes in the emissions as the fragmentation process progresses.

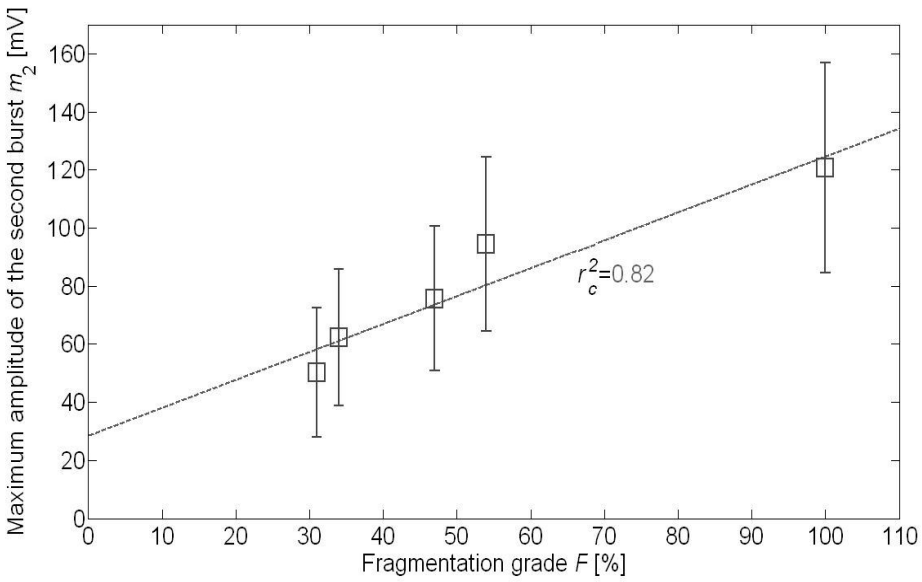

Figure 6.11: Maximum amplitude of the second burst (m_2) for soda-lime stone phantoms (see Subsection 4.5) at different grades of fragmentation. The average value over 10 measurements is shown for each set and the error bars represent bars represent ± one standard deviation from the average value of each set. The dotted line indicates the best linear fitting between the average points. The square of the correlation coefficient of the fitting is r^2_c=0.82.

[20] See Section 4.5 for details about the stone phantoms.

F [%]	**31**	**34**	**47**	**54**	**100**
31		1.18	**2.42**	**3.76**	**5.26**
34			1.24	**2.68**	**4.29**
47				1.53	**3.24**
54					1.77
100					

Table 6.4: Results of the *t*-test obtained for m_2 when comparing the different fragmentation stages represented in Figure 6.11, one couple a time. Each cell in the table indicates the *t*-value for the two stages indicated in its row and column headers. The *t*-values that satisfy the condition t_T>2.26, (which indicates that the difference between the averages of the two stages compared is statistically significant with **p**-value <0.05, see Subsection 6.3.1) are indicated in bold.

6.3.4 Influence of fragmentation on the durations of the two bursts

The duration of the first burst d_1 (Figure 6.12(a)) could not distinguish between the different phantoms (Table 6.5(a))). In contrast, the duration of the second burst d_2 (Figure 6.12(b)) decreased linearly with the fragmentation stage. The dotted line in Figure 6.12 indicates the best linear fitting between the averages [128]. A linear decrease in d_2 could be expected, as correlated with the linear increase in m_2 (Figure 6.13). This is because the ratio between the peak and average pressure amplitude in a burst influences the portion of signal allocated to that burst from the detection algorithm (see Subsection 5.2.1). The smaller is this ratio (i.e. the flatter is the burst), longer the burst appears to the algorithm.

However, d_2 could only clearly distinguish (Table 6.5(b)) between the water phantom (F=100%) from the others (F<54%).

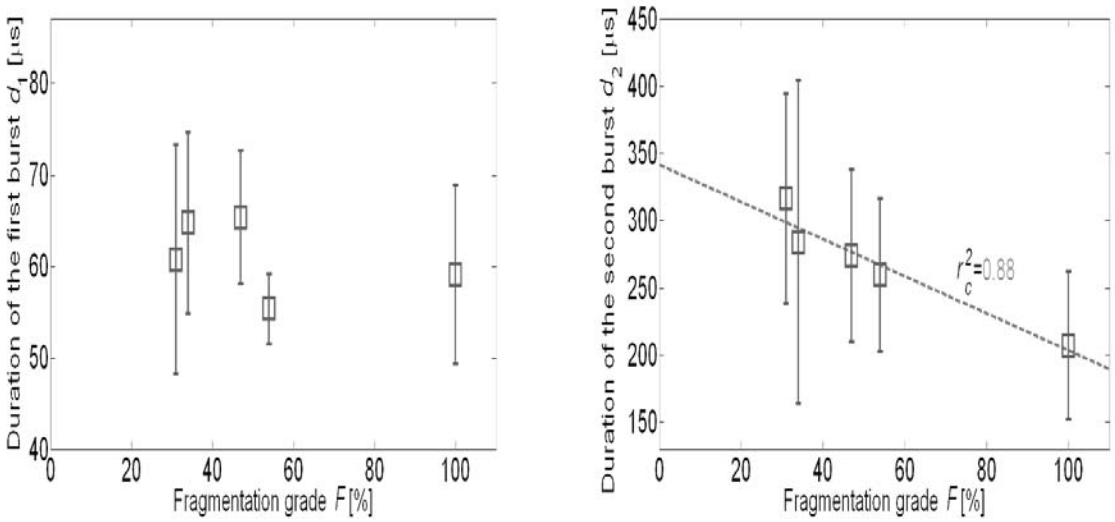

(a) **(b)**

Figure 6.12: Durations of (a) the first burst d_1 and (b) the second burst d_2 for soda-lime stone phantoms (see Subsection 4.5) at different grades of fragmentation. The average value over 10 measurements is shown for each set and the error bars represent ± one standard deviation from the average value of each set. The dotted line in (b) indicates the best linear fitting between the average points. The square of the correlation coefficient of the fitting is r^2_c=0.88.

F [%]	**31**	**34**	**47**	**54**	**100**
31		0.79	1.01	1.31	0.33
34			0.16	**2.80**	1.28
47				**3.84**	1.62
54					1.13
100					

(a)

F [%]	**31**	**34**	**47**	**54**	**100**
31		0.72	1.33	1.85	**3.61**
34			0.23	0.58	1.84
47				0.53	**2.50**
54					2.09
100					

(b)

Table 6.5: Results of the *t*-test obtained for (a) d_1 and (b) d_2 when comparing the different fragmentation stages represented in Figure 6.12, one couple a time. Each cell in the table indicates the *t*-value for the two stages indicated in its row and column headers. The *t*-values that satisfy the condition t_T>2.26 (which indicates that the difference between the averages of the two stages compared is statistically significant with **p**-value <0.05, see Subsection 6.3.1) are indicated in bold.

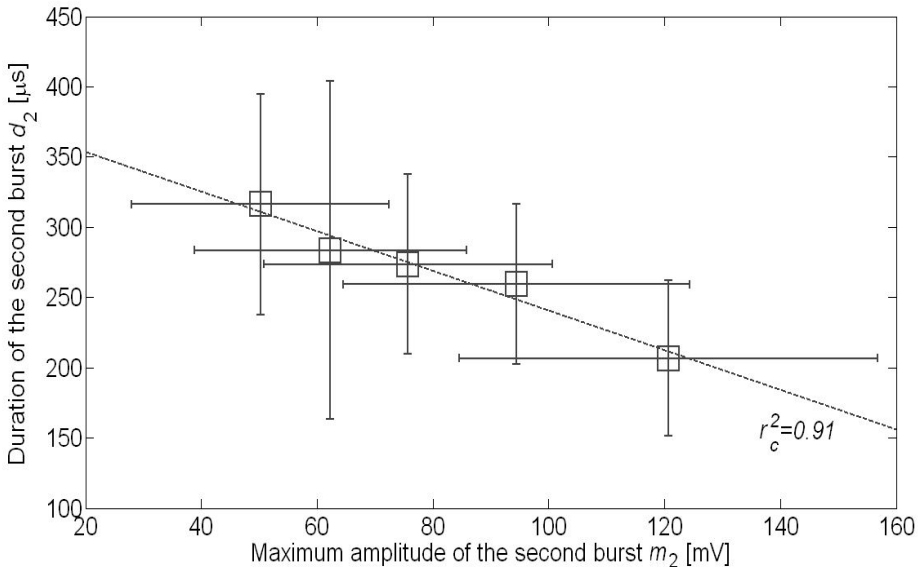

Figure 6.13: Correlation between the average amplitude (Figure 6.11) and the average duration (Figure 6.12(b)) of the second burst for stone phantoms at different grades of fragmentation. Each average is calculated over 10 measurements and the error bars represent ± one standard deviation from the average value of each set. The dotted line indicates the best linear fitting between the average points. The square of the correlation coefficient of the fitting is r^2_c=0.91.

6.3.5 Influence of fragmentation on the collapse time

The collapse time t_c could distinguish between the different samples[19] (Table 6.6). In addition, the parameter showed an increase with fragmentation for $F \leq 47\%$ and a decrease for $F > 47\%$ (Figure 6.14). The latter trend, observed also in other experiments [122] was caused, as explained in Subsection 6.2.4, by the introduction of a solid target at the focus of the bench-top lithotripter, which led to increases of the collapse time by about 20%. This effect must be less predominant for $F \leq 47\%$ and some other effect must be intervening causing the inverse trend. One hypothesis is that this increase, observed for $F \leq 47\%$, was caused by a gradual lengthening of the expansion phase of cavitation bubbles present within the phantom. This lengthening would have been allowed by larger diameters of the pores present in the phantoms (see Section 4.5.5 for details on stone structure).

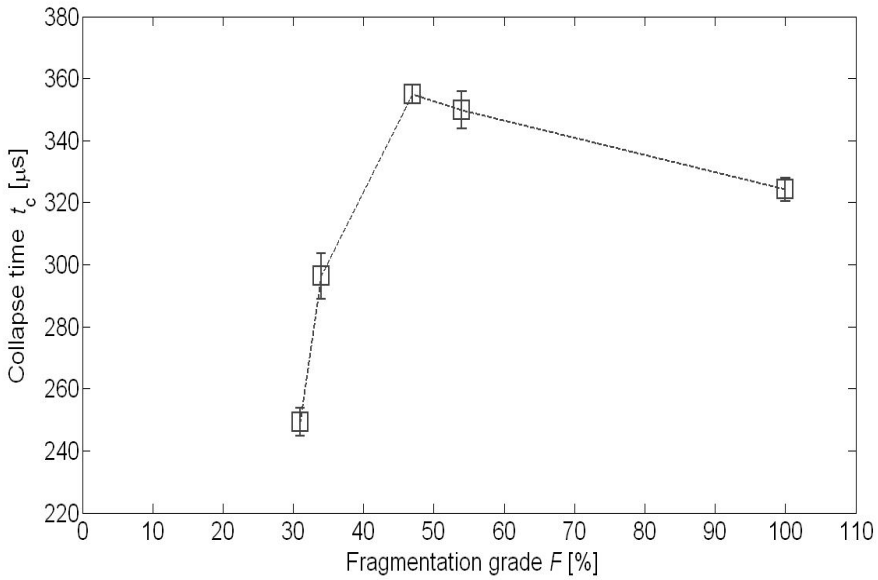

Figure 6.14: Collapse time t_c for soda-lime stone phantoms (see Subsection 4.5) at different grades of fragmentation. The average value over 10 measurements is shown for each set and the error bars represent ± one standard deviation from the average of each set. The dotted line indicates the linear interpolation between the average points.

F [%]	**31**	**34**	**47**	**54**	**100**
31		**6.02**	**20.51**	**15.16**	**14.03**
34			**8.26**	**6.50**	**3.86**
47				0.89	**7.21**
54					**4.30**
100					

Table 6.6: Results of the t-test obtained for t_c when comparing the different fragmentation stages represented in Figure 6.14, one couple a time. Each cell in the table indicates the t-value for the two stages indicated in its row and column headers. The t-values that satisfy the condition t_T>2.26 (which indicates that the difference between the averages of the two stages compared is statistically significant with **p**-value <0.05, see Subsection 6.3.1) are indicated in bold.

.

6.3.6 Influence of fragmentation on the kurtosis of the two bursts

The kurtosis of the first burst ku_1 seemed to discriminate between some grades of fragmentation (Table 6.7(a)). However there was no clear correlation (Figure 6.15(a)) between the changes in the parameter and the grade of fragmentation. The kurtosis of the second burst ku_2 (Figure 6.15(b)) could not distinguish between the different stages of fragmentation.

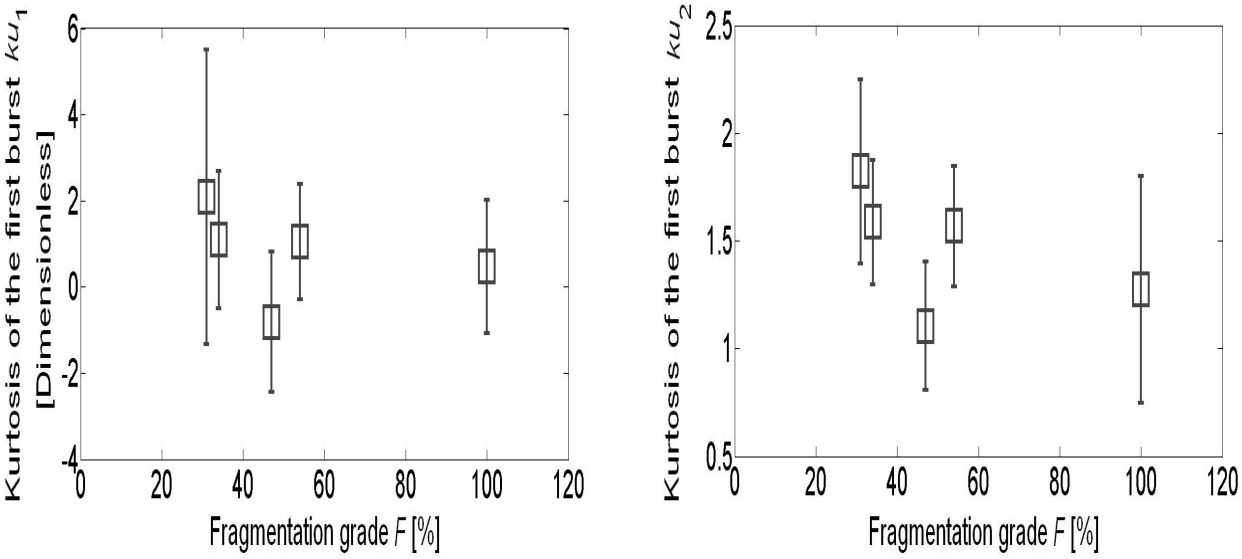

(a) **(b)**

Figure 6.15: kurtosis of (a) the first burst ku_1 and (b) the second burst ku_2 for soda-lime stone phantoms (see Subsection 4.5) at different grades of fragmentation. The average value over 10 measurements is shown for each set and the error bars represent ± one standard deviation from the average of each set.

F [%]	**31**	**34**	**47**	**54**	**100**
31		0.83	**2.42**	0.89	1.36
34			**2.66**	0.06	0.89
47				**2.80**	1.82
54					0.89
100					

(a)

F [%]	**31**	**34**	**47**	**54**	**100**
31		1.44	**4.36**	1.57	**2.56**
34			**3.68**	0.15	1.65
47				**3.59**	0.88
54					1.56
100					

(b)

Table 6.7: Results of the *t*-test obtained for (a) ku_1 and (b) ku_2 when comparing the different fragmentation stages represented in Figure 6.15, one couple a time. Each cell in the table indicates the *t*-value for the two stages indicated in its row and column headers. The *t*-values that satisfy the condition t_T>2.26 (which indicates that the difference between the averages of the two stages compared is statistically significant with **p**-value <0.05, see Subsection 6.3.1) are indicated in bold.

6.3.7 Influence of fragmentation on the skwenesses of the two bursts

The two skwenesses did not present any substantial differences for the different subsets that could be related to their different grades of fragmentation *F* (Figure 6.16 and Table 6.8).

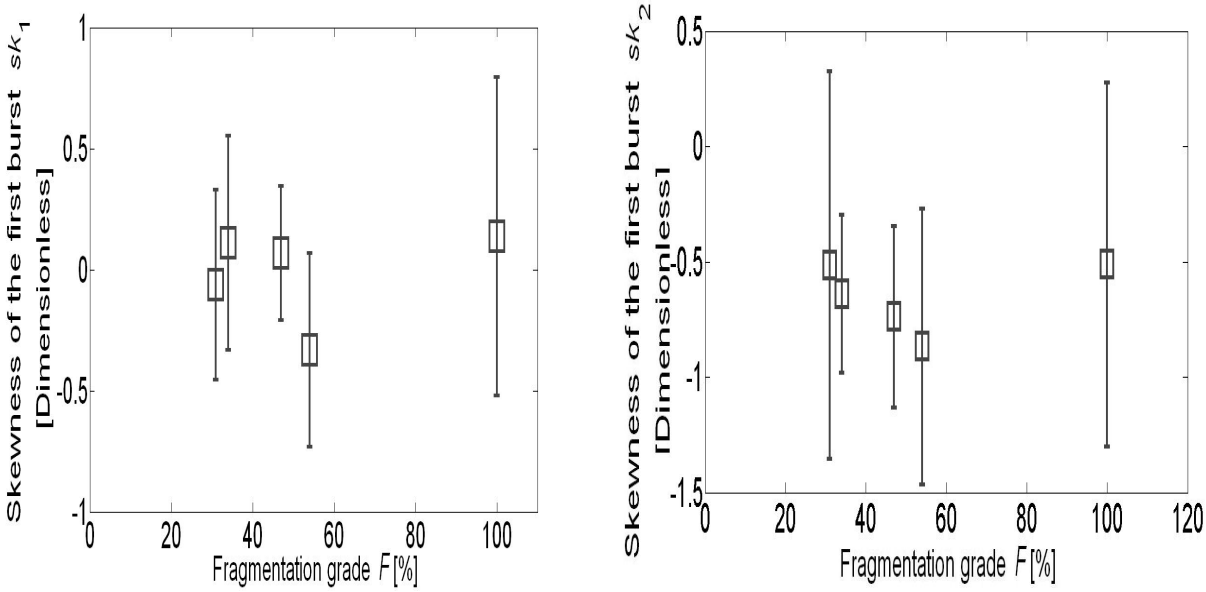

(a) **(b)**

Figure 6.16: Skewness of (a) the first burst sk_1 and (b) the second burst sk_2 for soda-lime stone phantoms (see Subsection 4.5) at different grades of fragmentation. The average value over 10 measurements is shown for each set and the error bars represent ± one standard deviation from the average of each set.

F [%]	**31**	**34**	**47**	**54**	**100**
31		0.89	1.55	0.24	1.58
34			1.15	0.55	2.26
47				1.20	**2.64**
54					1.72
100					

(a)

F [%]	**31**	**34**	**47**	**54**	**100**
31		0.44	0.77	1.08	0.01
34			0.60	1.04	0.48
47				0.56	0.82
54					1.14
100					

(b)

Table 6.8: Results of the *t*-test obtained for (a) sk_1 and (b) sk_2 when comparing the different fragmentation stages represented in Figure 6.16, one couple a time. Each cell in the table indicates the *t*-value for the two stages indicated in its row and column headers. The *t*-values that satisfy the condition t_T>2.26 (which indicates that the difference between the averages of the two stages compared is statistically significant with **p**-value <0.05, see Subsection 6.3.1) are indicated in bold.

6.3.8 Influence of fragmentation on the ratio of the two bursts maximum amplitudes

Changes in the ratio of the two amplitudes m_2/m_1 were also examined, as during preliminary experiments (see Section 6.2) the parameter showed for an intact plaster stone values significantly different from those in tap-water. In addition, the feature was supposed to be more useful than the two amplitudes for intercomparisons *in vivo*. This is because the ratio would compensate for the different absolute values of the amplitudes from patient to patient[21].

The feature could distinguish between the different grades of fragmentation (Figure 6.17). In addition, it showed a rapid increase with fragmentation for $F<54\%$ and a more gradual increase for $F>54\%$ (Figure 6.17). It was also noted that the stone phantoms with a considerable grade of fragmentation ($F>50\%$) showed a ratio $m_2/m_1>0.35$. These results indicated that this parameter could be used for monitoring stone fragmentation. In fact, it will be shown in Chapter 7, that the parameter is more suitable than others for monitoring *in vivo*. That is to say, it is less affected than others by the variability of the emissions features among patients.

[21] Differences in the amplitude of the emissions form patient to patient are caused by two main causes. First, the shock source might be set at different energy levels. Second, the acoustic path from the kidney to the sensor (and therefore the acoustic attenuation) differs from patient to patient.

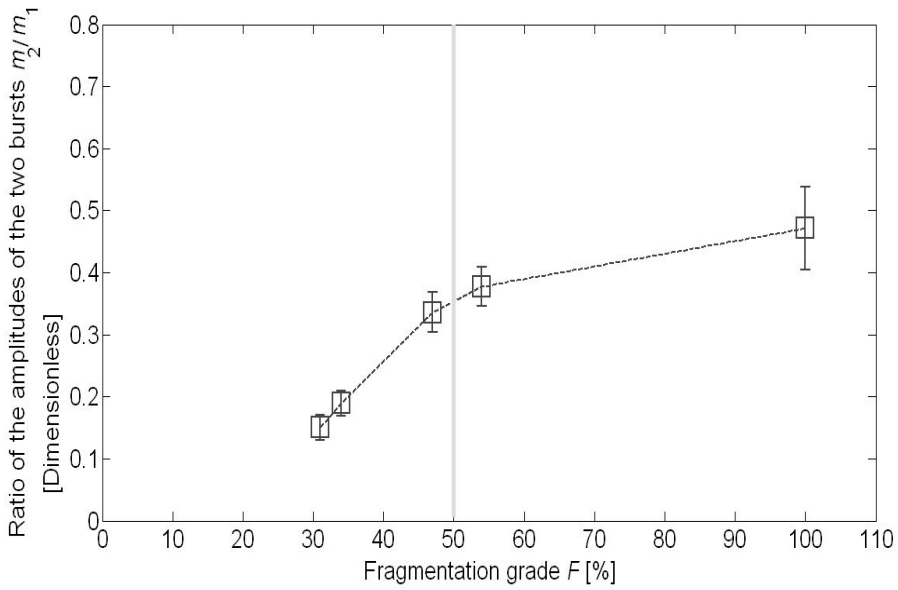

Figure 6.17: Ratio of the maximum amplitudes of the two bursts m_2/m_1 for soda-lime stone phantoms (see Subsection 4.5) at different grades of fragmentation. The average value over 10 measurements is shown for each set and the error represent ± one standard deviation from the average of each set. The dotted line indicates the linear interpolation between the average points.

F [%]	**31**	**34**	**47**	**54**	**100**
31		**4.34**	**15.43**	**18.99**	**14.68**
34			**12.11**	**15.66**	**12.87**
47				**2.92**	**5.83**
54					**4.03**
100					

Table 6.9: Results of the *t*-test obtained for m_2/m_1 when comparing the different fragmentation stages represented in Figure 6.17, one couple a time. Each cell in the table indicates the *t*-value for the two stages indicated in its row and column headers. The *t*-values that satisfy the condition $t_T>2.26$ (which indicates that the difference between the averages of the two stages compared is statistically significant with **p**-value <0.05, see Subsection 6.3.1) are indicated in bold.

6.3.9 Influence of fragmentation on the central frequencies of the two burst

The two frequency parameters f_{01} and f_{02} could not distinguish between different grades of fragmentation (Figure 6.18 and Table 6.10). However for all stone samples f_{01} was lower than f_{02} and the difference among the two was statistically significant for almost all samples (Figure 6.19). This characteristic was found also in preliminary experiments with stone phantoms made of sieved sand [119-122, 132].

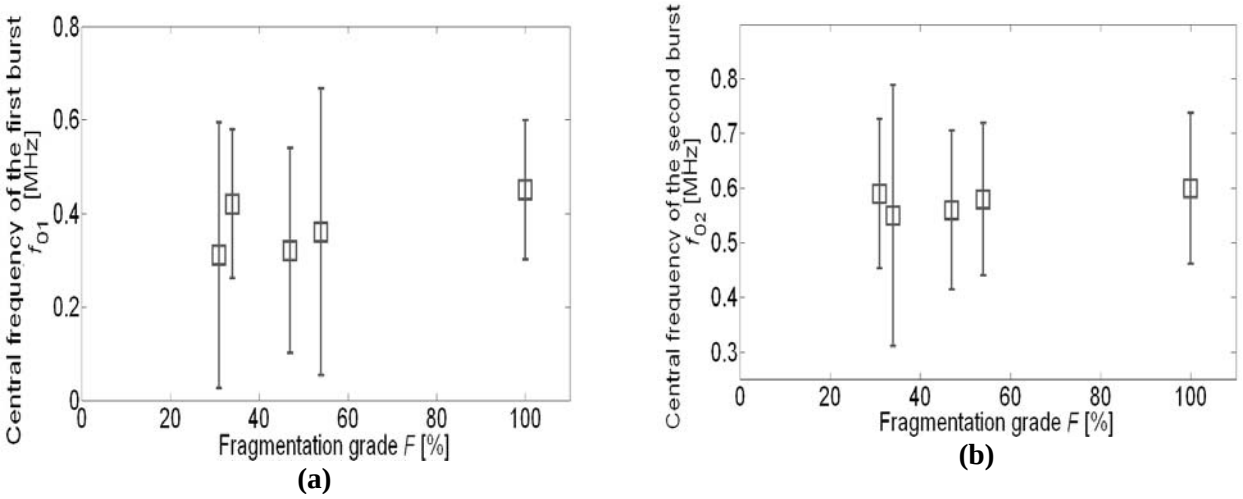

Figure 6.18: Central frequency of (a) the first burst f_{01} and (b) the second burst f_{02} for soda-lime stone phantoms (see Subsection 4.5) at different grades of fragmentation. The average value over 10 measurements is shown for each set and the error bars represent ± one standard deviation from the average of each set.

F [%]	**31**	**34**	**47**	**54**	**100**
31		1.07	0.04	0.38	1.38
34			1.22	0.55	0.44
47				0.38	1.60
54					0.83
100					

(a)

F [%]	**31**	**34**	**47**	**54**	**100**
31		0.46	0.48	0.16	0.16
34			0.11	0.34	0.57
47				0.31	0.63
54					0.32
100					

(b)

Table 6.10: Results of the *t*-test obtained (a) f_{01} and (b) f_{02} when comparing the different fragmentation stages represented in Figure 6.18, one couple a time. Each cell in the table indicates the *t*-value for the two stages indicated in its row and column headers. There are no *t*-values that satisfy the condition t_T>2.26 (which indicates that the difference between the averages of the two stages compared is statistically significant with **p**-value <0.05, see Subsection 6.3.1) are indicated in bold.

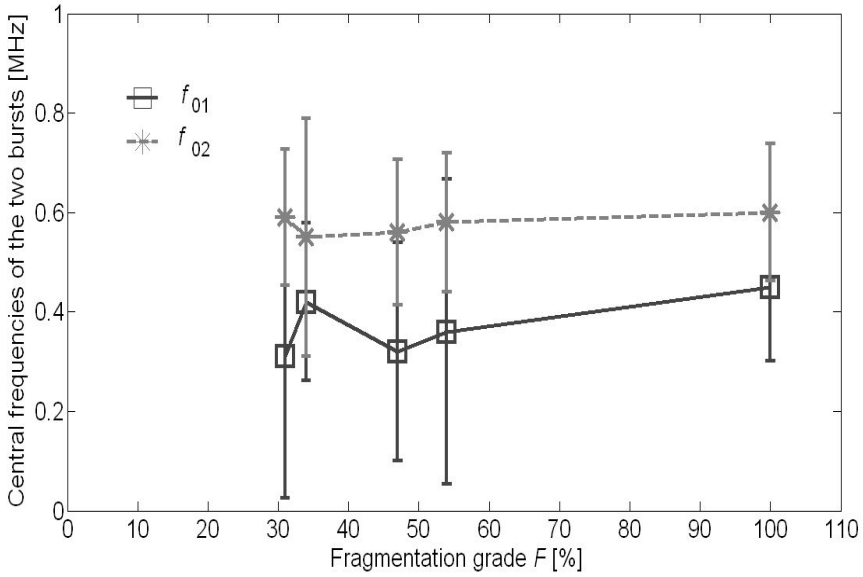

Figure 6.19: Comparison of the central frequency of the first burst f_{01} versus the central frequency of the second burst f_{02} for soda-lime stone samples (see Subsection 4.5) at different grades of fragmentation. The average value over 10 measurements is shown for each set and the error bars represent ± one standard deviation from the average of each set. The continuous line indicates the interpolation between the average values of f_{01}. The dotted line indicates the linear interpolation between the average values of f_{02}.

6.3.10 Influence of fragmentation on the frequency power ratios of the two bursts

The low frequency ratio of the first burst LF_1, as explained in Section 6.2, is a measure of the relative power of the acoustic scattering component in the first burst. As consequence, the ratio was smaller for stone phantoms at fragmentation 31%<F<100%, than it was for F=31%. However, unexpectedly, the water phantom showed about the same value of LF_1 of the stone sample at lowest fragmentation (F=31%). This was explainable in terms of a major contribution of the direct shock to the burst as, in practice, it was not attenuated by any target before reaching the sensor (see Section 3.2 for a description of the different emissions components). On the basis of these results, the feature appeared to be unreliable in discriminating between different stages of fragmentation.

The high frequency power of the second burst HF_2, represents the relative contribution of cavitation in the second burst (Section 6.2). The feature was not as influenced by fragmentation as the other two parameters linked to cavitation m_2 (6.3.3) and t_c (6.3.5). Preliminary experiments with stone phantoms made of sieved sands indicated an increase of this parameter with decreasing fragments size [122, 132]. However, on further investigations, the parameter, as showed Figure 6.20 for the glass micro-sphere phantoms, revealed such a variability within each set [119] that the differences between the averages of the different phantoms could not be considered statistically significant (Table 6.11).

However, the two considered ratios (LF_1 and HF_2) were higher than 50% for all phantoms. It might be argued that a HF_2 higher than 50% is somewhat predictable, as for its definition (see Equation (47)) even in the case of white noise this ratio would be about 80%. This is not the case for LF_1, then in the case of noisy data would be lower than 50%. Therefore low frequency ratios higher than 50% confirmed that in all configurations there is a higher concentration of power at the lower scattering frequencies for the first burst (see Subsection 6.2.1).

An *in vitro* analysis of the power distribution of secondary acoustic emissions in the frequency domain has been recently presented also by Owen *et al.* [77, 115, 116]. The idea

is similar, in that comparisons are made between the amounts of acoustic power above and below a certain frequency (500 kHz). However, Owen *et al.* [77, 115, 116] explain that the portion of signal analysed and the aim of their analysis are different from the earlier studies ([122, 132], detailed in this Chapter). In particular, Owen *et al*. [77, 115, 116] designed their experiments to minimise cavitation, as their objective was to analyse the sole contribute to the acoustic emissions of the scattering from the stone. They also did not include in their analysis the portion of signal that they identified as the main reflection of the shockwave [77, 115, 116]. In other words, if we consider the whole emission as analysed in this work (Figure 5.1), Owen *et al*. did neglect the portion of signal that corresponds approximately to the first 5 μs of the first burst. They also neglected cavitation emissions (i.e. the portion of signal corresponding to the second burst) limiting their analysis to about 15 μs. The experiments that used both glass epoxy stone phantoms (simulating an intact stone and a stone broken into two halves [77, 115]) and sieved cement stones [116] showed very promising results. In particular, similarly to preliminary experiments of this author [122, 132], stones with smaller fragments sizes showed an higher frequency contribute at frequencies above 500 kHz. However, further experiments are needed to verify if this method is suitable when cavitation is not negligible, as happens *in vivo* (see Section 3.2) and in the signals analysed in this work. In particular, it needs to be assessed if in those circumstances the variability in the feature is such that different stone samples can be distinguished significatively.

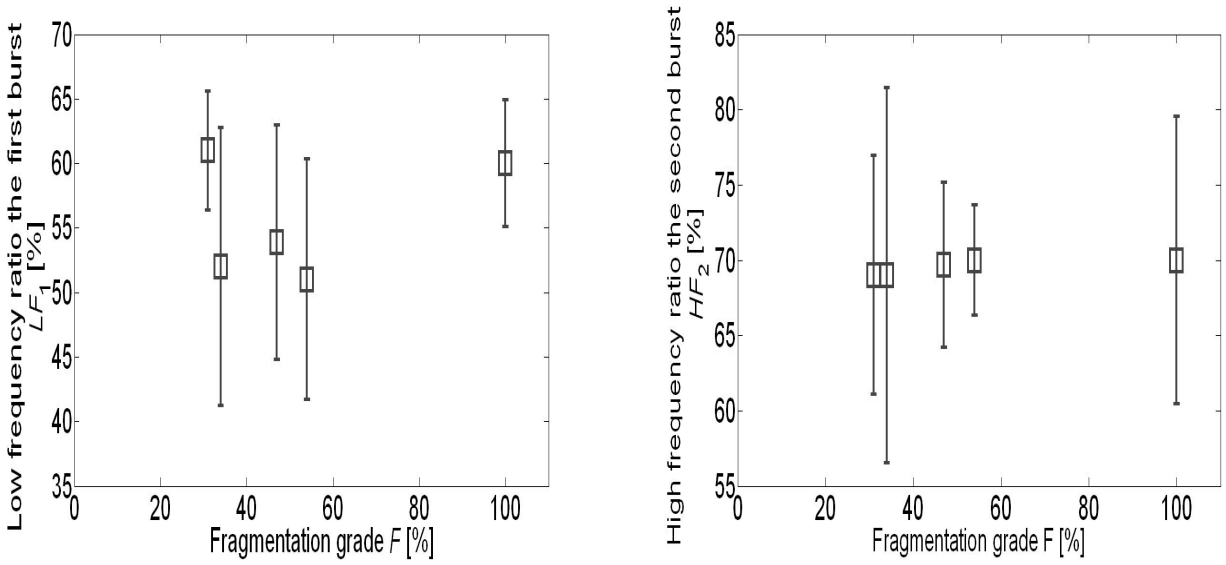

(a) **(b)**

Figure 6.20: (a) Low frequency ratio of the first burst LF_1 and (b) high frequency ratio of the second burst HF_2 for soda-lime stone phantoms (see Subsection 4.5) at different grades of fragmentation. The average value over 10 measurements is shown for each set and the error bars represent ± one standard deviation from the average of each set.

F [%]	**31**	**34**	**47**	**54**	**100**
31		**2.33**	2.20	**3.16**	0.46
34				0.39	2.04
47				0.80	1.87
54					**2.82**
100					

(a)

F [%]	**31**	**34**	**47**	**54**	**100**
31		0.03	0.13	0.16	0.09
34			0.05	0.07	0.04
47				0.03	0.01
54					0.03
100					

(b)

Table 6.11: Results of the *t*-test obtained for (a) LF_1 and (b) HF_2 when comparing the different fragmentation stages represented in Figure 6.20, one couple a time. Each cell in the table indicates the *t*-value for the two stages indicated in its row and column headers. The *t*-values that satisfy the condition t_T>2.26 (which indicates that the difference between the averages of the two stages compared is statistically significant with **p**-value <0.05, see Subsection 6.3.1) are indicated in bold.

6.3.11 The main emissions features correlated with fragmentation

Previous Subsections showed those secondary emissions features that were able to distinguish between stone phantoms at different grades of fragmentation. Furthermore they showed some correlation with the fragmentation process. These useful features were the maximum amplitudes of the two bursts m_1 (Section 6.3.2) and m_2 (Section 6.3.3), their ratio m_2/m_1 (Section 6.3.8), and the collapse time t_c (Section 6.3.5). The duration of the second burst d_2 was also shown to decrease linearly with fragmentation; however the feature could not distinguish between most features within a statistical significance of 0.05 (Section 6.3.4). In addition, as the behaviour of this parameter was correlated with that of m_2, it was not considered to add any additional information to the previous four parameters and it was excluded from further analysis.

In order to investigate whether any of these parameters were more representative of the process than others, the data were further analysed by means of Principal Component Analysis (PCA, see Subsection 5.5.1 for details). The analysis applied to the four features showed that 83% of the variability in those parameters, linked to the fragmentation process, could be described by only one principal component (ξ_1). This indicator of fragmentation was equal to the following linear combination of the examined features:

$$\xi_1 = -0.50m_1 + 0.48m_2 + 0.53\frac{m_2}{m_1} + 0.49t_c \qquad (58)$$

All four features contributed in about equal measure to the value assumed by ξ_1. Therefore it was concluded that they were all equally important in describing the fragmentation process. As a consequence, when moving to the following stage of analysis of secondary acoustic emissions *in vivo* (see Section 8.4), all the four parameters were considered as potential indicators of different classes of treatments (*successful* vs. *unsuccessful*).

6.4 Summary

This Chapter described the features of secondary acoustic emissions collected by means of the broadband NPL cavitation sensor (4.4) in various locations around the focus of the bench-top EM lithotripter described in Chapter 4.

First, the emissions were characterised in tap-water (Section 6.2.1) and it was shown they mainly originated from a spot in the focal region ahead of the geometrical focus (Section 6.2.2).

Second, it was observed that the introduction of an intact plaster of Paris stone sample affected two important emissions parameters m_1 and t_c. The latter, in particular, was very sensitive to displacements of the stone off-axis, a characteristic that would make it an eligible parameter to monitor targeting in *vivo* experiments (see Sections 7.4 and Chapter 8).

Finally, examinations were conducted to determine whether any emission feature could discriminate between different stages of stone fragmentation (Section 6.3). It was discovered that a few parameters (m_1, m_2, m_2/m_1 and t_c) had this capability. These will therefore be the candidate features to test as indicators to discriminate between *successful* and *unsuccessful* treatments *in vivo*. This will be the topic of the second half of Chapter 7.

Chapter 7 Design of the prototype diagnostic system

7.1 Introduction

Chapters 5 and 6 have described the characteristics of secondary acoustic emissions generated during ESWL. The emissions were recorded by means of a passive broadband sensor developed by NPL for industrial applications. Some features of these emissions (m_1, m_2, m_2/m_1 and t_c, see Chapter 6) contained information about the quality of a treatment (i.e. targeting and fragmentation) and were, therefore, considered suitable to be exploited to develop a clinical diagnostic system.

This Chapter concentrates on the design and preliminary tests *in vitro* and *in vivo* of a clinical prototype system, which was developed by the author and supervisors in collaboration with Precision Acoustics Ltd (PAL, Dorchester UK).

7.2 A new diagnostic system for extracorporeal shockwave lithotripsy

The different components of the prototype diagnostic system are illustrated in Figure 7.1. A first module of signal acquisition and conditioning is followed by analogue to digital conversion (A/D) and digital signal processing. A final unit displays the results of the processing, or in other words provides a visual feedback on the treatment.

Section 7.3 describes the different components of the first module of signal acquisition and conditioning. The section is mainly focused on the design (7.3.1) of the clinical passive ultrasound sensor.

A commercially available digital oscilloscope (TiePie Handyscope 3), operating at a sampling frequency of 5MHz, was used for the A/D conversion.

The signal processing module was developed in several stages. The first consisted of the development of MATLAB™ software to characterize the emissions. This characterization, part of the original contributions of the author, was described in the previous two Chapters. Sections 7.4-8.5 will be dealing with the final refinement of such processing *in vivo.* This was done by investigating the correlation between the four features identified in Chapter 6 as possible indicators of a treatment (m_1, m_2, m_2/m_1 and t_c) and effective treatment outcome, as established from follow-up X-ray. The structure of the processing software is briefly described in Appendix A.

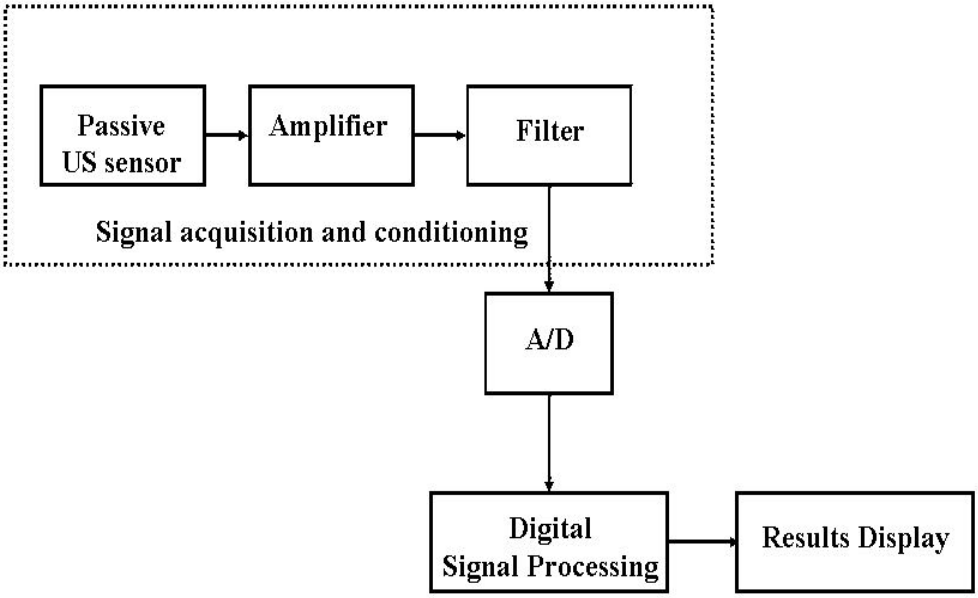

Figure 7.1: Diagram of the prototype ultrasound diagnostic system developed by the author in collaboration with PAL.

7.3 The module of signal acquisition and conditioning

This section describes the different components of the first module of the developed ultrasound system, which is the signal acquisition and conditioning (Figure 7.1). Subsection 7.3.1 is dedicated to the passive sensor specially designed for clinical use. Subsection 7.3.2 reports the characteristics of the commercially available PAL preamplifier used. Subsection 7.3.3 shows the characteristics of the filter, designed to improve the signal to noise ratio *in vivo*. Finally, subsection 7.3.4 reports the results of testing of this module *in vitro*.

7.3.1 The design of the clinical sensor

A clinical prototype ultrasound passive sensor [120-121, 140] was designed in collaboration with PAL, UK. Three different passive prototypes were developed (Figure 7.2). The first prototype, referred to as Mark I (Figure 7.2(a)), was a square multi-channel sensor. The three channels differed for a different diameter of the Polyvinylidene Fluoride (PVdF) sensitive element. That is to say, channel 1 was connected to a 1 mm sensitive element, channel 2 was connected to a 2 mm sensitive element and channel 3 was connected to a 3 mm element. The four features (m_1, m_2, m_2/m_1 and t_c) of the emissions extracted from the three channels did not appear significantly different when this prototype was tested *in vitro*. In addition, when tested *in vivo*, the channel at the highest sensitivity (channel 3) showed a poor signal to noise ratio. In fact, this ratio was less than 50% also for patients with regular body mass index (BMI<25). In addition, patients showed a certain dislike and diffidence towards the appearance of this prototype. This is because they are used to the application of either round and flat sensors (i.e. ECG leads) or anyway sensors with smooth rounded surfaces (i.e. ultrasound probes). Such was the dislike of this prototype that the rate of acceptance to participate in the trial was low (about 30%).

Therefore, for both technical and aesthetical reasons, such multi-channel design was abandoned to move towards a round smooth single channel sensor that could make the patient feel comfortable. The second prototype (Mark II), not reported in Figure 7.2, had the same appearance of the latest (Mark III, Figure 7.2 (b)). Both Mark II and Mark III have a

larger sensitive element than those used in Mark I. This element is 18 mm in diameter. The only difference in the two versions is the external diameter (20 mm vs. 25 mm), as Mark II had a smaller layer of protecting backing material than Mark III.

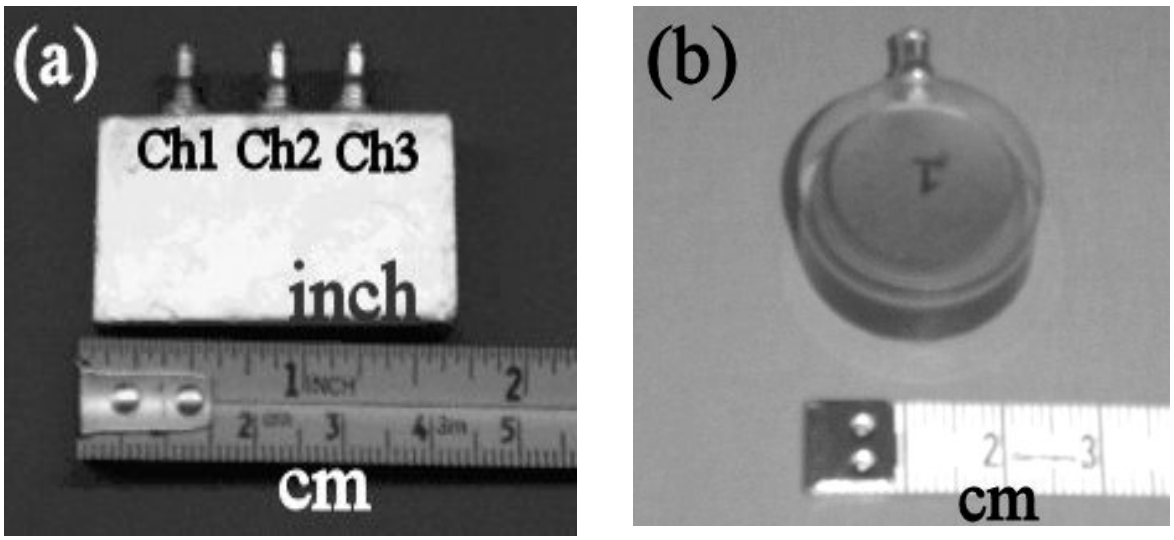

Figure 7.2: (a) First clinical prototype passive multi-channel ultrasound sensor, referred to as Mark I. (b) Final clinical passive ultrasound prototype sensor, referred to as Mark III. All prototypes were developed by the author and supervisors in collaboration with PAL.

Only the latest prototype sensor (Figure 7.2 (b)), which is the one employed by the developed diagnostic system is described in detail in this thesis. The sensor, as anticipated, is an entirely passive piezoelectric PVdF sensor with a diameter of 25 mm (Figure 7.2), which converts received pressure waves into measurable voltages. The sensitive element of the sensitive element is a thin (28 μm) PVdF film of 18 mm diameter with a broadband frequency response (up to 100 MHz).

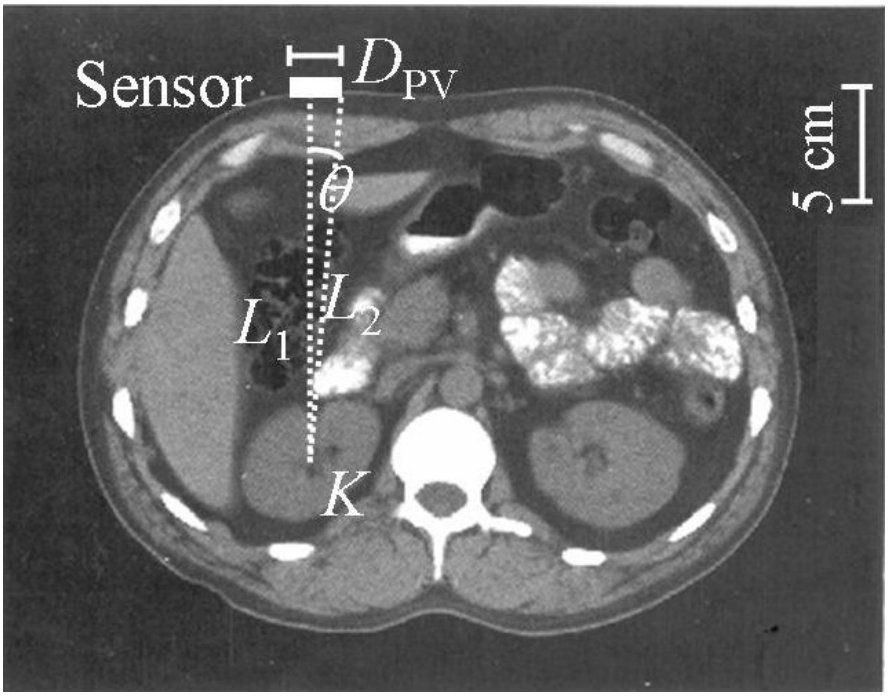

Figure 7.3: Computer Tomographic image of a section of a human torso. Reprinted from [141]. Copyright (1991), with permission from Elsevier. L_1 and L_2 indicates two possible paths of secondary acoustic emissions , that generated around the stone in the kidney (K) are collected by the sensor. These two paths are at a maximum distance, equal to half of the diameter (D_{PV}) of the piezoelectric sensor.

The diameter of this element was designed to ensure that at 3 MHz a maximum path difference (L_M=L_2-L_1, Figure 7.3) no greater than 0.25 mm (=0.5×λ_{3M}, with λ_{3M}= 500 μm sound wavelength at 3MHz) would occur for emissions coming from the kidney[22]. That is to say, the lengths L_1 and L_2 in Figure 7.3 show two possible emissions paths coming from the kidney.

[22] A frequency of 3MHz was considered as, because of ultrasound attenuation by the body [140], this is the maximum frequency was expected to reach the surface of the torso from the kidney (depths of about 17 cm)

If for these there is a maximum path difference (L_M), equal to half the diameter of the PVdF element $D_{PV}/2$= 1 mm (Figure 7.3), than the maximum allowable diameter D_{PV} can be derived from geometrical considerations as:

$$L_2 - L_1 = L_2(1-\cos\theta) < 0.5\lambda_{3M} \tag{59}$$

$$\frac{D_{PV}}{2} = L_2 \sin\theta$$

where θ is the angle between the two paths. The combination and manipulation of the two conditions leads to:

$$D_{PV} < \sqrt{4{L_2}^2\left[1-\left(1-\frac{0.5\lambda_{3M}}{L_2}\right)^2\right]} = 26 \text{ mm} \tag{60}$$

as L_2 has been estimated to be about 17 cm for the average patient. This information was gathered from anatomical data available as cross sectional images of the human body [141] and records of the distances of kidney stones from the patient torso reported in a database of sixty patients that had undergone the ESWL at Guy's hospital between 1998 and 2000.

The front face of the piezo-electric element (which is in contact with the patient) is protected by an insulating bio-compatible material whose acoustic properties were optimized by PAL to ensure the maximum acoustic sensitivity of the system. The insulation was necessary to comply with the requirements of electrical safety normative, which are imposed to avoid that a patient becomes part of any electrical path that connects to the main (IEC60601-1). This front face can also be disinfected easily with solvents such as Isopropyl Alcohol before applying the sensor to a patient. This is to prevent possible spread of infections among

patients. In contrast, the rear surface of the sensor is filled with a sound absorbing material developed by PAL and NPL (Aptflex) that prevents internal reverberations within the sensor.

Furthermore all is placed in an electrically conducting grounded enclosure, which is connected to both the ground electrode on the sensitive element and the signal ground of the connector on the enclosure wall. The voltage waveform generated within the piezo-polymer layer is extracted by means of a wide bandwidth RF connector mounted in the side wall of the sensor case.

All components of the acoustic sensor, with the exception of the connector and the wires attached to it, are polymeric. This results in a lightweight sensor (total weight 7g) to minimize patient discomfort.

The prototype, calibrated by PAL, has a sensitivity of 3.3 $VMPa^{-1}$ at 500 kHz.

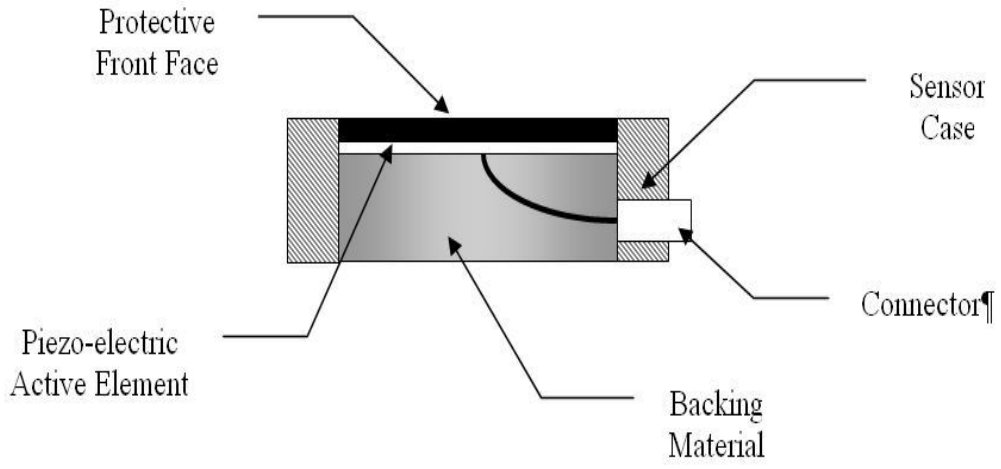

Figure 7.4: Diagram of the final prototype (Mark III, Figure 7.3) developed in collaboration with PAL. Figure courtesy of Precision Acoustic Ltd.

7.3.2 The preamplifier characteristics

The final prototype (Mark III), described in the previous subsection, did not always present signals of good quality when tested *in vivo* (see Section 7.4 for details on these experiments). That is to say that the signal to noise ratio, estimated as the ratio between the maximum amplitude of the first burst m_1 and the background noise level was greater than 50% only for patients underweight or of regular corporature, i.e. patients with body mass indices (BMI) less than 25. In order to overcome this problem, the output of the acoustic sensor was connected directly to a wideband preamplifier (Figure 7.5 HP1, Precision Acoustics Ltd, Dorchester, UK) that buffered the electrical impedance to 50 Ohms.

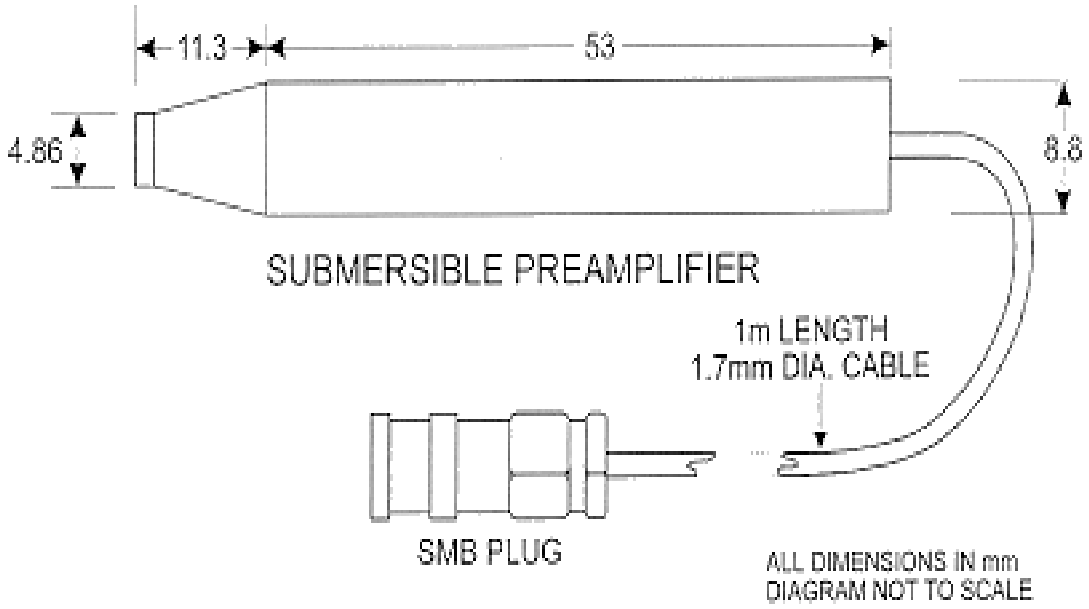

Figure 7.5: PAL commercial available broadband preamplifier HP1 (**www.acoustics.co.uk**).

This commercially available preamplifier, whose specifications are reported in Table 7.1, required a DC Supply voltage of 28±1 V (to ensure a variation in the system gain <1%) and was for this reason connected to a DC coupler (Figure 7.6). The preamplifier, though not specifically produced for this application, was also consistent with the design principles of a lightweight system (total weight of preamplifier/cable 29 g).

Patient safety (as mentioned in the previous subsection) required that, unless an insulating transformer or optical coupling was used, the sensor applied to the patient could not be connected to mains (IEC60601-1). Therefore a battery powered DC supply was commissioned to PAL. This supply uses four 9 V batteries to power the preamplifier.

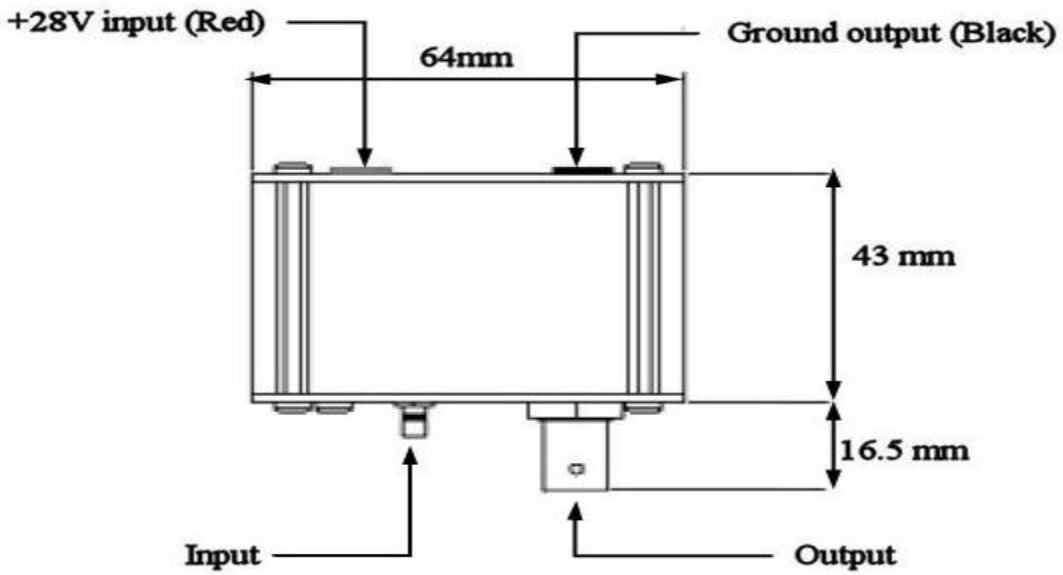

Figure 7.6: PAL DC coupler required for the use of the HP1 preamplifier (www.acoustics.co.uk).

Voltage Gain:	Nominal 8dB at 3.5 MHz
Bandwidth:	10 kHz to 50 MHz (-3 dB) 5 kHz to 100 MHz (-6 dB)
Maximum Output Level:	650 mV peak to peak into 50Ω load
Input Impedance:	1 MΩ in parallel with 8 pF
Output Impedance:	50Ω over the range 40kHz to 130MHz
Output Noise Level:	Typically 60 μV root mean square (100MHz bandwidth)
Terminations:	Input – Micro coaxial connector Output – Submicro coaxial connector
Power Requirements:	Supply Phantom fed by Precision Acoustics DC Coupler Model DC2
Operating Range:	Temperature 0 to 50 °C
Cable Details:	RG 174 Length 1.5 m minimum
Weight:	29 g

Table 7.1: Specifications of the PAL bandwidth preamplifier (**www.acoustics.co.uk**).

The combination of the sensor with the preamplifier showed a sensitivity of about 21 V/MPa, when calibrated at 500 kHz. The sensor and preamplifier were encapsulated in a rigid PMMA holder (Figure 7.7) that protected the components. In particular, the use of this holder avoided the possibility that any stress could be applied to the contact between the sensor and the preamplifier. This holder ensured, at the same time, the insulation of any possible electrical contact from the patients. The total weight of the part applied to the patient (sensor, preamplifier and PMMA holder, Figure 7.7) was still such as not to induce any discomfort to the patient (52 g).

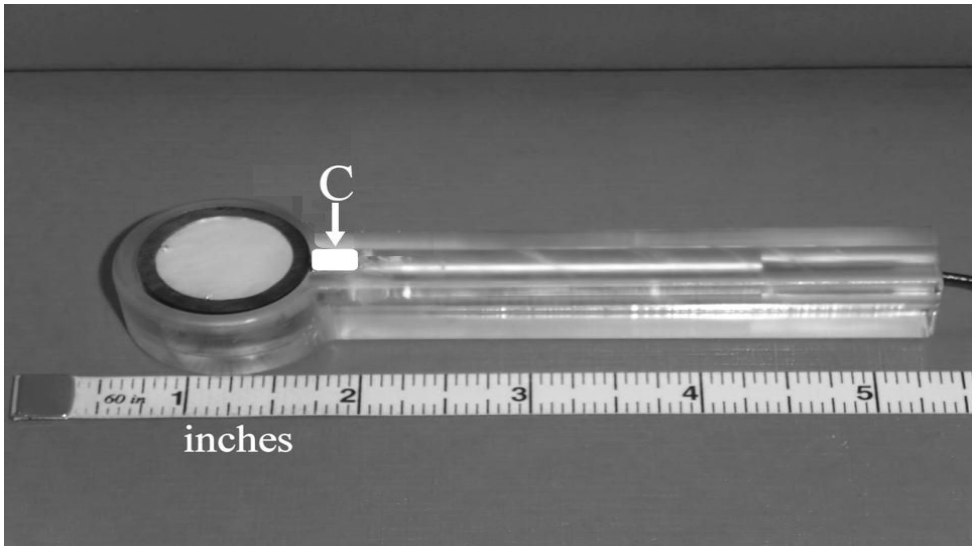

Figure 7.7: The final configuration of the part applied to the patient. The sensor (Figure 7.2(b)) and preamplifier are enclosed in a rigid PMMA holder. The detail of the connection between the sensor and the preamplifier is indicated by a letter C for "connection". Before starting measurements *in vivo*, the hole was filled with insulating silicon rubber to ensure electrical insulation.

7.3.3 The filter characteristics

The background noise and the lithotripter shock had to be filtered to extract the secondary acoustic emissions. This is because the cavitation components, as explained in Chapter 6, presented their main contribution at frequencies above 400 kHz. Figure 7.8(a) shows a raw signal collected by means of the clinical sensor (see Section 7.3, prototype Mark III) *in vivo*. Figure 7.8(b) shows the same signal after it has been filtered by means of digital high pass filter. The filter used was a Butterworth filter [142] of 4^{th} order with a cut off- frequency at 3 dB of 300 kHz and a reduction of about 128 dB at 120 kHz. The digital filtering was applied twice (forward and backward) to compensate for any phase shift introduced by the filter.

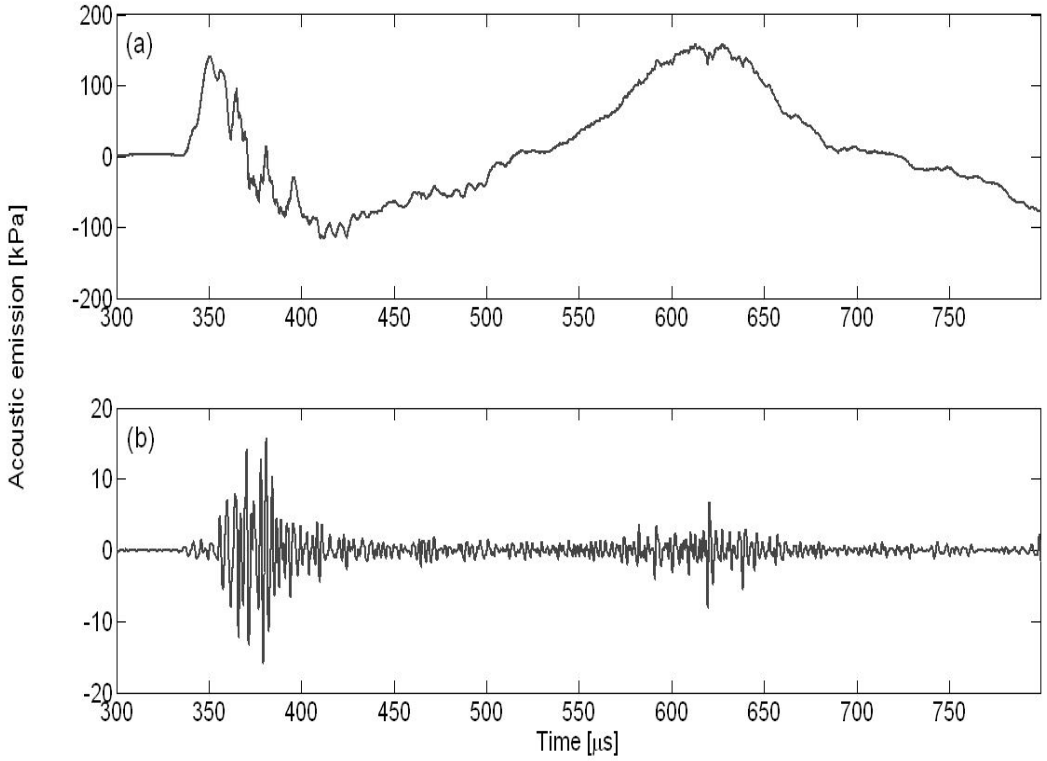

Figure 7.8: (a) A raw signal collected *in vivo* with the clinical prototype (Mark III) developed and (b) the same signal filtered by a high Pass Butterworth filter of 4th order with a cut-off frequency of 300 kHz.

Digital filtering was an option for signals with a signal to noise ratio of at least 50%, as the one shown in Figure 7.8(a). In all the other cases, it was desirable to filter the signal before digitalisation. Therefore PAL were commissioned to produce a high pass filter with characteristics as close as possible to that of the Butterworth filter that had been used. They produced a filter with the frequency response shown in Figure 7.9, which had a cut-off frequency f_c at 3 dB of 292 kHz and showed an attenuation of about 120 dB at 120 kHz. A phase diagram was not provided by PAL, but the phase spectrum was guaranteed to be linear in the main region of interest (0.3-1 MHz). This ensured that any delay introduced by the filter was constant for the different frequency components of the signal and did not alter the signal characteristics.

The following subsection deals with the test of the module of acquisition and conditioning *in vitro*.

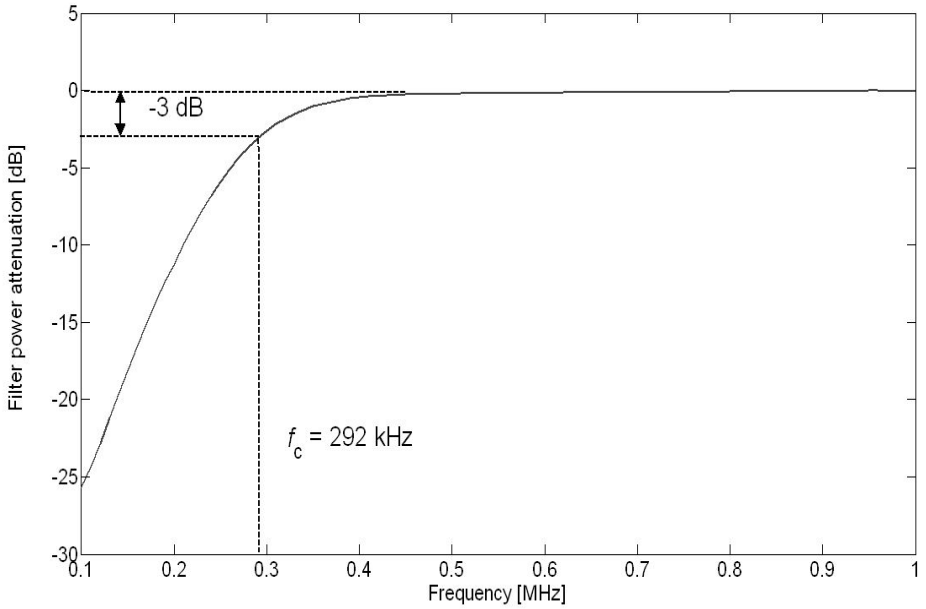

Figure 7.9: Frequency response of the high-pass filter produced by PAL. The filter shows a cut-off frequency at 3 dB (f_c) equal to 292 kHz.

7.3.4 Test of the data acquisition and conditioning module *in vitro*

The module of data acquisition and conditioning described in subsections 7.3.1-7.3.3 was preliminarily tested *in vitro*. First of all, the signal at the output of this system (without the use of the preamplification) was compared against the signal acquired exploiting the NPL cavitation sensor and the measurement system described in section 4.2. Figure 7.10 displays the set-up used for this test.

The NPL sensor (Figure 7.10, NPL) was left at the focus of bench-top lithotripter, while the sensor developed in collaboration with PAL (Figure 7.10, PAL) was placed laterally off-axis at different distances (d) varying from 0.5 to 30 mm.

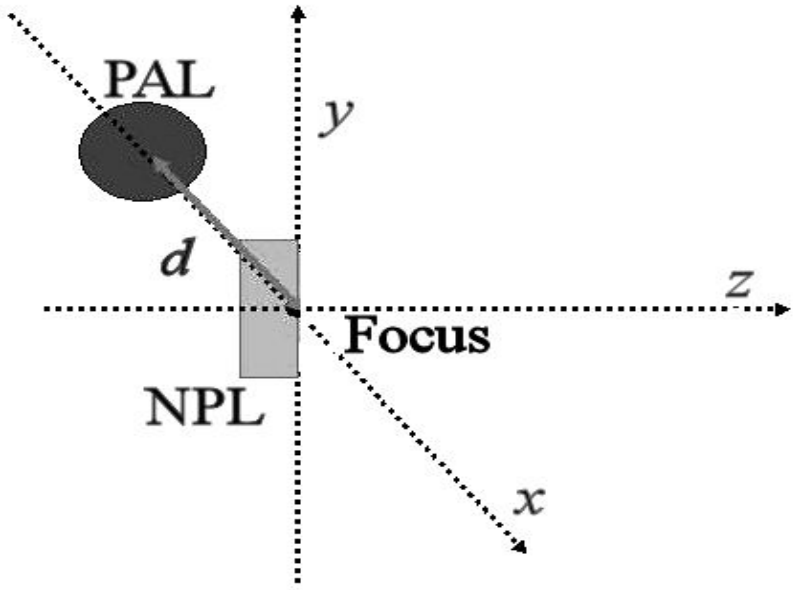

Figure 7.10: Set-up exploited for the test *in vitro* of the signal acquisitioning and conditioning system developed in collaboration with Precision Acoustics Ltd. The output of the developed prototype clinical system was compared against that of the experimental system which exploits the NPL sensor (see Section 4.2). The NPL cavitation sensor was positioned at the focus of the lithotripter. The clinical sensor (indicated as PAL in the figure) was positioned laterally off axis at a distance *d*.

Figure 7.11 shows two traces recorded while testing the prototype at the minimum distance of 0.5 mm. At this distance some correlation (square of the maximum correlation coefficient r_c^2 equal to 0.4) was found between the two signals and, most importantly, they did not show significantly different features. This is to say, the average collapse times t_c and the average fragmentation index m_2/m_1 of sets of 5 traces collected using the two systems were compared using *t*-test statistics (see Subsection 6.3.1 for details on this test). Neither value showed any statistical difference[23] when tested for a significance (**p**-value[18]) less than 0.01. In particular, the values estimated for the collapse time t_c were 240±5 μs for the NPL sensor and

[23] The *t*-test parameter t_T for the two populations compared is 2.11 for t_c and 2.58 for m_2/m_1. If $\nu_d=N_s-1=4$ degrees of freedom are considered (where $N_s=5$ in this case), the t-test parameter needs to be higher than 4.60 for a significance less than 0.01 (and higher than 2.78 for a significance less than 0.05) [139].

226±14 μs for the clinical sensor. The values estimated for the fragmentation index m_2/m_1 were 0.52±0.06 for the NPL sensor and 0.43±0.05 for the clinical sensor.

The correlation between the signals decreased when the clinical prototype sensor was moved further away. Traces collected at a distance d equal to 30 mm showed a square cross correlation coefficient equal to 0.15.

Following these experiments the clinical prototype was tested in the proximity of stone phantoms which had different grades of fragmentation. These stone phantoms were inserted in a body phantom placed on the treatment couch of the clinical lithotripter (Figure 7.12; see 7.4.1 for details about the clinical lithotripter). A similar behaviour was observed to that which had been found when using the NPL sensor in the benchtop lithotripter (see Section 6.3). That is to say, the relative amplitude of the second burst (m_2/m_1) increased with the fragmentation ratio (Figure 7.13) and, in particular, showed values higher than m_2/m_1=0.4 for a stone whose fragmentation was higher than 50%.

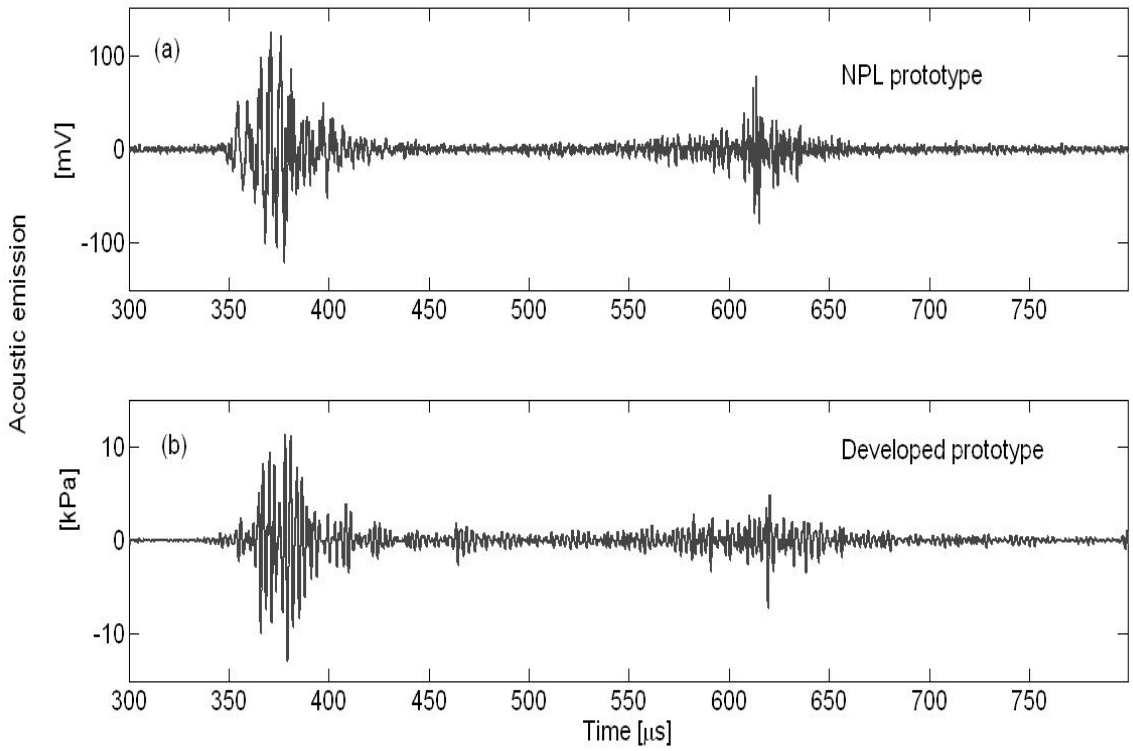

Figure 7.11: Comparison of two traces collected with (a) the NPL sensor and (b) the clinical prototype (Mark III) developed in collaboration with supervisors and PAL, when the two sensors where positioned as shown Figure 7.10 at a distance of d =5 mm.

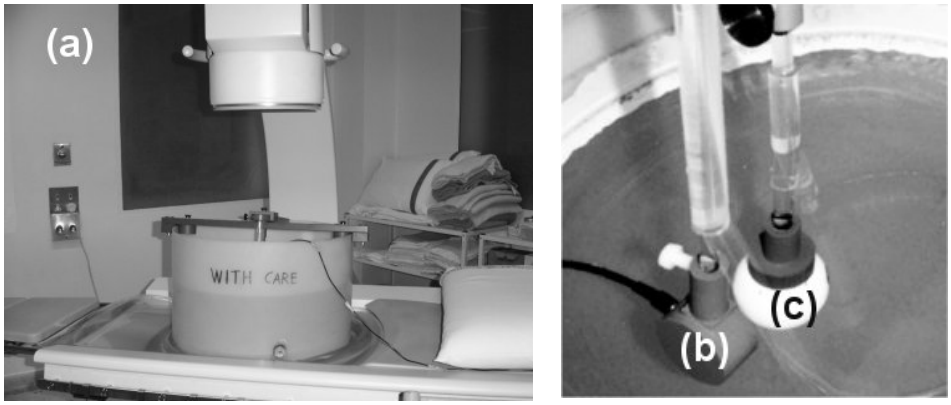

Figure 7.12: Frame (a) shows the body phantom placed on the treatment couch. The contents of the body phantom are shown in the second panel. They include (b) the prototype developed in collaboration with supervisors and PAL and (c) the stone phantom. The body phantom is made of a PMMA tank with an acoustic transparent window at the bottom that allows the transmission of the shock wave.

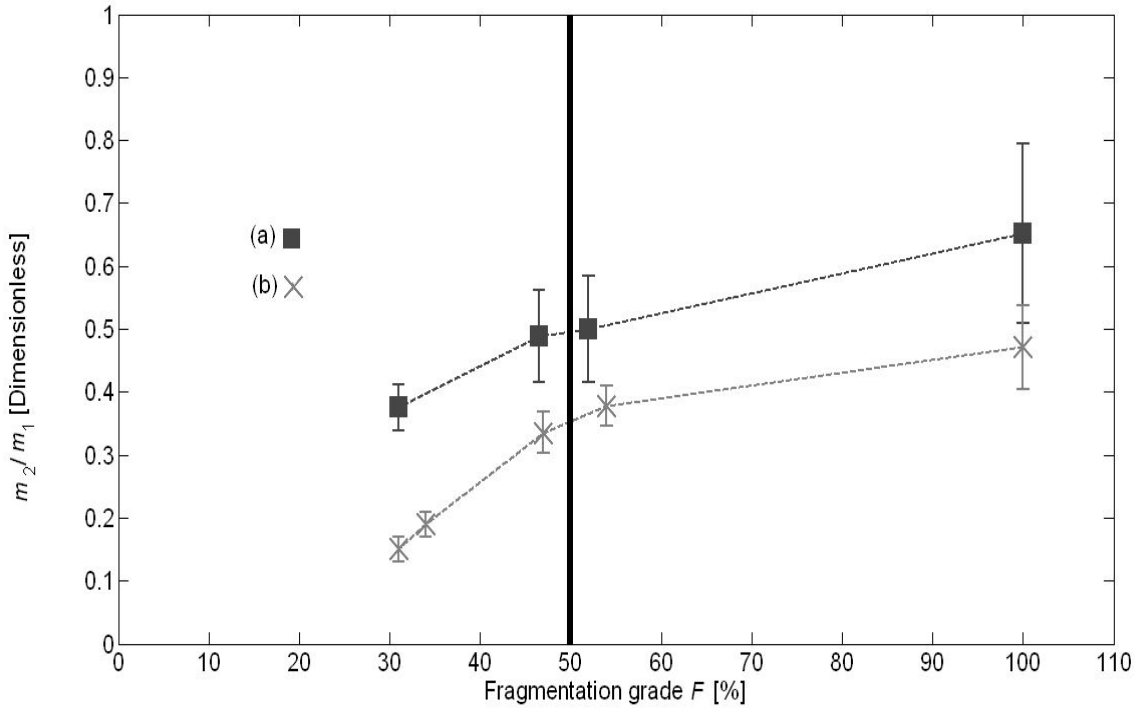

Figure 7.13: (a) Fragmentation ratios m_2/m_1 of emissions recorded using the clinical prototype sensor in the proximity of stones phantoms at different grades of fragmentations. The stone phantoms were inserted in a body phantom as shown in Figure 7.12. These ratios are compared against (b) those obtained for the same phantoms using the NPL sensor in the tank of the bench-top lithotripter (see Section 6.3).

These preliminary *in vitro* tests showed that the clinical prototype, when used in the clinical environment, could be used to gather information about targeting (t_c, see Subsection 6.2.3 for the link between this parameter and targeting) and fragmentation (m_2/m_1, see subsection 6.3.8 for the link between this parameter and fragmentation).

Each version of the module of data acquisition and conditioning described in section 7.3 was also tested *in vivo*. This preliminary clinical trial involved 51 patients whose acoustic signals were analysed to develop the module from the initial version exploiting only a single multichannel sensor (Mark I, Subsection 7.3.1) to the final version, which includes the latest acoustic sensor (sensor Mark III, Subsection 7.3.1), preamplification (Subsection 7.3.2) and filtering (Subsection 7.3.3). The trial is described in the following section.

7.4 Test and development of the module of data acquisition *in vivo*

Section 7.3 has described the development and testing of the module for signal acquisition and conditioning *in vitro*. The process partially overlapped with the first clinical trial of the system, because the characteristics of the system (consisting initially in a passive multi-channel sensor) had to be refined and optimised for the clinical environment.

Each component was tested for electrical safety before its use *in vivo* and the trial received the approval of Guy's and St. Thomas' NHS Trust Ethic Committee (Reference 06/Q0702/12). In compliance with the rules of this committee, consent was obtained before enrolling any patient in the trial. The trial included a total of 51 patients and can be divided into five stages (Figure 7.14).

The first stage (Figure 7.14, Stage I) involved 15 patients and was aimed at testing the sensitivity of the first developed multi-channel prototype sensor *in vivo* (see Subsection 7.3.1). As mentioned in subsection 7.3.1, the signals acquired by the three channels of the sensor did not show any significant difference when tested *in vitro*. Therefore only channel 3, which was that at the highest sensitivity, was tested *in vivo*. This prototype was not calibrated but a ratio of 1.5 was estimated between the sensitivity of channel 3 and channel 1, from the ratios of the peak to peak amplitudes in Volts of signals recorded by the two channels. Digital filtering was used to remove background noise. In this early stage, several factors affected the quality of the data. In 3 out of 15 patients the data were not saved because of malfunctioning of the digital oscilloscope, which was due to lack of power. These problems were solved exploiting an auxiliary power cable that was connected to the mouse port in conjunction with the standard USB cable. Another problem was the positioning of the sensor, for which several kinds of plasters were tested. At the beginning the plasters used (approximately 5cm by 5cm) were too small and in 2 out of 15 patients the sensor detached during recording. A good signal to noise ratio (SNR), that is a SNR greater than 40%, was obtained only for 2 out of the remaining 10 patients, which were characterised by a body mass index (BMI) below 22. That is to say, data of good quality were obtainable only for

patients where acoustic absorption was small. In addition, as explained in subsection 7.3.1, most patients (about 70%) disliked the shape of the sensor.

The second stage (Figure 7.14, Stage II) was dedicated to the testing of a new single channel, round, prototype and involved 18 patients. The sensitivity in this prototype had been increased by at least one order of magnitude by using a PVdF element whose diameter was sixty times larger (18 cm). A higher sensitivity showed in the magnitude of the signals acquired that were of the order of hundreds of mV instead of tens of mV, as those obtained with the previous sensor. This prototype performed well in terms of SNR (at least 30%) for patients of regular weight (BMI<25). However data of good quality were obtained only from the first 5 of the 9 patients with BMI less than 25, as the sensor was at some point damaged by the lithotripter source.

Therefore a third prototype (see Subsection 7.3.1), with the same sensitivity, but a thicker protective layer, was developed. This sensor was tested on a set of 10 patients (Figure 7.14, Stage III) and similar to the previous could not give data of acceptable SNR for overweight patients (6 out of 10). Analogue filtering was introduced (see Subsection 7.3.3) to improve the SNR before digitalisation and the system was tested on two patients (Figure 7.14, Stage IV). One of the patients was of regular weight (BMI=23) and one was obese (BMI=32). The system still did not give a good SNR (greater than 50%) in the latter case. Therefore this stage was almost immediately followed by the introduction of signal preamplification.

The final data acquisition module, which used both preamplification and filtering, provided data of good SNR (greater than 50%) for all patients. This stage (Figure 7.14, Stage V), which involved 6 patients, was also used to analyse the features of the acoustic emissions *in vivo* and to compare them against treatment outcomes. The treatment outcomes were established by the urologist at the patient follow-up examination 2-3 weeks after the treatment. The results of this comparison helped the development of the signal processing module of the diagnostic system, and in particular they were exploited to develop an interface to synchronise the operations of data acquisition with the following processing to

perform on-line monitoring. The results of this last stage will be described in detail in subsection 7.4.4. Subsections 7.4.1 to 7.4.3 describe the clinical experimental set-up and the experimental protocol followed for the data acquisition. Subsection 7.4.1 starts with a brief description of the clinical lithotripter, followed by some details about the positioning of the sensor in subsection 7.4.1. After this, data collection and analysis are described (Subsection 7.4.2). In particular, subsection 7.4.3 reports the details of the protocol used for the data acquisition.

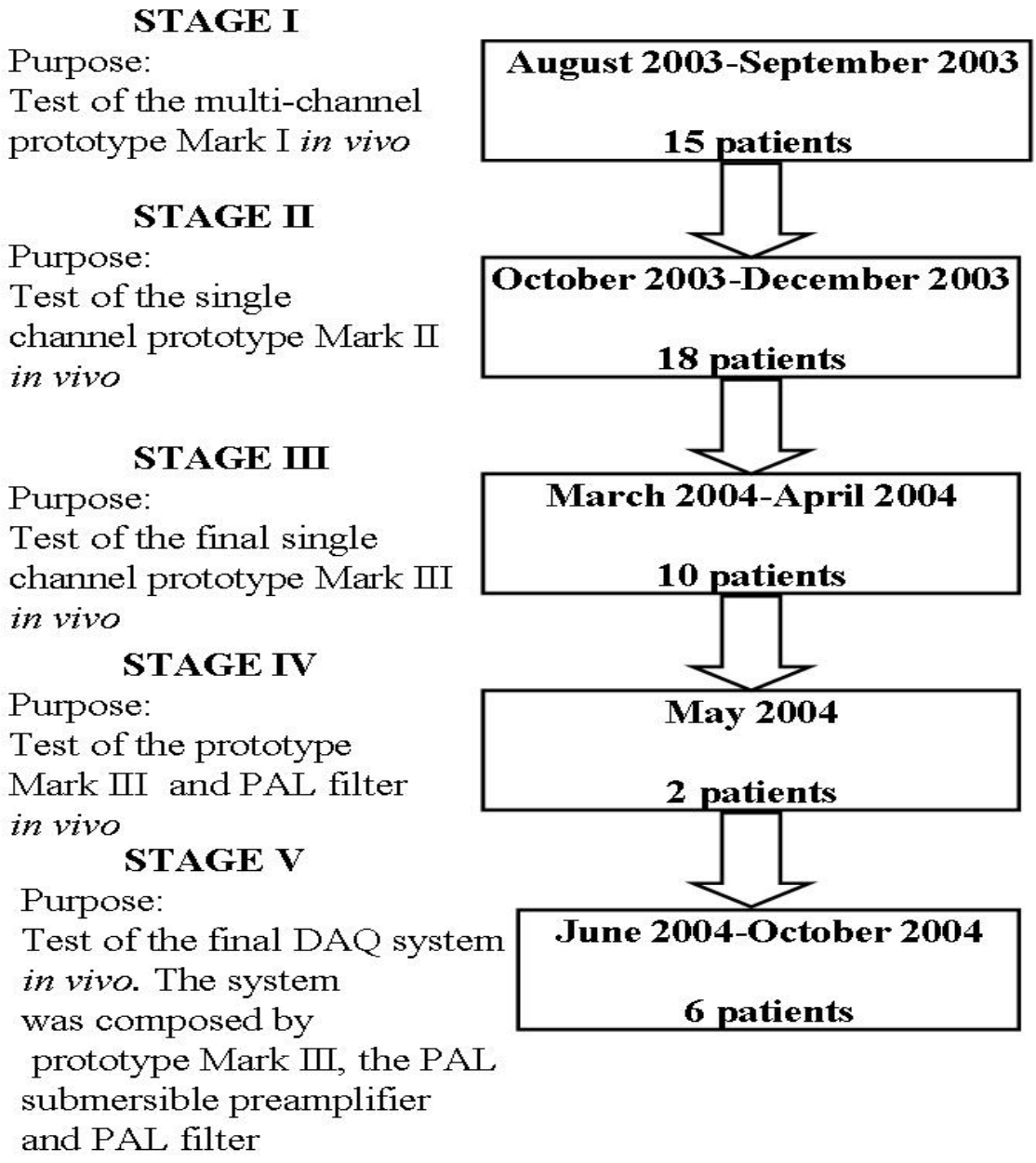

Figure 7.14: The five stages of the preliminary clinical trial of the data acquisition and conditioning system. The diagram lists the components tested at each stage and the number of patients participating. The aim of each phase is also briefly stated.

7.4.1 The clinical lithotripter

Figure 7.15 shows a picture of the clinical experimental set-up used in the lithotripsy theatre of Guys' Hospital. The lithotripter installed in the Day Surgery Unit is a Storz Modulith SLX-MX. This is an EM lithotripter where the operator can set an energy level, which basically controls the discharge potential of the coil (see Subsection 2.2.3 for details on EM lithotripters). The Storz Modulith energy settings vary from 1 to 9. The most common energy level used in the treatments object of this study was 4, which corresponds to a shock with a peak positive pressure P^+ of about 40 MPa and peak negative pressure P^- of about 20 MPa, measured *in vitro* at the focus of the lithotripter (see Section 2.2 for shock characteristics). The lithotripter stone targeting and monitoring devices consist of the usual low dose X-ray fluoroscopy and ultrasound B-mode imaging systems, whose components are clearly labelled in Figure 7.15.

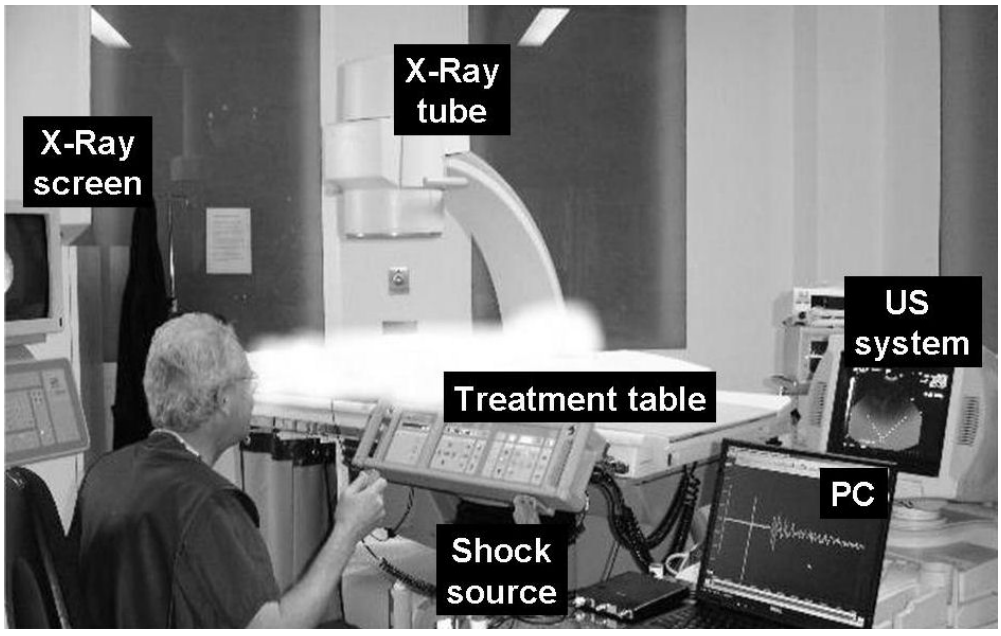

Figure 7.15: Test of the clinical prototypes *in vivo* in the lithotripsy theatre (Guy's Hospital, London). The patient has been ghosted out in the picture for privacy.

The prototype ultrasound sensor was placed on the side of the patient's abdomen corresponding to the treated kidney (Figure 7.16(a)). The preliminary *in vitro* analysis of the secondary emissions around the focus of the lithotripter (see Section 6.2.2), showed that they were mainly generated in the proximity of the focal area of the lithotripter. That is to say, the most powerful emissions occurred in a region between the lithotripter geometrical focus (i.e. the stone) and the source (see Figure 6.3). In the clinical trials it would have been practically impossible to place the sensor in this region, as it would have meant positioning it between the patient and the source and, therefore, interfering with the treatment. The closest accessible location to the area of interest was the side of the patient's torso, as close as possible to the treated kidney.

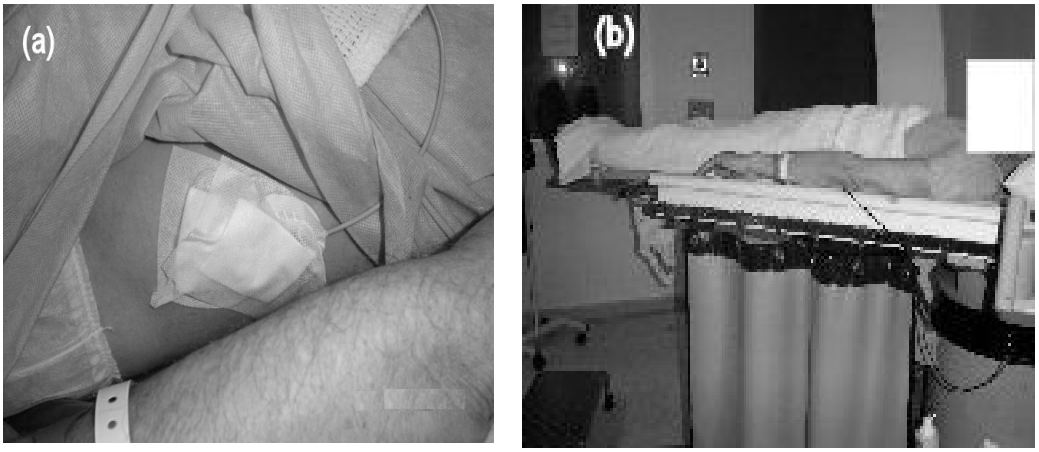

Figure 7.16: Positioning of the prototype sensor during the clinical tests at Guy's hospital (London): (a) the sensor is fixed on the patient torso using Elastoplast. (b) The same patient is shown with the sensor in place during acquisition.

7.4.2 Data acquisition and analysis

This trial, as explained in section 7.4, was divided into five stages and each stage was characterised by a different configuration of the module of data acquisition and analysis. Figure 7.17 shows, for generalisation, a scheme that includes all the elements of this module, even if such a configuration was used only in the last stage of the trial (Stage V).

The acoustic signal was acquired by one of the three prototype ultrasound sensors developed in collaboration with PAL and supervisors (Figure 7.17(a)). In the first three stages of the trial the signal was then directly transferred to the module of A/D conversion, a TiePie Handiscope 3 operating at a sampling frequency of 5MHz (Figure 7.17(d)). The oscilloscope was triggered by the electrical signal emitted by the EM at each shock (Figure 7.18(a)). The digital signal was sent to a laptop (Figure 7.17(e)) via a USB connection.

The TiePie digital oscilloscope was chosen among other available A/D modules essentially for its portability and the ability to operate without an external power supply. The latter feature ensured that the system could easily satisfy the electrical requirements of medical devices of class BF (according to the classification of the International Electrotechnical Commission), i.e. devices with floating parts applied to a patient (IEC60601-1), because it was powered such that it could operate using its own battery (20 V). However the whole system of data acquisition was also electrically tested with the laptop operating via the mains. This was done to verify that is was also safe for the patient that the laptop was operated from the mains power supply during prolonged acquisition sessions.

Any background noise present in the acquired signals was eliminated before any data processing by means of digital filtering (see Subsection 7.3.3).

In the last two stages of the trial the signal was filtered before digitalisation by an analogue high-pass filter[24] (Figure 7.17(c))with a cut-off frequency of about 300 kHz. (292 kHz). In

[24] See Section 7.3.3, for details on the filter

the final stage preamplification[25] was also added to the signal conditioning (Figure 7.17(b)) to further increase the SNR.

Sets of 30 consecutive traces were recorded at different stages of a treatment exploiting the interface of the TiePie oscilloscope (Figure 7.17(f)) and subsequently analysed off-line using MATLAB™. Subsection 7.4.3 describes the protocol that was designed for this non-continuous data acquisition.

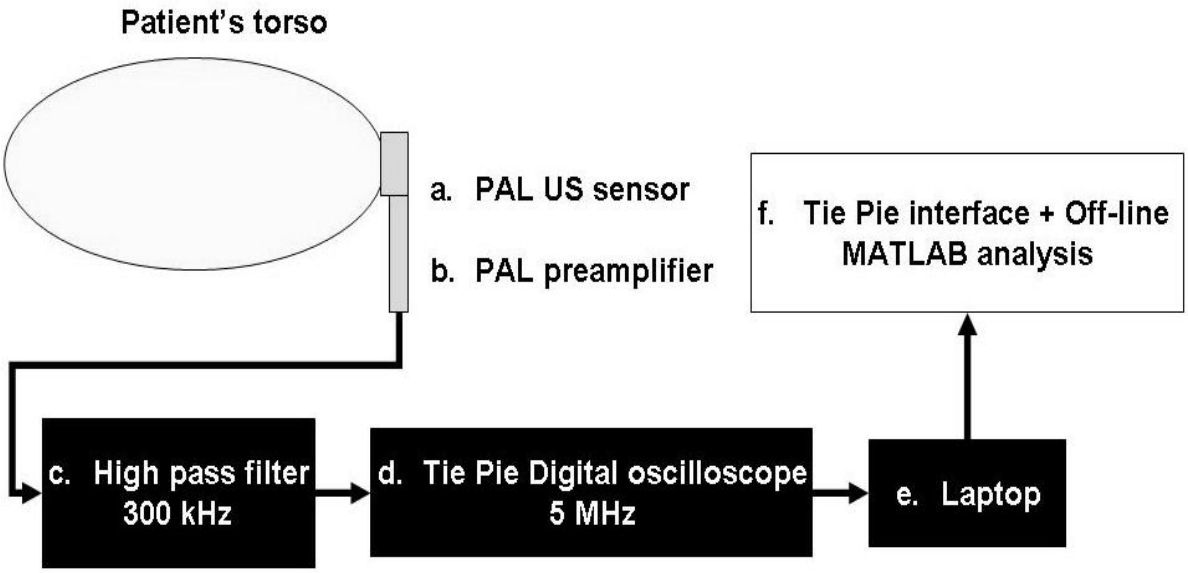

Figure 7.17: Schematic representation of the data collection and analysis during the first trial of the system *in vivo*. The scheme shows the final configuration that was used only in stage V (as defined in Figure 7.14). In the other stages either (b) the PAL preamplifier was missing (Stages I-IV) or (c) the analogue filter was absent and digital filtering was used (Stages I-III).

[25] See subsection 7.3.2 for details on the preamplifier

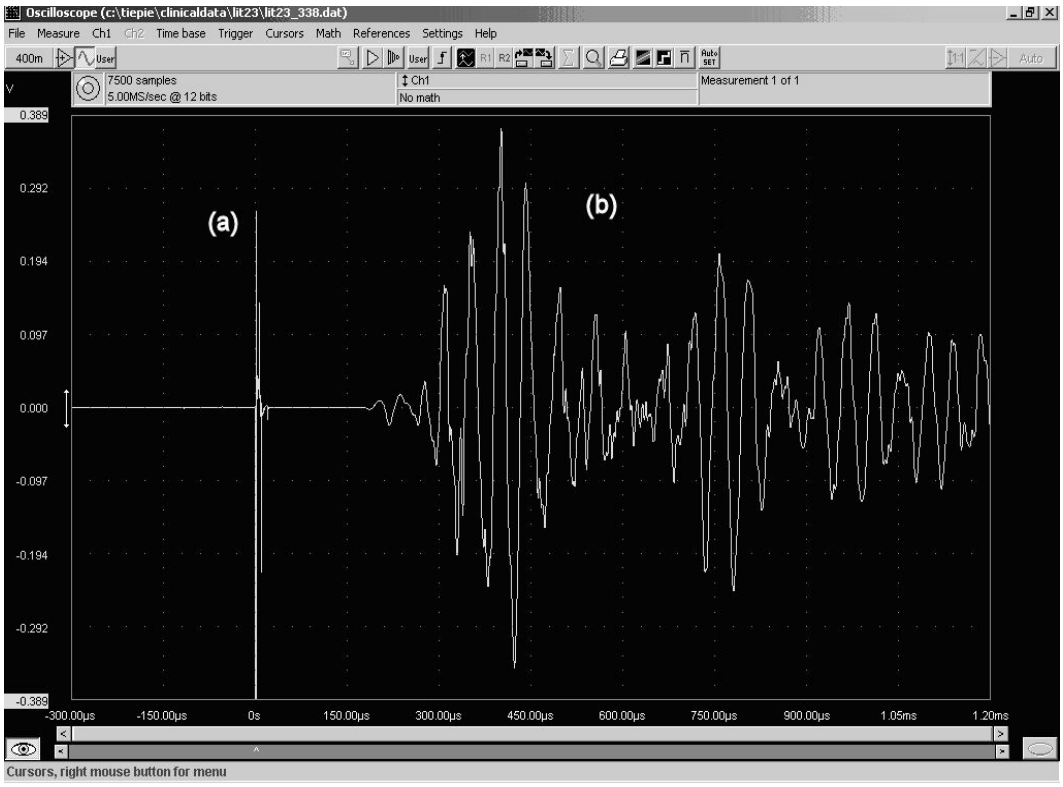

Figure 7.18: Example of a raw signal recorded *in vivo*, where (a) is the electrical triggering-signal and (b) is the acoustic signal. This signal was acquired in Stage II (Figure 7.14) with the prototype Mark III.

7.4.3 The protocol for data acquisition via TiePie interface

Sets of at least 30 consecutive traces were recorded at different stages of the treatment. The measurement protocol was developed during the course of the preliminary clinical trials themselves, taking into account the procedure characteristics and some technical issues. These are described below.

The first aspect of the procedure that was taken into consideration was that the lithotripter operator generally used up to 200 shocks gradually to increase the energy level of the machine from 1 to the desired level for the treated patient. The operator then kept the level stable for the rest of the treatment (except for a few interruptions for monitoring), which lasted 2000-3000 shocks. As explained in Chapter 3 and Chapter 6, the energy level influences the characteristics of the acoustic emissions. The objective of the study was to identify variations in the emissions linked exclusively to the targeting and fragmentation of the stone. Therefore it was decided to start the data acquisition once a stable energy level was reached.

A second constraint was imposed by the structure of the TiePie interface and, in particular, by the size of the saved data. The oscilloscope interface saved for each trace acquired three files of the total size of about 500 kB. The highest size of record per day compatible with the storage devices available at the time was 1 GB. The assumption was made that up to 8 treatments would be undertaken in a given day. Consequently, it was chosen to acquire 10 sets of 30 traces per treatment, spread across the duration of the treatment. That is to say, the acquisition would be started at 200 shocks and carried out every 300 shocks, with the last set of a given patient starting at 2900 shocks.

Figure 7.19 displays an example of the datasheet used for recording data from each treatment during this first stage of clinical trial. Patient data are covered by the Data Protection Act and cannot be disclosed. Therefore the data in the example are fictitious but verisimilar, and do not refer to any real patient. Each treatment was identified by a *Treatment ID*, which was an

alpha-numerical code starting with the letters *Lit.* The datasheet also contained a section to note all the treatment details. These were the patient personal data *Name*, *Surname*, Date of birth (*DOB*), *Weight*, *Height*. These anagraphical details were followed by information concerning the treatment, such as the *Date,* any eventual information on the *Stone* (such as presence of single or multiple stones or the size of the stone), the stone location (*Site*) and the total number of *Shock*s administered to the patient during the treatment.

Following this section with the details of the treatment, there was the data acquisition section which specified the acquisition channel (1 or 2) and the details of the different data sets recorded. For each set, note was taken of the number of *Shocks* already administered at the start of the set*,* the identification numbers of the records saved for that set (*Records*) and the number of shocks delivered for minute (*Freq*). There was also a section available to record eventual *Comments* (the most common was information about re-targeting) and the energy *Level* of the Storz EM source used when the set was recorded. The form also had a *Treatment Output* box, available to record the first impression on the treatment of the radiographer operating the lithotripter.

TREATMENT ID	NAME	SURNAME	HOSPITAL No	DOB	DATE
Lit999	John	Smith	1234567X	09/09/1909	25/12/2004
SITE	**STONE**	**WEIGHT**	**HEIGHT**	**TOT SHOCKS**	**CHAN**
Right Kidney	single	78 Kg	180 cm	3000	(1) 2
SCHOCKS	**RECORDS**		**FREQ**	**COMMENTS**	**LEVEL**
200	1-30		120		4
500	31-60		120		4
800	61-90		120	Retargeting	4
1100	91-120		120		4
1400	121-150		120	Retargeting	4
1700	151-180		120		4
2000	181-210		120		4
2300	211-240		120		4
2600	241-270		120		4
2900	271-300		120		4
TREATMENT OUTPUT	Stone looks less dense than when started				

Figure 7.19: Example of a datasheet used for recording data non-continuously during the first clinical trial of the prototype ultrasound system. *Treatment ID* indicates an alpha-numerical code identifying the treatment. This is followed by the anagraphical details of the patient *Name*, *Surname*, Date of birth (*DOB*), *Weight*, *Height* and the treatment *Date.* There are sections to take note of the kind of *Stone* treated (if the information is available) and its location (*Site*). These are followed by a note of the number of *Shock*s administered to the patient during the treatment and the channel of the oscilloscope used (1 or 2). This preliminary information is followed by details on the saved data. For each set of consecutive traces recorded are reported the number of *Shocks* already administered to the patient at the start of the set, the identification numbers of the *Records* saved for that set and the number of shock delivered for minute (*Freq*) and the energy Level setting of the Storz EM source during recording. A final box is for taking note of the first opinion on the treatment of the radiologist operating the lithotripter. The data in this example are fictitious but verisimilar to comply with the Data Protection Act.

7.4.4 Preliminary results *in vivo*

The first four stages of this clinical experimentation which included 45 patients were, as explained at the beginning of section 7.4, mainly devoted to the optimisation of the features of the module of data acquisition and conditioning. The final configuration was tested on a further 6 patients. The data recorded from these patients confirmed the potential, predicted *in vitro* of the main secondary acoustic emissions features[26] (m_1, m_2, m_2/m_1 and t_c) to distinguish between treatments that failed and treatments that caused some stone breakage. Table 7.2 reports for each treatment both the follow-up assessment carried out by the urologist at 2-3 weeks and the first opinion of the radiographer at the end of the treatment. The specific fragmentation was not estimated for any patient at this stage, which only aimed at detecting any stone breakage. Therefore the two columns show either a 'B', where breakage was assessed (or supposed in the case of the first opinion), or a 'NB' for failures. In one case (*LitD*), the resolution of the X-ray fluoroscopy was not adequate to let the radiographer formulate a first opinion. In this case the opinion is expressed as 'N/A' for not available. It can be observed that the two opinions did not always agree, which is another consequence of the limited resolution of the lithotripter imaging systems.

Table 7.2 also reports the main characteristics of the emissions. Treatments that showed some stone breakage (Table 7.2, *LitA* and *LitE*) were characterised by a combination of higher collapse times t_c (at least 170 μs) and higher fragmentation indices m_2/m_1 (0.72 and 0.43 respectively). These results were consistent with those of the *in vitro* experiments, which showed that long collapse times were an indication of good targeting (see Subsection 6.2.4). As explained in subsection 3.2.1 collapse times measured *in vivo* (Table 7.2) are shorter than those measured *in vitro* (about 200 μs in average). Therefore the analogy between the two configurations is limited to the expectancy of a shorter collapse time in case of mistargeted stones. This situation is more likely to occur for treatments that failed, even if, as often mentioned in this thesis, targeting is not the only factor affecting a treatment.

[26] See Section 5.2 for a definition of the features and Chapter 6 for an analysis of the performances of these parameters *in vitro*.

That is to say, a stone can be well on target during a whole treatment but still not break because it is too hard.

In contrast, the values assumed by the fragmentation index m_2/m_1 in those treatments that showed some success (Table 7.2, *LitA* and *LitE*) were the same as those shown by stone phantoms at a fragmentation grade *F* of at least 30% (see subsection 7.3.4). This index was clearly lower for the other treatments.

Experimentation *in vitro* had also showed some correlation between m_1, m_2 and t_c and the fragmentation stage (see Section 6.3). Therefore it was examined whether the variations in these parameters showed any particular trend in the course of each treatment. This was done by correlating the initial shock number of the 10 stages examined per patient with the average values of the parameters at that stage. The best linear fitting of the points present in each of the three relative scattered graphs was calculated and the variation of each parameters per shock was estimated from this fitting. These estimates ($\Delta m_1/\Delta shock$, $\Delta m_2/\Delta shock$, $\Delta t_c/\Delta shock$) are also reported in Table 7.2. In accordance with *in vitro* experiments, most of the failed treatments showed null or small negative trends in m_2. However there was no substantial difference between the behaviour in the trends of m_1 and t_c for the two sets of treatments ('B' or 'NB').

The number of patients participating in the fifth stage was not large enough to draw any statistically significant conclusions on the reliability of the system in differentiating between the two classes of treatments. However it was useful to gather information on the features of data collected *in vivo* that was used to develop a MATLAB™ interface which allowed on line analysis of the data. The maximum amplitude of the acoustic emissions (m_1) ranged from 70 mV to 477 mV and these emissions showed a delay from the electrical triggering signal (Table 7.2, *Delay*) that varied from a minimum of 257 μs to a maximum of 310 μs.

The interface will be described in the following subsection.

ID	*Delay* [μs]	m_1 [mV]	m_2/m_1	t_c [μs]	$\Delta m_1/\Delta shock$ [mV/shock]	$\Delta m_2/\Delta shock$ [mV/shock]	$\Delta t_c/\Delta shock$ [μs/shock]	X-ray assessment	First Opinion
LitA	283	70	0.72	170	0.00	0.00	0.02	B	B
LitB	280	78	0.37	165	0.00	0.00	0.01	NB	B
LitC	310	356	0	0	0.02	N/A	N/A	NB	NB
LitD	276	145	0.25	320	0.00	0.00	0.02	NB	N/A
LitE	287	267	0.43	204	0.03	0.01	0.01	B	B
LitF	257	477	0.22	228	-0.02	-0.01	-0.01	NB	NB

Table 7.2: This table summarizes the preliminary results *in vivo* on a set 6 treatments. Each treatment is identified by an alpha-numerical *ID*. The *Delay* between the electrical and acoustic signal is reported for each treatment. This is followed by the values assumed by the main emission features. These are the maximum amplitude of the acoustic signal m_1 over the whole treatment, the average fragmentation index m_2/m_1 and the average collapse time t_c. The table also reports the slopes of eventual trends in m_1, m_2 and t_c with the shock number. These are followed by the urologist's assessment of the treatment based on the comparison of X-rays before and after treatment. This assessment is indicated as a 'B' for breaking, in the case of stone fragmenting. In the other cases it is classified as NB for not breaking. This assessment is compared with the *First opinion* of the radiographer operating the lithotripter. This could not be formulated in one case because of the limited resolution of the X-ray fluoroscopy system. Whenever one of the fields listed in the table was not available or could not be estimated it is indicated as 'N/A', for not available.

7.4.5 The first version of the SEAC software interface

Once EPSRC follow-up funds were available (EP/D503310/1), the knowledge of the characteristics of the signals *in vivo* derived from the preliminary experimentation[27] was exploited to design a dedicated MATLAB™ interface. This interface had to be able to display on-line the results of the processing, and at the same time save both these results and the collected raw data into MATLAB™ data files (.mat files).

It has to be clarified that, whilst the processing modules of the final software are an essential part of the original contributions of this work[28], the interface was developed in collaboration with Dr Antonio De Stefano (St Mary's Hospital, Portsmouth). Dr De Stefano is an expert in designing interfacing software.

A first version of this interface displayed the acquired signal (Figure 7.20, bottom left box) and two of the main parameters extracted from the secondary emissions m_1 and t_c (Figure 7.20, respectively blue dots and green crosses in the bottom right box). Both emission features, as explained in Chapter 6, were linked to targeting and fragmentation to some extent. However the collapse time t_c was more sensitive than the former feature to movements of the stone off-axis (see Subsection 6.2.4).

Besides providing a visual feedback, the interface also included four other sections that are described below.

1. A section containing the treatment details (Figure 7.20(a)). These were:

   - *Treatment ID*, a unique integer number that was associated to a specific treatment.
   - *Date*, the date of the examined treatment.

[27] See Subsection 7.4.4 for a summary of these results.
[28] See Section 5.2 for a description of the signal processing made by the SEAC software and Appendix A for a description of the structure of the algorithm.

The patient's details were omitted and saved in a separate electronic database to comply with the Data Protection Act. That is to say, this precaution ensured that data analysed off-line could not be associated with any specific patient. The patients' database will be described in the following subsection.

2. A Set-up section (Figure 7.20(b)) to control the settings of the TiePie oscilloscope:

- *Trigger Channel*, the channel on which the signal to trigger the oscilloscope was acquired. This was set as default to Channel 1, which was normally used for both triggering and acquisition. The signal used for triggering was the electrical signal emitted by the lithotripter EM source.
- *Acquisition Channel*, the channel of the oscilloscope on which the acquisition was made. This was also set to Channel 1 by default but could be changed to Channel 2.
- *Trigger level*, a slider that controlled the trigger level of the oscilloscope and could assume any value between 0 μV and 1V. This level was set to the default of 50 μV.
- *Trigger Hyst*, another slider to control the triggering that could assume any value between 1 mV and 100mV. The default hysteresis was 50 mV.
- *Range (Full Scale)*, the full scale sensitivity of the scope. This could assume several values in the range from 200 mV to 80000 mV. The most used setting was the default one (200 mV), followed by 500 mV for a few patients, and 10000 mV, which was used for a couple of patients.
- *Capture 1 out every,* a command that gave the operator the option to record only one acoustic signal every so many shocks. This control was introduced to reduce the size of the saved files. However the value that

was used for all the patients who participated in the trial was 1 (see Section 7.5 for details on the clinical trial).

Section (2) included also included two additional settings:

- *Source Power Level*, a pop-down menu that allowed selecting the power level of the lithotripter at the time of recording (1 to 9). This was set to the minimum level as default. This information was saved in the header of the data files and would be useful in the phase of the analysis and follow-up of the treatments.
- *Analysis Start Time,* a control slider that allowed the operator to choose the starting time for the analysis. On the basis of the preliminary experiments *in vivo*[29] this starting time, which corresponded to the delay between the electrical triggering and the acoustic signal, was set to a default value of 200 μs. However it could be changed to any delay between 0 μs and 500 μs to suit the characteristics of the recorded signal. This information was necessary because otherwise the analysis software[30] would fail as it would interpret the electrical spike (higher than 2V) as the maximum amplitude of the first burst m_1.

3. A block of digital filters (Figure 7.20(c)) was introduced to give the operator either the option to select specific frequency bands or improve the signal to noise ratio. As default the digital filtering was disabled and to be used it needed to be enabled by ticking the option *Enable Filtering*. Three filters were available:

   - *High Pass,* a Butterworth high pass filter of the 4th order with a cut-off frequency at 3dB of 300 kHz.

[29] See Subsection 7.4.4
[30] See Section 5.2 for details on the analysis of the acoustic emissions and, in particular, on the adaptive detection of the two bursts.

- *Band Pass*, a Butterworth band pass filter of the 4th order with cut-off frequencies at 3dB of 30 kHz and 300 kHz respectively.
- *Low Pass,* a Butterworth high pass filter of the 4th order with a cut-off frequency at 3dB of 30 kHz.

Any operation of filtering would be applied twice to a signal (forward and backward). This would compensate for any phase shift introduced by a filter to a signal and would correspond to applying a filter of the 8th order to its spectrum of amplitudes. The filtering option was not enabled for any of the treatments examined in the clinical trial described in the following sections and Chapter 9.

4. A synchronisation section (Figure 7.20(d)) that contained a few utilities to check the synchronisation between the laptop and the oscilloscope and run some tests:

   - *Search Hardware*, instructed MATLAB™ to search for the oscilloscope on the USB port and load its drivers.
   - *Try Connection*, tested the communication between the scope and the interface for a few shocks (10).
   - *Test ON*, allowed the operator to run the software in test mode (i.e. without saving any data). The button was replaced by a *TEST OFF* one (not showed in the figure), once the option was activated. This utility was normally used prior to starting the acquisition in order to check the appropriate settings for a specific treatment.
   - *START*, a command that activated data acquisition. This button once active was replaced by a STOP button (not showed in the figure).

The section also included a counter of the shock number (*Shock Number*). The operator could update manually this number at the start of the acquisition to be the same as that

indicated on the lithotripter counter[31]. Once the acquisition started the number was incremented automatically. Multiple acquisition sessions were possible for a treatment. This option was necessary to avoid recording during stages that, following realignment and repositioning, were at variable energy levels. A normal treatment of 3000 shocks consisted of two-three sessions of about 700-1500 shocks.

The bottom of the control interface had a text box for inserting eventual *Comments* on the treatment; another section displayed the filename where the treatment data would be saved at the end of each acquisition session. Finally, on the bottom right corner there is an *EXIT* button which could be used to exit the program at any time.

The on-line diagnostic software was named SEAC (Secondary Emissions Analysis in Clinic). This first version was tested on a set of 30 patients. That is to say the main features extracted from the software m_1, m_2 and t_c were compared against the patients' treatment outcome. The gold standard method used to assess these outcomes was the follow-up examination of patients X-rays by the urologists. This was done to verify whether the system could discriminate between treatments with a significant fragmentation (at least 50%) indicated as *successful* treatments and the other *unsuccessful* treatments. This first training stage will be described in Chapter 8.

[31] This initial shock number, as explained in subsection 7.4.3, was 200 or higher. It all depended on when was reached a stable operating energy level for the lithotripter.

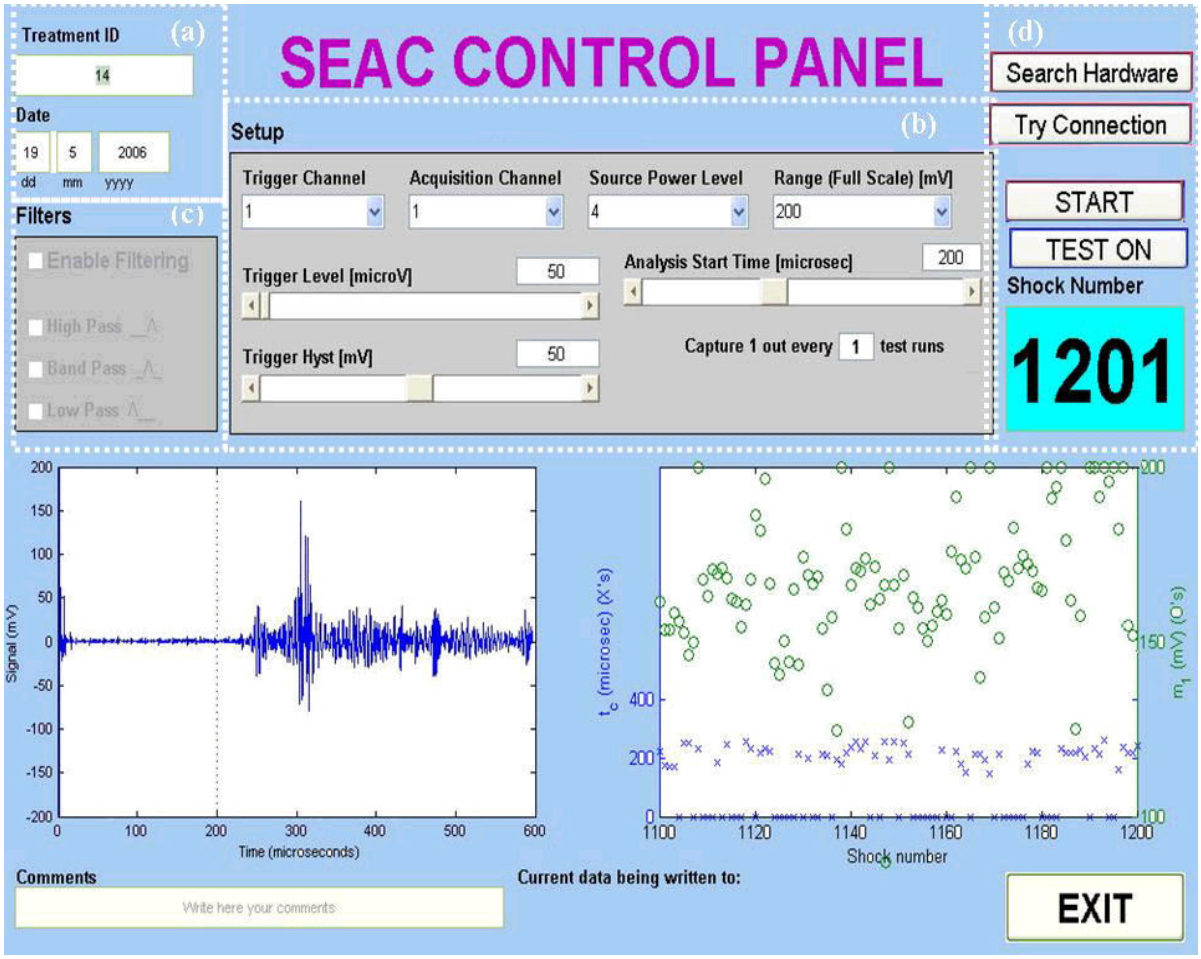

Figure 7.20: First version of the developed SEAC MATLAB™ interface for on-line monitoring. The white dotted boxes identify 4 different control panels, (a) is a section where the treatment details are inserted (*Treatment ID* and *Date*). Panel (b) hosts the controls for the scope data acquisition. Panel (c) shows some optional filtering options (that normally are not used). Panel (d) presents some controls of the synchronisation between the software and hardware (*Search Hardware*, *Try Connection*). A test facility (*Test ON*) consents to run the program without saving any data and a button *Start* activates the acquisition. The bottom left box displays the raw signal being collected and the bottom right box shows the two parameters m_1 (green dots) and t_c (blue crosses) being calculated for each shock. Further down there are a *Comment*s box, that is for the operator to introduce eventual comments on the treatment, a Section that displays where data are saved at the end of each session, and an *EXIT* button to quit the program.

7.4.6 The Database of the patients' treatments

A Microsoft Access electronic database containing the details of the recorded treatments and the patients participating in the project was developed. In order to avoid loss of data, a hard copy of the information was stored in a logbook.

The database (Figure 7.21) was organised in three sections described below.

1. TREATMENT DETAILS, a section that could be used to insert the treatment information:

- *ID*, a unique identifier for the treatment. This was the same as that entered for the specific treatment in the acquisition interface (see Figure 7.20).
- *DATE*, the treatment date.
- *TOT SHOCKS*, the total number of shocks administered during the treatment.
- *STONE SITE*, an indication of the location of the treated kidney. This could be chosen from left kidney (LK), right kidney (RK) and urethra (UR). However only renal stones where considered in the trials analysed in this thesis.
- *TS*1, a first treatment score (TS_1) that could assume any value between 0 and 5. This score was assigned by the radiographer operating the lithotripter. It will be described in details in subsection 8.3.
- *SCL1*, a confidence level associated with TS_1. This level could be low (L), medium (M) or high (H).
- *TS2*, a second treatment score (TS_2) that could assume any value between 0 and 5. This score was assigned by the urologist when performing the follow-up of the patients. It will be described in details in subsection 8.3.
- *SCL2,* a confidence level associated to TS_1. This level could be low (L), medium (M) or high (H).
- *DATE* (*TS2*), the date of the follow-up X-ray. This occurred, on average, three weeks after the treatment.

2. PATIENT DETAILS, a section that was used to record all the useful information regarding the patient:

   - *SURNAME*, the family name.
   - *NAME*, the first name.
   - *DOB*, the date of birth.
   - *HOSPITAL No*, the patient's hospital number
   - *HEIGHT* (*cm*), the height of the patient in cm.
   - *WEIGHT* (*kg*), the weight of the patient in kg.

   The patient's information was used for the follow-up assessment and to derive some statistics.

3. COMMENTS, a section that allowed writing in any comments about the treatment. During the trials described in these last Chapters of this work, this section was mainly used to add information about the treated stone. In particular, it was exploited to specify if a treatment involved a single stone or multiple stones.

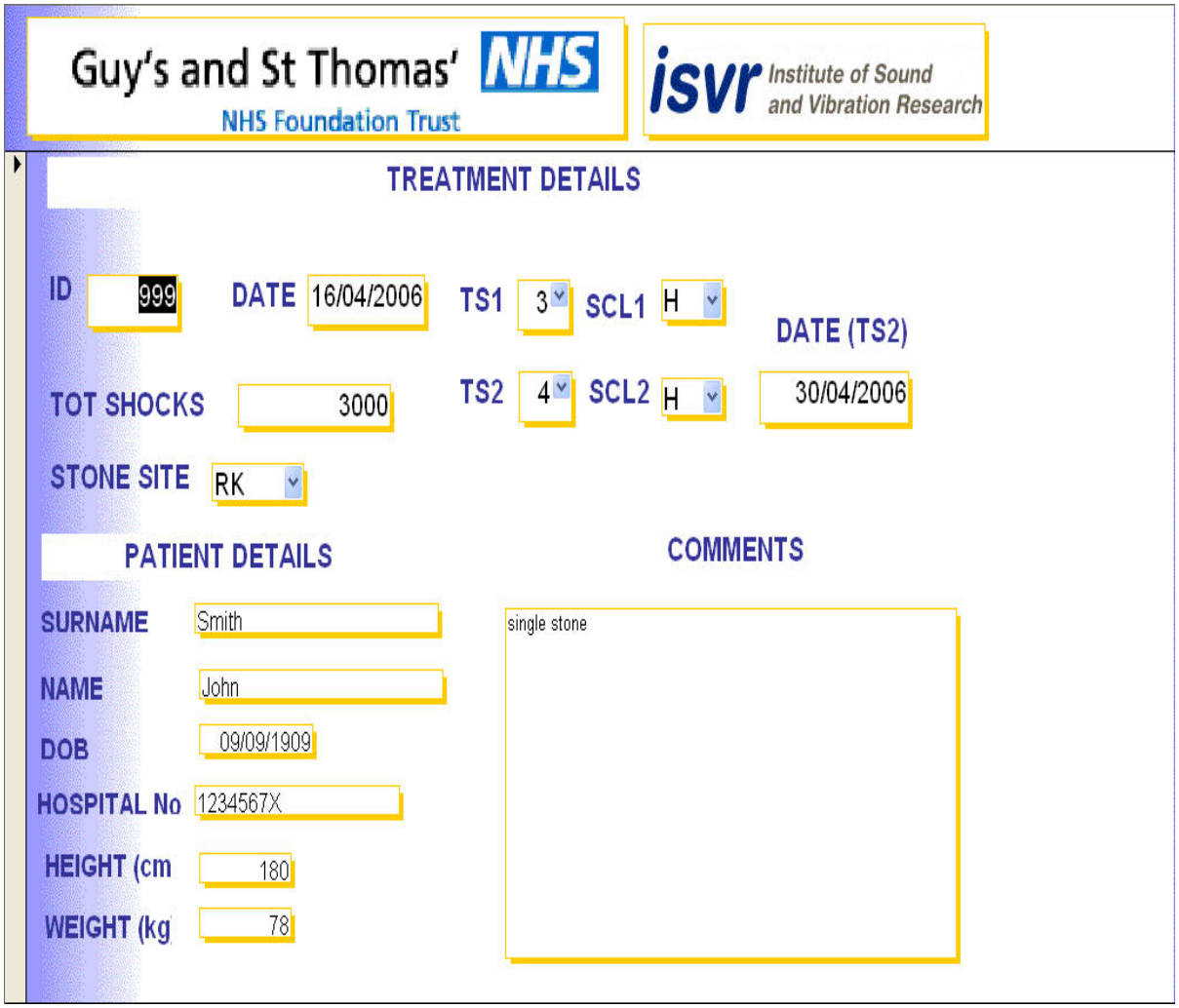

Figure 7.21: Example of a hypothetical record in the Treatments Database. The data in this example are fictitious but verisimilar to comply with the Data Protection Act.

7.5 Summary

Previous Chapter 6 showed that it was possible to extract information about the quality of an ESWL treatment, i.e. stone targeting (see Subsection 6.2.4) and fragmentation (see Subsection 6.3), from secondary acoustic emissions collected by means of a broadband non focused ultrasound sensor, developed by the National Physical Laboratory for commercial applications.

This Chapter has described the exploitation of that preliminary knowledge to develop a prototype passive ultrasound diagnostic system. The development was divided into two stages.

The first stage was devoted to the design of the module of signal acquisition and conditioning. This was done in collaboration with Precision Acoustics Ltd. The acquisition sensor (Subsection 7.3.1) was specifically designed to be safe in terms of both electrical safety and infection control. The sensor shape and weight were also engineered so that the sensor would be comfortable when applied to the patient. The sensor was directly coupled to a commercial PAL preamplifier (Subsection 7.3.2). This was done in order that good SNR (at least 50%) could be obtained from patients who were overweight (BMI>25). In addition, high pass filtering was introduced to remove the background noise and enhance the secondary emissions cavitation components (Subsection 7.3.3). Preliminary tests of the module *in vitro* (Subsection 7.3.4) showed the system was able to give signals containing information about the quality of the treatment, as well as the NPL sensor.

Once ethical approval was obtained, the signal acquisition and conditioning module was tested *in vivo* on a first set of 51 patients (See subsection 7.4.4). This preliminary clinical trial, which was divided into five stages, confirmed the potential of features of the acoustic emissions to be used as a discriminant between *successful* and *unsuccessful* treatments. The information gathered on clinical emissions was used to develop a first on-line version of the monitoring system. This was done developing an interface that allowed the synchronisation of the data acquisition and processing (Subsection 7.4.5).

Chapter 8 and Chapter 9 will describe, respectively, the first testing phase and second validation phase of the on-line monitoring system *in vivo*, during a clinical that involved 203 patients.

Chapter 8 First clinical trial of the on-line monitoring system

8.1 Introduction

This Chapter reports the first phase of a clinical trial of the on-line monitoring system developed as described in Chapter 7. The aim of this first trial was to test and refine rules derived from *in vitro* studies prior to a second phase of validation of the system [143], which will be reported in Chapter 8. In particular the main features extracted from the acoustic system (m_1, m_2, m_2/m_1 and t_c) were compared against the treatment output, as defined by the three weeks X-Ray follow-up assessment. One hundred and eighteen patients were recruited during this trial, and data from 30 patients were suitable for analysis.

8.2 On-line system training during a clinical trial

The first version of the on-line diagnostic system described in section 7.4.5 was tested on a set of 30 patients (Figure 8.1, Phase 1). In this trial, the system output was compared against the first opinion of the radiographer and the current gold standard assessment of lithotripsy treatments carried out at about three weeks after the treatment. In particular, the main parameters extracted from the emissions m_1, m_2, m_2/m_1 and t_c were compared against these outputs to identify any correlation [143].

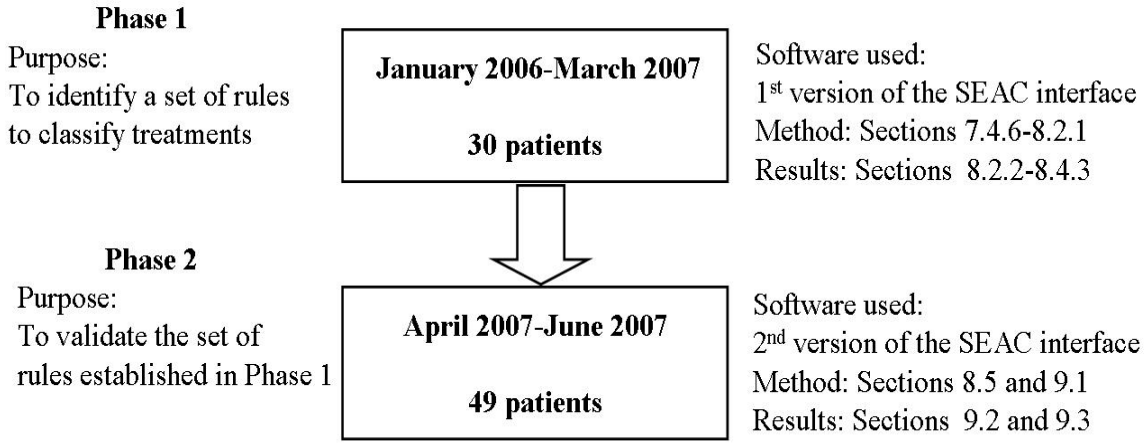

Figure 8.1: The two phases of the clinical trial of the SEAC diagnostic system. The diagram indicates the purpose of each stage, the number of patients participating and the sections of these thesis that deal with a specific stage.

The set-up used for this trial is similar to that described in subsection 7.4.2. The main difference is that the TiePie oscilloscope interface was replaced by the SEAC interface described in subsection 7.4.5. As a consequence also the treatment protocol differed. The main principle was still the same, namely to record only those sessions at stabilised energy levels. However the new interface allowed the storage of all the data in any of these sessions. This was because of the different file format used (.mat)[32], which was more efficient in terms of memory occupied [33] and also because of a more powerful laptop with a bigger hardisk[34].

[32] See subsection 7.4.5.
[33] The memory occupied was about 30 MB for 2500 shocks vs. 0.5 MB per shock for the TiePie format.
[34] The hardisk of the new laptop was 50 GB, the hardisk of the old laptop was only 1 GB.

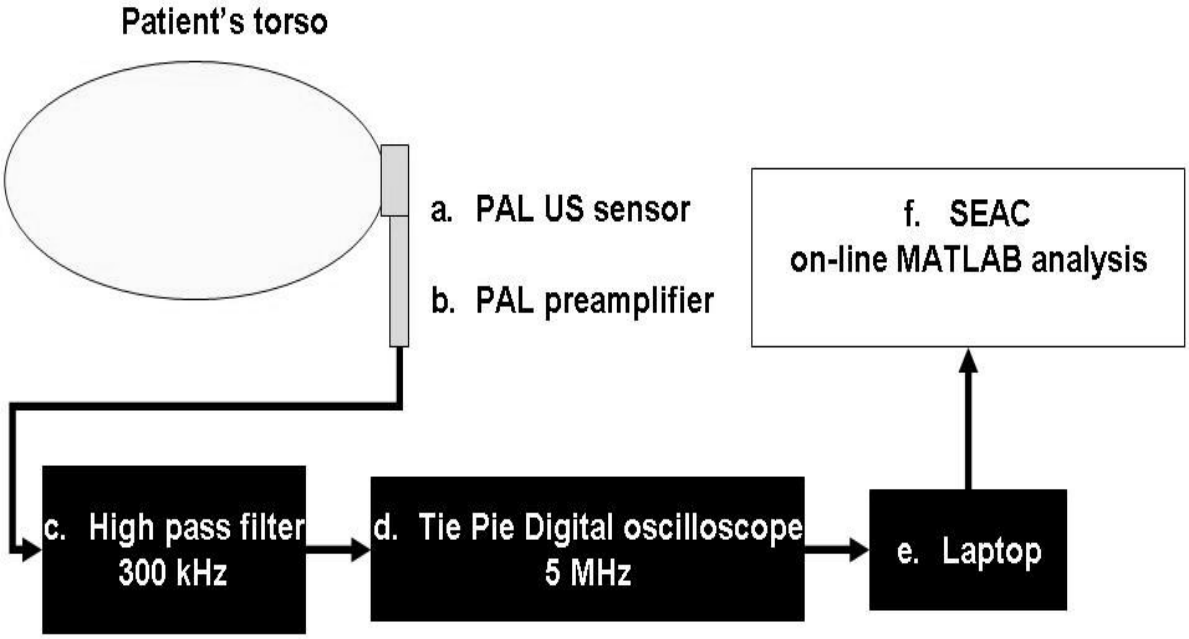

Figure 8.2: Schematic representation of the data collection and analysis during the training stage of the clinical system.

A score system from 0 to 5 was used to quantify the clinician assessments. The two corresponding treatment scores will be described in the following subsection.

Phase 1 trial was used to finalise the laws upon which the system would discriminate between different treatment outcomes. This stage lasted 15 months, from January 2006 to March 2007, for a total of 92 days spent in the clinic. The total number of patients that consented to take part in the trial was 118. However, as mentioned, only 30 subjects could be used for the analysis. The high recruitment attrition rate reflected a relatively high incidence of equipment failure early on in the study as well as administrative difficulties in getting X-rays reported. This is examined in more detail in Appendix B, which reports a summary of the statistics of both phases of the trial.

The age of the patients taking part in Phase 1 was 54±18 years (average ±1 standard deviations). Eighty percent of patients were male and 20% were female. The ratio between the two male/female subpopulations is normal, as it is mainly men that are affected by kidney stones [8]. The patients had an average of 2473±602 shocks administered during treatment using the Storz Modulith. Energy settings from 1 to 6 were used.

Subsections 8.4 to 8.4.3 report the results of the comparative analysis of the data from these 30 patients. The devised diagnostic rules were incorporated into a final version of the software (Section 8.5). The final SEAC software version was then validated on a second set of 49 patients (Figure 8.1, Phase 2). This last validation stage will be described in Chapter 9.

8.3 The treatment follow-up

The treatment follow-up, as explained in the previous sections, was carried out in two stages. The first opinion of the radiographer operating the lithotripter was asked soon after a treatment was completed. This opinion was based on the fluoroscopy and ultrasound images of the lithotripter.

Subsequently, after the patient's follow-up appointment, the treatment assessment was obtained from the urologist. The assessment was based on the comparison of pre-treatment and follow-up X-rays. This was considered to be the 'gold standard' method for treatment assessment since the clinical decision on the need for further treatment was based on it. The ideal time between the treatment and this follow-up assessment would be around 10-15 days after treatment. This is because after this period most fragments would have been passed, but the time would not have been enough for recalcification to form. In practice the real time was dictated by when the patients come back for treatments or follow-up visits. The average time for the 79 treatments examined in the two phases of the trial was 22±21 days (average ± 1 standard deviation). The urologist score was assigned blindly of the treatment score of the radiologist.

Two forms were devised to allow the clinicians to quantify their judgement of the treatment. These provided a six point scale of treatment scores (0-5) based on the degree of stone fragmentation, with '0' indicating no fragmentation, '3' indicating 50% fragmentation and '5' complete fragmentation. The formulation of both scores relied on the quality of either the fluoroscopy or X-rays images available. This quality, also in the case of standard X-ray images, was not always the optimum. As a consequence, the clinicians could not express a clear judgement in a few cases. Therefore the clinicians were requested to associate a score confidence level to each score given. This level could be low, medium or high.

Figure 8.3 and Figure 8.4 show examples of the form used to assign, respectively, the first treatment score (TS_1) and the second follow-up treatment score (TS_2). The data reported in the two examples are verisimilar but fictitious. Both forms are characterised by four sections. A header contained the treatment unique identification number (*ID*), the patient identification number (*Hospital No*) and the date (*Date*) when the score was assigned. This date was the treatment date for TS_1 and the date of the follow-up X-ray for TS_2. The header also had a box for the signature of the clinician assigning the score.

On the left of each form was a multi-selection section containing the 6 scores (0-5) and a brief description of each point. This section differed in the two cases. In the case of TS_1 each point was related with a qualitative change in the fluoroscopy screen shot. In the case of TS_2 each point was related to an estimate of the stone fragmentation which happened between the pre-treatment and follow-up X-ray. A sketch was used to represent the grade of fragmentation. In the case of a TS_2 equal to 3, for example, a stone half the size of the initial one is showed in the follow-up column.

On the right of both forms there was a section that asked for indication of single or multiple stones. In the case of multiple stones the clinician was also requested to indicate the site of the stone treated, and the number of stones that were in the focal area. This is because in most cases, even if a patient presented multiple stones, these were distant enough that only one stone would have been in the focal area[13]. On the contrary in a few cases some stones were treated at the same time. In those few cases the assessment on fragmentation had to be done considering the variation in the mass of the whole stone set treated.

Finally on the bottom left both forms had a multiple choice section to assign a score confidence level (respectively SCL_1 and SCL_2) to the score. In all the ambiguous cases, when the X-ray images were not very clear (SCL low), two independent experts were requested to assign a TS_2. Except in the case of two patients, where zero fragmentation was assessed consistently by both experts, treatments with TS_2 low were discarded from the analysis.

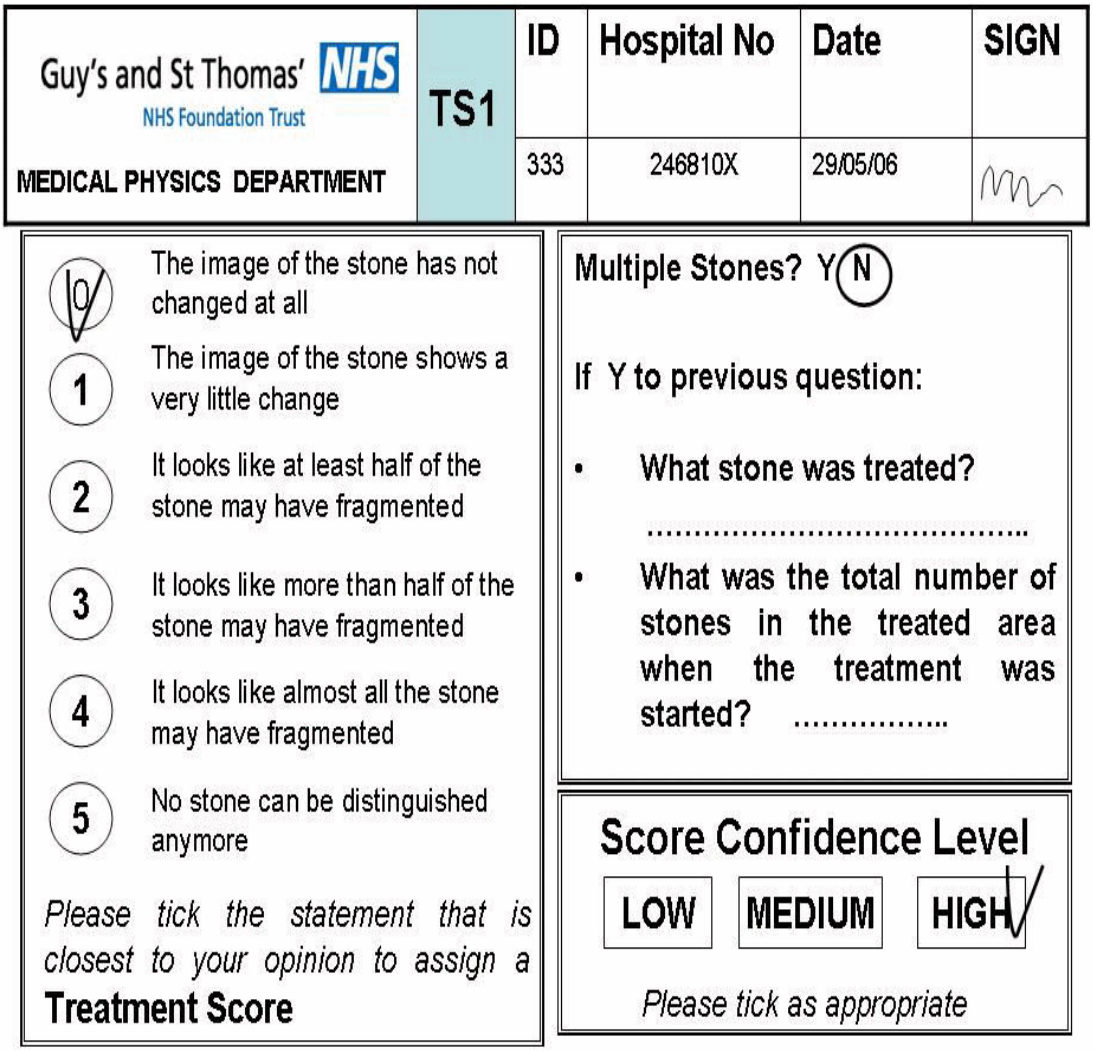

Figure 8.3: Form used by the radiographer at the end of a treatment to assign the Treatment Score (TS_1), with an example of evaluation of a treatment with no apparent effect on the stone size. The form asks for treatment details, *ID* and *DATE*. This information is the same saved by the SEAC software (see Subsection 7.4.5). The patient Hospital number is also requested. This was done to be sure that the assessment was done on the right patient. The form also requires a feedback on whether the patient presented single or multiple stones. In case of multiple stones the assessor is also asked to indicate on which stone treatment and assessment were performed. Moreover the specification of the number of stones in the treatment area is requested. The form needs to be completed with the signature of the radiographer who performs the assessment (*SIGN*). Please note that the data used in this example are verisimilar but fictitious. In particular the signature in the SIGN box is also invented.

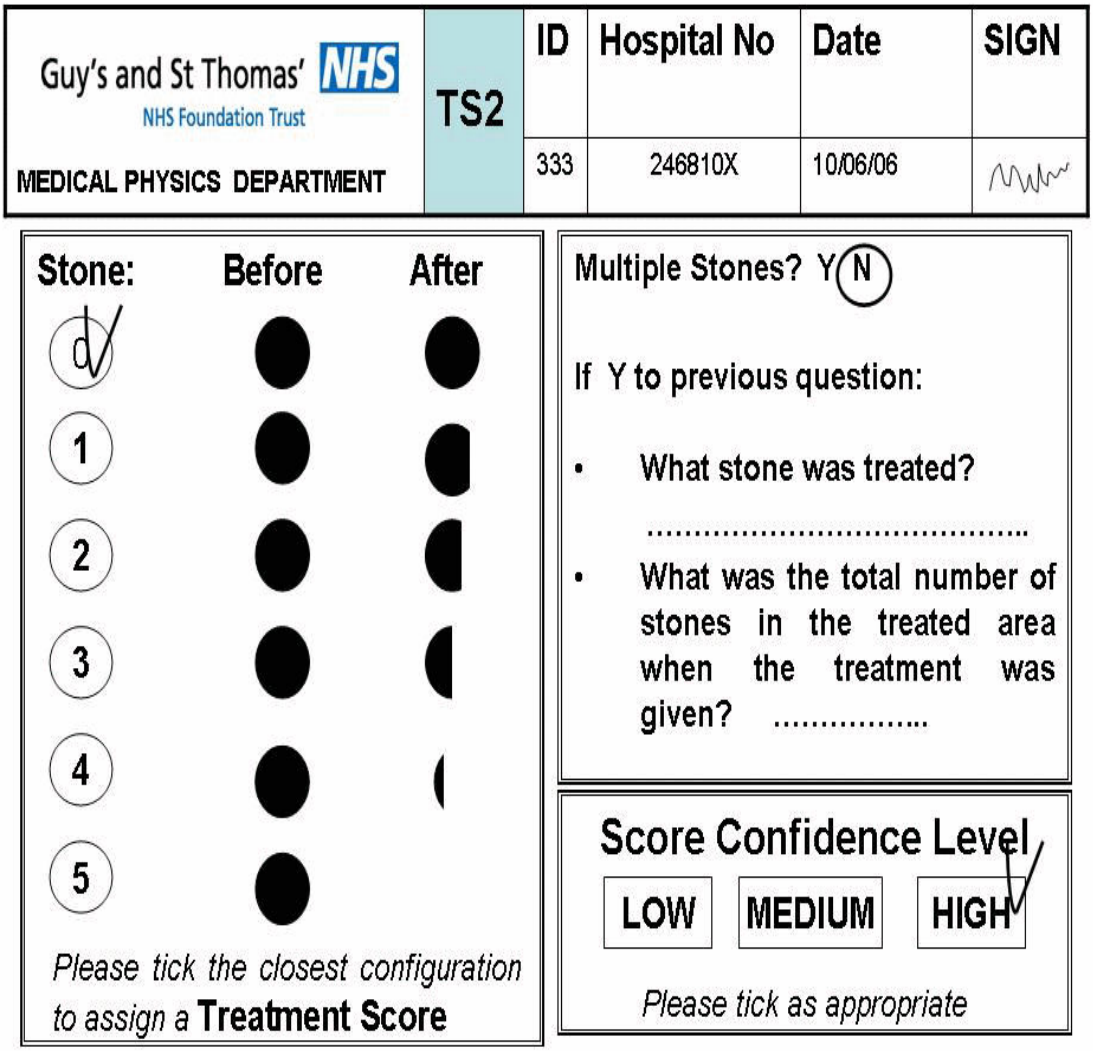

Figure 8.4: Form used by the urologist after the patient's follow-up visit to assign the treatment score (TS_2), with an example of evaluation of a treatment with no apparent effect on the stone size. The form asks for the treatment identification number *ID*. This number is the same saved by the SEAC software (see Subsection 7.4.5). The form also asks for the *DATE* of the follow-up X-ray used for the assessment. This date is also recorded in the patients' treatments database (see Subsection 7.4.6).The patient Hospital number is also requested. This was done to be sure that the assessment was done on the right patient. The form also requires a feedback on whether the patient presented single or multiple stones. In case of multiple stones the assessor is also asked to indicate on which stone treatment and assessment were performed. Moreover the specification of the number of stones in the treatment area is requested. The form needs to be completed with the signature of the radiographer who perform the assessment (*SIGN*). Please note that the data used in this example are verisimilar but fictitious. In particular the signature in the SIGN box is also invented.

8.4 Results of the training stage of the clinical trial

The first phenomenon observed from the SEAC on line analysis of patients' treatments was that targeting is influenced by respiration. In particular, ultrasound B-scans of kidney stones performed during treatments showed that stones oscillate around the focal point with respiration. The amplitude of these oscillations depends on the depth of respiration. These oscillations were reflected in the time histories of the maximum amplitude of the first burst m_1 (see Subsection 8.4.1), as that is a feature linked to scattering[35]. For most of the treatments that showed a higher collapse time t_c, indicator of good targeting[36] were characterised by a negligible influence of respiration on the stone position.

No significant trend was observed in the main emission features that could be associated to the treatment outcome as established from the follow-up assessment (see Subsection 8.4.2). This happened also after the time histories of these features were compensated for any influence due to respiration.

However treatments were at least 50% of fragmentation had happened, termed in this work as *successful* treatments, were characterised by (see Subsection 8.4.3):

$$0.4<m_2/m_1<0.8 \text{ and } t_c>100\ \mu s \text{ for at least 50\% of the sampled shocks} \quad (65)$$

These shocks were the ones that discriminated between *successful* (TS_2 at least 3) and *unsuccessful* treatments; they were therefore termed as *effective* shocks. The percentage of effective shocks, that is an estimate of shock efficiency rate, was used as a treatment score (TS_0). The kappa statistic [144] was exploited to establish the threshold TS_0 that best separated the two populations of *successful* and *unsuccessful* treatments. This statistic is widely used for quantifying inter-observer agreement in radiographic interpretations. The

[35] See Section 6.2 and Subsection 6.3.2.
[36] See Subsection 6.3.

threshold of 50% showed a kappa[37] equal to 0.95 (substantial agreement). No particular difference was observed among treatments of the same category. That is to say, in the case of *successful* treatments for example, a treatment with TS_2 equal to 3 did not show features statistically different from a treatment with score TS_2 of 5. The first opinion of the radiologist did not perform as well in distinguishing between the two classes of treatments (kappa = 0.38).

Rule (65) was incorporated in the final version of the SEAC software. Employing this rule the software, described in section 8.5, classifies each shock as *effective* or *ineffective*. Moreover it calculates the treatment score TS_0 at the end of the treatment. The following subsections describe the details of the results summarised in this subsection.

8.4.1 The effect of respiration on the maximum amplitude of the first burst

The maximum amplitude of the first burst m_1, linked to scattering from the stone[35], showed oscillations linked to respiration. These oscillations were caused by the cyclic movement of the stone around the focus caused by the patient's breathing. It was noted that the oscillations were larger in *unsuccessful* treatments. This is because the larger the oscillations the longer is the time the stone is away from the focus [122, 132, 145]. Therefore the smaller is the number of shocks that effectively hit the stone [122, 132, 145]. Figure 8.5 shows as an example in the inset, 5 minutes extracted from a recorded treatment with TS_2 equal to 1. The relative influence of respiration on m_1 was estimated from the parametric spectrum of the trace. An autoregressive (AR) model with 5 poles (i.e. 3 lobes) was used [128]:

$$S_{m_1 m_1}(f) = \frac{a_{r0}^{\,2}}{\left| 1 + \sum_{k=1}^{5} a_{rk} e^{-\frac{j 2\pi f k}{f_S}} \right|^2} \qquad (61)$$

[37] The kappa values were computed exploiting a webtool: http://faculty.vassar.edu/lowry/kappa.html.

where f is the frequency , a_{rk} (k = 0,..5) are the model parameters, and f_S =2 Hz is the sampling frequency. This frequency was estimated considering that a sample of m_1 was available for each shock and that the shocks were given at a rate of 120 per minute.

The analysis was performed for all 30 treatments in the training set. Before performing any AR analysis, the treatments were visually scanned for the presence of any significant oscillation. If these oscillations were present and they lasted at least 33% of the sampled treatment, then the AR regressive analysis was restricted to the portion (tract) of the signal that showed such oscillations. In all the other cases, the analysis was applied to the whole data set. This choice was justified by the fact that, except in a couple of dramatic cases, the respiratory oscillations were present or more significant only in some tracts of the treatment. That is because, as explained before, both the stone targeting and the patient positioning vary during a treatment.

The depth of respiration was estimated as the relative amplitude of the respiratory lobe. That is to say, the spectral lobe centred at respiratory frequencies. Figure 8.5 shows the parametric spectrum of the treatment showed in inset. In the case of this treatment, where 2500 shocks were administered to the patient, the spectrum was calculated on 1233 points, i.e. 49% of the whole treatment. The spectrum presents lobe attributed to respiration at 0.31 Hz (which corresponds to a respiration rate of about 19 breaths/minutes) with relative amplitude of 0.65.

In general, respiration lobes were searched in the range 0.1 Hz-0.85 Hz. A respiratory frequency of 0.1 Hz corresponds to 6 breaths per minutes. Such respiratory rate is possible in a patient sedated or at rest. A respiratory frequency of 0.85 Hz corresponds to 50 breaths per minute, which are not unlikely in an anxious patient. When more than one lobe was present in this range the dominant one was considered.

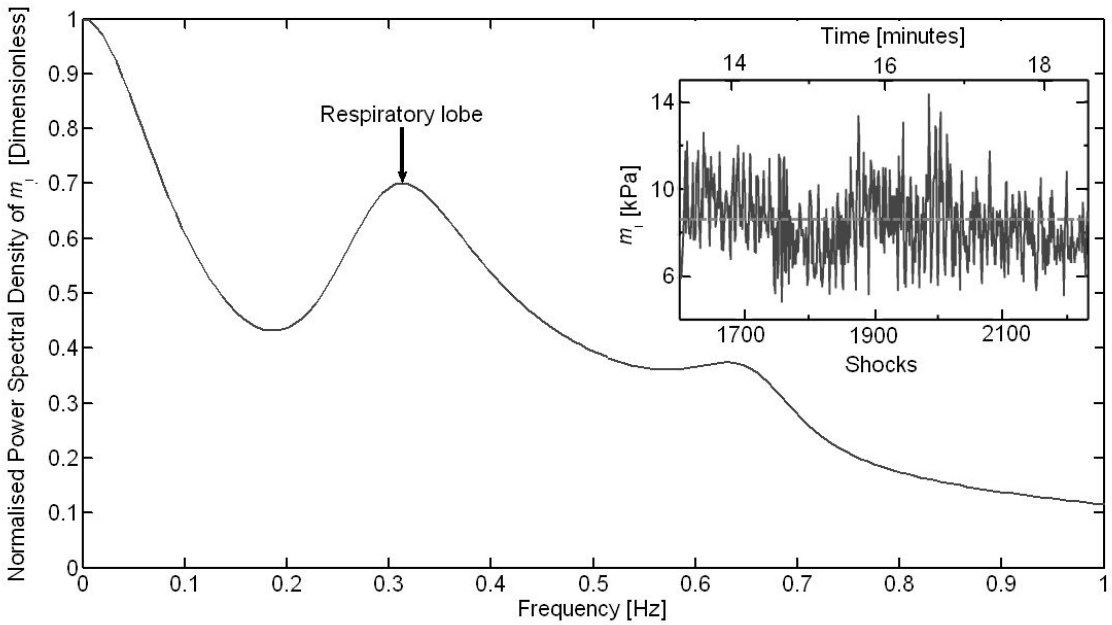

Figure 8.5: Normalised power spectral density of a sample trace of the acoustic feature m_1. The trace of m_1 is shown as an inset. The average value of m_1 is about 8.6 kPa (dotted line). A respiratory lobe occurs in the PSD at about 0.3 Hz. This corresponds with the recorded respiration rate of the patient and suggests that the SEAC system is capable of detecting stone motion caused by respiration. The shocks were administered with a rate of 120 shocks per minute. The PSD was normalised so that the maximum is unit.

The results of this analysis of the influence of respiration on the training set are reported in detail in Table 8.1. Each treatment in the set is identified, for simplicity, by an alpha-numeric code made of the letter T (for training) followed by a sequential number, rather than the treatment identification number. Table 8.1 reports for each treatment the follow-up score (TS_2) and the score confidence level (SCL_2). These are followed by the central frequency of the respiratory lobe (f_R) and the relative amplitude of this lobe. The average collapse time for the whole treatment is also reported. The calculation of this time is explained in subsection 8.4.3. Successful treatments (T_1-T_7) were characterised by a respiration influence lower than 50%. Moreover most of the treatments with a negligible respiration influence (less than 20%) showed higher collapse times (t_c greater than 100 μs, Figure 8.6), which is consistent with better targeting[36].

Treatment	TS_2	SCL_2	f_R [MHz]	Amplitude [dimensionless]	t_c [μs]
T_1	5	H	N/A	0	281
T_2	5	M	0.8	0.07	158
T_3	4	L	0.55	0.11	137
T_4	5	H	N/A	0	171
T_5	5	H	N/A	0	121
T_6	3	H	N/A	0	182
T_7	3	H	0.41	0.42	174
T_8	0	H	0.73	0.62	113
T_9	0	H	0.96	0.28	60
T_{10}	0	H	0.54	0.45	0
T_{11}	0	H	N/A	0	158
T_{12}	0	H	0.41	0.43	147
T_{13}	0	M	0.3	1	58
T_{14}	0	H	N/A	0	117
T_{15}	0	H	0.54	0.25	81
T_{16}	1	H	N/A	0	137
T_{17}	0	M	0.19	1	70
T_{18}	0	H	0.66	1	21
T_{19}	0	H	N/A	0	166
T_{20}	1	M	0.54	0.29	26
T_{21}	0	H	0.42	0.44	64
T_{22}	1	M	0.31	0.65	31
T_{23}	0	M	0.45	0.22	66
T_{24}	0	H	N/A	0	122
T_{25}	2	H	0.48	0.52	104
T_{26}	0	H	N/A	0	102
T_{27}	0	H	0.52	0.84	7
T_{28}	0	H	0.52	0.85	23
T_{29}	0	H	N/A	0	89
T_{30}	0	H	0.66	0.46	69

Table 8.1: Results of the analysis of the influence of respiration. For each treatment in the training set (T_1-T_{30}) is indicated the follow-up score (TS_2) with its confidence level SCL_2 (H: high, M: medium). These are followed by the central frequency (f_R) of the dominant respiratory lobe (0.1-0.85 Hz) in the AR power spectrum of m_1 and the lobe relative amplitude. When no respiratory influenced was found f_R is indicated as not available (N/A). In these cases the amplitude is set to zero. The table also reports the average collapse time (t_c) for the considered treatment. The specific average used is defined in Section 8.4.3.

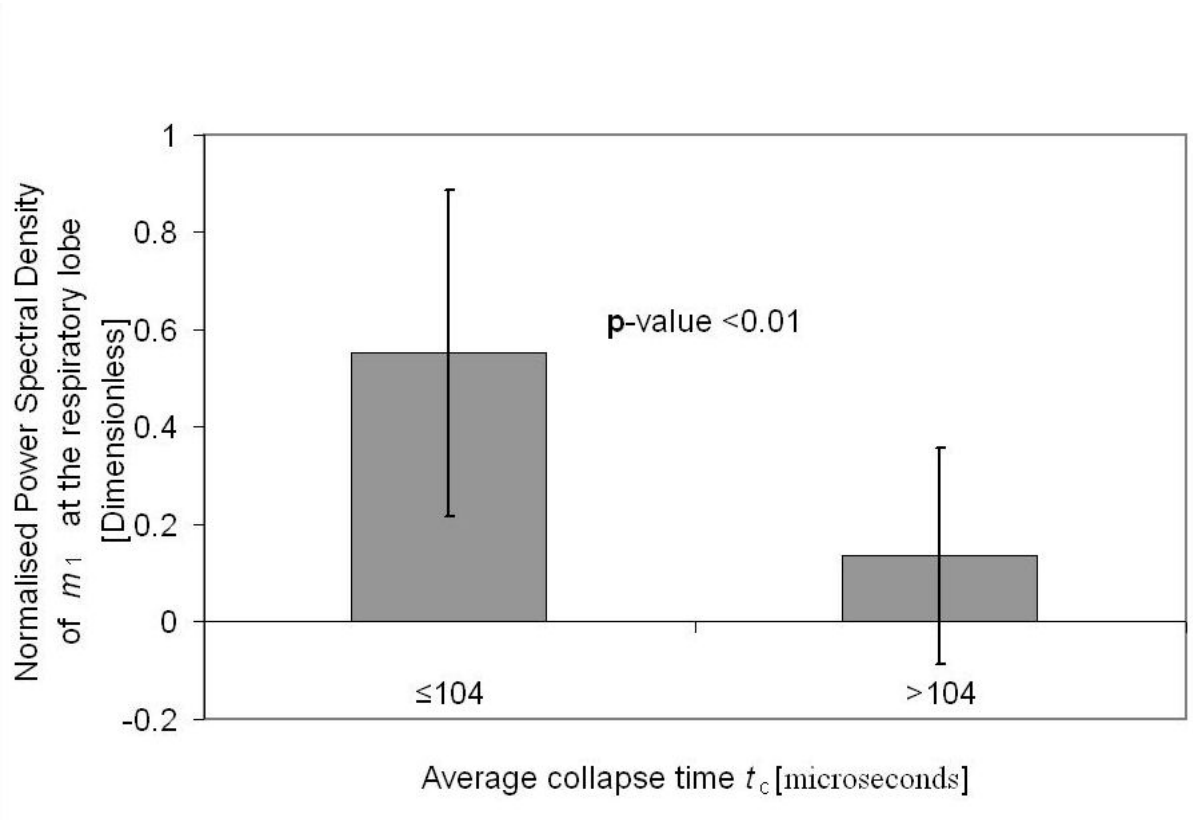

Figure 8.6: Correlation between the amplitude of the respiratory lobe and average collapse time (i.e. targeting[36]) for the treatments in the training set. The errorbars indicate for both populations ± one standard deviation from the average. The averages of the two populations[38] were statistically significant different with a **p**-value[18] less than 0.01.

[38] The second population (t_c>104 μs) is clearly not gaussian, therefore the *t*-test is not strictly applicable (see 6.3.1. However, as the real populations are, in this case, less spread than the gaussian assumed (see Table 8.1) the test was considered as a reliable indication of the separation between two populations.

8.4.2 Exploration of trends in the emissions features

Preliminary *in vivo* experiments (see Subsection 7.4.4) had not shown any significant trend in the three main emission features m_1, m_2 and t_c that could be associated to either *successful* or *unsuccessful* treatments. However those analyses were limited to the observation of a few moments spread along the treatment. Therefore they could have missed some phenomena happening on shorter time scales. That is to say, after moving to continuous monitoring, the possibility of observing any trend in the data was not excluded *a priori*. Consequently the features of each set of data in the training set were examined for the presence of any trend.

Prior to the analysis, a minimum selection process was applied to the raw data in order to eliminate outliers in the examined features. In particular the records of the acoustic emissions were purged of any electrical artefacts (Figure 8.7). These artefacts were caused by false triggering of the digital oscilloscope concomitant with the activation of the X-ray system. They normally happened before or after pausing the treatment and repositioning, i.e. at the end or beginning of a recorded session. Even after this operation each set still contained a number of samples that represented at least 30% of the treatment.

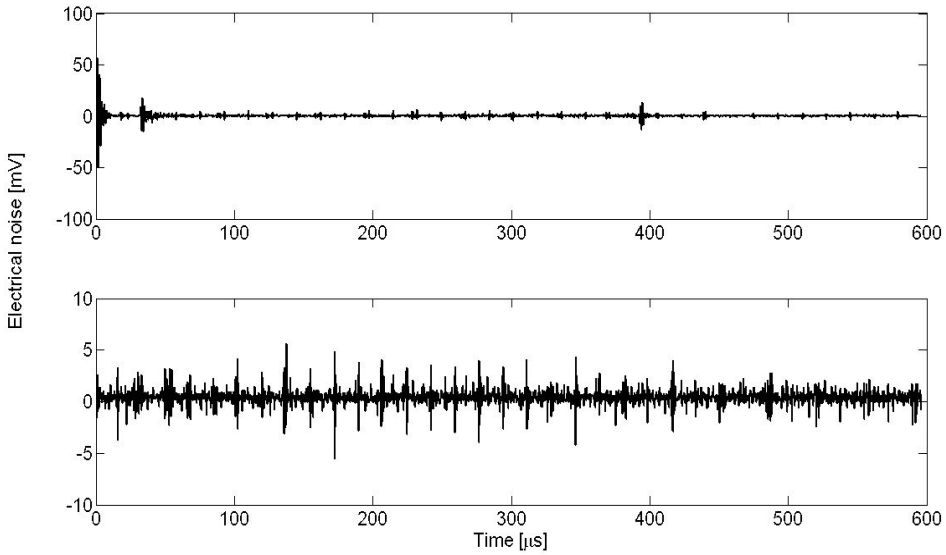

Figure 8.7: Example of two typical artefacts due to electrical noise generated at the activation of the X-ray fluoroscopy system.

The purged data set were then processed to reduce the influence of respiration on m_1 (described in the previous subsection). This was done in order to emphasize any existing trend. The process used consisted in calculating the average m_1 value every 30 shocks. This is because a period of 30 shocks covered at least three respiration cycles[39]. Figure 8.8 shows, as example, (a) the same time series of m_1 shown in Figure 8.5 and (b) the averaged series. The line in Figure 8.8(b) is the best linear fitting of the data points in the figure. It clearly shows that for this treatment, the measure of m_1 was highly influenced by the respiration[40]. This feature oscillated around the average value of about 8.6 kPa and presented no significant variation during the treatment.

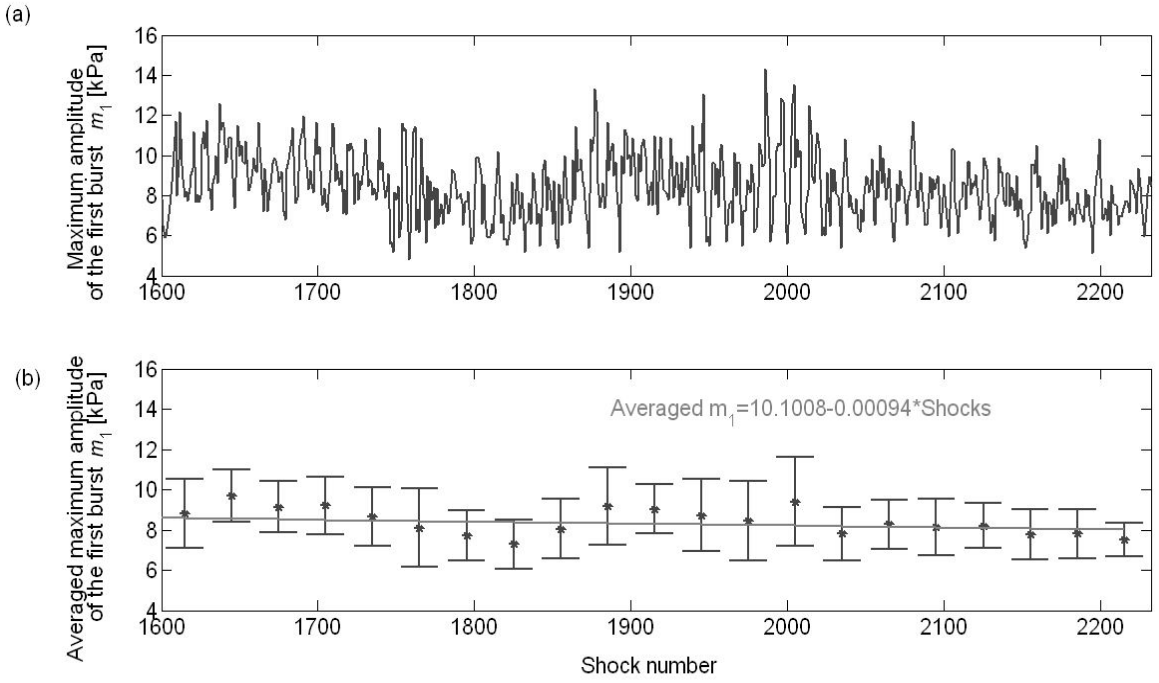

Figure 8.8: (a) Extract from the original m_1 sequence and (b) the averaged sequence for the same treatment data shown in Figure 8.5. The error bars in (b) represent one standard deviation from the average. The line is the best linear fitting among the averaged points. The equation of this line is also reported in the box.

[39] If the minimum observed (see Table 8.1) respiration frequency of 0.2 Hz is considered, the longer observed respiration period is $(0.2\ \text{Hz})^{-1}$= 5s. At a rate of 120 shocks per minute this corresponds to 10 shocks. Hence 30 shocks cover 3 periods.

[40] The estimated relative amplitude of oscillation was 0.65, see T_{22} in Table 8.1.

The rate of change in m_1 with the shock number was estimated from the linear interpolation (Figure 8.8(b)) as about 0.001 kPa per shock. The same averaging operation was applied, for consistency to m_2 and t_c as well. This was done despite the fact that the influence of respiration on these two parameters was not as marked as for m_1. Moreover it has to be clarified that, in contrast to the case with m_1, the feature extraction algorithm would not necessarily estimate a value for m_2 and t_c for each shock. This is because, even during a successful treatment, the occasional mistargeting could happen. When a stone is totally off target, the detected acoustic emission shows a negligible cavitation component[41] and differs from the typical double-peak structure. In those cases the detection algorithm[42] only estimates a single peak (m_1) and m_2 and t_c are assigned a conventional zero value.

Even after the removal of the influence of respiration the time series of the analysed features showed complex behaviour. This is to say, if we concentrate on m_1, only in five cases the feature showed one trend that lasted the whole treatment. In contrast, the time series of the feature could normally be divided into two or more different subsets of different behaviour. Tracts with positive, negative or no trends at all could coexist within the same treatment. Figure 8.9 shows the example of a treatment that showed up to six different subsets. Similar behaviour was also shown by the two other features and was independent of the treatment outcome. This was caused by the combination of several circumstances dependent on the procedure. The first was stone retargeting, the second was the possible movement of the patient. The third arose as a result of small changes in the stone position with progression of the treatment.

Excluding the possibility of one particular combination of trends in the three features characterising *successful* treatments, it was investigated whether these treatments were distinguished by a dominant trend. Therefore, each treatment was divided into segments and each segment was analysed separately. The segmentation was somewhat arbitrary, as besides the information about retargeting, the other two circumstances affecting the treatment were

[41] See Subsection 6.2.2 for a map of the secondary emissions distribution.
[42] See Subsection 5.2.1 for details on the detection algorithm.

not known. The choice made was to segment each treatment in parts that showed specific trends in m_1. Each feature (m_2 and t_c included) was then assigned a rate of variability for each segment. This rate was estimated as the slope of the linear interpolation of the feature sequence in the analysed segment. In the example of Figure 8.9, the treatment was segmented in six segments. Therefore six different rates of variability were estimated for m_1, m_2 and t_c. If we concentrate again on m_1 for simplicity, the first segment in Figure 8.9 of length N_1 equal to 379 shocks showed a rate $\alpha_1\_m_1$ equal to 0.042 kPa per shock. The second segment of length N_2 equal to 256 shocks showed a rate $\alpha_2\_m_1$ equal to 0.019 kPa per shock. The third segment of length N_3 equal to 313 shocks showed a rate $\alpha_3\_m_1$ equal to 0.030 kPa per shock. The fourth segment of length N_4 equal to 248 shocks showed a rate $\alpha_4\_m_1$ equal to 0.046 kPa per shock. The fifth segment of length N_5 equal to 444 shocks showed a rate $\alpha_5\_m_1$ equal to 0.021 kPa per shock. The sixth segment of length N_6 equal to 425 shocks showed a rate $\alpha_6\_m_1$ equal to 0.021 kPa per shock.

The predominant trend in each feature was then estimated from the weighted average of the different rates of variability. That is to say, in the case of the example reported in Figure 8.9 the average variability in m_1 (α_m_1) was equal to:

$$\alpha\_m_1 = \frac{\sum_{k=1}^{6} N_k \alpha_k\_m_1}{\sum_{k=1}^{6} N_k} = 0.023 \qquad (62)$$

Table 8.2 reports the results obtained for the 30 treatments in the training set applying the described analysis. Most of the treatments (17) showed a quite small variation with the shock (< 0.01 units per shock) for all three parameters. At a first glance, most of the treatments with negligible (about 0 kPa per shock) or negative trends in both m_1 and m_2 were mainly those with no stone fragmentation (Table 8.2, elements T_8, T_9, T_{11}, T_{16}, T_{19}, T_{22}, T_{24}).

However this behaviour was also present in two treatments with a noticeable stone fragmentation (Table 8.2, element T_1 and T_7). Moreover, positive or negative trends were not exclusive to one class of treatments. Therefore, it was concluded that the information contained in the trends of the emission features was not of any use to discriminate *successful* and *unsuccessful* treatments. This in contrast to what was prospected from *in vitro* experimentation[43]. This section will show that such a discrimination was instead possible on the basis of the values assumed by the collapse time t_c and the fragmentation index m_2/m_1.

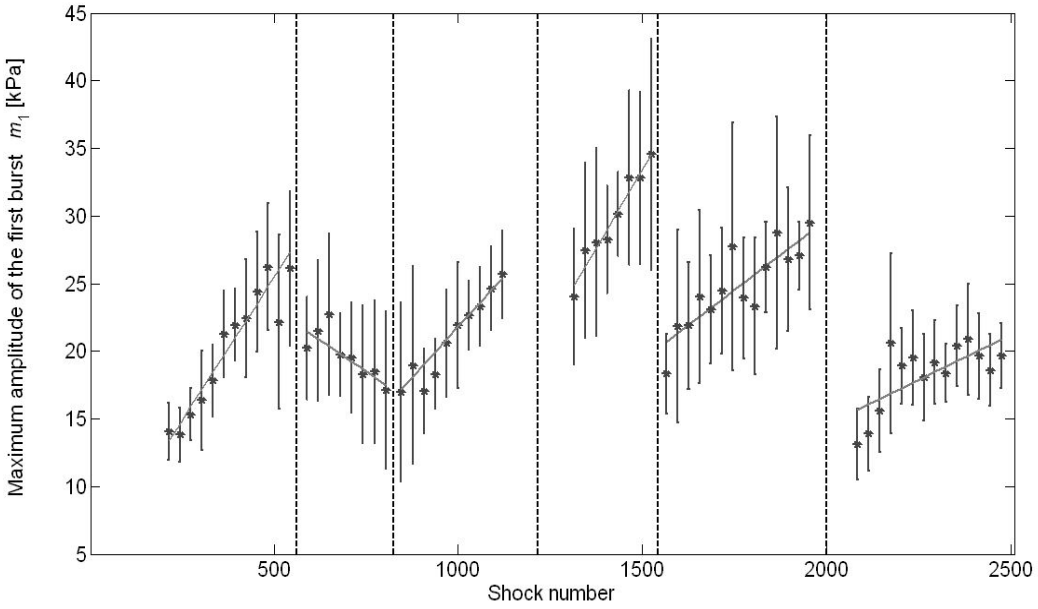

Figure 8.9: Example of a treatment (Table 8.1-T_4) where the averaged time series of m_1 could be divided in six different sets. The first segment of length N_1 equal to 379 shocks showed a rate $\alpha_1\_m_1$ equal to 0.042 kPa per shock. The second segment of length N_2 equal to 256 shocks showed a rate $\alpha_2\_m_1$ equal to 0.019 kPa per shock. The third segment of length N_3 equal to 313 shocks showed a rate $\alpha_3\_m_1$ equal to 0.030 kPa per shock. The fourth segment of length N_4 equal to 248 shocks showed a rate $\alpha_4\_m_1$ equal to 0.046 kPa per shock. The fifth segment of length N_5 equal to 444 shocks showed a rate $\alpha_5\_m_1$ equal to 0.021 kPa per shock. The sixth segment of length N_6 equal to 425 shocks showed a rate $\alpha_6\_m_1$ equal to 0.021 kPa per shock. The majority of trends were positive and the weighted average rate of change with the shocks resulted to be α_m_1=0.023 kPa per shock. The straight lines indicate the best fitting for each subset and the error bars are equal to one standard deviation from the average.

[43] See Chapter 6

Treatment	TS_2	SCL_2	Number of segments	α_m_1 [kPa Shocks^{-1}]	α_m_2 [kPa Shocks^{-1}]	α_t_c [μs Shocks^{-1}]
T_1	5	H	3	0.000	0.000	0.222
T_2	5	M	2	0.137	0.008	-0.273
T_3	4	L	3	0.003	0.006	0.026
T_4	5	H	6	0.023	0.003	-0.011
T_5	5	H	3	-0.001	0.000	0.000
T_6	3	H	2	0.004	-0.001	-0.069
T_7	3	H	4	-0.001	-0.001	0.024
T_8	0	H	1	0.000	0.000	0.219
T_9	0	H	3	0.000	0.000	-0.073
T_{10}	0	H	2	0.004	0.000	0.000
T_{11}	0	H	1	0.000	0.000	-0.041
T_{12}	0	H	1	0.001	0.005	-0.005
T_{13}	0	M	3	0.005	-0.003	-0.076
T_{14}	0	H	3	0.007	0.006	0.129
T_{15}	0	H	3	-0.001	0.001	0.050
T_{16}	1	H	5	-0.002	-0.004	-0.074
T_{17}	0	M	5	0.005	-0.001	-0.051
T_{18}	0	H	3	0.006	-0.001	-0.010
T_{19}	0	H	6	-0.002	-0.005	0.014
T_{20}	1	M	2	0.003	0.000	-0.005
T_{21}	0	H	2	0.004	0.001	0.006
T_{22}	1	M	3	-0.003	-0.002	-0.043
T_{23}	0	M	4	0.004	0.001	0.020
T_{24}	0	H	1	0.000	0.000	-0.052
T_{25}	2	H	2	0.004	-0.001	-0.034
T_{26}	0	H	3	0.007	-0.001	-0.033
T_{27}	0	H	3	0.013	0.000	0.000
T_{28}	0	H	1	-0.008	0.002	0.039
T_{29}	0	H	2	0.006	-0.001	-0.058
T_{30}	0	H	4	0.009	0.002	0.011

Table 8.2: Summary of the analysis of eventual trends in m_1, m_2 and t_c in the treatments of the training set (T_1-T_{30}). The treatment follow-up score (TS_2) with its confidence level (SCL_2) are reported for each treatment. These are followed by the number of different segments in which the treatment could be divided and the weighted average rates of variations for the three features α_m_1, α_m_2, α_t_c.

8.4.3 The correlation between treatment success and the emissions features

The success of an ESWL treatment, as explained throughout this thesis, is the combination of several factors. The most important factors are, of course, good targeting and an efficient fragmentation of the stone. The latter does not necessary follow the former, as very hard stones cannot break using this technique[44].

Previous subsections 7.4.4 and 8.4.1 have already shown that *successful* treatments ($TS_2 > 2$) were characterised by higher average values of the collapse times ($t_c > 104$ μs). That is to say that, consistently with *in vitro* experiments[45], the higher values of the average collapse time indicated better targeting than for the *unsuccessful* treatments.

Treatments were then explored for indications of fragmentation. First of all, as shown in the previous subsection, the main emission features were explored for trends. In contrast with *in vitro* experimentation[46] no correlation was found between stone fragmentation and trends in these features. *In vitro* experiments[47] also showed that the emissions collected in proximity of stones with higher grades of fragmentation were characterised by higher fragmentation indices ($0.4<m_2/m_1<0.75$). Therefore, the second attempt followed in searching for indications of fragmentation was to examine the values assumed by this ratio in the emissions collected for the 30 data sets.

It was actually found that *successful* treatments were characterised by a higher percentage of traces with a fragmentation index between 0.4 and 0.77 (Figure 8.10) than the *unsuccessful* ones. In contrast, the *unsuccessful* treatments were characterised by traces with either a fragmentation index less than 0.4 (Figure 8.11) or noisy traces. The noisy traces (Figure 8.12) showed an apparent fragmentation index higher than 0.77.

[44] See Chapter 2.
[45] See Subsection 6.2.4.
[46] See Section 6.3
[47] See Subsection 7.3.4.

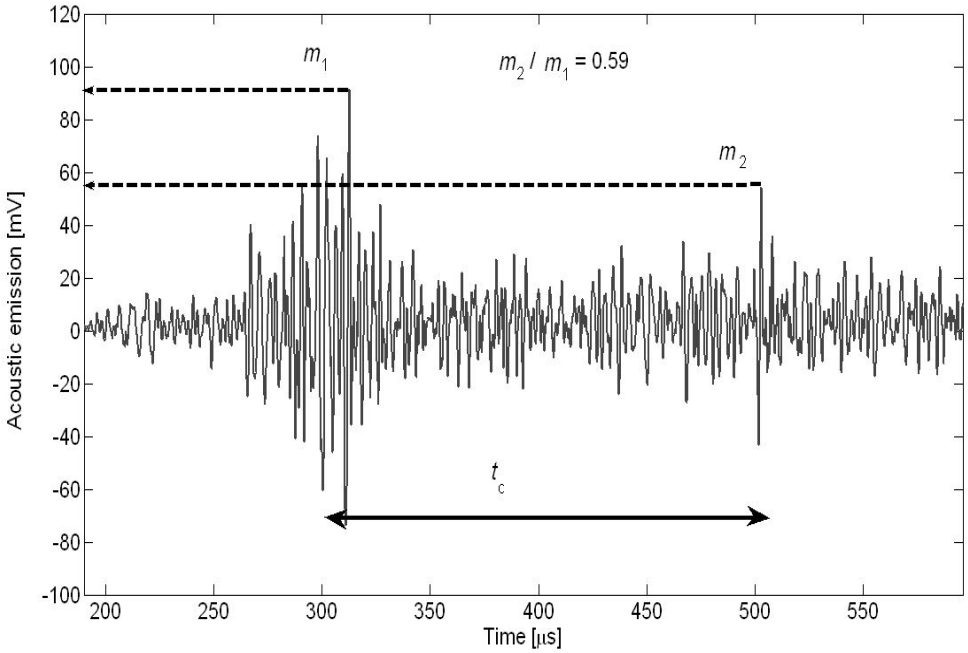

Figure 8.10: Example of trace from a *successful* treatment. The time t=0 corresponds to the electrical noise used for triggering.

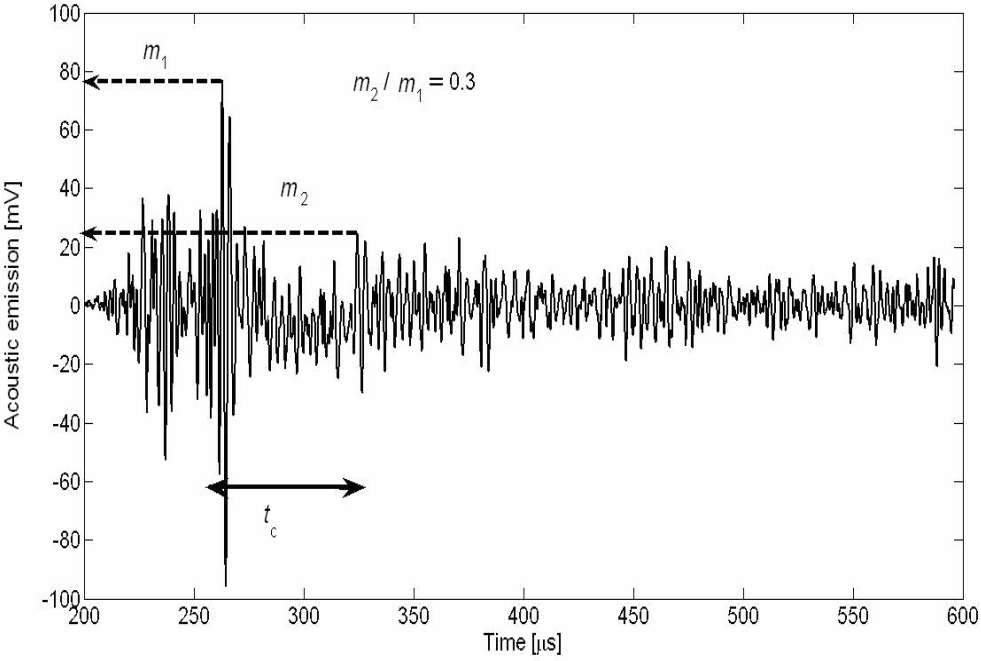

Figure 8.11: Example of trace from an *unsuccessful* treatment. The time t=0 corresponds to the electrical noise used for triggering.

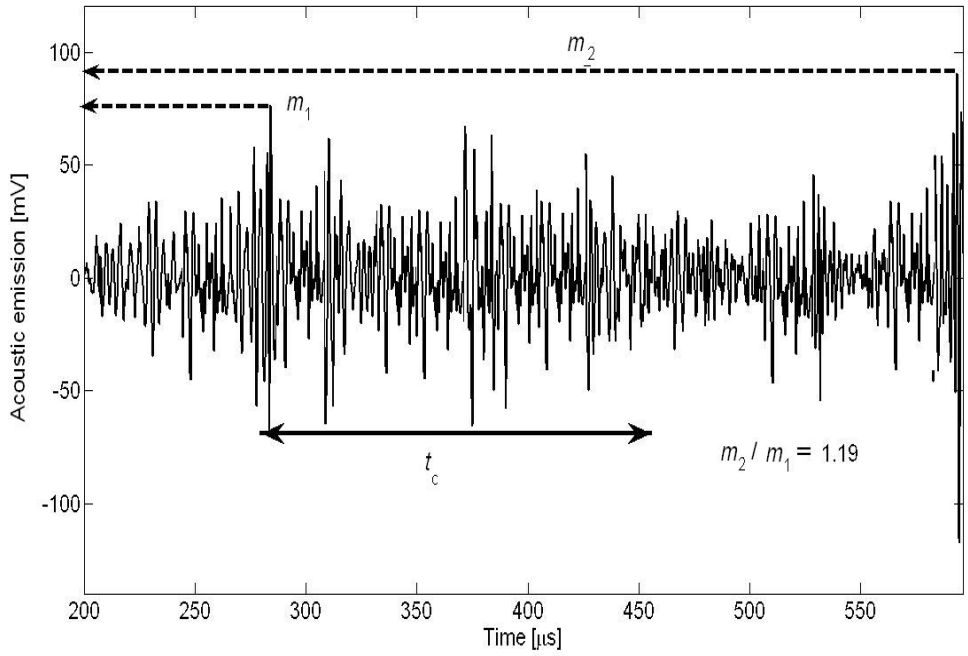

Figure 8.12: Example of a noisy trace from a *unsuccessful* treatment. The time t=0 corresponds to the electrical noise used for triggering.

In order to establish which ranges of values in m_2/m_1 and t_c discriminated the *successful* treatments from the *unsuccessful*, the weighted averages of both features were calculated. The weighting factor, as explained in the previous subsection, was the length of the different subsets that compose a treatment. The results of these calculations are reported in Table 8.3. They show that *successful* treatments were characterised by average parameters that satisfied the condition:

$$0.42<m_2/m_1<0.77 \text{ and } t_c>104\ \mu s \qquad (63)$$

Treatment	TS_1	SCL_1	TS_2	SCL_2	t_c [μs]	m_2/m_1	% points
T_1	2	M	5	H	281	0.44	65
T_2	3	M	5	M	158	0.43	52
T_3	2	L	4	L	137	0.76	51
T_4	3	H	5	H	171	0.53	59
T_5	4	M	5	H	121	0.62	68
T_6	1	H	3	H	182	0.54	55
T_7	0	M	3	H	174	0.57	77
T_8	1	H	0	H	113	0.03	17
T_9	0	H	0	H	60	0.00	10
T_{10}	0	H	0	H	0	0.41	0
T_{11}	5	H	0	H	158	0.82	38
T_{12}	0	H	0	H	147	0.39	39
T_{13}	2	M	0	M	58	0.36	4
T_{14}	3	M	0	H	117	0.33	49
T_{15}	0	H	0	H	81	0.34	45
T_{16}	1	M	1	H	137	0.14	33
T_{17}	4	M	0	M	70	0.05	15
T_{18}	0	M	0	H	21	0.82	3
T_{19}	1	M	0	H	166	0.12	48
T_{20}	0	H	1	M	26	0.23	8
T_{21}	0	H	0	H	64	0.05	17
T_{22}	2	H	1	M	31	0.21	3
T_{23}	0	M	0	M	66	0.78	27
T_{24}	1	M	0	H	122	0.25	4
T_{25}	1	H	2	H	104	0.18	22
T_{26}	0	M	0	H	102	0.02	20
T_{27}	0	H	0	H	7	0.08	1
T_{28}	0	H	0	H	23	0.28	4
T_{29}	0	M	0	H	89	0.11	31
T_{30}	1	M	0	H	69	0.04	12

Table 8.3: Comparison of the radiographer first opinion (TS_1 with confidence SCL_1) against the treatment assessment (TS_2 with confidence SCL_2) and the weighted average of the two emissions features m_2/ m_1 and t_c. The last column reports the number of points that satisfy condition (65).

On the basis of this observation of the average values, it was decided to classify a shock as *effective* if these two emission features satisfied the condition:

$$0.4<m_2/m_1<0.8 \text{ and } t_c>100\ \mu s \qquad (64)$$

The 30 treatments were then reanalysed to establish the percentage of sampled shocks that satisfied condition (64). This percentage, which was an estimate of the treatment efficiency, was indicated as TS_0. The results of the analysis are reported in the last column of Table 8.3. Kappa statistics [144] were used to determine the threshold TS_0 that best separated the two classes of treatments. The statistic computes[37] the agreement between two observers in classifying a binary phenomenon and is quite robust to observer bias [144]. The optimum threshold that resulted from this analysis was 50% with a kappa equal to 0.95, which is an indication of almost perfect agreement. If the treatments analysed contained a percentage of shocks for which t_c and m_2 were both equal to zero less than 30%, these shocks were eliminated from the analysis. These points will be referred to as *null* points from now on. The elimination was done, considering that these points correspond to noisy traces, in order to optimise the performances of the classification algorithm. However if those shocks were included in the analysis the system could still discriminate between the two classes, and there is still substantial agreement with the treatment assessment TS_2 (kappa = 0.79).

On the basis of these results the automatic elimination of *null* points, described above, and the following classification rule was incorporated in the final version of the SEAC software MATLAB™ interface:

$$0.4<m_2/m_1<0.8 \text{ and } t_c>100\ \mu s \text{ for at least 50\% of recordings} \qquad (65)$$

The interface will be described in the following section.

Figure 8.13 shows an example of the distribution of the two features for (a) a *successful* and (b) an *unsuccessful* treatment. The total number of points in Figure 8.13(a) is 2231, which represents the 74% sample of shocks obtained using the SEAC software. This was one of the few cases[48] (3) where no recorded signals showed m_2=0 and t_c=0 (*null* points). The total number of points in Figure 8.13(b) is 2185, which represent 87% of the total treatment. Of these points 629 are *null* points and, as they are less than 30%, they have been removed in the calculation of the TS_0 score, that otherwise would have been even lower.

Figure 8.14 presents the overall clinical results on the thirty subjects included in this training stage of the system. Figure 8.14(a) compares the treatment X-ray assessment TS_2 with the first opinion of the radiographer (TS_1). The graph includes all 30 treatments, however only 16 points are discernable. This is because some treatments presented the same combination (TS_2, TS_1). Precisely, in the graph there are 11 treatments with both TS_2 and TS_1 equal to zero, 4 treatments with TS_2 equal to 1 and TS_1 equal to zero, and 2 treatments with TS_2 equal to 5 and TS_1 equal to 3 (see Table 8.3).

The agreement between the two scores was poor (kappa=0.32) and the first opinion only detected correctly 43% of the *successful* treatments.

Figure 8.14(b) compares TS_2 with TS_0, the treatment efficiency estimated applying rule the classification rule (65).

This Phase 1 clinical trial therefore indicates the unreliability of TS_1, and greater reliability of TS_0, as judged against the gold standard of TS_2.

[48] Only three treatments out of the 79 examined in the two phases of this clinical trial showed no *null* point at all. Otherwise *null* point (attributed to mistargeting), even if in a small percentage, was always present.

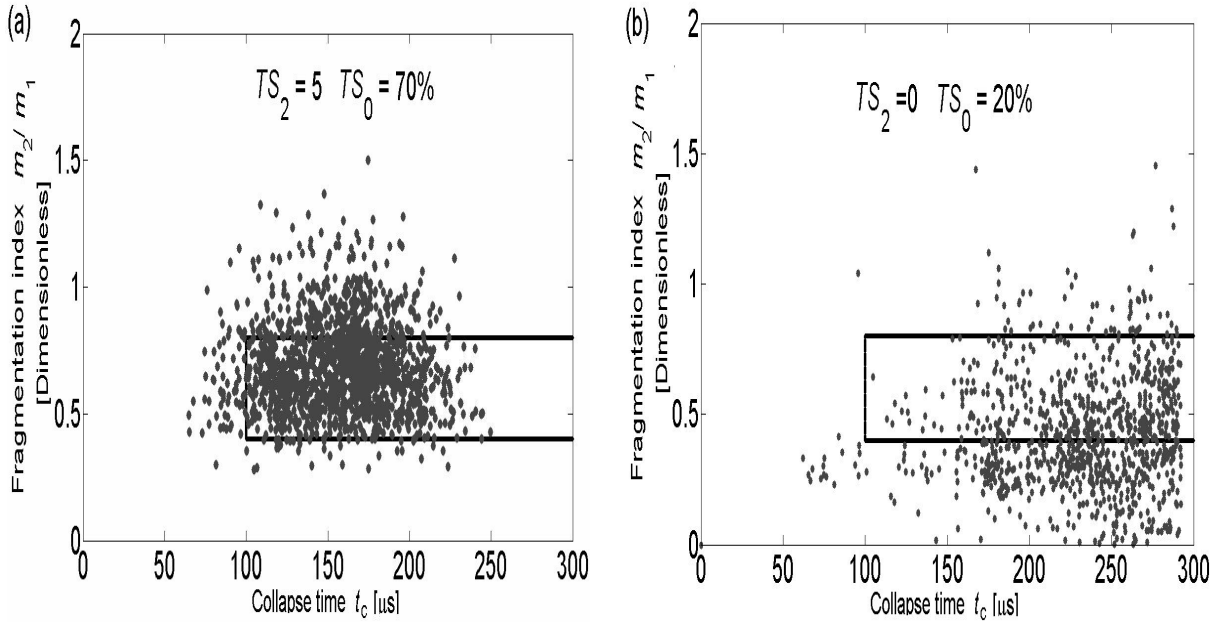

Figure 8.13: These two plots give the values of the acoustic parameters m_2/m_1 and t_c for each shock from two sample treatments. The first plot (a) is for a *successful* treatment and the second plot (b) is for an *unsuccessful* treatment as classified by the clinician from the X-rays (TS_2). The area delimited by the solid line ($0.4 < m_2/m_1 < 0.8$ and $t_c > 100$ μs) represents the semi-empirical rules that appear from the phase 1 study to give the optimum indication of *effective* and *ineffective* shocks.

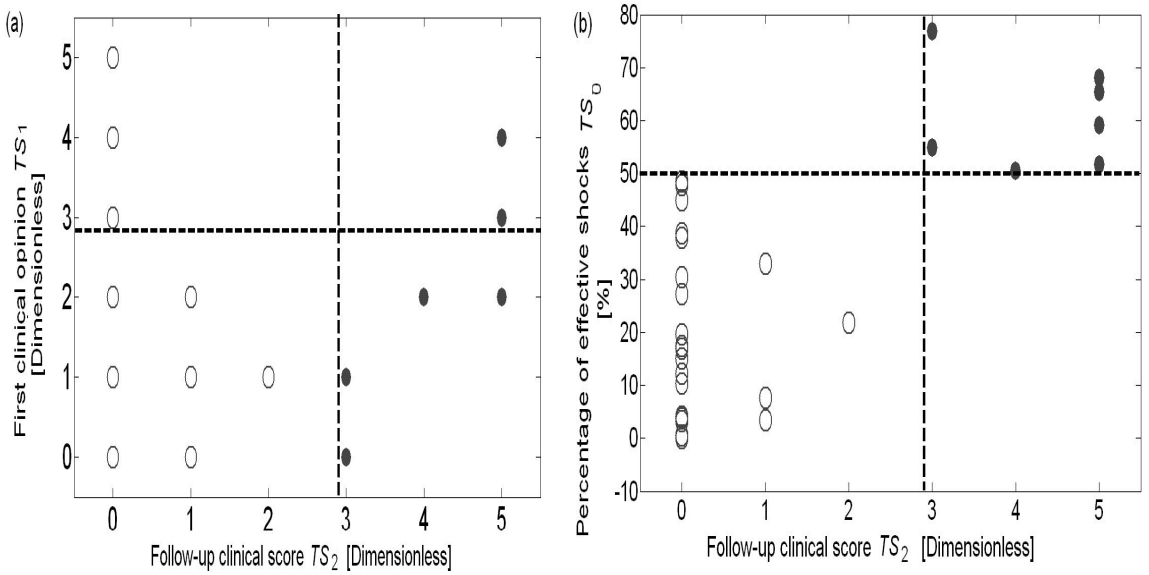

Figure 8.14: In the first plot (a) the initial clinical treatment score, TS_1, is compared with the clinical treatment score obtained at the three-week follow-up assessment, TS_2. In the second plot (b) the treatment score from the SEAC system, TS_0, is compared with TS_2. Each point represents the result obtained from a single treatment of 2473 ± 602 shocks. The second plot (b) indicates that *successful* treatments as classified at the follow-up (i.e. $TS_2 \geq 3$) have values of $TS_0 \geq 50\%$.

8.5 The final version of the SEAC software interface

The final version of the SEAC interface was built upon the results of the training stage. It shows an extra *Shock Effective* button in the panel (b) of Figure 8.15. This button changes at each shock and it indicates *YES* or *NOT* depending on the features of the emissions being recognised as that of a *successful* treatment or not (see Section 8.4 for details on the classification). In the same panel it also has added a *Classification* button that can be pressed at the end of the patient treatment for a global treatment evaluation, which appears in a new small window (panel (e) of Figure 8.16). The single right bottom box, displaying m_1 and t_c, present in the previous version (Figure 7.20), has been replaced by two boxes (Figure 8.15 and Figure 8.16) showing the two parameters used for the classification (see Section 8.4 for classification details), the fragmentation index m_2/m_1 (blue dots, top box) and the targeting indication t_c (green crosses, bottom box), with the thresholds (red dotted lines) of classification (see Section 8.4 for details on the classification algorithm). The dotted red lines, as will be explained in Section 8.4, indicate the boundaries of the classification ranges.

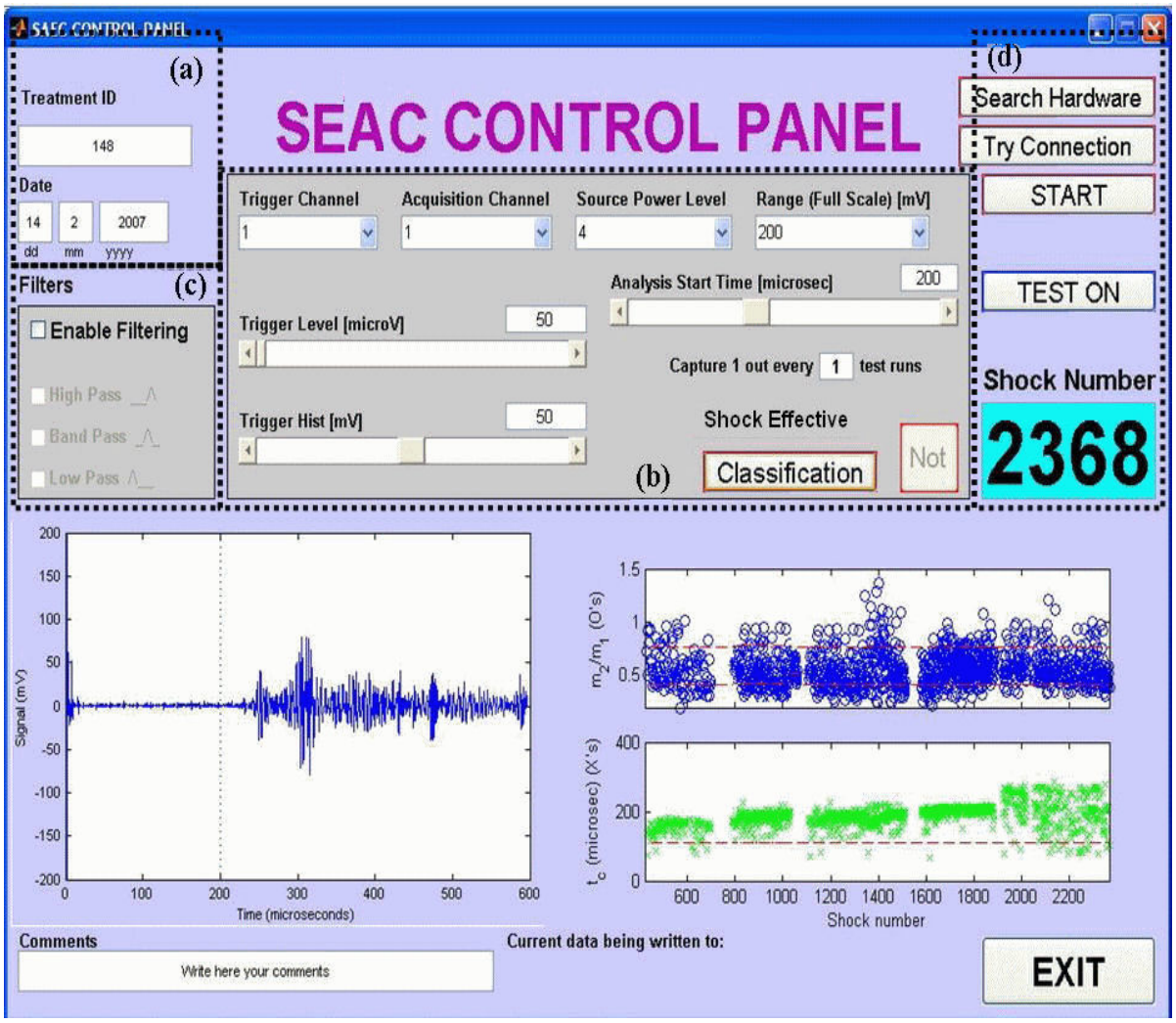

Figure 8.15: Final version of the developed SEAC MATLAB™ interface for on-line monitoring. The black dotted boxes identify 4 different control panels, (a) is a section where the treatment details are inserted (*Treatment ID* and *Date*). Panel (b) hosts the controls for the scope data acquisition. Panel (c) shows some optional filtering options (that normally are not used). Differently from the previous version this panel shows also a *Shock Effective* button that at each shock indicates YES or NOT dependently on the features of the emissions satisfying rule (64) or not. There is also a *Classification* button that can be pressed at the end of the patient treatment for a global treatment evaluation TS_0. Panel (d) presents some controls of the synchronisation between the software and hardware (*Search Hardware*, *Try Connection*). A test facility (*Test ON*) consents to run the program without saving any data and a button *Start* activates the acquisition. The bottom left box displays the raw signal being collected and the bottom right box shows the two parameters m_2/m_1 (blue dots on the top) and t_c (green crosses on the bottom box) on which the is based the shock classification. The dotted red lines indicate the boundaries of the classification ranges. Further down there are a *Comment*s box, that is for the operator to introduce eventual comments on the treatment, a Section that displays where data are saved at the end of each session, and an *EXIT* button to quit the program.

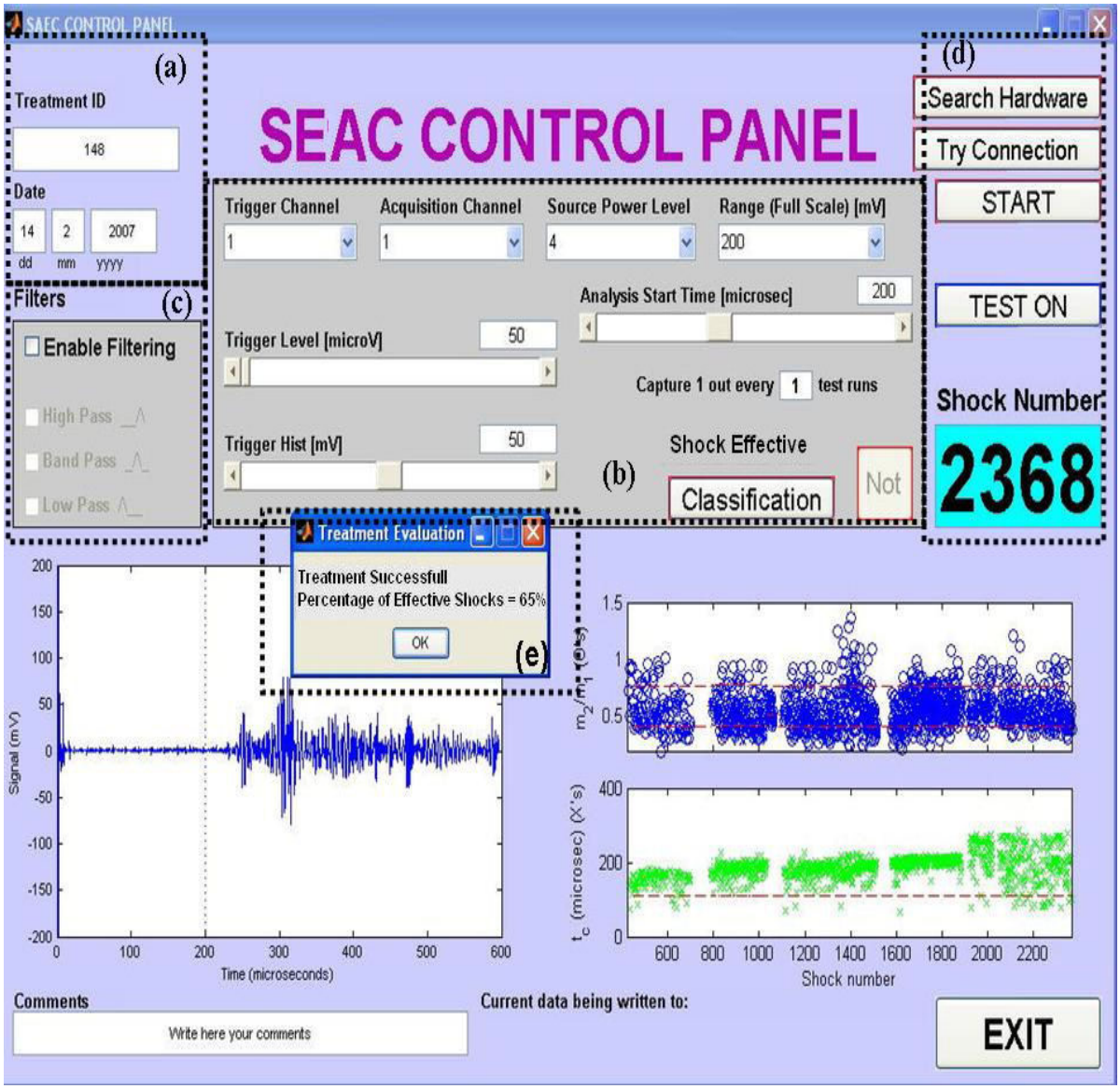

Figure 8.16**:** Final version of the SEAC control interface. This figure differs from the previous for the presence of a box (e) that shows the treatment evaluation for the same treatment as Figure 8.15. This box appears after the Classification button is pressed. In this case the percentage of shocks whose emissions satisfied the rules (64) is 65% and therefore the whole treatment is scored as *successful*.

8.6 Summary

The second stage of the system development *in vivo* was done after new funding (EP/D503310/1) was obtained for a second clinical trial [143]. A first stage of the trial included 30 patients and was used to train the system (Section 7.5). That is to say, it was used to establish the laws upon which the system could classify treatments outcomes (see Equation (65)). A binary classification of treatments into either *successful* or *unsuccessful* was used. This classification was based on a clinical score TS_2 assigned by the urologist at the treatment X-ray follow-up assessment 15-20 days after the treatment (Section 8.3).

A classification rule (65) was designed such that perfect agreement (kappa=0.95) was obtained between the SEAC system classification and the treatment assessment (TS_2) on the whole set of 30 treatments. During this trial also the first opinion on the treatment of the radiographer administering the treatment was collected. In particular the radiographers were required to assign a treatment score TS_1 based on changes in the fluoroscopy images of the treated stone (Section 8.3). This judgment classified correctly less than 50% of the *successful* treatments and, when compared against TS_2, proved quite unreliable (kappa=0.32).

This training stage was followed by a blind validation stage on further 49 treatments. In this stage the output of the SEAC system was blindly compared against the clinical assessment TS_2. The results of this stage will be reported in Chapter 9.

Chapter 9 Clinical validation and conclusions

9.1 Introduction

This Chapter illustrates the results of the validation of the prototype system developed on a set of 49 patients (Figure 9.2). Three independent assessments were compared: the on-line binary classification (see Subsection 8.5), the first opinion of the radiographer administering the treatments (TS_1, see Subsection 8.3) and the gold standard X-ray treatment follow-up (TS_2, see Subsection 8.3).

The system agreed with the follow-up TS_2 scores in 98% of cases and, in particular showed a higher sensitivity (92%) than the first opinion of the radiographer TS_1 (33%) [143]. This evidence shows that the device provides valuable real-time feedback to the lithotripter operator about the effectiveness of the treatment. It is likely that once introduced into the clinical practice, the system will also help to reduce the number of shocks administered to a patient.

9.2 The binary classification of the acoustic system

The SEAC system provides a binary classification *successful*/*unsuccessful*, which is based on the examination of two features extracted from the secondary acoustic emissions[49]:

1. The collapse time t_c, which is used as an indicator of the quality of the targeting. When the effect of respiration on targeting was negligible the acoustic emissions showed t_c>104 μs (see Subsection 8.4.1).
2. The fragmentation index m_2/m_1. This index was on average above a certain threshold (0.42) for treatments where at least 50% of the stone had fragmented (see Subsection 8.4.2).

[49] See Subsection 5.2.5 for the definition of these parameters.

$$0.4<m_2/m_1<0.8 \text{ and } t_c>100\ \mu s \text{ for at least } 50\% \text{ of recordings} \quad (65)$$

That is to say, the system divides the space (t_c, m_2/m_1) in the four different regions represented in Figure 9.1 and assigns each shock of a treatment to one of these regions. Region (c) in Figure 9.1 represents shocks that are *effective*. Region (d) in Figure 9.1 represents shocks that are *ineffective* despite a good targeting. This, as explained, happens in the case of very hard stones. Regions (a) and (b) in Figure 9.1 represent shocks that are *ineffective* because of mistargeting. The shocks in region (a) are characterised by signals close to the noise level where the algorithm returns large values of the m_2/m_1 ratio. These noisy acoustic signals are interpreted here as ones in which there is minimal scattered or cavitational signal due to the lack of targeting.

The physical interpretation of the two features used by the classification rule[50] suggests that they are not entirely independent. Nevertheless the value of the model used in this work is proved by the clinical interpretation of its feedback in terms of treatment efficacy.

[50] See Subsection 5.2and Chapter 6.

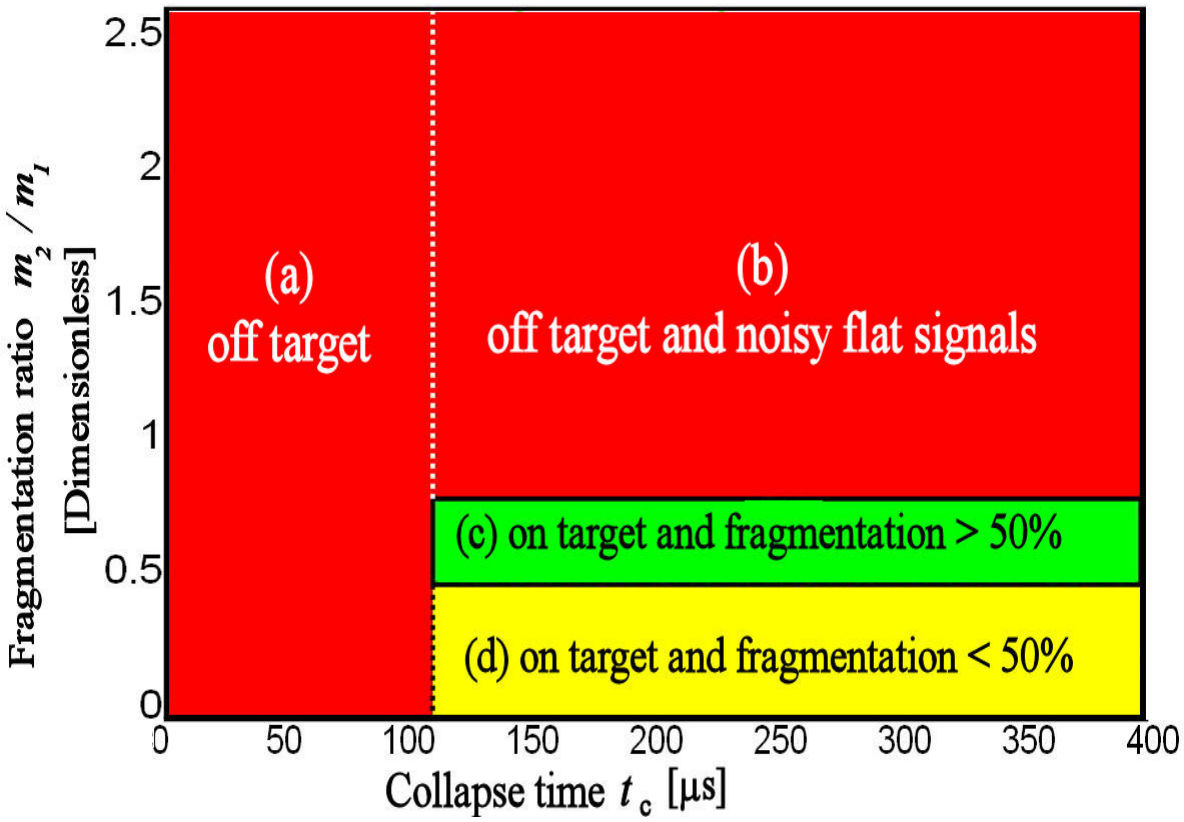

Figure 9.1: Classification regions of the SEAC algorithm. Regions (a) and (b) represent ineffective shocks where the stone is off-target. Region (c) represents effective shocks. Region (d) represents shocks that are on target but ineffective as do not cause any fragmentation.

9.3 Results of the validation stage

The reliability of the binary classification into *successful* and *unsuccessful* treatments made by the system developed[51] was tested during a clinical trial where 85 patients were recruited. This was a blind stage, where the system output was derived independently from the treatment follow-up assessment (TS_2, see Subsection 8.3), and compared against it. The analysis of the acoustic signals was done off-line as for the previous stage[52], after eliminating noisy outliers. Data from 49 treatments were suitable for the analysis[52], that is each represented at least 30% of the treatment and had a complete follow-up at three weeks available[53].

Figure 9.2 presents the overall clinical results on the 49 subjects included in this validation stage. The dotted lines show the thresholds for the treatment scores that provide a binary classification of *successful* and *unsuccessful* treatments and the points in bold print have TS_2 greater than 2. Figure 9.2(a) compares the treatment X-ray assessment TS_2 with the first opinion of the radiographer (TS_1). In this case the agreement between the two scores was poor (kappa=0.38) and the first opinion only detected correctly 33% of the *successful* treatments. The graph includes all 49 treatments, however only 16.points are discernable. This is because, similarly to what happened for Phase 1 (see Subsection 8.4.3), some treatments presented the same combination of clinical scores (TS_2, TS_1). Such combinations and the relative number of treatments are listed in Table 9.1

[51] See Subsections 8.4 and 8.5.
[52] See Subsection 8.4.
[53] See 9.B.1 for details on the attrition rate.

TS_2	TS_1	Number of treatments
0	0	18
0	1	9
0	2	3
1	1	3
3	1	4
5	4	2

Table 9.1: The table lists the combinations of clinical scores TS_1 and TS_2 that were common to more than one treatment in Phase 2 clinical trial. For each combination is listed the specific number of treatments.

Figure 9.2(b) compares TS_2 with TS_0, the treatment efficiency estimated applying the classification rule (65). The level of agreement between the SEAC device and the 'gold standard' TS_2 remains good, in this case with kappa=0.94. The sensitivity of the device in categorising the treatment success is 92%, with 11 individuals identified as having a TS_0 of 50% or more compared with 12 individuals having a TS_2 of 3 or more. The specificity of the SEAC system in this phase was 100% with all 37 individuals with $TS_2<3$ identified by the device as having *unsuccessful* treatments.

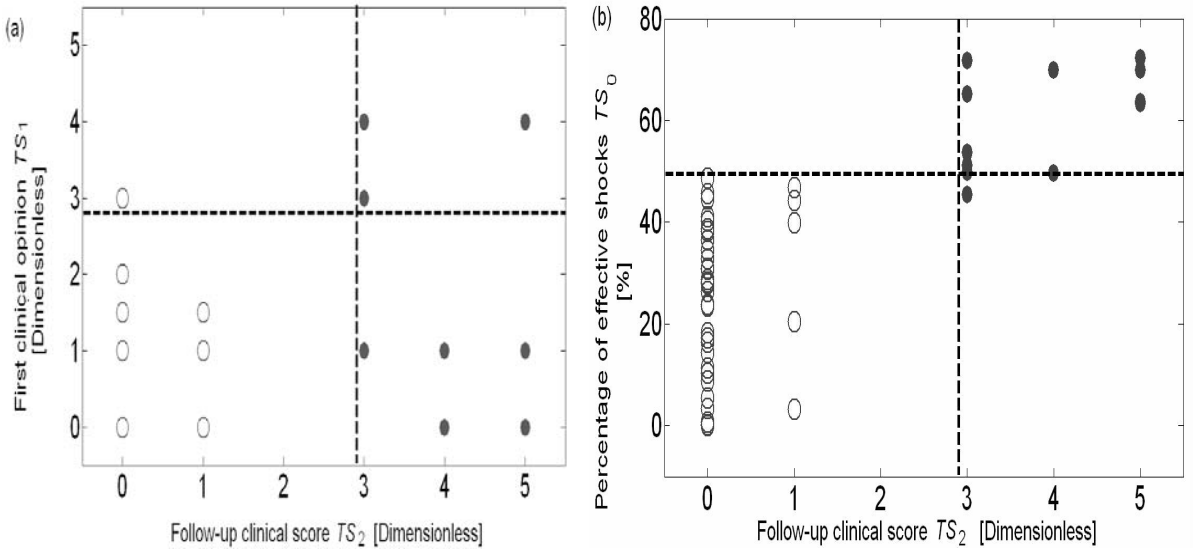

Figure 9.2: In the first plot (a) the initial clinical treatment score, TS_1, is compared with the clinical treatment score obtained at the three-week follow-up assessment, TS_2. In the second plot (b) the treatment score from the SEAC system, TS_0, is compared with TS_2. Each point represents the result obtained from a single treatment of 2461 ± 580 shocks. The dotted lines indicate the position of the thresholds determined from phase 1.

9.4 Conclusions

The original objective of this work was to investigate the feasibility of developing a passive ultrasound diagnostic system for lithotripsy that exploited secondary acoustic emissions (Chapter 1). Preliminary *in vitro* experiments proved that features extracted by such emissions could provide information on the quality of stone targeting and stone fragmentation (Chapter 4-Chapter 6). This accomplished a prototype diagnostic system was developed (Chapter 7) and tested on a set of six patients (see Subsection 7.4.4). The availability of EPSRC follow-up funds (EP/D503310/1) allowed the training and validation of the system on a set of 79 patients. The clinical validation showed that the system provides clinically relevant real-time feedback to the operator that relates to the targeting of the stone and to the degree of fragmentation achieved on completion of the treatment. In particular, the concept of an *effective* shock has been introduced in terms of measurable acoustic parameters. The precise clinical interpretation of these acoustic parameters is not fully

explored here. Indeed, because of the complexities of the interactions that can be expected to occur *in vivo*, neither the underlying model, nor the hypotheses as to the cause of the signal characteristics, will capture all aspects of the interaction. To avoid misclassification of *successful* treatments an uncertainty band was included in the real time classification (see Section 8.5). That is to say, the real time system will classify a treatment as *successful* if shocks are considered *effective* (see Equation (63)) for at least 50% of the sampled treatment and *unsuccessful* if it is verified for less than 30%. In all other cases that fall in the intermediate range 30%-49% the system alerts the operator but does not assign a definite classification.

The system also showed the potential to track stone movements caused by respiration (See Section 8.4.1) and could be adapted to provide a respiratory gating signal for the shockwave release.

The system that was operated at Guy's Hospital by research nurse Catherine McCarthy, was greatly appreciated by all the staff in the Stone Unit for its user friendly interface. The radiographers in the unit learned quickly to interpret the features and how to exploit the system to adjust targeting. Simon Ryves, the lead radiographer (see letter in Appendix B), suggested that the use of the system would not only reduce the length and intensity of the treatments, but would also help in reducing the X-ray dose for both patient and operator.

9.5 Discussion

One limitation of the study is that about 20% of shocks have been excluded from the analysis. These occur at the very start of the treatment and immediately after each retargeting of the stone on X-ray and therefore tend to be at lower energy settings than those used for the majority of the treatment. This omission has made the device-derived treatment score, TS_0, higher than it would have been if more of these probably *ineffective* shocks had been included. Clearly, if the SEAC system were incorporated into the construction of the lithotripter, this limitation might be designed out by allowing automated capture of the setting. The key clinical value of the system lies in its ability to assist the operator in making decisions during ESWL concerning the ongoing effectiveness of the treatment, in terms of both the targeting and the likelihood of stone fragmentation. Currently lithotripter operators have little feedback on these critical treatment success factors. The system described would be particularly valuable if it could reduce the re-treatment rate seen in ESWL, and lower the consequent morbidity and cost.

9.6 Future work

Future work may include both further exploitation of the system in ESWL and its introduction in other areas of therapeutic ultrasound. Companies such as Storz, Siemens and Dohrnier showed an interest in the prototype and a future collaboration with any of them to incorporate the system in a commercial lithotripter is not excluded at the moment.

On the other hand, the capability of the system to monitor cavitation is particularly appealing in other areas of ultrasound. The system could be used either in diagnostic ultrasound, to ensure that a scan operates safely without the generation of any inertial cavitation [146], or in other applications of therapeutic ultrasound which exploit cavitation, such as ultrasound mediated drug and gene delivery [23, 95, 147]. This application uses ultrasound contrast agents, which essentially are gas microbubbles encapsulating the specific therapeutic compound. Once the microbubbles have been injected in the patient, the release of the active substance is activated by means of high intensity ultrasound that causes the bubble rupture. This process of inertial cavitation is accompanied as usual by the emission of broadband noise that can be detected by a passive detector [23, 95], such as that described in this work. Another important therapeutic application of ultrasound to cancer treatment is High Intensity Focused Ultrasound (HIFU). This technique exploits a high intensity focused ultrasound beam to thermally ablate cancer [148, 149]. Inertial cavitation has been shown to help also this procedure by enhancing tissue heating [23, 150]. Coussios *et al.* [150, 151] have already successfully employed a passive focused cavitation detector to monitor the onset of this bubble enhanced heating *in vitro*. At present, researchers at the Institute of Cancer Research [152], who have been lent one of the previous prototype sensors developed in collaboration with PAL (Figure 7.2(a)), are evaluating the use of a non focused detector.

Appendix A

A.1. The SEAC MATLAB™ analysis software

The block-diagram in Figure A.1 describes the structure of the SEAC software. Once the raw data have been collected, the portion of signal to analyse is selected according to the START time specified by the operator (see sections 7.4.5 and 8.5).

The analysis algorithm, has a modular structure, and operates assuming that the secondary acoustic emissions have the typical double burst structure described in Chapter 3.

The sub-routine 'EMI_C_2' identifies the two bursts as those two portions of the signal whose power distribution, calculated as expressed in Equation (29) by the sub-function 'Engfun1', is above the threshold level of 96 percentile (see Section 5.2). The routine always detects a first burst; however a second burst may not be detected, and therefore, before progressing with its analysis, the SEAC software needs to check for this event.

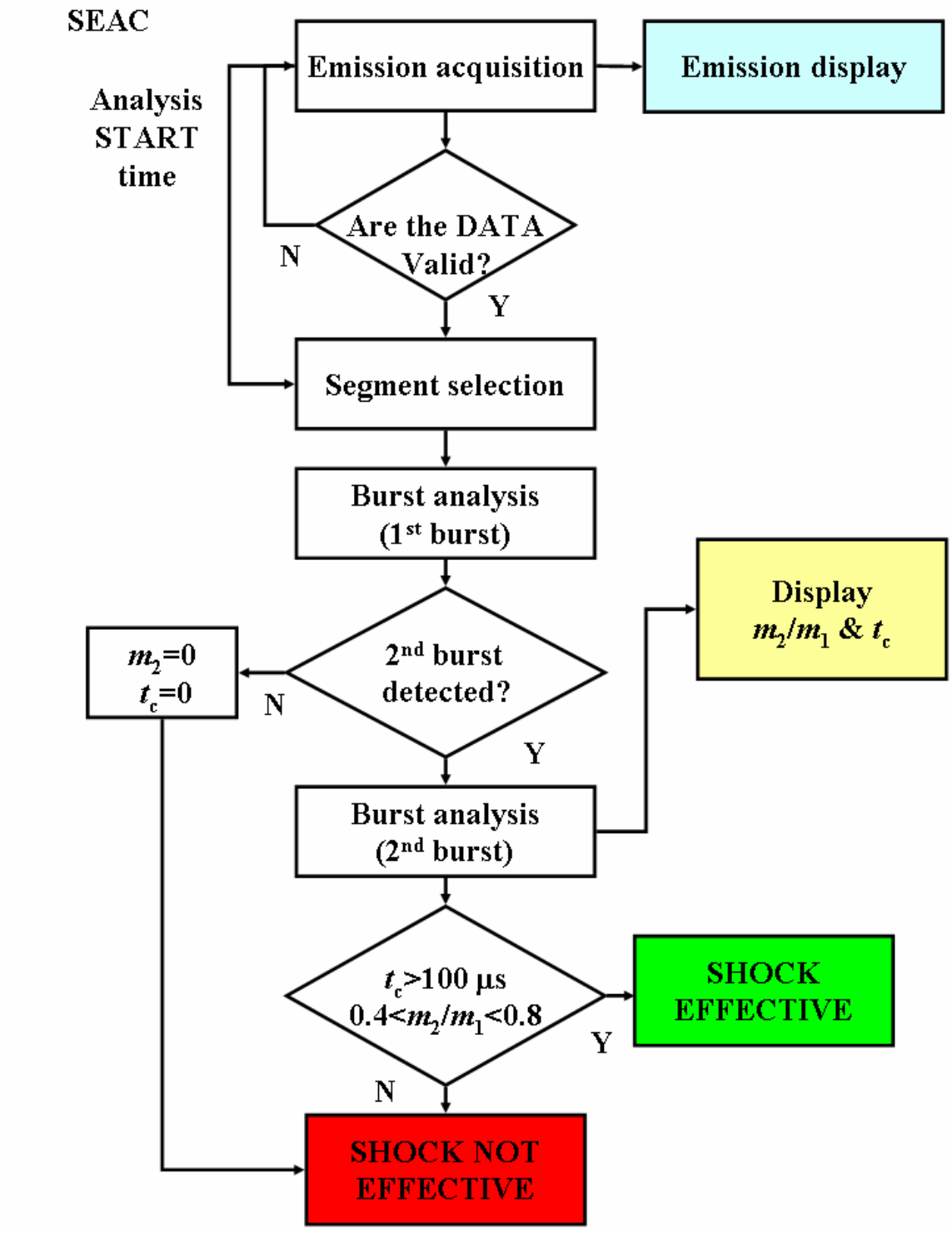

Figure A.1: Secondary Emissions Analysis in the Clinic (SEAC) block-diagram.

The analysis of each bursts is carried out by the routine 'Burst_analysis', which exploits the sub-function 'Engfun1' to calculate the distribution function of both bursts to derive their central times (t_1 and t_2), and the collapse time $t_{c,}$ as explained in Subsection 5.2. The routine also computes the maximum amplitudes of the bursts, m_1 and m_2, and their ratio m_2/m_1. When a second burst is not detected m_2, and t_c are set to zero.

At each shock the two parameters m_2/m_1 and t_c are compared against the classification rule (Equation (63)) to establish whether that particular shock is effective. At the end of the treatment, the cumulative percentage of effective shocks is calculated and the treatment is classified as *successful* if this is at least 50% (Equation (65)). If less than 40% of the shocks are classified as effective treatment is considered *unsuccessful*. To the contrary, a definite classification is not assigned when the percentage of *effective* shocks is between 30% and 49%, but the operator receives a warning (see Subsection 7.4.5 and Section 8.5 for details on the interface).

Appendix B

B.1. Clinical Trial Statistics

Table B.1 summarises some statistics relative to the treatments which occurred during the fourteen months of the clinical trials. The number of treatments (79) that could be exploited for the two phases of the clinical trial of the on-line system was only 18% of the total number of treatments scheduled for the 92 days spent in the clinic (435).

A first reduction of the treatments set (23%) was caused by cancellations, due either to patients not showing-up for treatment or the patient being referred for invasive treatment. In addition, of all the patients treated (333) only 234 (70%) were suitable for the trial. This is because 27% had to be discounted, as their stones were ureteric. One percent had latex allergy or other physical conditions (1%) which would forbid the patient taking part in the trial.

Thirdly, even if the majority of the suitable patients proved to be willing to take part in the trial (87%), there were a few that did not consent. In most cases, the refusal was due to a non comprehension of what the trial involved. This happened, for example, when the first language of the patient was not English (4%). Occasionally a patient who had consented, could not tolerate the lithotripsy treatment (10%).

A further 52 data sets were lost during the device development, as the collection of the treatments data was impaired by software or hardware malfunctioning. The software problems were due to limitations of the early version of the MATLAB™ interface and were confined to the first six months of the trial, when the interface was still in its development phase (Section 7.4.5). These problems were solved in the last two robust versions of the interface described in Chapter 7.

The hardware problems were essentially due to the accidental damage of one of the components of the acquisition system, such as one of the BNC cables (9 treatments) or the ultrasound sensor (20 treatments). This damage would affect the quality of the collected data, that would present such a very low Signal to noise Ratio (<10%) that could not be used for any analysis.

In order to spot any degradation in the acquisition system promptly and, therefore, to limit the number of data of poor quality, a Quality Assurance (QA) procedure was developed. This consisted in testing the output of the acquisition system regularly *in vitro* by means of a test ultrasound signal. It has to be clarified that electrical faults can happen also in commercial clinical devices. The use of QA procedures for testing the performance of clinical devices is, in fact, a quite a common routine that is generally performed in house by Medical Physics Departments of NHS structures. Therefore, in the vision of a future implementation of the proposed system in the clinical routine, the development of a QA procedure adds to the value of the system produced.

Finally, of all the recorded treatments with a good SNR (>10%), only those for which a minimum duration had been recorded (30%), were considered for the analysis (130). The analysis could be completed only for those patients (79) that had come back for a follow-up X-ray and both assessments (see next Subsection 8.3) had been completed.

Total number of treatments scheduled	435
Treatments cancelled	102
Treatments of Ureteric stones	90
Patients with latex allergies	4
Patients with other adverse physical conditions	5
Patients suitable for the trial	234
Patients that consented	203
Treatments interrupted after consent	21
Data lost during the device development	52
Treatments data suitable for the analysis	130
Suitable data completely assessed	79

Table B.1: Summary of treatment statistics for the clinical trial.

B.2. Clinicians feed-back

The system was highly appreciated by the clinicians of the Stone Unit at Guy's Hospital, where the clinical trials took place. The following letter was written for the EPSRC by the lead radiographer, Simon Ryves:

Guy's and St Thomas' NHS
NHS Foundation Trust

REPORT TO EPSRC

ON PROJECT EP/D503310/1

My name is Simon Ryves, Lead Radiographer Litho G&STT. I have been involved in a clinical capacity for the past 18 months with the above project.

My role has been the radiological assessment of the treatments and the interpretation of the findings of the passive ultrasound system in comparison with the past treatment radiological findings.

I have concluded that using this system:

- The (DAP) dose area product can be significantly reduced
- Targeting the stone is made more accurate by continual monitoring.
- There is a potential for reducing the length and intensity of the treatment so trauma to the patient can be minimised.
- By looking at the percentage of accurate "shocks" achieved during the treatment I have a better informed understanding of the efficacy of the session.

SIMON RYVES
LEAD RADIOGRAPHER STONE UNIT G&STT

Figure B.1: Letter to EPSRC from the lead radiographer of the Stone centre at Guy's and St Thomas' NHS Foundation Trust.

Appendix C

C.1. Press reports

The system raised the interest of the Media and Companies producing of Lithotripters; some of the published articles are reported in this Appendix. Please refer to. http://www.isvr.soton.ac.uk/fdag/Litho_07/litho_07(main).htm for a complete list of Press Coverage.

Kidney stone breakthrough

A NEW probe could dramatically improve the treatment of kidney stones. The device works by monitoring echoes inside the body to tell doctors if the treatment used to smash the stones has worked.

Stones affect twice as many men as women. They are caused by high levels of calcium in the urine or blood, which can form rock-hard pellets as small as a grain of rice or as big as a tennis ball.

They can also be brought on by dehydration, infection and obstruction of urine.

The usual treatment is lithotripsy — thousands of sound waves are beamed into the body to break up the stones so the body can dispose of them.

X-rays are taken before and after treatment, but these are not reliable. Instead, doctors wait to see if the symptoms return.

Researchers from Southampton University and Guy's and St Thomas's hospitals came up with a probe which is taped to the patient's side during treatment.

When a stone is intact, the sound it gives off is like a 'tick'; when it has been smashed into pieces, the noise changes to a 'tock'.

The device may also operate on a 'traffic light' system. The computer would flash red if the treatment was not working, amber if it was on target but not breaking down the stone and green if the stone was being hit.

Figure C.1: Daily Mail, 1st November 2004, pg. 43.

SMART THINKING: Professor Tim Leighton, who has helped to invent the new 'smart stethoscope'.
Echo picture by Gordon Agg-Jones. Order no: rad75d77.

A sound way to speed up patients' treatment

Invention could save thousands of pounds

By **Clare Kennedy** ◆
newsdesk@soton-echo.co.uk

A SOUTHAMPTON University professor has helped to invent a new 'smart stethoscope' that can hear when a kidney stone has been successfully treated.

Professor Tim Leighton, of the university's world-renowned Institute of Sound and Vibration Research, says the device could prevent healthy kidney tissue being destroyed, make treatments quicker and save hospitals thousands of pounds.

The stethoscope listens to echoes created by shock wave therapy known as lithotripsy, used to shatter kidney stones.

Until now doctors have been unable to tell when the treatment has succeeded and patients sometimes experience more shocks than necessary.

They also have to have X-rays taken before and after treatment but these often fail to show whether the kidney stone has been broken up.

"It's a bit like a railwayman walking along the length of a train, hitting the metal wheels with a hammer," said Prof Leighton of the listening device.

"If the wheel rings nicely, he knows that it's not cracked. If the wheel is cracked it gives a duller sound.

"We are looking for the stone to go from being intact at the start of treatment, when it will give a nice 'tick' sound, to being fragmented at the end of the treatment, when it will give a duller 'tock' sound."

Already 50 patients have benefited from the invention at London hospitals Guys and St Thomas.

Now Prof Leighton, along with Dr Andrew Coleman of Guy's and St Thomas NHS Foundation Trust and their team of researchers, are hoping to expand the use of the smart stethoscope nationwide.

They are currently in negotiations with the university's Centre for Enterprise and Innovation and manufacturers of lithotripters to draw up contracts.

Although Prof Leighton first began investigating the Smart Stethoscope in 1990 it was only thanks to funding from the Engineering and Physical Science Research Council four years ago that the project was able to go ahead.

Kidney stones: the facts

KIDNEY stones are hard, stone-like masses that can form in one kidney or both.

They can become very painful when they travel from the kidney to the bladder and can cause bleeding and block the flow of urine.

If left untreated, they can cause permanent damage to the kidneys.

Men are more prone to get kidney stones than women.

Other factors in getting kidney stones include a family history of them, eating a high-protein and low-fibre diet, and not drinking enough fluids.

Symptoms include back pain, nausea and vomiting, a frequent urge to urinate, fever and chills.

Figure C.2: Southern Daily Echo, 2nd December 2004, pg. 22.

Figure C.3: BBC Southampton News 30th October 2004, http://news.bbc.co.uk/1/hi/health/3963025.stm.

Figure C.4: The author (in the middle) celebrating with her supervisor Prof. T. G. Leighton (on the right) and Dr. A. J. Coleman (on the left) at the London NHS award 2007 ceremony.

References

[1] Coleman A. J., Whitlock M., Leighton T. G. and Saunders J. E.: The spatial distribution of cavitation induced acoustic emission, sonoluminescence and cell lysis in the field of a shock wave lithotripter. Phys. Med. Biol., 1993, 38 (11), 1545-1560.

[2] Coleman A. J., Choi M. J., Saunders J. E., Leighton T. G.: Acoustic emission and sonoluminescence due to cavitation at the beam focus of an electrohydraulic shock wave lithotripter. Ultrasound Med. Biol., 1992, 18 (3), 267-281.

[3] Leighton T. G.: The Acoustic Bubble, 1994, London. Academic Press.

[4] Leighton T. G., Birkin P. R., Hodnett M., Zeqiri B., Power J. F., Price G. J., Mason, T., Plattes, M., Dezhkunov, N., and Coleman, A. J.: Characterisation of measures of reference acoustic cavitation (COMORAC): An experimental feasibility trial. Bubble and Particle Dynamics in Acoustic Fields: Modern Trends and Applications, 2005, Kerala. 37-94.

[5] Zeqiri B., Davies S. C., Gelat P. N., Hodnett M. and Lula U I: Novel sensors for monitoring acoustic cavitation. 1, 417-420.

[6] Zeqiri B., Gelat P. N., Hodnett M., and Lee N. D.: A novel sensor for monitoring acoustic cavitation. Part II: prototype performance evaluation. IEEE Transaction on Ultrasonics, Ferroelectrics, and Frequency Control, 2003, 50 (10), 1351-1362.

[7] Zeqiri B., Gelat P. N., Hodnett M., and Lee N. D.: A novel sensor for monitoring acoustic cavitation. Part I: concept, theory, and prototype development. IEEE Transaction on Ultrasonics, Ferroelectrics, and Frequency Control, 2003, 50 (10), 1342-1350.

[8] Auge B. K. and Preminger G. M.: Update on shock wave lithotripsy technology. Curr. Opin. Urol., 2002, 12 (4), 287-290.

[9] Coleman A. J. and Saunders J. E.: A review of the physical properties and biological effects of the high amplitude acoustic field used in extracorporeal lithotripsy. Ultrasonics, 1993, 31 (2), 75-89.

[10] Delius M.: Biological effects of extracorporeal shock waves. Proceedings of the IEEE Ulrasonics Symposium, 1989, 983-990.

[11] Madbouly, K., Sheir, K. Z., Elsobky, E., Eraky, I., and Kenawy, M.: Risk factors for the formation of a steinstrasse after extracorporeal shock wave lithotripsy: a statistical model. J.Urol., 2002, 167 (3), 1239-1242.

[12] Seitz G., Neisius D., Wernert N., and Gebhardt T.: Pathological-anatomical alterations of huma kidneys following extracorporeal piezoelectric shock wave lithotripsy. J. Litho. Stone Dis., 1991, 3 (2), 165-170.

[13] Skolarikos A., Alivizatos G. and de la Rosette J.: Extracorporeal shock wave lithotripsy 25 years later: complications and their prevention. Eur. Urol., 2006, 50 (5), 981-990.

[14] Madaan S. and Joyce A. D.: Limitations of extracorporeal shock wave lithotripsy. Curr. Opin. Urol., 2007, 17 (2), 109-113.

[15] Tan Y. M., Yip S. K., Chong T. W., Wong M. Y., Cheng C. and Foo K. T.: Clinical experience and results of ESWL treatment for 3,093 urinary calculi with the Storz Modulith SL 20 lithotripter at the Singapore general hospital. Scand. J. Urol. Nephrol., 2002, 36 (5), 363-367.

[16] Tolley D. A. and Downey P.: Current advances in shock wave lithotripsy. Curr. Opin. Urol., 1999, 9 (4), 319-323.

[17] Schmitt R. M., Wuster H., Kraus W. and Bibinger M.: The effects of errors in positioning lithotriptor and imaging kidney stones ultrasound. Annual international conference of the IEEE Engineering in Medicine and Biology Society, 1990, 12 (1), 252-253.

[18] Chang C. C., Liang S. M., Pu Y. R., Chen C. H., Manousakas I., Chen T. S., Kuo C. L., Yu F. M. and Chu Z. F.: In vitro study of ultrasound based real-time tracking of renal stones for shock wave lithotripsy: part 1. J. Urol., 2001, 166 (1), 28-32.

[19] Sandilos P., Tsalafoutas I., Koutsokalis G., Karaiskos P., Georgiou E., Yakoumakis E. and Vlahos L.: Radiation doses to patients from extracorporeal shock wave lithotripsy. Health Phys., 2006, 90 (6), 583-587.

[20] Olsson L., Almquist L. O., Grennberg A. and Holmer N. G.: Analysis and classification of secondary sounds from the disintegration of kidney stones with acoustic shock waves. Ultrasound Med. Biol., 1991, 17 (5), 491-495.

[21] Chang C. C., Manousakas I., Pu Y. R., Liang S. M., Chen C. H., Chen T. S., Yu F. M., Yang W. H., Tong Y. C. and Kuo C. L.: In vitro study of ultrasound based real-time tracking for renal stones in shock wave lithotripsy: Part II--a simulated animal experiment. J. Urol., 2002, 167 (6), 2594-2597.

[22] Bohris C., Bayer T. and Lechner C.: Hit/miss monitoring of ESWL by spectral doppler ultrasound. Ultrasound Med. Biol., 2003, 29 (5), 705-712.

[23] Coussios C. C and Roy R. A.: Applications of Acoustics and Cavitation to Noninvasive Therapy and Drug Delivery. Annu. Rev. Fluid. Mech. 2008, 40 (395-420.

[24] Crum L. A.: Cavitation microjets as a contributory mechanism for renal calculi disintegration in ESWL. J. Urol., 1988, 140 (6), 1587-1590.

[25] Sass W., Braunlich M., Dreyer H. P., Matura E., Folberth W., Preismeyer H. G. and Seifert J.: The mechanisms of stone disintegration by shock waves. Ultrasound Med. Biol., 1991, 17 (3), 239-243.

[26] Carnell M. T. and Emmony D. C.: A schlieren study of the interaction between a lithotripter shock wave and a simulated kidney stone. Ultrasound Med. Biol., 1995, 21 (5), 721-724.

[27] Kedrinskii V. K.: The role of cavitation effects in the mechanisms of destruction and explosive processes. Shock waves, 1997, 7, 63-76.

[28] Lokhandwalla M. and Sturtevant B.: Fracture mechanics model of stone comminution in ESWL and implications for tissue damage. Phys. Med .Biol., 2000, 45 (7), 1923-1940.

[29] Cleveland R. O., McAteer J. A. and Muller R.: Time-lapse nondestructive assessment of shock wave damage to kidney stones *in vitro* using micro-computed tomography. J. Acoust. Soc. Am., 2001, 110 (4), 1733-1736.

[30] Xi X. and Zhong P.: Dynamic photoelastic study of the transient stress field in solids during shock wave lithotripsy. J. Acoust. Soc. Am., 2001, 109 (3), 1226-1239.

[31] Zhu S., Cocks F. H., Preminger G. M. and Zhong P.: The role of stress waves and cavitation in stone comminution in shock wave lithotripsy. Ultrasound Med. Biol., 2002, 28 (5), 661-671.

[32] Ikeda T., Yoshizawa S., Tosaki M., Allen J. S., Takagi S., Ohta N., Kitamura T. and Matsumoto Y.: Cloud cavitation control for lithotripsy using high intensity focused ultrasound. Ultrasound Med. Biol., 2006, 32 (9), 1383-1397.

[33] Cleveland R. O. and Tello J. S.: Effect of the diameter and the sound speed of a kidney stone on the acoustic field induced by shock waves. Acoust. Res. Lett. Online, 2004, 5 (2), 37-43.

[34] Cleveland R. O. and Sapozhnikov O. A.: Modelling elastic wave propagation in kidney stones with application to shock wave lithotripsy. J.Acoust.Soc.Am., 2005, 118 (4), 2667-2676.

[35] Eisenmenger W.: The mechanisms of stone fragmentation in ESWL. Ultrasound Med. Biol., 2001, 27 (5), 683-693.

[36] Coleman A. J., Kodama T., Choi M. J., Adams T. and Saunders J. E.: The cavitation threshold of human tissue exposed to 0.2-MHz pulsed ultrasound: preliminary measurements based on a study of clinical lithotripsy. Ultrasound Med. Biol., 1995, 21 (3), 405-417.

[37] Hausler E., Rech V. and Wache M.: Transient cavitation based ultrasonic lithotriptor positioning system. Annual international conference of the IEEE Engineering in Medicine and Biology Society, 1991, 13, 185-186.

[38] Ball G. J., Howell B.P., Leighton T. G. and Schofield M. J.: Shock-induced collapse of a cylindrical air cavity in water: a Free-Lagrange simulation. Shock Waves, 2000, 10, 265-276.

[39] Jamaluddin A. R., Ball G. J. and Leighton T. G.: Free-Lagrange simulations of Shock/Bubble Interaction in Extracorporeal Shock Wave Lithotripsy. Proceedings of the 2nd International Conference on Computational Fluid Dynamics, 2003, 541-546.

[40] Turangan C. K. and Ball G. J.: A Free-Lagrange Simulation of Cavitation Bubble collapse near a Rigid Boundary. Proceedings of the 23rd International Symposium on shock Waves, 2001 793-799.

[41] Choi M. J., Coleman A. J. and Saunders J. E.: The influence of fluid properties and pulse amplitude on bubble dynamics in the field of a shock wave lithotripter. Phys. Med. Biol., 1993, 38 (11), 1561-1573.

[42] Choi M. J.: Numerical implementation of the Gilmore model of bubble dynamics. Medical Physics Directorate St Thomas' Hospital London.Internal Report, 1994.

[43] Guzman H. R., Nguyen D. X., Khan S. and Prausnitz M. R.: Ultrasound-mediated disruption of cell membranes I. Quantification of molecular uptake and cell viability. J. Acoust. Soc. Am., 2001, 110 (1), 588-596.

[44] Haake M., Deike B., Thon A. and Schmitt J.: Exact focusing of extracorporeal shock wave therapy for calcifying tendinopathy. Clin. Orthop., 2002, (397), 323-331.

[45] Maier M., Milz S., Tischer T., Munzing W., Manthey N., Stabler A., Holzknecht N., Weiler C., Nerlich A., Refior H. J. and Schmitz C.: Influence of extracorporeal shock-wave application on normal bone in an animal model in vivo. Scintigraphy, MRI and histopathology. J.Bone Joint Surg. Br., 2002, 84 (4), 592-599.

[46] Mesiwala A. H., Farrell L., Wenzel H. J., Silbergeld D. L., Crum L. A., Winn H. R. and Mourad P. D.: High-intensity focused ultrasound selectively disrupts the blood-brain barrier in vivo. Ultrasound Med. Biol., 2002, 28 (3), 389-400.

[47] Song J., Tata D., Li L., Taylor J., Bao S. and Miller D.: Combined shock-wave and immunogene therapy of mouse melanoma and renal carcinoma tumours. Ultrasound Med. Biol., 2002, 28 (7), 957

[48] von Eiff C., Overbeck J., Haupt G., Herrmann M., Winckler S., Richter K. D., Peters G. and Spiegel H. U.: Bactericidal effect of extracorporeal shock waves on Staphylococcus aureus. J.Med. Microbiol., 2000, 49 (8), 709-712.

[49] Gerdesmwyer L., von Eiff C., Horn C., Henne M., Roessner M., Diehl P. and Gollwitzer H.: Antibacterial effects of extracorporeal shock wave. Ultasound Med. Biol., 2005, 31 (1), 115-119.

[50] Lamotte M., Annemans L., Bridgewater B., Kendall S. and Siebert M.: A health economic evaluation of concomitant surgical ablation for atrial fibrillation. Eur.J.Cardiothorac. Surg., 2007, 32 (5), 702-710.

[51] Nakagawa H., Antz M., Wong T., Schmidt B., Ernst S., Ouyang F., Vogtmann T., Wu R., Yokoyama K., Lockwood D., Po S. S., Beckman K. J., Davies D. W., Kuck K. H. and Jackman W. M.: Initial experience using a forward directed, high-intensity focused ultrasound balloon catheter for pulmonary vein antrum isolation in patients with atrial fibrillation. J.Cardiovasc. Electrophysiol., 2007, 18 (2), 136-144.

[52] Coleman A. J. and Saunders J. E.: Comparison of extracorporeal shock-wave lithotripters. Lithotripsy II. Textbook of second generation extracorporeal lithotripsy, 1987, London. BDI Publishing. Chapter 8, 121-131.

[53] Coleman A. J. and Saunders J. E.: A survey of the acoustic output of commercial extracorporeal shock wave lithotripters. Ultrasound Med. Biol., 1989, 15 (3), 213-227.

[54] Cunningham K. B., Coleman A. J., Leighton T. G. and White P. R.: Characterising *in vivo* acoustic cavitation during lithotripsy with time-frequency methods. Acoustics Bulletin, 2002, 26 (5), 10-16.

[55] Church C. C.: A theoretical study of cavitation generated by an extracorporeal shock wave lithotripter. J. Acoust. Soc. Am., 1989, 86 (1), 215-227.

[56] Delius M., Muller M., Vogel A. and Brendel W.: Extracorporeal Shock Waves: Proprieties and principles of generation. Biliary Lithotripsy, 1989, London. Year Book medical Publishers,Inc.9-15.

[57] Ison K. T.: Physical and technical introduction to lithotripsy. Lithotripsy II. Textbook of second generation extracorporeal lithotripsy, 1987, London. BDI Publishing. Chapter 2, 7-12.

[58] Folberth W., Kohler G., Rohwedder A. and Matura E.: Pressure distribution and energy flow in the focal region of two different electromagnetic shock wave sources. J. Stone. Dis., 1992, 4 (1), 1-7.

[59] Leighton T. G.: What is ultrasound? Prog. Biophys. Mol. Biol., 2007, 93 ((1-3)), 3-83.

[60] Batchelar D. L., Chun S. S., Wollin T. A., Tan J. K., Beiko D. T., Cunningham I. A. and Denstedt J. D.: Predicting urinary stone composition using X-ray coherent scatter: a novel technique with potential clinical applications. J. Urol., 2002, 168 (1), 260-265.

[61] Johrde L. G. and Cocks F. H.: Fracture strength studies of renal calculi. J. Mat. Sc. Letters, 1985, 4, 1264-1265.

[62] Ebrahimi F. and Wang F.: Fracture behaviour of urinary stones under compression. J. Biomed. Mat. Res., 1989, 23, 507-521.

[63] Stranne S. K., Cocks F. H. and Gettliffe R.: Mechanical property studies of human gallstones. J.Biomed. Mat. Res., 1990, 24, 1049-1057.

[64] Liu Y. and Zhong P.: BegoStone-a new stone phantom for shock wave lithotripsy research (L). J. Acoust. Soc. Am., 2002, 112 (4), 1265-1268.

[65] Nambiraj N. A.: Thesis synopsis: a study of the constituents and properties of urinary stones and its application to stone fragility in extracorporeal shock wave lithotripsy. BJU. Int., 2001, 88 (4), 443

[66] Singh V. R. and Agarwal R.: Mechanical and ultrasounic parameters of kidney stones. J. Litho.Stone Dis., 1990, 2 (2), 117-123.

[67] Cheng P. T., Reid A. D. and Pritzker K. P.: Ultrastructural studies of crystal-organic matrix relations in renal stones. Scan. Electron. Microsc., 1985, (Pt 1), 201-207.

[68] Singh V. R., Lafaut J. P., Wevers M., Vincent C. and Baert L.: Stress-generated potential in renal calculi and lithotripsy. Proceedings of the first joint BMES/EMBS conference, 1999, Atlanta, 830.

[69] Heimbach D., Munver R., Zhong P., Jacobs J., Hesse A., Muller S. C. and Preminger G. M.: Acoustic and mechanical properties of artificial stones in comparison to natural kidney stones. J. Urol., 2000, 164 (2), 537-544.

[70] Rassweiler J.: Acoustic and mechanical properties of artificial stones in comparison to natural kidney stones. J. Urol., 2000, 164 (2), 273

[71] Eisenmenger W., Du X. X., Tang C., Zhao S., Wang Y., Rong F., Dai D., Guan M. and Qi A.: The first clinical results of "wide-focus and low-pressure" ESWL. Ultrasound Med. Biol., 2002, 28 (6), 769-774.

[72] Chaussy C., Schmiedt E., Jocham D., Brendel W., Forssmann B. and Walther V.: First clinical experience with extracorporeally induced destruction of kidney stones by shock waves. 1981. J. Urol., 2002, 167 (5), 1957-1960.

[73] Coleman A. J., Saunders J. E., Crum L. A. and Dyson M.: Acoustic cavitation generated by an extracorporeal shockwave lithotripter. Ultrasound Med. Biol., 1987, 13 (2), 69-76.

[74] Lifshitz D. A., Williams J. C. Jr., Sturtevant B., Connors B. A., Evan A. P. and McAteer J. A.: Quantitation of shock wave cavitation damage in vitro. Ultrasound Med. Biol., 1997, 23 (3), 461-471.

[75] Zhong P., Lin H., Xi X., Zhu S and Bhogte E. S.: Shock wave-inertial microbubble interaction: Methodology, physical characterization, and bioeffect study. J. Acoust. Soc. Am., 1999, 105 (3), 1997-2009.

[76] Holmer N. G., Almquist L. O., Hertz T. G., Holm A., Lindstedt E., Persson H. W. and Hertz C. H.: On the mechanism of kidney stone disintegration by acoustic shock waves. Ultrasound Med. Biol., 1991, 17 (5), 479-489.

[77] Owen N. R., Bailey M. R., Crum L. A., Sapozhnikov O. A. and Trusov L. A.: The use of resonant scattering to identify stone fracture in shock wave lithotripsy. J.Acoust.Soc. Am., 2007, 121 (1), EL41-EL47.

[78] Kodama T. and Takayama K.: Dynamic behaviour of bubbles during extracorporeal shock-wave lithotripsy. Ultrasound Med. Biol., 1998, 24 (5), 723-738.

[79] Zhong P., Cioanta I., Cocks F. H. and Preminger G. M.: Inertial cavitation and associated acoustic emission produced during electrohydraulic shock wave lithotripsy. J. Acoust. Soc. Am., 1997, 101 (5), 2940-2950.

[80] Ball G. J., Howell B.P. Leighton, T. G. and Schofield M. J.: Shock-induced collapse of a cylindrical air cavity in water: a Free-Lagrange simulation. The 22nd International Symposium on Shock Waves, 2000, Paper 0060, 1363-1368.

[81] Jamaluddin A. R., Ball G. J. and Leighton T. G.: Free-Lagrange simulations of shock/bubble interaction in shock wave lithotripsy. Proceedings of the 24th International Symposium on Shock Waves, 2004, 1211-1216.

[82] Leighton T. G.: From seas to surgeries, from babbling brooks to baby scans: the acoustics of gas bubbles in liquids. Int. J. Mod. Phys. B, 2004, 18 (25), 3267-3314.

[83] Turangan C. K., Jamaluddin A. R., Ball G. J. and Leighton T. G.: Free-Lagrange simulations of expansion and jetting collapse of air bubbles in water. J. Fluid. Mech., 2008, 598 (1-25.

[84] Carnell M. T. and Emmony D. C.: Quantitative Schlieren measurements of a high energy electromagnetic transducer acoustic shock field. Ultrasound Med. Biol., 1995, 26 (6), 385-391.

[85] Carnell M. T., Alcock R. D. and Emmony D. C.: Optical imaging of shock waves produced by a high-energy electromagnetic transducer. Phys. Med. Biol., 1993, 38 (11), 1575-1588.

[86] Bailey M. R., Pishchalnikov Y. A., Sapozhnikov O. A., Cleveland R. O., McAteer J. A., Miller N. A., Pishchalnikova I. V., Connors B. A., Crum L. A. and Evan A. P.: Cavitation detection during shock-wave lithotripsy. Ultrasound Med. Biol., 2005, 31 (9), 1245-1256.

[87] Bailey M. R., Crum L. A., Pishchalnikov Y. A., McAteer J. A., Pishchalnikova I. V. and Evan A. P.: Observation of cavitation during shock wave lithotripsy. J. Acoust. Soc. Am., 2005, 117 (4), 2371.

[88] Cleveland R. O., Sapozhnikov O. A., Bailey M. R. and Crum L. A.: A dual passive cavitation detector for localized detection of lithotripsy-induced cavitation *in vitro*. J. Acoust. Soc. Am., 2000, 107 (3), 1745-1758.

[89] Bailey M. R., Pishchalnikov Y. A., Sapozhnikov O. A., Cleveland R. O., McAteer J. A., Miller N. A., Pishchalnikova I. V., Connors B. A., Crum L. A. and Evan A. P.: Cavitation detection during shock-wave lithotripsy. Ultrasound Med. Biol., 2005, 31 (9), 1245-1256.

[90] Pishchalnikov Y. A., McAteer J. A., Williams J. C. Jr., Pishchalnikova I. V. and VonDerHaar R. J.: Why stones break better at slow shockwave rates than at fast rates: in vitro study with a research electrohydraulic lithotripter. J.Endourol., 2006, 20 (8), 537-541.

[91] Matula T. J., Hilmo P. R., Bailey M. R. and Crum L. A.: In vitro sonoluminescence and sonochemistry studies with an electrohydraulic shock-wave lithotripter. Ultrasound Med. Biol., 2002, 28 (9), 1199-1207.

[92] Bourne N. K. and Fishman E. K.: Bubble collapse and initiation of explosion. Proc. R. Soc. Lond., 1991, 435, 423-435.

[93] Leighton T. G., Ho W. L. and Flaxman R.: Sonoluminescence from the unstable collapse of a conical bubble. Ultrasonics, 1997, 35, 399-405.

[94] Leighton T. G., Cox B. T. and Phelps A. D.: The Rayleigh-like collapse of a conical bubble. J. Acoust. Soc. Am., 2000, 107 (1), 130-142.

[95] Sassaroli E. and Hynynen K.: Cavitation threshold of microbubbles in gel tunnels by focused ultrasound. Ultrasound Med. Biol., 2007, 33 (10), 1651-1660.

[96] Coleman A. J., Choi M. J. and Saunders J. E.: Detection of acoustic emission from cavitation in tissue during clinical extracorporeal lithotripsy. Ultrasound Med.Biol., 1996, 22 (8), 1079-1087.

[97] Leighton T. G., White P. R. and Marsden M. A.: Applications of one-dimensional bubbles to lithotripsy, and to diver response to low frequency sound. Acta Acoustica, 1995, 3 (517-529.

[98] Leighton T. G., White P. R. and Marsden M. A.: The one-dimensional bubble: An unusual oscillator,with applications to human bioeffects of underwater sound. Eur. J. Phys., 1995, 16 (275-281.

[99] Leighton T. G., Phelps A. D., Cox B. T. and Ho W. L.: Theory and preliminary measurements of the Rayleigh-like collapse of a conical bubble. Acoustica with Acta Acoustica, 1998, 84 (6), 1014-1024.

[100] Leighton T. G., Cox B. T., Birkin P. R. and Bayliss T.: The Rayleigh-like collapse of a conical bubble: Measurements of meniscus, liquid pressure, and electrochemistry. Proceedings of the 13th Meeting of the Acoustical Society of America and the 2nd Convention of the European Acoustic Association, 1999, Berlin, Paper 3APAB_1 (4pp).

[101] Prosperetti A., Crum L. A. and Commander K. W.: Nonlinear bubble dynamics. J. Acoust. Soc. Am., 1988, 83 (2), 502-514.

[102] Chapman R. B. and Plesset M. S.: Thermal effects in free oscillation of gas bubbles. Trans ASME D, J. Basic. Eng., 1971, 93, 373-376.

[103] Prosperetti A.: Nonlinear oscillation of gas bubbles in liquid: steady-state solutions. J. Acoust. Soc. Am., 1974, 58 (3), 878-885.

[104] Prosperetti A. and Hao Y.: Modelling of spherical gas bubble oscillations and sonoluminescence. Phil. Trans. R. Soc. Lond. A, 1999, 357, 203-223.

[105] Nigmatulin R. I and Khabeev N. S.: Heat exchange between a gas bubble and a liquid. Fluid. Dyn., 1974, 9 (5), 759-764.

[106] Nigmatulin R. I and Khabeev N. S.: Dynamics of vapour-gas bubbles. Fluid. Dyn., 1977, 11 (6), 867-871.

[107] Prosperetti A.: The thermal behaviour of oscillating gas bubbles. J. Fluid. Mech., 1991, 222 587-616.

[108] Leighton T. G., Meers S. D. and White P. R.: Propagation trough nonlinear time-dependent bubble clouds and the estimation of bubble populations from measured acoustic characteristics. Proc. R. Soc. Lond. A, 2004, 460, 2521-2550.

[109] Prosperetti A. and Lezzi A.: Bubble dynamics in a compressible liquid. Part 1. First-order theory. J. Fluid. Mech., 1986, 168, 457-478.

[110] Zhu S and Zhong P.: Shock wave-inertial microbubble interaction: A theoretical study based on the Gilmore formulation for bubble dynamics. J. Acoust. Soc. Am., 1999, 106 (5), 3024-3033.

[111] Bailey M. R.: Control of acoustic cavitation with application to lithotripsy. Technical Report under Grant N00014-89-J-1109 and ARL: UT IR & D Program. Applied Research Laboratories. The University of Texas. Report No. ARL-TR-97-1, 1997.

[112] Morfey C. L.: Dictionary of Acoustics, 2001, London. Academic Press

[113] Beyer R. T.: The parameter B/A. In: Hamilton M. F. Blackstock D. T. (Eds.). Nonlinear Acoustics, 1998, San Diego. Academic Press. Chapter 2, 25-37.

[114] Cleveland R. O., Lifshitz D. A., Connors B. A., Evan A. P., Willis L. R. and Crum L. A.: In vivo pressure measurements of lithotripsy shock waves in pigs. Ultrasound Med. Biol., 1998, 24 (2), 293-306.

[115] Owen N. R., Sapozhnikov O. A., Bailey M. R., Trusov L. and Crum L. A.: A Passive Technique to Identify Stone Comminution During Shock Wave Lithotripsy. Proceedings of the first Annual International Urolithiasis Research Symposium. Evan A. P., Lingeman J. E., Williams J. C. Jr. (Eds.), 2007, 364-367.

[116] Owen N. R., Sapozhnikov O. A., Bailey M. R., Trusov L. and Crum L. A.: Use of acoustic scattering to monitor kidney stone fragmentation during shock wave lithotripsy. Proceedings of the 2006 IEEE Ultrasonic Symposium, 2006, 736-739.

[117] Wells P. N. T.: Biomedical Ultrasonics, 1977, Academic Press.

[118] Fedele F., Coleman A. J. and Leighton T. G.: Use of cylindrical PVdF hydrophone in a study of cavitation adjacent to stone phantoms during extracorporeal shockwave lithotripsy. Proceedings of the IPEM Annual Scientific Meeting, Bath, 2003, 66.

[119] Fedele F.: Design of an acoustic device for monitoring shock-tissue interactions during Extracorporeal Shock Wave Lithotripsy. University of Southampton. MPhil/PhD Transfer report. Report No. 2004,

[120] Fedele F., Coleman A. J., Leighton T. G., White P. R. and Hurrell A. M.: A new sensor for detecting and characterising acoustics cavitation in vivo during ESWL. Proceedings of the Spring Conference of the Institute of Acoustics, 2004, 26(1), 422-432.

[121] Fedele F., Coleman A. J., Leighton T. G., White P. R. and Hurrell A. M.: Development of a new diagnostic sensor for Extra-corporeal Shockwave Lithotripsy. Proceedings of the first conference in Advanced Metrology for Ultrasound in Medicine. J. Phys.: conference Series 1, 2004, 134-139.

[122] Fedele F., Coleman A. J., Leighton T. G., White P. R. and Hurrell A. M.: Development of a new diagnostic device for Extracorporeal Shock-Wave Lithotripsy. Proceedings of the X Mediterranean Conference on Medical and Biological Engineering "Health in the Information Society". IFMBE Proceedings, 2004, paper no.54 (4 pg).

[123] Eisenmenger W.: Eine elektromagnetische Impulsschallquelle zur Erzeugung von Druckstößen in Flüssigkeiten. Akust.Beihefte, 1962, 185-202.

[124] Weisstein E. W.: Sphere Packing.
Webpage http://mathworld.wolfram.com/SpherePacking.html. Last accessed 2005.

[125] Torquato S., Truskett T. M. and Debenedetti P. G.: Is random close packing of spheres well defined? Phys. Rev. Lett., 2000, 84, 2064-2067.

[126] Pallavi L. and Wei S.: Computer modelling approach for microsphere-packed bone scaffold. Comput. Aided Design., 2005, 36, 487-497.

[127] Altman D. G. and Bland J. M.: Diagnostic tests. 1: Sensitivity and specificity. BMJ, 1994, 308 (6943), 1552

[128] Papoulis A. and Pillai S. U.: Probability, Random Variables and Stochastic processes, 2001, McGraw-Hill

[129] Szabo T.: Diagnostic Ultrasound Imaging: Inside Out, 2004, London. Elsevier Academic Press.

[130] International Commision on Radiological Protection: ICRP Publication 23: Reference Man: Anatomical, Physiological and Metabolic Characteristics, 1975, Elsevier Science

[131] Bendat J. S. and Piersol A. G.: Random Data: analysis and Measurements Procedures., 1986, John wiley & Sons Inc.

[132] Leighton T. G., Coleman A. J., Fedele F. and White P. R.: A passive acoustic system for evaluating the *in-vivo* performance of extracorporeal shockwave lithotripsy.Patent No. 0319863.7, 2004.

[133] Hesse C. W. and James C. J.: Blind source separation through multispectral signal decorrelation applied to multi-channel ictal EEG. Proceedings of the X Mediterranean

Conference on Medical and Biological Engineering "Health in the Information Society". IFMBE Proceedings, 2004, paper 93 4 pages (CD).

[134] James C. J. and Hesse C. W.: Semi-Blind Source Separation in EM Brain Signal Processing. Proceedings of the 3rd IEE International Seminar on Medical Applications of signal Processing, 2005, London. Printed by Wrightsons, Earls Barton, Northants.

[135] Morrison D. F.: Multivariate Statistical Methods, 1990, New York. McGraw-Hill.

[136] Everitt S. and Dunn G.: Principal components analysis. Applied Multivariate Data Analysis, 2001, London. Arnold. Chapter 3, 48-73.

[137] Delacretaz G., Rink K., Pittomvils G., Lafaut J. P., Vandeursen H. and Boving R.: Importance of the implosion of ESWL-induced cavitation bubbles. Ultrasound Med Biol., 1995, 21 (1), 97-103.

[138] Tong H. L., Zhong P., Cocks F. H. and Preminger G. M.: Transient cavitation and associated shock wave generation near a stone surface during electrohydraulic lithotripsy. BED-Advances in Bioengineering ASME, 1996, 33, 45-46.

[139] Mourad P. D.: Introductory Medical Statistics, 1976, London. Pitman Medical Publishing

[140] Duck F. A., Baker A. C. and Starritt H. C.: Ultrasound in Medicine, 2004, Bristol and Philadelphia. Institute of Physics Publishing

[141] Ellis H., Logan B. M. and Dixon A.: Human cross-sectional anatomy. Atlas of body selections and CT images, 1991, Butterworth-Heinemann Ltd.

[142] Carlson A. B.: Signal Transmission and Filtering. Communication Systems. An Introduction to Signals and Noise in Electrical Communication, 1986, Singapore. McGraw-Hill International. Chapter 3, 97-100.

[143] Leighton T. G., Fedele F., Coleman A. J., McCarthy C., Ryves S., Hurrell A. M., De Stefano A. and White P. R.: A passive acoustic device for real-time monitoring of the efficacy of shockwave lithotripsy treatment. Ultrasound Med. Biol., 2008 (in press).

[144] Viera A. J. and Garrett J. M.: Understanding Interobserver Agreement: The Kappa Statistic. Farm. Med., 2005, 37 (5), 360-363.

[145] Cleveland R. O., Anglade R. and Babayan R. K.: Effect of stone motion on in vitro comminution efficiency of Storz Modulith SLX. J. Endourol., 2004, 18 (7), 629-633.

[146] Church C. C.: Spontaneous homogeneous nucleation, inertial cavitation and the safety of diagnostic ultrasound. Ultrasound Med. Biol., 2002, 28 (10), 1349-1364.

[147] Leighton T. G. and Dumbrell H. A.: New approaches to contrast agent modelling. Proceedings of the First Conference in Advanced Metrology for Ultrasound in Medicine. J. Phys.: Conference Series,2004,91-96.

[148] Ter Haar G. and Coussios C.: High intensity focused ultrasound: past, present and future. Int.J.Hyperther., 2007, 23 (2), 85-87.

[149] Ter Haar G. and Coussios C.: High intensity focused ultrasound: physical principles and devices. Int.J.Hyperther., 2007, 23 (2), 89-104.

[150] Coussios C. C., Farny C. H., Haar G. T. and Roy R. A.: Role of acoustic cavitation in the delivery and monitoring of cancer treatment by high-intensity focused ultrasound (HIFU). Int.J.Hyperther., 2007, 23 (2), 105-120.

[151] Coussios C., Collin J. R. T. and Muckle A. P.: Non-Invasive Monitoring and Control of Inertial Cavitation Dynamics during HIFU Exposure In Vitro. Proceedings of the 6th International Symposium on Therapeutic Ultrasound, 2006, 21, 164-170.

[152] McLaughlan J., Rivens I. H. and Ter Haar G.: A passive cavitation detection system for the monitoring of acoustic emissions for use in the optimisation of focused ultrasound surgery cancer treatments. Proceedings of the Spring Conference of the Institute of Acoustics, 2006, 28 (Pt1), 754-760 (CD).

[153] Fedele F, Coleman A. J. ,Leighton T. G, White P. R, Hurrell A. M. A new diagnostic sensor for Extracorporeal Shockwave Lithotripsy. Acoustics Bulletin, July/August 2004, 34-39.

[154] Fedele F., Coleman A. J., Leighton T. G., White P. R., Humphrey V. F., Ryves S., Hurrell A. M., Finfer D. C. : An ultrasound based passive monitoring system for ESWL. Proceedings of the Spring Conference of the Institute of Acoustics, 2006, 28 (Pt1), 770-773 (CD).

[155] Leighton T. G., Fedele F., Coleman A., McCarthy C., Jamaluddin A. R., Turangan C. K., Ball G. J., Ryves S., Hurrell A., De Stefano A., White P. R.. The development of a passive acoustic device for monitoring the effectiveness of shockwave lithotripsy in real time. Proceedings of the 7th European Acoustics Association International Symposium on Hydroacoustics, 2008 (in press).

[156] Leighton T. G., Fedele F., Coleman A., McCarthy C., Ryves S., Hurrell A., De Stefano A., White P. R. Clinical Studies Of Real-Time Monitoring Of Lithotripter Performance Using Passive Acoustic Sensors. Proceedings of the 2nd International Urolithiasis Research Symposium, 2008, Indianapolis, (submitted).